



University Library

Author/Filing Title AL-ANZI, B.

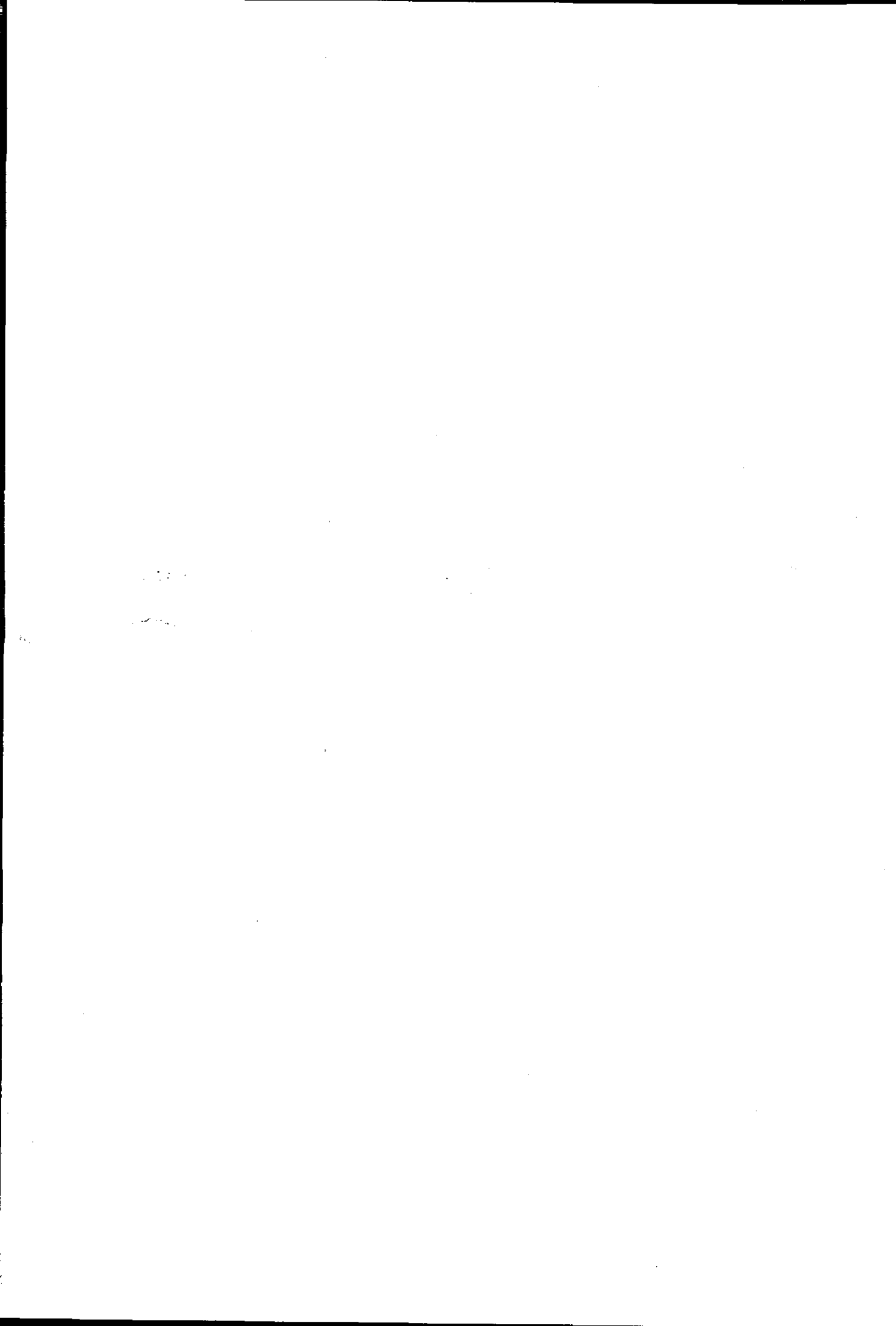
Class Mark T

Please note that fines are charged on ALL
overdue items.

FOR REFERENCE ONLY

0403604060







**PERFORMANCE OF A NOVEL CONFINED
PLUNGING JET REACTOR INCORPORATING
AN ANNULAR AIR LIFT COLUMN**

by

BADER AL-ANZI

**A Doctoral Thesis submitted in partial fulfilment of the requirements
for award of degree of Doctor Philosophy of Loughborough
University**

© by B. Al-Anzi (2007)



Loughborough
University
Fitzington Library

Date 6/2008

Class T

Acc
No. 0403604060

Acknowledgements

Beginning I thank Almighty Allah (God) for blessing me with this success and prosperity.

Thanks and gratitude to my parents who have done their utmost to be there for me throughout my life.

I wish to express my deep thanks to my employer KISR represented by Dr. Abdul-Hadi Al-Otaibi , Dr. Nader Al-Awahdi and Dr. Mohammed Al-Rashed for their trust and support. Also I would like to appreciate the management and the sponsorship provided by the training department at KISR to pursue my study leading towards a PhD degree at Loughborough University. My gratitude and thanks go to the Embassy of the State of Kuwait for the proper follow-up that I have received.

I was blessed to have a very kind giving person such as professor Richard Wakeman. He took a great deal of his time to meet with me regularly. Thank you Professor Richard Wakeman for your supervision and being there for me as well as my colleagues.

I would like to take this golden opportunity to show my appreciation, gratitude and deep thanks to Dr. Iain W. Cumming for his guidance and contribution. Your comments were valuable and very helpful, thank you for taking a great deal of your time to improve my work. The assistance received by Professor Chris D. Rielly is highly appreciated.

I wish to acknowledge Mr. Chris Manning for improving the AutoCAD sketches.

Also, I would like to thank the lab technicians Graham Moody and Kim Winfer for helping me with the fittings and connections. My thanks also go to Steve Syson and Steve Bowler for doing a great job manufacturing the new equipment.

To all of my family members especially my older brother Fahad, my ideal, I do not know how to thank you after what you have given me of love and prayers.

Last, I would like to acknowledge my wife for her support and encouragement throughout my PhD.

ABSTRACT

In this thesis experiments were carried out to achieve the desired objectives of investigating the performance of a novel confined plunging liquid jet reactor incorporating an annular riser. Air entrainment measurements were made using different confining tubes and the induced flow in the annular tube surrounding the confining tube was measured. The oxygen transfer achieved was also determined and compared with other contacting devices. A literature survey regarding the theoretical and experimental work relevant to unconfined and confined systems, air-lift column and mass transfer has been carried out. The experiments include novel equipment utilized to make the lab measurements including air entrainment and novel air-lift column measurements. The theoretical part of the thesis contains a new model derivation to predict the liquid flow rate in the annular riser, which compares well with the experimental measurements.

The objective of the first pilot plant experiments is to make air entrainment rate measurements and to investigate the effect of main variables on air entrainment rate. This enables the research to develop a better understanding of the Confined Plunging Liquid Jet Reactor (CPLJR) as an aeration process, of interest of Kuwait Institute for Scientific Research (KISR) and Kuwait, that can be used in various systems such as wastewater treatment as an aerobic activated sludge process, fermentation and gas-liquid reactions.

The equipment used to make air entrainment measurements are described (section § 3.3). This enables the researcher to conduct many experimental runs using different geometries (downcomer diameters and lengths, jet length, nozzle diameters and annulus diameters) in relatively short time.

The effects of the jet velocity, nozzle diameter, jet length and confining downcomer diameter on the gas entrainment ratio, Q_g / Q_j , have been investigated in a confined plunging liquid jet reactor. Various downcomer diameters (23 – 89 mm), jet lengths (200 – 400 mm) and nozzle diameters (6 – 15 mm) were used. Air entrainment results showed that the measured air entrainment ratio, for confined systems, depends on these main parameters. Further experiments studied the effects of various downcomer lengths on Q_g / Q_j , which led to a better understanding of conditions where gas could disentrain within the confining column. Greater bubble penetration depth was achieved with longer and narrower downcomer (23 mm in this case) for all of the nozzles. The highest gas entrainment ratios were achieved when the downcomer to nozzle diameter was greater than about 5, so long as the liquid superficial velocity was sufficient to carry bubbles downward. A non-dimensional correlation relating Q_g / Q_j to Re_j , L_j / d_n and D_c / d_n has been obtained, which satisfactorily characterised the experimental results. Mechanisms are proposed in the present study that explain gas disentrainment and other phenomena inside the confining downcomer as the jet velocity is varied.

A method of measuring the induced flow in an annular riser surrounding the downcomer tube is described. This used annular rings, measuring conductivity, fitted inside of the annular tube and the time for a salt tracer to pass from one ring to next was used to determine the induced flow.

The effects of the air entrainment rate and annulus diameter on water flow rate in the riser have been investigated experimentally and have been compared to a derived hydraulic model. Various nozzle diameters (6 – 15 mm) and annulus diameters (74 – 144 mm) were used. The hydraulic model is developed to predict the water flow rate (Q_{la}) in the annulus induced by the gas-liquid mixture produced by the plunging jet. The model is based on an energy balance carried out over the annular riser. This model is tested against experimental data over a range of liquid flow rates, nozzle and annulus diameters; it was found that the theoretical model predicted the experimental data fairly well. The agreement improves as the jet velocity increases and for decreasing nozzle diameter. Better predictions are achieved with narrower annular risers. Results also show that Q_{la} increases as annulus diameter increases. The annulus effect on gas entrainment rate (Q_g) was found to be negligible.

The gas absorption rate was measured for a confined plunging liquid jet, issuing into an air-lift column in a receiving pool, over a range of jet operating conditions and annulus diameters. Two risers 94 mm and 144 mm diameter, two nozzles 8 mm and 12 mm diameter and a downcomer of 23 mm diameter were used when making the absorption measurements. A plunging liquid jet reactor (confined and unconfined) is characterised by plug flow, where the concentration changes as gas liquid mixture flow downwards together. Hence, in the present work emphasis is on use of Overall Efficiency of the device, OE , because the system is not well mixed and therefore it is not accurate to express mass transfer by K_La without a satisfactory model of the process. Overall efficiency of the device measures the amount of dissolved oxygen per unit of the jet power (kg O_2 /kWh). All of the results show that mass transfer rate decreases gradually and then levels off at high jet power. Gas absorption rate increases with nozzle and annulus diameters. High OE were measured at low jet velocity and hence power input. Similar behaviour was reported by previous authors utilizing various Plunging Liquid Jet Reactors (i.e. confined and unconfined systems). However, the values obtained in the current work exceeded those of other PLJR systems by up to two to five times of that obtained by confined and unconfined devices respectively.

Finally, new ideas (chapter 10) and modifications are proposed that may enhance and improve the measurements of air entrainment, air-lift column and mass transfer rate.

Keywords: Plunging jet; air entrainment; downcomer length; bubble penetration depth; conductance; electrode rings; air-lift; theoretical model; annulus; mass transfer.

Table of Contents

Acknowledgements.....	i
ABSTRACT.....	ii
Table of Contents.....	iv
List of Figures.....	viii
List of Tables.....	xv
Nomenclature.....	xvi
Introduction.....	1
1.1 Objective	4
1.2 Structure of the Thesis.....	7
Chapter 2: Literature Survey and Background.....	9
2.1 Unconfined Plunging Liquid Jet Reactors	10
2.1.1 Background.....	10
2.1.2 Mechanisms of air-entrainment	10
2.1.3 Gas entrainment rate	13
2.1.4 Apparatus.....	21
2.1.5 Main variables.....	23
2.1.6 Gas entrainment rate results in an unconfined system	24
2.2 Confined Plunging Liquid Jet Reactors	25
2.2.1 Mechanisms	25
2.2.2 Gas entrainment rate in a confined system	26
2.2.3 Apparatus.....	27
2.2.4 Main variables.....	32
Chapter 3: Experimental Apparatus and Methodology for Air Entrainment Rate.....	33
3.1 Introduction.....	34
3.2 Experimental Work:.....	34
3.2.1 Air tapping design.....	36
3.3 Novel Designed Equipment	37
3.3.1 Nozzle and cover flange design	37
3.3.2 Supporting flanges design.....	39
3.3.3 Downcomer design	41
3.4 Modifications:.....	50
3.4.1 Soap bubble meter:	50
3.5 Experimental Methodology.....	51
3.5.1 Air entrainment rate measurements	51
3.6 Conclusions.....	52
Chapter 4: Results and Discussions.....	53

4.1	Introduction.....	54
4.2	Results and Discussion:	54
4.2.1	Effect of main variables	54
4.3	Fitting the Data	74
4.4	Mechanisms	78
4.4.1	Smooth (low velocity) jets	78
4.4.2	Moderate velocity jets.....	80
4.4.3	Rough (high velocity) jets.....	80
4.4.4	Bubble formation	87
4.5	Conclusions.....	90
Chapter 5: Background of two phase flow behaviour in Air-lift Column.....		
92		
5.1	Air-Lift Column Literature Survey	93
5.1.1	Introduction.....	93
5.1.2	Void Fraction calculation.....	94
5.2	Velocity in Air-Lift Column.....	100
5.3	Prediction of Air-Lift Reactor Performance.....	103
5.3.1	Frictional pressure gradient.....	104
5.4	Objective and Conclusions	110
Chapter 6: Conductance Measurements Utilising Electrode Rings		
112		
6.1	Introduction.....	113
6.2	Experimental Apparatus	113
6.3	Experimental Methodology.....	114
6.4	Results and Discussion.....	116
6.4.1	Concentration of salt measurement.....	116
6.5	Conclusions	118
Chapter 7: Air-Lift Column Model Development and Experimental work.....		
119		
7.1	Introduction.....	120
7.2	Air-Lift Column Model	120
7.2.1	Entrained liquid flow rate	121
7.3	Void Fraction.....	125
7.3.1	Downcomer.....	125
7.3.2	Annulus (Annular riser)	126
7.4	Pressure Drop (Energy Balance):.....	127
7.4.1	Energy Balance at 1	128
7.4.2	Energy Balance at 2	130
7.5	Experimental Work	131

7.5.1	Apparatus	131
7.5.2	Air-lift column design details	132
7.5.3	Experimental methodology	135
7.6	Estimation of Liquid velocity and Axial Dispersion in the Annulus.....	137
7.6.1	Theory	138
7.7	Solving for Air-Lift Column Variables.....	143
Chapter 8:	Air-Lift Column Results and Discussions.....	145
8.1	Results and Discussion.....	146
8.1.1	Introduction.....	146
8.1.2	Experimental measurements and discussions of induced Flow	146
8.1.3	Comparison between the model and experimental measurements.....	156
8.1.4	Prediction of frictional pressure gradient (dp/dl) _f	165
8.1.5	Sensitivity analysis	173
8.1.6	Phenomena.....	177
8.2	Conclusions	181
Chapter 9:	Mass Transfer.....	182
9.1	Introduction.....	183
9.1.1	Oxygenation efficiency (<i>OE</i>)	188
9.1.2	Unconfined Systems	189
9.1.3	Confined Systems	190
9.2	Experimental Work	191
9.2.1	Apparatus	191
9.3	Theory	194
9.4	Results and Discussions	200
9.4.1	Evaluating time constant and oxygen efficiency.....	200
9.4.2	Nozzle effect on mass transfer	205
9.4.3	Riser Effect on Mass Transfer	206
9.4.4	Comparison of oxygenation efficiency (<i>OE</i>) with literature.....	208
9.4.5	Correlation	211
9.5	Conclusion.....	212
Chapter 10:	Conclusions and Recommendations.....	213
10.1	Conclusions.....	214
10.2	Recommendations.....	216
10.2.1	Downcomer with longitudinal baffles and sieve	217
10.2.2	Downcomer with arms	218
10.2.3	Downcomer as a bubble distributor	219
10.2.4	Total, measured and dis- entrainment apparatus	220
10.2.5	Recycling of oxygen in CPJR	222
Appendices.....	232	
Appendix I	Example of an Induced Air Calculations.....	233
Appendix II	Air Entrainment System.....	234

Appendix III	Mass Transfer Calculations.....	238
Appendix IV	Risk Assessment.....	241
Appendix V	Technical Designs	243
Appendix VI	Publications	246

List of Figures

Figure 1.1 Unconfined plunging jet reactor (Cumming and Rielly, 2004).....	2
Figure 1.2 Confined plunging jet (Al-Anzi <i>et al.</i> , 2006).	3
Figure 2.1 Air entrainment mechanisms as jet velocity increases from (a) to (b) (van de Donk, 1981; Bin, 1993; After van de Sande, 1974).....	11
Figure 2.2 Air entrainment mechanisms (Dvaoust <i>et al.</i> 2002, after McKeogh and Ervine, 1981; Ohl <i>et al.</i> , 2000).	12
Figure 2.3 Unconfined bubble column used by Yamagiwa <i>et al</i> (1990)..	14
Figure 2.4 Experimental set-up utilized by Ohkawa <i>et al.</i> (1986a)..	15
Figure 2.5 Nozzle types that were used by van de Donk (1981), a) Conical nozzles, b) Flat entry and c) Twisted spiral.	17
Figure 2.6 The apparatus used by Van de Donk (thesis, 1981).	17
Figure 2.7 Experimental apparatus used by McKeogh and Ervine (1981).....	18
Figure 2.8 Air entrainment rate due to jet surface and boundary layer.	20
Figure 2.9 Correlations for unconfined systems.	24
Figure 2.10 A plunging jet reactor used by Cumming <i>et al.</i> (2002).....	29
Figure 2.11 Experimental set-up for the jet system with downcomer utilized by Ohkawa <i>et al.</i> (1986a).....	30
Figure 2.12 Experimental apparatus used by Evans <i>et al.</i> (1996)	30
Figure 2.13 Experimental apparatus used by Evans and Jameson (1995).....	31
Figure 3.1 Experimental apparatus for confined plunging liquid jet reactor used in the current study.....	35
Figure 3.2 Nozzle design; a) nozzle geometry and b) nozzle cap.	38
Figure 3.3 Schematic diagram of a) pipe and cover flange, and b) nozzle, pipe and cover flange connected together.	39
Figure 3.4 a) Top and b) lower parts for the supporting flanges.	40
Figure 3.5 Complete set of the supporting flanges where 1 and 2 refer to top and lower flanges, respectively.....	41
Figure 3.6 Final shape of the downcomers for $50 \leq D_c \leq 89$ mm.....	42
Figure 3.7 Downcomer with extended neck.	43
Figure 3.8 Downcomer fixed directly to the nozzle.	44

Figure 3.9 Schematic of the new design equipments.....	45
Figure 3.10 Gradual contraction for conical nozzle.....	47
Figure 3.11 Pressure drop due to gradual contractions for various angles	49
Figure 3.12 Downcomers utilized in the current work.	49
Figure 3.13 Bubble meter with slight modification.	50
Figure 4.1 The effect of the liquid jet velocity and jet length on the entrainment air flow rate 600 mm downcomer length, $d_n = 6$ mm and $D_c = 23$ mm.	57
Figure 4.2 The effect of the liquid jet velocity and jet length on the entrainment air flow rate 600 mm downcomer length, $d_n = 15$ mm and $D_c = 23$ mm.	57
Figure 4.3 Air entrainment with same d_n , D_c , Q_j and a) $L_j = 30$ mm and b) $L_j = 40$ mm.	59
Figure 4.4 The effect of jet length and jet velocity on the entrained gas flowrate 600 mm downcomer length, $d_n = 6$ mm and $D_c = 23$ mm.	59
Figure 4.5 The effect of jet length and jet velocity on the entrained gas flowrate 600 mm downcomer length, $d_n = 8$ mm and $D_c = 38$ mm.	60
Figure 4.6 The effect of downcomer diameter and jet velocity on the entrained gas flowrate 600 mm downcomer length, $d_n = 15$ mm and (a) $L_j = 200$ mm, $H_c = 400$ mm (b) $L_j = 400$ mm, $H_c = 200$ mm.	61
Figure 4.7 Effect of nozzle diameter on air entrainment rate.	63
Figure 4.8 Air entrainment rate for both pumps with $D_c = 71$ mm, $d_n = 15$ mm and $L_j = 400$ mm.	65
Figure 4.9 Air entrainment rate for both pumps with $D_c = 50.5$ mm, $d_n = 15$ mm and $L_j = 400$ mm.	65
Figure 4.10 Air entrainment rate for new pump with and without a baffle for $L_j = 400$ mm, $D_c = 23$ mm, $d_n = 12$ mm and $L_D = 1350$ mm.	66
Figure 4.11 The effect of the downcomer length on the entrainment rate ratio $d_n = 15$ mm and $D_c = 23$ mm, filled symbols: 600 mm downcomer and open symbols: 1350 mm downcomer	69
Figure 4.12 The effect of the downcomer length on the entrainment rate ratio $d_n = 12$ mm and $D_c = 23$ mm, filled symbols: 600 mm downcomer and open symbols: 1350 mm downcomer	70
Figure 4.13 Expansion of the two-phase jet in (a) a long downcomer and (b) a short downcomer.....	71

Figure 4.14 The effect of the downcomer length on the entrainment rate ratio $d_n = 12$ mm and $D_c = 23$ mm, filled symbols: 600 mm downcomer and open symbols: 1350 mm downcomer72

Figure 4.15 The effect of the downcomer length on the entrainment rate ratio $d_n = 6$ mm and $D_c = 23$ mm, filled symbols: 600 mm downcomer and open symbols: 1350 mm downcomer73

Figure 4.16 The effect of the downcomer length on the entrainment rate ratio $d_n = 12$ mm and $D_c = 23$ mm, square symbols: 600 mm downcomer, circle symbols: 800 mm downcomer and open symbols: 1350 mm downcomer.....74

Figure 4.17 Comparison of the dimensionless correlation of eq.(8) with the experimental data set, showing an error band of $\pm 30\%$77

Figure 4.18 Cavity in a vortex manner inside the downcomer caused by smooth jet.79

Figure 4.19 Smooth Jet surface and a reduction on the jet diameter at low jet velocity.79

Figure 4.20 Top part of the 23 mm downcomer a) side and b) front view, where small bubbles can be barely seen.....81

Figure 4.21 Sporadic (ellipsoidal) bubbles at the a) middle and b) bottom parts of the downcomer.....82

Figure 4.22 Circular and vortex motions pivots.82

Figure 4.23 a) Top part that shows longer L_{cm} and b) bottom parts that shows train of bubbles of the downcomer at moderate jet velocity.83

Figure 4.24 a) Top, b) middle and c) bottom parts of the downcomer that show the dense white cloud, of air and water, surrounded by water ring toward the end of the downcomer.....85

Figure 4.25 White cloud diameter did not change in the downward direction, and visible bubbles form outside of the downcomer.86

Figure 4.26 Schematic of the mechanisms at high turbulent jet.87

Figure 4.27 a) Schematic and b) actual picture of air entrainment mechanism for high jet velocity (Turbulent).89

Figure 4.28 Schematic that shows Q_{TA} , Q_N and Q_{DS}91

Figure 5.1 Apparatus of the CPLJR air-lift column used in the current study..94

Figure 5.2 Experimental apparatus utilized by Akita *et al.* (1988).99

Figure 5.3 Schematic of the apparatus used by Jones (1985).100

Figure 5.4 Schematic diagram of fermenter configuration and electronic units (<i>Fields et al.</i> , 1983).	101
Figure 6.1 Apparatus used to make voidage measurements.	115
Figure 6.2 Bubbles as they leave the pipette filler (Sparger).	116
Figure 6.3 Electrode rings responses for different salt concentrations.	117
Figure 6.4 Voltage responses by the probes as salt concentration increases.	118
Figure 7.1 Schematic of the air-lift column in CPLJR.	120
Figure 7.2 Schematic for the downcomer.	122
Figure 7.3 Schematic of the annulus as a control volume.	123
Figure 7.4 Schematic of the air-lift column utilized in CPLJR.	128
Figure 7.5 One of the annuli (74 mm) utilised in the thesis.	133
Figure 7.6 (a) Connection point between the annulus and the PC, and (b) Top part of the annulus that shows the strand wire, electrode rings and the balloon.	134
Figure 7.7 Schematic of the air-lift column in the CPLJR used in the current study.	136
Figure 7.8 Typical concentration (dimensionless) time histories for input and output probe locations in a two-phase upflow recorded in the current study.	138
Figure 7.9 Algorithm for the parameter estimation method (Rielly, 2006).	141
Figure 7.10 Typical concentration histories for the input and out put probe locations in an upflow bubble column. The best fit convoluted response is also shown.	142
Figure 8.1 Effect of annulus diameter on O_{la} for 12 mm nozzle.	147
Figure 8.2 Effect of annulus diameter on Q_{la} for 8 mm nozzle.	147
Figure 8.3 Effect of annulus diameter on O_{la} for 6 mm nozzle.	148
Figure 8.4 Effect of various nozzle diameters (d_n) on water flow rate up the riser (Q_{ta}) for 94 mm annulus as jet flow rate (Q_j) increases.	149
Figure 8.5 Air entrainment measured by three different annuluses and 6 mm for a given conditions.	150
Figure 8.6 Air entrainment measured by three different annuluses and 8 mm for a given conditions.	150
Figure 8.7 Concentration time histories of injected tracer detected by electrode rings mounted on the wall of the air-lift column for 6 mm as the jet flow rate increases from 16 L/min to 30 L/min for the 74 mm Annulus.	152

Figure 8.8 Concentration time histories of injected tracer detected by electrode rings for 6 mm nozzle and 16 L/min as the annulus diameter increases from 74 mm to 144 mm. 154

Figure 8.9 a) Concentration time histories and b) delay time responses for tracers before and after the increase of salt concentration and dosage volume for 144 mm Annulus. 155

Figure 8.10 Bubbles distribution inside 74 mm annulus for a) and c) moderate V_j where most of the bubbles are located in one side of the annulus, and b) and d) high V_j where the two phase flow occupies all of the annulus. 158

Figure 8.11 Experimental and theoretical results for all nozzles and 74 mm annulus diameter. 159

Figure 8.12 Experimental and theoretical results for all nozzles and 94 mm annulus diameter. 160

Figure 8.13 Comparison between the experimental and theoretical results for all of the nozzles and the 74 mm annulus. 161

Figure 8.14 Experimental and theoretical results for 74 mm annulus and 8 mm nozzle. 162

Figure 8.15 Experimental and theoretical results for larger annulus, 94 mm, and 8 mm nozzle. 163

Figure 8.16 Experimental and theoretical results for largest annulus, 144 mm, and 8 mm nozzle. 163

Figure 8.17 Time history generated by $d_n = 8$ mm and $Q_j = 36$ l/min for $D_a =$ a) 94 with one peak and b) 144 mm with two peaks respectively. 164

Figure 8.18 Layout of the theoretical model used to calculate Q_{ta} and other variables. 166

Figure 8.19 Theoretical and experimental results, using different models, for 6 mm nozzle and 74 mm annulus. 167

Figure 8.20 Theoretical and experimental results, using different models, for 8 mm nozzle and 74 mm annulus. 168

Figure 8.21 Theoretical and experimental results, using different models, for 12 mm nozzle and 74 mm annulus. 169

Figure 8.22 Theoretical and experimental results, using different models, for 15 mm nozzle and 74 mm annulus. 170

Figure 8.23 Effect of using different frictional pressure gradient correlations on the theoretical model for 6 mm nozzle and 74 mm annulus.	171
Figure 8.24 Effect of using different frictional pressure gradient correlations on the theoretical model for 12 mm nozzle and 74 mm annulus.	172
Figure 8.25 Differences between the correlations that are used to predict pressure frictional gradient $(dp/dl)_f$	172
Figure 8.26 Effect of V_b and C_0 on the theoretical model.	174
Figure 8.27 Effect of the frictional pressure gradient on the theoretical model ($d_n = 6\text{mm}$ and $D_a = 74\text{ mm}$).	175
Figure 8.28 Effect of the constant and sudden contraction on the theoretical model ($d_n = 6\text{ mm}$ and $D_a = 74\text{ mm}$).	177
Figure 8.29 Penetration depth for two-phase mixture increases as the jet flowrate increases for a given conditions.	179
Figure 8.30 Fountain head increases as the jet velocity for a given condition increases.	180
Figure 9.1 Proposed model for the flow rates in the pool liquid (van de Sade and Smith, 1975).	184
Figure 9.2 Schematic of the plunging liquid jet reactor used by Evans and Machniewski (1999) and Evans <i>et al.</i> (2001).	185
Figure 9.3 Schematic of the model proposed by Low (2003).	186
Figure 9.4 limits of Overall Efficiency OE	187
Figure 9.5 Schematic of air-lift column apparatus combined with confined jet to measure OE	193
Figure 9.6 Oxygen removal by introducing nitrogen.	194
Figure 9.7 an example of aeration carried out in the current work.	195
Figure 9.8 Idealized performance of plunging jet reactor.	197
Figure 9.9 First step response of the concentration generated experimentally.	199
Figure 9.10 Adjusted oxygen reading.	200
Figure 9.11 Probe response.	201
Figure 9.12 Probe response for measured and theoretical data.	201
Figure 9.13 Dissolved oxygen concentrations measured in the current work.	203
Figure 9.14 Oxygenation efficiency measured by different nozzles and larger riser.	205

Figure 9.15 Oxygenation efficiency measured by different nozzles and smaller riser	206
Figure 9.16 Effect of riser diameter on <i>OE</i> for larger nozzle	207
Figure 9.17 Effect of riser diameter on <i>OE</i> for smaller nozzle.....	207
Figure 9.18 <i>OE</i> results measured by Low (2003) and current work for 12 mm nozzle	208
Figure 9.19 <i>OE</i> results measured by van de Sande (1975) and current work for 12 mm nozzle.	209
Figure 9.20 <i>OE</i> results measured by van de Sande (1975) and current work for 8 mm nozzle.	210
Figure 9.21 <i>OE</i> results measured by van de Dank (1981) and current work for different nozzles	210
Figure 9.22 Correlation for the present work.....	211
Figure 10.1 Downcomers featuring a) longitudinal baffles and b) seive.....	219
Figure 10.2 Downcomer with extended arms.....	220
Figure 10.3 Downcomer (as a bubble distributor) with pipe network	221
Figure 10.4 A system to measure total, net and dis- air entrainment flowrate rates in the ame run.....	222
Figure 10.5 Reuse of the feed gas by installing a hood on top of the annulus riser	223

List of Tables

Table 2.1 Dimensions of the variables used in the experiment (Yamagiwa <i>et al.</i> , 1990).	13
Table 2.2 Experimental conditions and correlations by various authors for unconfined system.	23
Table 2.3 Experimental conditions and correlations by various authors for confined systems.	32
Table 3.1 Range of parameters used in the experiment.	46
Table 4.1 Values of C and n by numerical and regression methods.....	55
Table 4.2 Variables in fundamental dimensions.....	76
Table 5.1 Values of constant C for various flow combinations.....	109
Table 9.1 Variables in fundamental dimensions.....	192
Table 9.2 Values of constant C for various flow combinations.....	205

Nomenclature

$A =$	cross sectional area
$C_E =$	capacitance
$C =$	constant or concentration at time t
$C_c =$	contraction coefficient
$C_i =$	initial concentration
$C_0 =$	ratio of centre line velocity: the mean velocity (Kay and Nedderman) or distribution parameter (Zuber and Findlay)
$C_\infty =$	final concentration
$C_f =$	friction coefficient
$D_r =$	air ring diameter surrounding the jet
$D_a =$	annulus diameter
$d =$	diameter
$d_e =$	equivalent diameter
$D_c =$	downcomer diameter
$D_{dis} =$	dispersion coefficient
$E =$	energy or dielectric energy
$E/r =$	roughness factor
$g =$	acceleration
$G =$	mass flux
$H =$	height or vertical distance
$h =$	static head
$h_f =$	pressure loss head
$\Delta h =$	height displayed by the manometer
$i =$	number of independent dimensionless (Buckingham's pi theorem)
$j =$	superficial velocity
$K_I =$	resistance coefficient for gradual contraction
$L =$	length
$l =$	straight part of the nozzle
$M =$	mass flowrate
$n =$	velocity index
$n_v =$	number of variables in Buckingham's theorem
$Pe =$	peclet number
$P =$	pressure
$P_L =$	Wetted perimeter
$P_w =$	jet power
$\Delta P =$	pressure drop
$\Delta P_k =$	pressure drop due to kinetic energy
$Q =$	volumetric flowrate
$r =$	rank of the dimensional matrix
$t_{corr.} =$	mean residence time (convective time)
$T =$	time
$\bar{V} =$	average specific volume, a function of the gas and liquid specific volumes and the mass fraction of gas.
$VG =$	gas volume
$v =$	interstitial (linear) velocity

$V_L =$	liquid volume
$\bar{V} =$	mean velocity
$\bar{v} =$	specific volume
$V_\infty =$	terminal rise velocity of a bubble in an infinite medium (rise velocity for a single bubble)
$V =$	velocity
$w =$	weight fraction
$z =$	depth of liquid in annulus

Greek Letter

$\alpha =$	angle
$\rho =$	density
$E =$	dielectric constant
$\nu =$	kinematic viscosity
$\bar{\mu} =$	mean viscosity
$\Delta\rho =$	mixture density
$\Theta =$	nozzle or contraction angle
$\tau =$	shear stress
$\sigma =$	surface tension
$\phi^2 =$	two-phase multiplier
$\varepsilon =$	void fraction
$\pi =$	viscosity

Subscript

$A =$	air
$A1 =$	air entrainment as boundary layer
$A2 =$	air entrainment by the jet surface
$Ad =$	air in the downcomer
$At =$	air tube
$a =$	annulus
$b =$	bubble
$DS =$	disentrainment
$D =$	downcomer (concentric tube)
$ds =$	downcomer submergence
$E =$	electric rings
$e =$	equivalent
$em =$	minimum entrainment rate velocity
$f =$	friction
$g =$	gas
$gl =$	gas relative to liquid
$H =$	head
$i =$	inside of a pipe
$j =$	jet
$jd =$	jet in the downcomer
$le =$	entrained liquid from the surrounding
$l =$	liquid
$la =$	liquid in the annulus

$ld =$	liquid in the downcomer
$N =$	net entrainment air
$n =$	nozzle
$o =$	outside
$p =$	probes
$sa =$	liquid surface of the annulus
$SB =$	soap bubble
$sd =$	liquid surface of the downcomer
$TA =$	total entrained air
$tm =$	toroidal motion
$t =$	tube
$w =$	tube wall
$1 =$	pressure at the bottom of the downcomer
$2 =$	pressure surrounding the annulus

Dimensionless group

$Fr =$ Froude number $= V_j^2 / d_n g$

$Re =$ Reynolds number $= \frac{d_n V_j}{\nu}$

Acronyms

CPLJR = confined plunging liquid jet reactor

OE = oxygenation efficiency

Introduction

Gas entrainment can naturally occur due to the impact of a liquid, moving at high velocity, into a stagnant pool of the same fluid. This phenomenon can be helpful or harmful depending on the application. It is desirable when it reduces the abrasion (e.g. waterfall, breaking waves and chutes) or increases the gas-liquid interfacial area, which increases the mass transfer. However, it is highly unwanted when it comes to certain fluid processes such as filling and pouring of molten glass and metals during industrial applications. Therefore, studying this phenomenon has been of interest to many authors. A commonly used system to provide a large gas/liquid interfacial area is a plunging jet reactor.

Gas-liquid reactors are employed in a variety of processes, such as reaction in the chemical industry as well as aerobic for wastewater treatment, air pollution abatement, froth flotation and fermentation, where typically the objective is to contact the two phases to promote mass transfer. The plunging jet reactor concept has been in use for several decades, as a means of achieving high mass transfer rates by entraining gas bubbles into a liquid, at low capital and operating costs. In comparison to conventional sparged systems, such as bubbling a gas into a liquid pool, plunging jet devices are able to improve gas absorption rates by creating a fine dispersion of bubbles and by increasing the contact time between the gas bubbles and the water, at relatively low power inputs.

As the liquid plunges through the surrounding headspace of the reactor (Figure 1.1), gas is being entrained by the jet. This entrainment can be classified as entrainment due to jet roughness (within the jet envelope) or as a boundary layer that is established along the jet. However this depends on the flow regime (e.g. laminar, transition or turbulent). As a high velocity jet hits the surface of a stagnant liquid, a depression (cavity) in the liquid surface is established that is rapidly (in some cases) converted into a swirl motion. This phenomenon drags the gas downward into the receiving liquid as shown in Figure 1.1. The entrained gas travels downward in the form of bubbles, beneath

the pool surface, forming a two-phase flow to a certain depth. A conical biphasic region is established beneath the liquid surface. This region contains two types of bubbles: primary bubbles (tiny bubbles about 1mm) located at the top and secondary bubbles (about 4 mm). The secondary bubbles result from the coalescence of the primary bubbles. Usually, the secondary bubbles are located at the bottom of the conical region. As shown in Figure 1.1, the two-phase mixture rises back up as the larger bubbles (secondary) escape from the sides of the conical region, due to buoyancy. The penetration depth depends on the jet velocity as well as the entrained gas buoyancy, and the type of reactor (confined or unconfined). Mass transfer occurs at the bubble surface contacts the surrounding liquid (interfacial area), which depends on the time of contact, jet penetration depth and the level of turbulence.

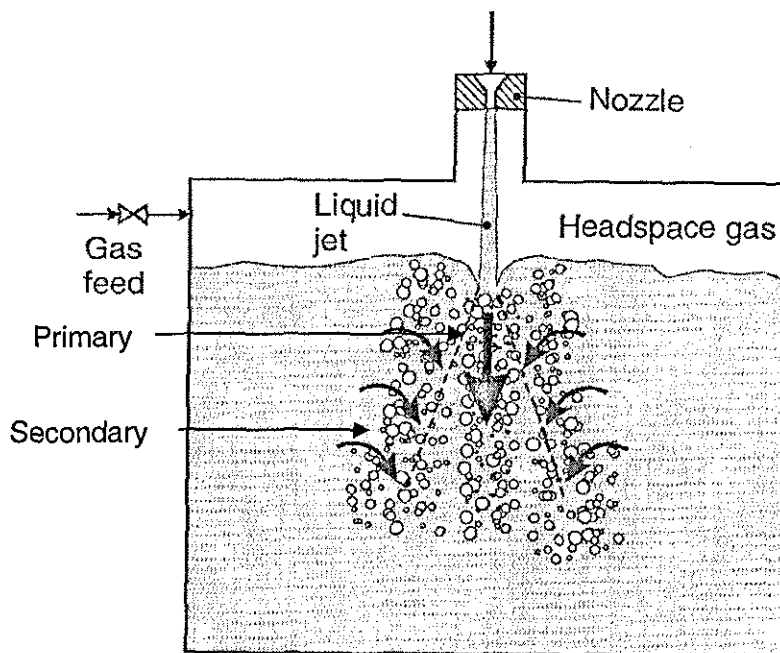


Figure 1.1 Unconfined plunging jet reactor (Cumming and Rielly, 2004)

Plunging jets can be used as either unconfined or confined devices. An unconfined plunging jet reactor comprises a tank filled with liquid to a desired level and a

nozzle located at the top of the tank as shown in Figure 1.1. In unconfined systems the liquid jet plunges into an open liquid pool, creating a conical downflow dispersion of fine bubbles and a surrounding upflow of larger coalesced bubbles (Figure 1.1). In this case, the penetration depth of the bubbles is small, due to spreading of the submerged jet and hence the bubble contact time with liquid is short. Another type of jet reactor is defined as Confined Plunging Liquid Jet Reactor (CPLJR). As shown by Figure 1.2, this system consists of a vertical tube that is partially immersed in the liquid pool. The top end of the tube is connected to a nozzle, whilst the other end (bottom) is left open to the receiving liquid pool. This tube is called a confining tube. The CPLJR reactor is utilized to try to improve the gas mass rate transfer into liquid. This can be achieved by increasing the jet penetration depth and the contact time between the gas and liquid. Also, by increasing the gas-liquid contact surface through hindering or reducing primary bubbles coalescence into secondary ones (smaller bubbles give better mass transfer rate) may in turn enhance the plunging jet reactor efficiency with regards to mass transfer rate.

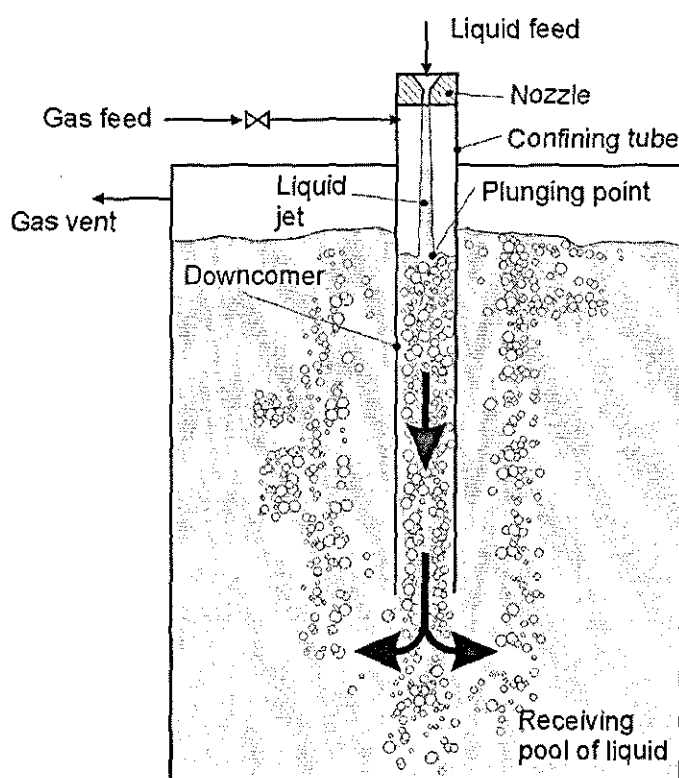


Figure 1.2 Confined plunging jet (Al-Anzi *et al.*, 2006).

1.1 Objective

The main objective of this study is to investigate a new aeration process of interest to Kuwait Institute for Scientific Research (KISR) and countries like Kuwait for efficient aerobic wastewater treatment. A confined plunging liquid jet reactor has many advantages over the conventional methods. The advantages can be summarized into the following points,

- (i) Economical system: no compressor is needed for gas recycle (e.g. pure oxygen), low energy input (liquid pump) and small footprint.
- (ii) Wide range of applications: (wastewater treatment, fermentation and gas-liquid reaction)
- (iii) Efficient mass transfer mechanisms: potential for high kg O₂ /kWh.

Objectives of the current work can be broadly classified based on the order of the systems studied as shown below:

- (a) Two-phase flow in CPLJR
 - (i) To investigate the effect of the experimental variables such as jet velocity V_j (or Reynolds number Re), jet length to nozzle diameter L_j/d_n , nozzle inside diameter d_n and downcomer diameter D_c on the hydrodynamics of confined plunging liquid jet reactor (e.g. minimum entrainment rate velocity for CPLJR systems and penetration depth), which will be shown in subsequent chapters.
 - (ii) To study the effect of the downcomer length on the net air entrainment rate by carrying out experimental measurements for various downcomer lengths to provide a solution to the disagreement presented in the literature over the effects of the downcomer length on the rate of

gas entrainment in confined plunging jet systems. The effect of different types of pumps is also investigated.

- (iii) To design a new equipment that is flexible (e.g. parts can be interchanged easily and quickly, and help the worker to follow the process closely) to accommodate wide range of operating variables such as d_n , L_D and D_c and provide firm support. This design will be used to make the experimental measurements.
- (iv) To conduct air entrainment experimental measurement utilising wide range of variables i.e. , downcomer diameters range from 23-89 mm, nozzle diameters range from 6-15 mm, jet lengths range from 200-400 mm and downcomer lengths range from 600-1350 mm. The effect of the main factors (jet velocity V_j , jet length L_j , nozzle diameter d_n , and downcomer diameter D_c and length L_D) on the entrainment ratio (Q_A/Q_j) utilizing a vertical plunging jet for a confined reactor will be investigated. This enables researcher to develop a better understanding and have a deeper look into the role of these factors on entrainment ratio in a CPLJR. A dimensionless correlation will be provided to predict the gas entrainment rate from the main operating variables.
- (v) To investigate the mechanisms of confined plunging jet systems to describe the bubble formation and motion within the downcomer and report any interesting observation for future work.

(b) Induced water flow rate

- (i) To investigate the validity of utilizing wall-mounted ring electrodes to detect a tracer as it passes two conductivity measuring rings in an annular riser. Using the time taken for the salt tracer to pass from one ring to the next the induced flow could be determined.
- (ii) To derive a new model to predict the induced water flow rate (Q_{la}) in the annulus.
- (iii) To carry out experimental measurements utilizing a wide range of nozzle diameters 6 – 15 mm and annulus diameters 74-144 mm. The effect of annulus diameter on water flow rate Q_{la} and gas entrainment rate Q_g will also be investigated. Comparison between the theoretical and experimental results will be provided to check the validity of the model.

(c) Mass transfer measurement

- (i) The oxygen transfer achieved by annular riser in a CPLJR device was measured and compared with that achieved by other gas liquid contacting techniques used in the water treatment industries.

1.2 Structure of the Thesis

Chapter 2 starts with an overview of the plunging jet concepts with regards to unconfined and confined reactors. Then more emphasis is put on confined plunging liquid jet reactor systems including discussion and comparison of apparatus design, results, mechanisms and correlations utilized by various authors.

Chapter 3 presents experimental setup and methodology that are used and followed to make air entrainment flow rate measurements. It features novel equipment that are designed and used to make the air entrainment measurements.

Chapter 4 contains results and discussions of the air entrainment rate experiments. Effect of main variables (V_j , L_j , D_c , d_n and L_D), fitting experimental data, observations and mechanisms are investigated in this chapter. Some mechanisms are presented in this chapter concerning. One of them is the effect of downcomer length on net air entrainment rate, which is studied and discussed in more details.

Chapter 5 provides a summary of two-phase behaviour in air lift columns utilized previously in the literature.

Chapter 6 presents an experimental set up of a new rig that was assembled by the author, to assess electrode rings performance for measuring salt concentration in two phase gas/liquid mixtures. Experimental measurements and results are discussed in the same chapter.

Chapter 7 describes the air-lift column design and a model derivation to predict induced water flow rate inside the annulus.

Chapter 8 discusses the induced flow measured in the air-lift column equipment. Results comprise: model sensitivity tests, frictional pressure gradient prediction, nozzle effect on Q_{la} , annulus diameter effect on Q_{la} and Q_A and electrode response.

Chapter 9 is about mass transfer measured in the air-lift column described in chapter 6. This chapter comprises literature review, experimental work, theory and results and discussions. Mass transfer is measured as an overall efficiency in kg O₂/kWh.

Chapter 10 presents conclusions that are drawn from the previous work (design, mechanisms, results and discussions) concerning air entrainment rate, induced water flow rate up the riser and mass transfer rate. Recommendations are provided to solve some of the existing problems and also new ideas for future work are also proposed in this chapter.

Chapter 2: Literature Survey and Background

2.1 Unconfined Plunging Liquid Jet Reactors

2.1.1 Background

Unconfined plunging jet systems have been extensively studied by a number of authors and Bin's (1993) review discusses much of the earlier work in this area.

2.1.2 Mechanisms of air-entrainment

Mechanisms of air-entrainment vary depending upon the system main parameters (jet velocity, jet length, nozzle and downcomer diameters). Above a minimum entrainment velocity, the plunging jet deforms the surface of the receiving pool and entraps gas as it passes through the liquid surface. For water jets the meniscus formed from the pool liquid is distorted by tiny ripples travelling up the jet in a stationary wave (Ciborowski and Bin, 1972; Lienhard, 1968; Lin and Donnelly, 1969; Perry, 1967). The most common mechanisms which have been adopted by many authors, are those proposed by van de Sande (1974) and McKeogh and Ervine (1981) as shown in Figures 2.1 and 2.2 respectively.

Figure 2.1 shows the stages of bubble formation described by van de Sande. At low jet velocity the entrainment is due to irregularity of the jet surface that forms a small cavity around the impact point (Figure 2.1a). At higher velocity, more gas is entrained and therefore the pool surface experiences a greater depression (Figure 2.1b). This depression goes further downward leaving a gap of air around the jet (Figure 2.1c). Shear stress forces the water to close the gap establishing bubbles under pool surface (Figure 2.1d). This technique has been adopted by Bin (1988a, 1993) and van de Donk (1981).

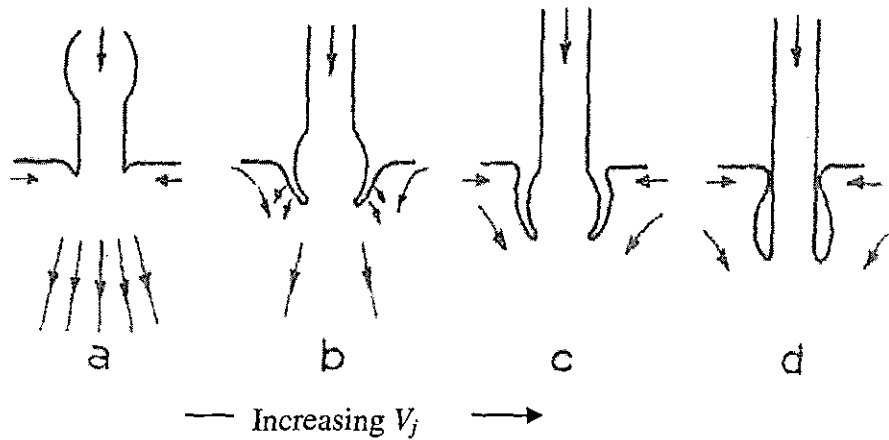


Figure 2.1 Air entrainment mechanisms as jet velocity increases from (a) to (b) (van de Donk, 1981; Bin, 1988a, 1993; After van de Sande, 1974).

Another mechanism was proposed by MecKeogh and Ervine (1981). They divided the process into four stages as shown in Figure 2.2; a) at low velocity the jet is considered to be laminar, and the depression is caused due to boundary layer accompanied with the jet (oscillating annulus, Figure 2.2 scenario #I), b) at transition state where the jet velocity lies between laminar and turbulent, the jet surface is rippled and indentation is established around the jet in a vortex manner (Figure 2.2 scenario #II), c) as jet velocity continues to increase to reach turbulent flow, jet surface as well as pool surface become rough and therefore air is captured by the intense surface roughness at the impingement point (Figure 2.2 scenario #III). As the jet velocity increases beyond scenario # III, the jet breaks up (complete disintegration) into scattered droplets. In this case entrainment is caused by each droplet when it hits the pool. However, this is beyond the interest of the present work.

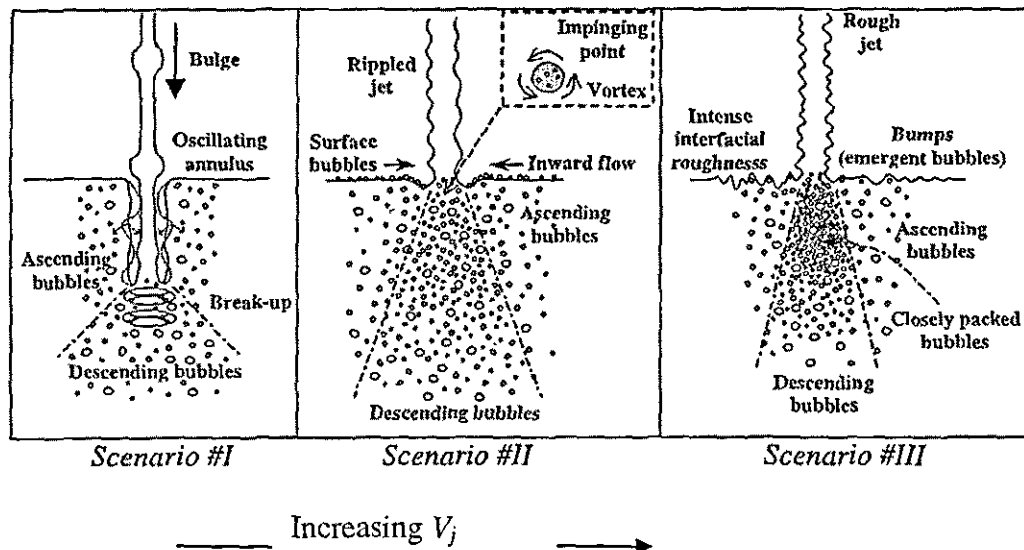


Figure 2.2 Air entrainment mechanisms (Dvaoust *et al.* 2002, after McKeogh and Ervine, 1981; Ohl *et al.*, 2000).

Comparing the foregoing mechanisms, the following points can be drawn for low and high jet velocities:

- a) At low jet velocities (below 5 ms^{-1}), both studies (Van de Sande, McKeogh and Ervine) reported almost the same path leading to bubble formation. However, they differ in how the air is being entrained. Van de Sande suggested that the entrainment is attributed to jet surface irregularities, whereas in McKeogh and Ervine the entrainment is due to the boundary layer accompanying the jet.
- b) At high jet velocities (turbulent), both of the authors suggested that the entrainment is caused by jet surface roughness and a boundary layer. McKeogh and Ervine reported that the entrainment, caused by jet and pool surfaces, is more than that of the boundary layer. Van de Sande did not specify which factor dominates at this stage.

As a conclusion from the previous work, for low jet velocity Van de Sande provides a more reasonable approach than that of McKeogh and Ervine, because at this velocity very little air is carried with the jet as a boundary layer, which is evident from the effect of the jet on the receiving pool surface (dirt or cavity instead of depression), because the jet is not surrounded with an air ring at the impingement point. This implies that little air is

associated with the jet as a boundary layer. Therefore, the entrainment is due to jet surface roughness. This was originally suggested by Henderson *et al.* (1970) and later by Burgess *et al.* (1972). At high jet velocity, neither of them provides a proper explanation. It appears that at high jet velocity, the boundary layer contribution to air entrainment rate cannot be neglected. It could reach up to 70% of the total entrainment based on Bin's (1993) suggestion.

The effect of the boundary layer can be seen at high jet velocity where the jet surface is surrounded by an air ring at the impingement point forming a surface depression on the pool surface.

2.1.3 Gas entrainment rate

This phenomenon has been of concern to many researchers trying to develop an understanding of the kinetics and mechanisms that govern gas-liquid mixture flow that affect gas mass transfer rate. Yamagiwa *et al.* (1990) investigated two phase flow, gas-air flow, under high liquid flow rates while varying the main variables within the ranges summarized in Table 2.1;

Table 2.1 Dimensions of the variables used in the experiment (Yamagiwa *et al.*, 1990).

Variable	Dimensions
d_n (nozzle diameter, mm)	8, 10, 11, 13, 15, 18, 20
L_j (jet length, mm)	30, 60, 60, 150
D_c (downcomer diameter, mm)	34, 50, 60, 70
H_{ds} (liquid height, mm)	1200, 1500, 1800, 2000

They utilized the apparatus shown in Figure 2.3, which is defined as a downflow bubble column. It is an unconfined plunging jet system, however instead of using a reservoir they used a column, which was effectively a confining tube. They showed that gas entrainment rate increased as jet velocity, V_j , jet length, L_j and nozzle diameter, d_n increased. The authors also proposed a correlation as a function of these factors, which is expressed as the following;

$$Q_A = 0.0404 V_j^{1.66} L_j^{0.48} d_n^{1.59} \quad (2.1)$$

However, they found that the gas entrainment rate was not strongly affected by the column diameter, nor by the liquid height, and hence they did not include these variables in their correlation shown as equation (2.2) in a dimensionless form.

$$\frac{Q_A}{Q_j} = 0.00224 Fr^{0.40} Re^{0.26} \left(\frac{L_j}{d_n} \right)^{0.48} \quad (2.2)$$

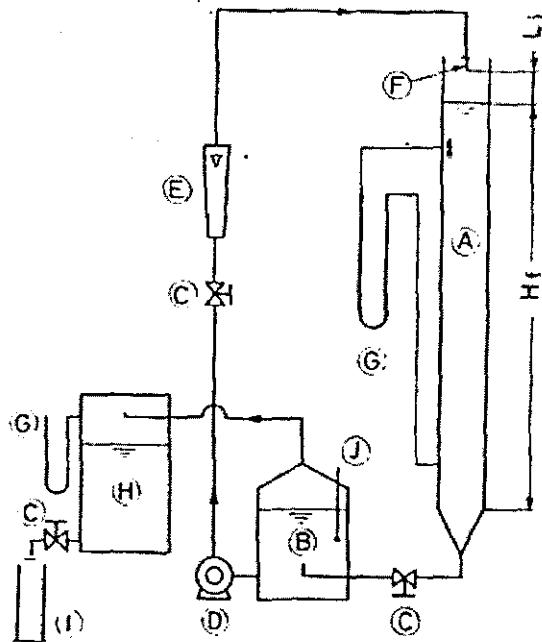


Figure 2.3 Unconfined bubble column used by Yamagiwa *et al* (1990). A, column; B, bubble separator; C, valve; D, pump; E, flowmeter; F, nozzle; G, Manometer; H, replacement vessel; I, measuring cylinder; J, thermometer.

In the previous study the author did not include the effect of the nozzle geometry and column walls on air entrainment rate. This may have significant effect in air entrainment rates and bubble penetration depth.

Jet liquid system without downcomers has been investigated by Ohkawa *et al.* (1986a, Figure 2.4). He used short cylindrical nozzles (l/d_n) with diameter ranges from 7 to 13 mm (Figure 2.4). Where l in this case is the nozzle length. The gas entrainment rate (Q_A) and ratio (Q_A/Q_j), nozzle depth, gas holdup and bubble penetration depth were measured experimentally by manipulating the main parameters such as nozzle diameter, jet velocity and nozzle height. Obtained results show that air entrainment rate (Q_A) increases linearly with jet length (L_j). It is directly proportional to jet velocity raised to power 2.3 for $V_j \leq 5$ m/s. For the middle region, $5 \leq V_j \leq 10$ m/s, Q_A is directly proportional to $V_j^{1.4}$. As jet velocity increases further, $V_j \geq 10$ m/s, Q_A is directly proportional to V_j^2 .

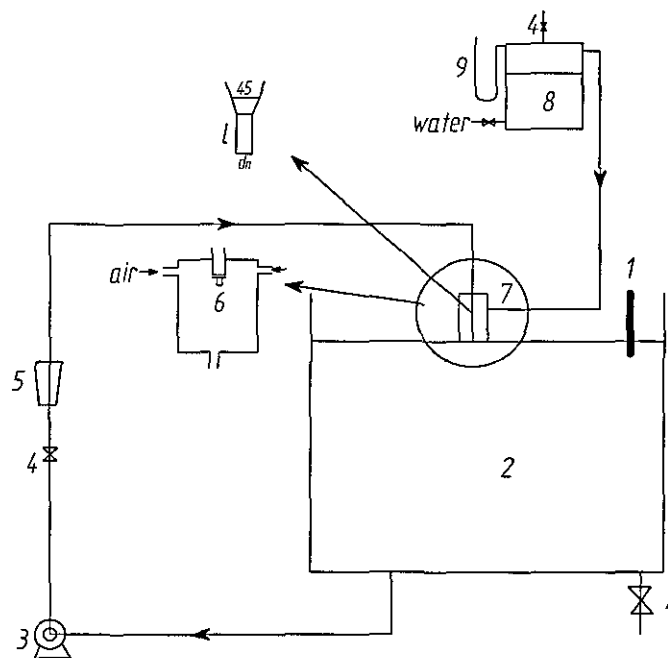


Figure 2.4 Experimental set-up utilized by Ohkawa *et al.* (1986a). 1, Thermometer; 2, water tank; 3, pump; 4, valve; 5, flow meter; 6, nozzle; 7, cylinder; 8, replacement vessel; 9, manometer.

A study by van de Donk (1981, 1979) investigated the effect of the main variables – jet length, L_j , roughness of jet surface (which depends on nozzle design and jet Reynolds number, Re_j), jet velocity, V_j and nozzle diameter, d_n - on air entrainment rate.

The apparatus used by him is shown in Figure 2.6. He found out that “for relatively low velocity turbulent jets the entrainment is irregular and the disturbances of the jet surface are dominant factor in the entrainment mechanism. For relatively high jet velocity air friction controls the surface roughness of the jet. Air entrains within the jet and a boundary layer is also developed, which is carried down below the water surface”. Therefore at low velocity (turbulence), air entrainment is mainly due to jet envelop (encompassed air). At higher jet velocity, air entrainment is due to jet surface roughness as well as air in the boundary layer.

Entrainment was measured by increasing the ring diameter in an attempted to investigate the effect of the ring diameter on gas entrainment. Results show that the entrainment of gas increased with ring diameter to a certain value (when the ring diameter is approximately twice that of nozzle diameter) and dropped down as the ring diameter continued to increase beyond this value. This was due to the fact that when the ring diameter is small the entrained gas is limited. When the ring diameter is larger than a certain size (twice nozzle diameter) some of the entrained gas escaped without being measured (disentrainment). Ring diameter results may help in determining the proper downcomer diameter for the current study.

The nozzles and a conical nozzle (shown in Figure 2.5) with air injection were utilized to study their effect on entrainment ratio (Q_A/Q_j) for increasing jet velocity. All of them show a high dependence on jet velocity except that of the simple conical nozzle. This can be attributed to the fact that this sort of nozzle produces a smooth jet surface. Which means less air was accompanying the jet.

In the case of the other nozzles, rough jet surfaces were developed that enhanced the entrainment ratio. However, this behaviour must be monitored closely because the disrupted jets tend to carry less gas under the liquid pool surface. This causes a wider distribution of the jets on the receiving pool and lower penetration depths are achieved, which agrees with Bin (1993).

Conical nozzles with larger diameters have been also considered in this experiment, along with three different jet lengths. The recorded observations show that higher entrainment ratios were obtained with larger nozzles and longer jet lengths.

The previous study helps in choosing a nozzle geometry that does not promote a disrupted jet, which could result in less penetration depth. As a result mass transfer rate may be affected due to shorter retention time between the bubble and the liquid phase.

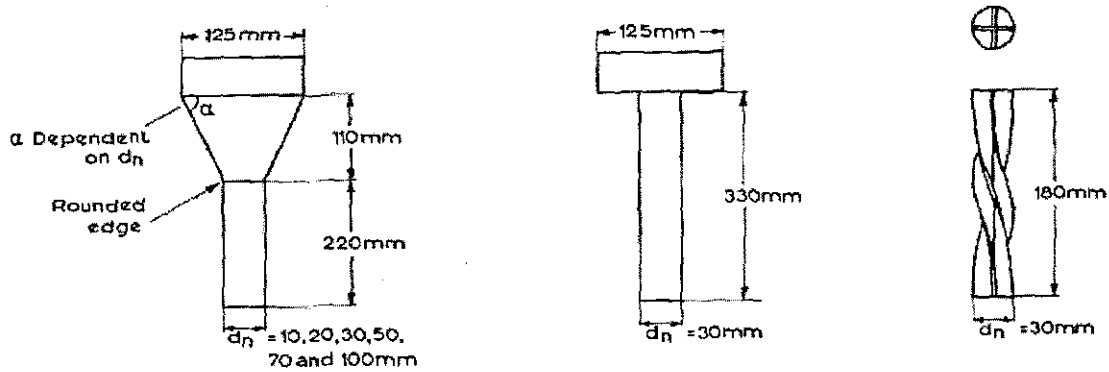


Figure 2.5 Nozzle types that were used by van de Donk (1981), a) Conical nozzles, b) Flat entry and c) Twisted spiral.

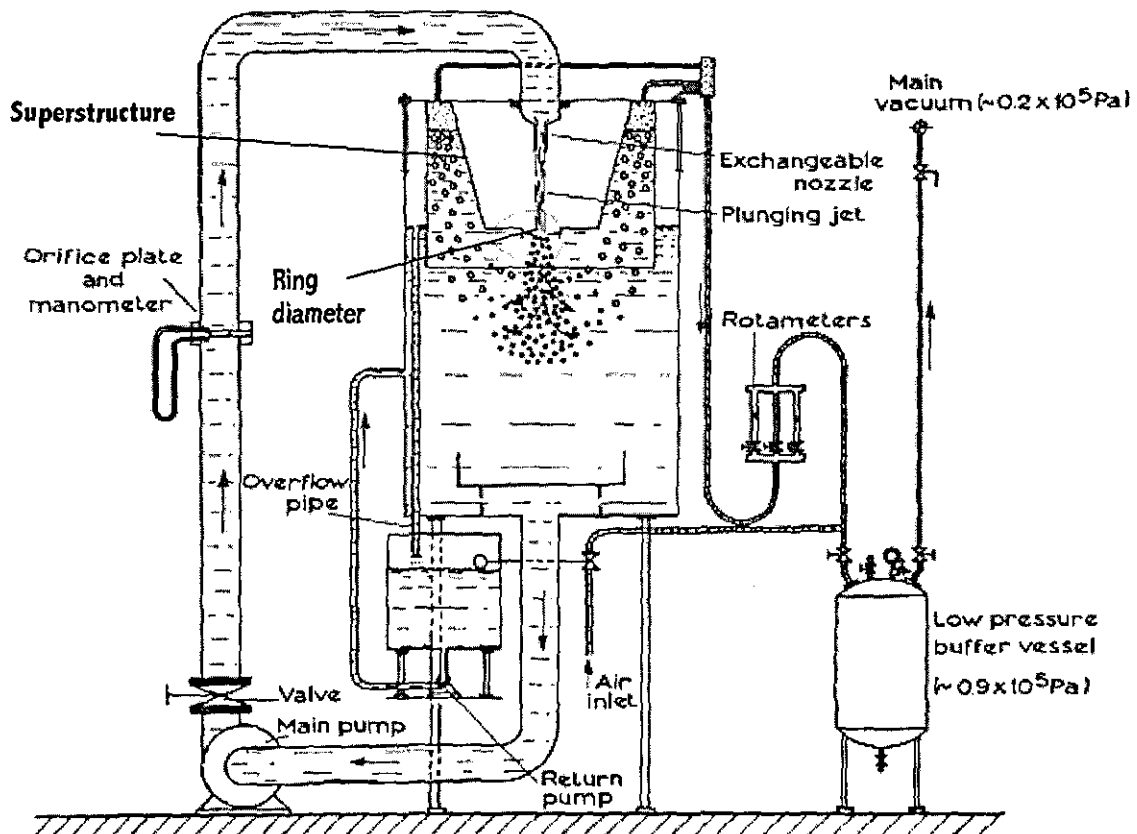


Figure 2.6 The apparatus used by van de Donk (thesis, 1981).

McKeogh and Ervine (1981) studied the effect of jet velocity (V_j), jet diameter (d_j) and jet turbulence level and the height of fall (jet length) from the end of the nozzle on air entrainment utilizing the apparatus shown Figure 2.7. Q_A vs. L_j plots showed that air entrainment increases in all cases as the above factors increase until it levels off. In the case of turbulence flow, gas entrainment rate increases depending on the degree of turbulence. Jets with high turbulence give more gas entrainment for short fall lengths until it reaches a maxima then it drops down. This may be attributed to the fact that at this point the jet breaks up into scattered droplets that tend to entrain less air. Jets with less turbulence give less entrainment rate at the beginning and continue to increase even further to exceed that of high turbulence, because entrainment rate increases as the jet turbulence increases until it reaches a point just before the break up of the jet occurs. A higher entrainment rate was obtained in the second case because the break up point was reached at longer jet length.

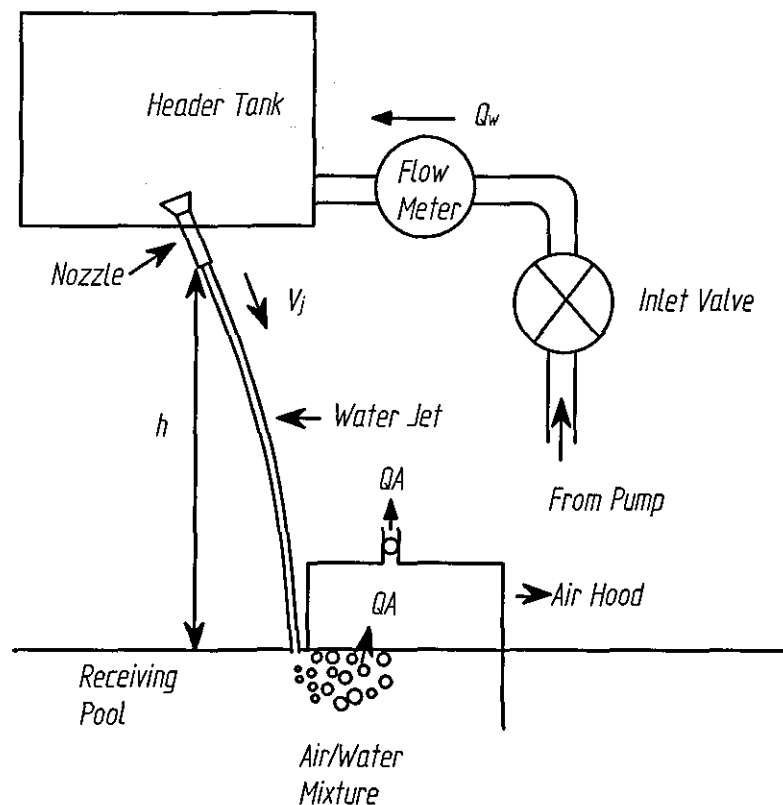


Figure 2.7 Experimental apparatus used by McKeogh and Ervine (1981).

Bin (1993) has provided valuable information and a general review discusses much of the earlier work with regards to gas entrainment by plunging liquid jets. In his paper, he presented a correlation (1984, 1988b) for a vertical jet perpendicular to the receiving pool. This equation accounts for air entrainment ratio as a function of the main variables such as jet velocity, jet length, nozzle geometry. As shown in equation (2.3), the gas entrainment ratio is directly proportional to Froude number raised to power 0.28 and L_j/d_n raised to power 0.4. It is valid for $L_j/d_n \leq 100$, $l/d_n \leq 10$ and $Fr^{0.28} \left(\frac{L_j}{d_o} \right)^{0.4} \geq 10$ (Bin, 1988b; Ohkawa *et al.*, 1987)

$$\frac{Q_A^{90^\circ}}{Q_j} = 0.04 Fr^{0.28} \left(\frac{L_j}{d_n} \right)^{0.4} \quad (2.3)$$

Another correlation is developed by the same author, for the volumetric gas entrainment rate for a vertical jet plunging into an unconfined receiving pool, based on a fit to Ohkawa *et al.* (1986a) data and is shown below:

$$\frac{Q_A^{90^\circ}}{Q_j} = 0.016 \left[Fr_j^{0.28} \left(\frac{L_j}{d_n} \right)^{0.4} \right]^{1.17} \quad (2.4)$$

The Froude number is equal to $V_j^2/d_n g$ and $Q_A = d_n^2 V_j \pi/4$. Bin has investigated a wide range of experiments carried out by various authors for unconfined plunging jet reactors. He concluded that nozzles with short cylindrical length (l) give lower entrainment rate values than those of long cylindrical length (Figure 2.8). Entrainment rate phenomenon was also discussed in detail in his study. He suggested that the total air entrainment rate (Q_A) by the jet depends upon certain conditions. It comprises; air entrainment by jet surface roughness (Q_{A1}) and that associated with the jet as boundary layer (Q_{A2}) as shown below in Figure 2.8,

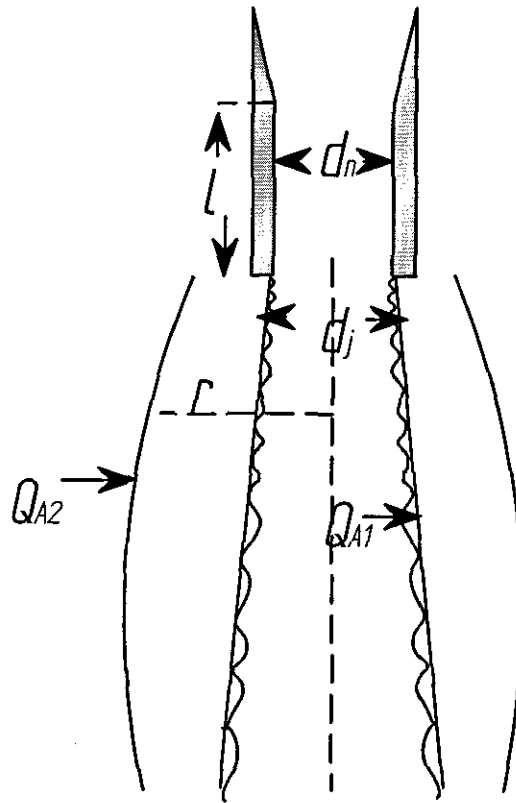


Figure 2.8 Air entrainment rate due to jet surface and boundary layer.

$$Q_A = Q_{A1} + Q_{A2} \quad (2.5)$$

where,

$$Q_{A1} = \frac{\pi V_j}{4} (d_j^2 - d_n^2)$$

$$Q_{A2} = \int_{d_j/2}^{\infty} V_A 2\pi r dr$$

Where V_A is the local velocity of the boundary layer air at a given radius (r) measured from the jet axis, d_j and d_n are the jet and nozzle diameters respectively (Figure 2.8). Contribution of the boundary layer to the total entrained rate may reach up to 70%. Furthermore, this comprehensive study presents a comparison between the results obtained by various authors. It also involves basic hydrodynamic features of liquid jets and considers many other topics related to plunging jets (Bin, 1993).

Sene (1988) used hydraulic models to investigate air entrainment mechanisms by a plunging jet. He showed that air entrainment rate varies with n^{th} power of the jet velocity $Q_A \propto V_j^n$, where n is 3 at low jet velocities and $3/2$ at high jet velocity. He presented a theoretical model that describes air entrainment rate for high jet velocities. This model is listed in Table 2.2.

Suciu and Smigelschi (1976) presented a note giving an estimate of the biphasic region and its dependency on the parameters of the plunging jet. The biphasic volume was calculated by measuring the penetration depth and the cone base diameter. They showed that with increasing jet length, the penetration depth decreases at first strongly and then levels off. Results show that the primary bubbles diameter is of the order 0.02-0.2 mm, and the secondary bubbles diameter is approximately 2-3 mm.

2.1.4 Apparatus

The unconfined system is employed by most of the authors, for example, Ohkawa *et al.* (1986a), McKeogh and Ervine (1981), van de Donk (1981) and Yamagiwa (1990). They showed that air entrainment rate was measured after the impingement had occurred. However, method of measuring air entrainment rate may vary depending upon the apparatus as shown below,

Yamagiwa measured air entrainment rate using the bubble column shown in Figure 2.3. In this study a bubble column is used to contain the receiving pool. Air entrainment rate was measured by separating entrained air from water in a separate

vessel. Then air is introduced into replacement vessel for final measurement, and the water is recycled to the column.

Figure 2.4 represents the apparatus used by Ohkawa *et al* (1986a). Gas entrainment was obtained by measuring the volume of liquid replaced by the entrained gas. This was achieved by utilizing a length-variable cylinder where the actual entrainment took place. The volume of water replaced by gas was introduced into a replacement vessel for final measurements.

Van de Donk has conducted experiments by implementing a vertical liquid jet system. In this experiment he introduces a superstructure on top of the receiving liquid pool (Figure 2.6). The liquid jet plunges through a conical shape with limited head space, which is open to the annular hood through an adjustable ring hole. This structure is also used to capture gas after it has been entrained. The captured gas flows via a rotameter for final measurement. Water level in the annular hood is designed to be at a certain level above the receiving pool level, which is kept constant during the run. The nozzle geometries that were used in his study are shown in Figure 2.5. Three types of short nozzles were used: conical, flat entry and cruciform section strip twisted through 180° for the 30 mm nozzles. The conical nozzle diameter was varied from 10 to 100 mm, whereas the other types of nozzles all had a diameter of 30 mm.

McKeogh and Ervine used an unconfined system where the nozzle was fixed at the bottom of a feed tank in an inclined position (Figure 2.7). An inclined jet plunges through the atmosphere to impinge onto the surface of a receiving pool. Figure 2.7 shows that air is captured, after it was entrained by the jet, utilizing an air hood.

2.1.5 Main variables

All of the proposed correlations do not count for (l/d_n) effect (cylindrical part of the nozzle to the nozzle diameter), despite the fact that this factor has a significant effect on the jet surface and therefore gas entrainment rate. Table 2.2 presents a summary of empirical correlations obtained by various authors for unconfined systems.

Table 2.2. Experimental conditions and correlations by various authors for unconfined system.

Author	Year	V_j (or Q_j)	L_j (mm)	d_n (mm)	D_c (mm)	Correlation	Remarks
Van de Donk	1981	0-10 (ms^{-1})	Up to 1000	Conical; 10 -100 Flat entry; 30 Twisted spiral; 30	-	$\frac{Q_A}{Q_j} = 0.09 * \left(\frac{L_j}{d_n}\right)^{0.65}$	Unconfined with a ring
McKeogh and Ervine	1981	0 – 10 (ms^{-1})	0 - 5000	6, 9, 14 and 25	-	$\frac{Q_A}{Q_j} = 1.4 \left[\left(\frac{E}{r}\right)^2 + 2\left(\frac{E}{r}\right) - 0.1 \right]^{0.6}$	Unconfined with inclined jet
Ohkawa <i>et al.</i>	1986a	2 – 14.3 (ms^{-1})	25 - 750	7 - 13	-	-	Unconfined
Sene	1988	0-3.2 (ms^{-1})				$Q_g \propto \left(\frac{\mu_g}{\rho_l g \sin \alpha}\right)^{1/2} V_j^{3/2} d_n$	Hydraulic models
Yamagiwa	1990	$(0.317 - 2) \times 10^{-3}$ ($\text{m}^3 \text{s}^{-1}$)	30, 60, 90 and 150	8, 10, 11, 13 and 15	34, 50, 60 and 70	$\frac{Q_A}{Q_j} = 2.24 \times 10^{-3} Fr_j^{0.4} Re^{0.26} \left(\frac{L_j}{d_n}\right)^{0.48}$	Unconfined (bubble column)

2.1.6 Gas entrainment rate results in an unconfined system

The previous studies showed that gas entrainment rate ratio is proportional to the jet velocity raised to power n , except for one of Van de Donk nozzles (simple conical nozzle) where jet velocity ranges from $2 < V_j < 5$ m/s gave a decreasing gas entrainment ratio behaviour. He did not provide a valid explanation why this was the case. He agreed with the general form proposed by Van de Sande (1974), which is actually little different from what he attained. Constant n varies from study to study depending upon experimental conditions.

There are various correlations for the gas entrainment rate (see Table 2.2) proposed by different authors for unconfined plunging jet reactor. These equations were obtained by fitting measured data. Some of them are plotted below in Figure 2.9.

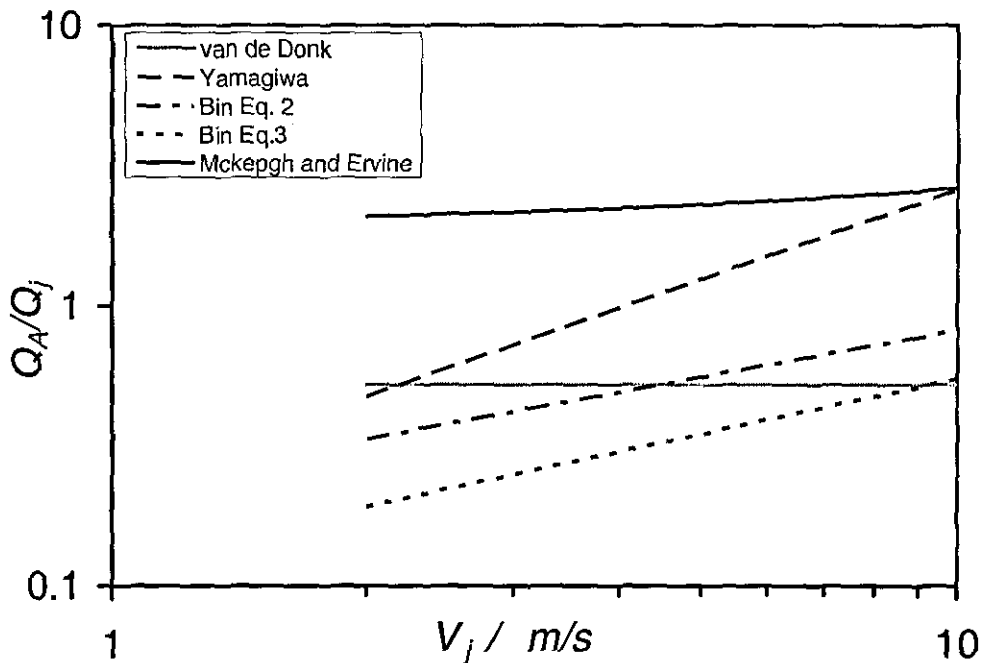


Figure 2.9 Correlations for unconfined systems.

The plot above contains unconfined plunging liquid jet reactor data for Van de Donk (1981), McKeogh and Ervine (1981), Yamagiwa (1990) and Bin (1993). This plot is generated, using the proposed correlations in Table 2.2, for 10 mm nozzle, 150 mm jet length and jet velocity between 2-10 m/s. Looking at the plot, one can see that McKeogh and Ervine correlation gives the highest entrainment rate compared to the rest of them. This may be due to the fact that in their work they used an inclined jet while the rest of the authors have used vertical jets. As shown by previous authors (Bin 1993), inclined jets have the tendency to entrain more air than vertical ones. Besides the fact that McKeogh and Ervine correlation is a function of surface roughness (E/r), different geometries were used in their experiment. This makes it even harder to directly compare this correlation to the rest of the correlations. However, they generated a method that relates jet velocity to surface roughness, which were used to calculate air entrainment ratio shown in Figure 2.9.

Regarding vertical jets, Yamagiwa's correlation predicts higher entrainment ratio than the rest of them (Table 2.2). This is may be due to using the downflow bubble column (see Figure 2.3) with small diameter in comparison to tank diameter utilized in typical unconfined systems. The bubble column may reduce disenrainemnt rate and therefore bubbles can penetrate deeper to be measured. As expected, van de Donk's correlation is shown by a constant horizontal line in Figure 2.9 because it is independent of jet velocity. It is important to realize that the previous authors have used different nozzle geometries and dimensions in their experiments. Therefore, to establish accurate comparison these facts must be considered.

2.2 Confined Plunging Liquid Jet Reactors

2.2.1 Mechanisms

The vast majority of the work on plunging jet entrainment mechanisms has been conducted with unconfined plunging liquid jets, whereas relatively little has been reported with regard to a confined plunging jet reactor. Low (2003) noted that confined and unconfined systems share rather similar entrainment mechanisms, the main

difference being that in the former the flows in the receiving pool are restricted by the proximity of the downcomer wall. At low jet velocities, the jet is smooth, but as V_j increases the flow becomes more turbulent and the surface roughness increases. Low velocity jets cause a depression of the free surface at the plunging points and bubbles are entrained from the jet periphery, following a similar mechanisms to those previously reported by McKeogh and Ervine (1981) and Bin (1988), for unconfined systems. Bayly *et al.* (1992) and Evans *et al.* (1996) briefly described bubbles motion inside the downcomer. Nothing new was added to the previous mechanisms that govern entrainment rate. The mechanisms of air entrainment rate are significantly affected by the downcomer diameter and length especially for relatively narrow downcomers, where the walls play an important role in the process.

2.2.2 Gas entrainment rate in a confined system

Cumming *et al.* (2002) conducted an experimental study using CPLJ to measure gas entrainment rates as shown in Figure 2.10. In the first part of their study four nozzle diameters were used along with fixed downcomer diameter and length. Experiments were carried out for controlled and uncontrolled jet lengths. Controlled jet length was achieved by controlling the downcomer space pressure; and uncontrolled jet length occurred when head space pressure (P_I) was close to atmospheric. Results showed that higher entrainment ratio rates were obtained for uncontrolled jet for the same jet flow rates. In the second part, the jet length remained constant whilst the downcomer and nozzle diameters were varied for each run. The observed results were compared against equation (2.4) presented by Bin (1993), using Ohkawa *et al.* (1986a) data for unconfined jet. The study showed that the downcomer with the largest diameter, in this case 29 mm, gave similar dependence on Fr , compared to Bin's equation (2.4). Downcomers with smaller internal diameter (17.5 mm) gave lower entrainment ratios and exhibited different dependence on Fr . Cumming *et al.* (2002) concluded that downcomer length had little effect on the entrained rate, and downcomers with large diameters exhibit similar entrainment flow rate to that of an unconfined plunging jet reactor. No comparison was done between their results and Bin's equation (2.3), which gives higher entrainment rate.

No valid explanation was provided for the deviation of the 29 mm downcomer results from Bin's equation (2.4).

Ohkawa *et al.* (1986a) measured air entrainment rates utilizing six columns with diameter ranges from 20 to 26 mm. The actual downcomer length (H_{ds}), distance from pool surface to the bottom of the downcomer, ranges from 2.00 to 2.90 m. As shown in Figure 2.11 a disk was used below the downcomer to stabilize and direct the gas-liquid motion out of the downcomer by preventing the entrained bubbles from penetrating further downward from the lower end of the downcomer. Their results show that for a confined reactor, air entrainment rate (Q_A) increases linearly with the jet velocity (V_j).

Generally, higher entrainment rates were achieved with higher jet velocity and larger nozzle diameter, however lower entrainment rates were observed with longer downcomer (H_{ds}). Ohkawa *et al.* (1986a) reported that systems that employed a downcomer were able to produce gas entrainment rates 25-60% larger and deeper penetration depth than that without downcomer operated at comparable conditions, which also increases gas-liquid contact time. They (Ohkawa *et al.*, 1986) expressed Q_A as a function of d_n , V_j , D_c and H_{ds} (Table 2.3). This correlation shows a fairly weak effect of the downcomer diameter, but rather a strong effect of downcomer length. Nozzle geometry was not brought up in this study, and they did not explain how downcomer length could have reduced air entrainment rate.

2.2.3 Apparatus

This section presents a comparison between the apparatus used by different authors for confined plunging jet reactors. As shown below (Figure 2.10–Figure 2.13) the only difference between the two systems (confined and unconfined) is the use of the extra downcomer that is inserted around the plunging and impingement point. This imposes an extra constraint for the two phase dispersion, and potentially enhances mass transfer rate by increasing the bubble penetration depth. Also having a downcomer affects the entrainment mechanisms. This category includes Ohkawa *et al.* (1986a), Evans and Jameson (1995), Evans *et al.* (1996) and Cumming *et al.* (2002).

There are two methods of measuring air entrainment rate; a) capturing gas after it has been entrained (Ohkawa *et al.*, 1986a); b) measuring the removal of gas from the headspace above the receiving pool surface (Cumming *et al.*, 2002; Evans and Jameson, 1995; Evans *et al.*, 1996).

Cumming *et al.* (2002) used a different method to measure air entrainment rate. They used the same method that is adopted in the current work. Air entrainment rate was measured utilizing a bubble flow meter and a stop watch. Experimental work in § 3.2 chapter 3 explains this method in more details.

Ohkawa *et al.* (1986a) measured the air entrainment rate, after it has been entrained, by separating the entrained air from water utilizing a square section with a tapered bottom fixed at the top part (Figure 2.11). The gas was introduced into a replacement vessel to measure the volume of liquid replaced by the gas to determine the volumetric rate of entrained gas.

Figures 2.12 and 2.13 represent the same apparatus that is utilized by Evans and Jameson (1995), and Evans *et al.* (1996) respectively. Air entrainment rate was measured using a network of calibrated rotameters.

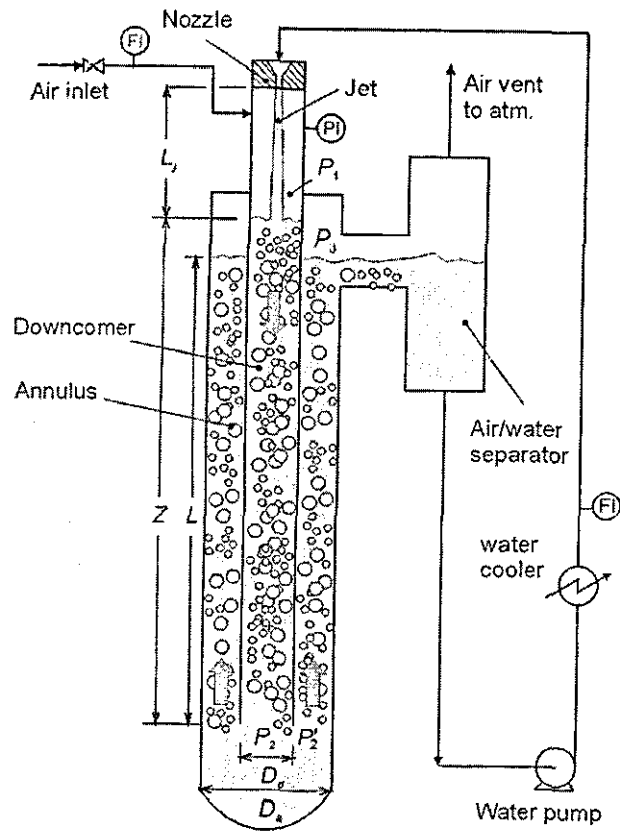


Figure 2.10 A plunging jet reactor used by Cumming *et al.* (2002).

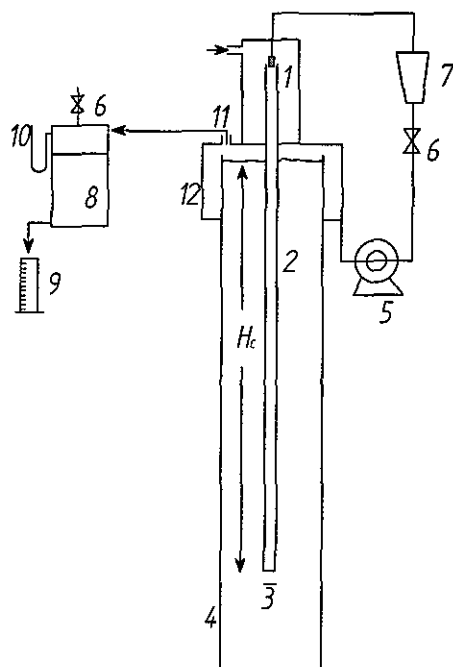


Figure 2.11 Experimental set-up for the jet system with downcomer utilized by Ohkawa *et al.* (1986a). 1, nozzle; 2, downcomer; 3, disk; 4, square tank; 5, pump; 6, valve; 7, flow meter; 8, replacement vessel; 9, measuring cylinder; 10, manometer; 11, air outlet; 12, square section.

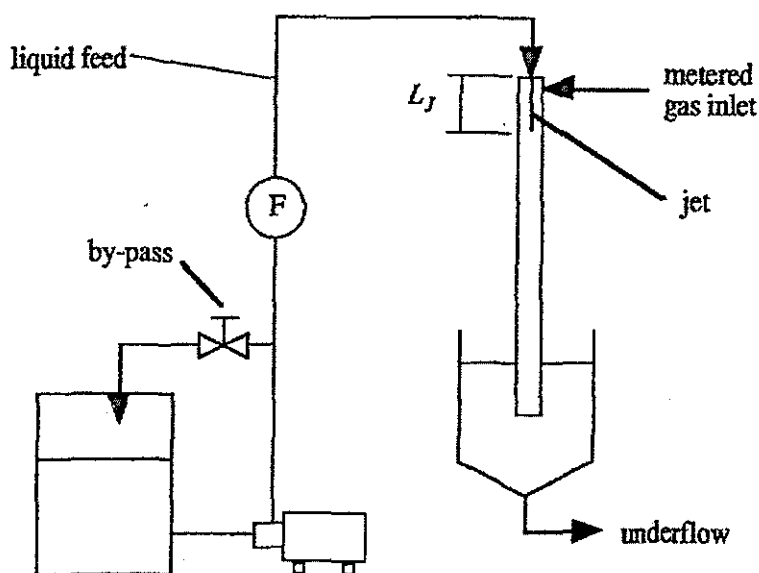


Figure 2.12 Experimental apparatus used by Evans *et al.* (1996)

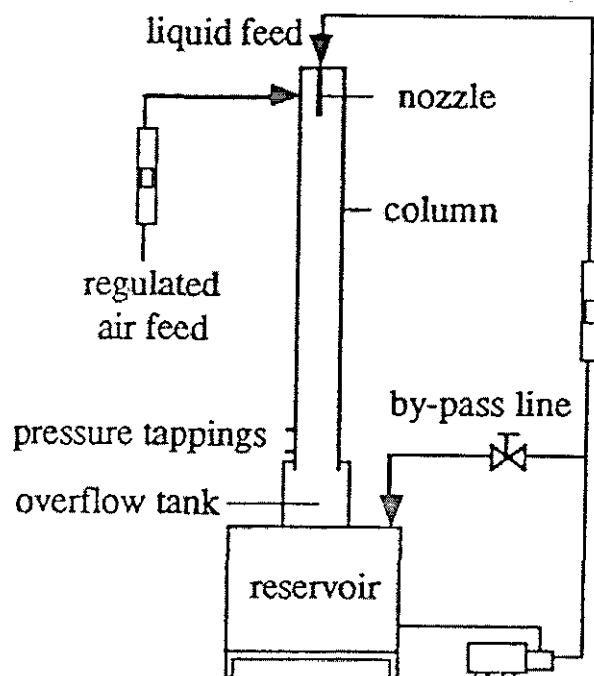


Figure 2.13 Experimental apparatus used by Evans and Jameson (1995).

2.2.4 Main variables

There are not many empirical correlations developed for confined plunging jet reactor. One of the few is Ohkawa *et al.*'s (1986a) correlation shown in Table 2.3. In this correlation they accounted for the downcomer length effect H_{ds} (distance from the pool surface to the bottom end of the downcomer). This contradicts with Cumming *et al.* (2002) conclusion, whereas Cumming *et al.* (2002) found out that downcomer effect on air entrainment rate is negligible. Correlations adopted (or proposed) by various authors are summarized below,

Table 2.3 Experimental conditions and correlations by various authors for confined systems.

Author	Year	V_j (or Q_j)	L_j (mm)	d_n (mm)	D_c (mm)	Correlation	Remarks
Ohkawa <i>et al.</i>	1986a	2 – 14.3 (ms^{-1})	25 - 750	7 - 13	200 and 260	$Q_g = 0.698(V_j^3 d_n^2)^{0.8} \left(\frac{d_n}{D_c}\right)^{1.3} \left(\frac{D_c}{H_{ds}}\right)$	Confined
Evans and Jameson	1995			2.38, 4.76 and 7.12	44, 74 and 95	-	Confined
Evans <i>et al.</i>	1996	7.8-15 (ms^{-1})	-	2.38, 4.76 and 7.12	44, 74 and 95	-	Confined
Cumming <i>et al.</i>	2002	20 – 50 (l/min)	220	4.9, 6.0, 8.2, 10.3 and 12.2	17.5, 23.5 and 29	$\frac{Q_A^{90^\circ}}{Q_j} = 0.016 \left[Fr_j^{0.28} * \left(\frac{L_j}{d_n}\right)^{0.4} \right]^{1.17}$ (Bin)	Confined

**Chapter 3: Experimental Apparatus and Methodology
for Air Entrainment Rate**

3.1 Introduction

This chapter describes in details the rig used in the current study including the equipment that was developed in this thesis and was used to make the experimental air entrainment measurements in a confining tube for a wide range of main variables. It also discusses the methodology adopted to calculate air entrainment flow rate.

3.2 Experimental Work:

Figure 3.1 represents the large scale system for measuring entrainment rate in a Confined Plunging Liquid Jet Reactor at Loughborough University. The rig comprised $1.9 \times 0.78 \times 0.38 \text{ m}^3$ reservoir that contained water (6) and a support system, that was easy to use, mounted inside the reservoir that was used for experimental measurements (§ 3.3). Tap water at room temperature was pumped from the bottom of the tank and into the rig using a mono pump (5) through 30 mm PVC pipe which is connected to a conical nozzle fixed at the top of the rig (9). The nozzle internal geometry was similar to that used by Ohkawa *et al.* (1986a) with a straight cylindrical section having a length diameter ratio of 5. However, the inlet section converged at a 20° angle, rather than the 45° used by Ohkawa *et al.*. The nozzle exit was placed concentrically within the downcomer column. The jet plunges through the head space onto the receiving pool inside a downcomer (1) at a certain distance from the nozzle, which is defined as jet length (L_j) (2). The following jet lengths were used in the current work 200, 300 and 400 mm. In all cases, jet length was less than the break-up length, so that the entrainment was due to a continuous stream of liquid impinging on the receiving pool surface. The maximum liquid flowrate that could be pumped was 62 l/min. Two rotameters were used to measure the jet flowrates (3), which have been, previously, calibrated using a scaled bucket (appendix II). The air entrainment rate (Q_A) was measured utilizing a soap bubble meter (7), which provided negligible resistance to the flow. It is a cylindrical tube with 71 mm inside diameter and 1000 mm in length. The bubble meter is divided into 10 intervals. The height of each interval is 100 mm. Bubbles were generated using soap solution. The solution was prepared by mixing 5% of glycerine and 10% household detergent in water. A small tube

was connected to the bottom of the column to help organizing the bubbles by squeezing the spherical bulb rubber. A bubble trap (8) was used to prevent any detergent from entering the gas feed to the downcomer column. It is located between air tapping (12) and soap bubble meter (10). Due to the downward momentum of the plunging jet, slightly negative pressure can be generated in the downcomer headspace, this was monitored by a water manometer (4) connected to a pressure tapping in the column wall (13). Thus variations in the gas entrainment rate can cause the water level inside the downcomer to fluctuate. In some cases, to keep the jet length constant, air was fed at very low pressure from a compressed air supply (11), which allowed a better control of the liquid level inside the downcomer. This air enters the system via 10 mm side tube (Figure 3.13), which is connected to the bottom of the bubble meter.

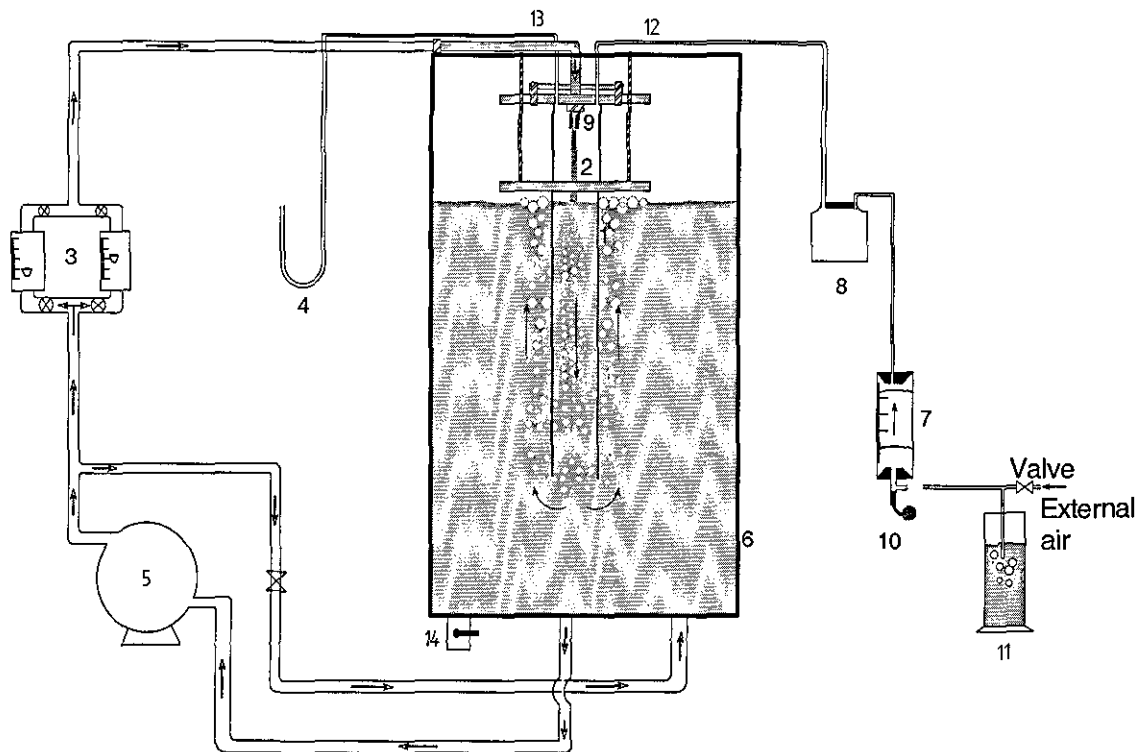


Figure 3.1 Experimental apparatus for confined plunging liquid jet reactor used in the current study. 1, downcomer; 2, jet length; 3, rotameter; 4, manometer; 5, mono-pump; 6, water tank; 7, bubble meter; 8, bubble trap; 9, nozzle; 10, soap solution; 11, external air; 12, air tapping; 13, pressure tapping; 14, drain.

3.2.1 Air tapping design

This section presents calculation of the air supply tube design. The design focuses on the tube diameter. For the air supply tube, the diameter must be designed to minimize the pressure drop between the air inlet and headspace in the downcomer. When the liquid jet plunges through the downcomer headspace, a pressure drop is established as a result of air entrainment by the jet pulling air through the air supply pipe. Consequently, the water in the head space will rise. The tube diameter connecting to the air supply pipe must be of a diameter that can handle the largest air flow rate. To do this, simple calculations were carried out.

The pressure loss in the pipe is,

$$\Delta P = 2\rho_A C_f V_A^2 \frac{L_A}{d_A} \quad (3.1)$$

where,

$$V_A = \frac{Q_A}{A_A} \quad (3.2)$$

The air entrainment rate can be estimated from equation (2.4) (Bin, 1993),

$$Q_A = 0.016 \left[Fr_j^{0.28} \left(\frac{L_j}{d_n} \right)^{0.4} \right]^{1.17} Q_j$$

Where,

$$A_A = \pi \frac{d_A^2}{4} \quad (3.3)$$

Solving for d_A by combining equations (3.1) to (3.2),

$$d_A = \sqrt[5]{\frac{32\rho_A C_f L_A Q_A^2}{\pi^2 \Delta P}} \quad (3.4)$$

Where,

L_A = length of air tube = 100 mm

ρ_A = air density = 1.21 kg/m³

C_f = friction factor = 0.005

Calculations show that for $\Delta P = 100$ Pa and $Q_A = 0.0081$ m³/s, the tube diameter (d_A) should be 12.6 mm. So a tube of 12.5 mm diameter was chosen. As far as the tapping tube for the pressure concerns, a tube with 4 mm is used to measure the pressure drop in the top of the downcomer. Full results are in appendix II.

3.3 Novel Designed Equipment

This section presents a new design that is designed by the author and manufactured at Loughborough University work shop. This design has been used to measure the experimental data in the current work (air entrainment data and air-lift column data). Since the current study requires changing the plunging jet reactor parts frequently, to accommodate wide range of downcomers as well as nozzles geometries, it would be wise to come up with suitable apparatus to meet the requirements. This problem is approached by dividing the system into three main steps: nozzle and cover flange design, supporting flange design and downcomer design.

3.3.1 Nozzle and cover flange design

The objective here is to design a support that can firmly hold various nozzles of different diameters. To achieve this, the outside diameter of the nozzle (d_o) was constant

for all inner radii as shown in Figure 3.2. In other words, the inside diameter (d_n) can be changed while the outside diameter of the nozzle is constant. In this experiment the outside diameter of the nozzle must be greater than 15 mm (largest nozzle inside diameter used). Next step was to fit the nozzle with a matching tube that goes through a disc (cover) flange. This disc has two holes, for air and pressure tapplings, located at the top of the disc (cover) flange as shown in Figure 3.3. The tube and disc are connected permanently (glued together). The lower end of the tube is threaded to screw the nozzle on it (Figure 3.3a). The other end of the tube is connected to the pump delivery pipe work. The assembled parts are connected to the supporting flange, which also holds the confined tube (see § 3.3.2, supporting flange design). Figure 3.3b shows all of the parts connected together.

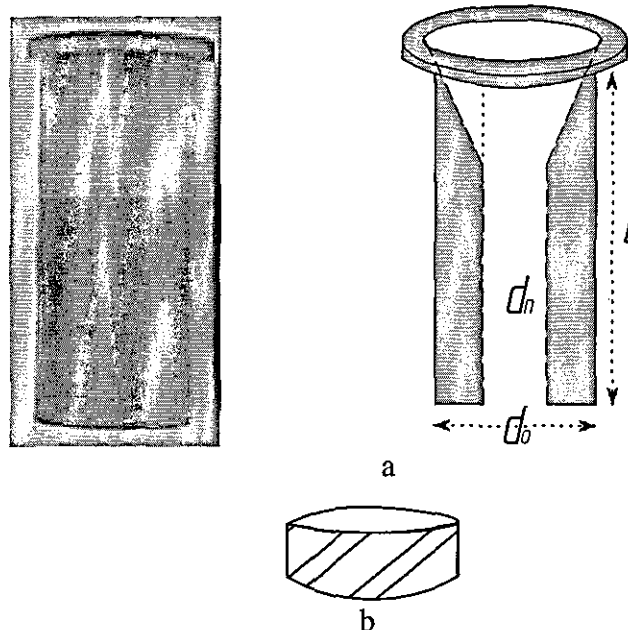


Figure 3.2 Nozzle design; a) nozzle geometry and b) nozzle cap.

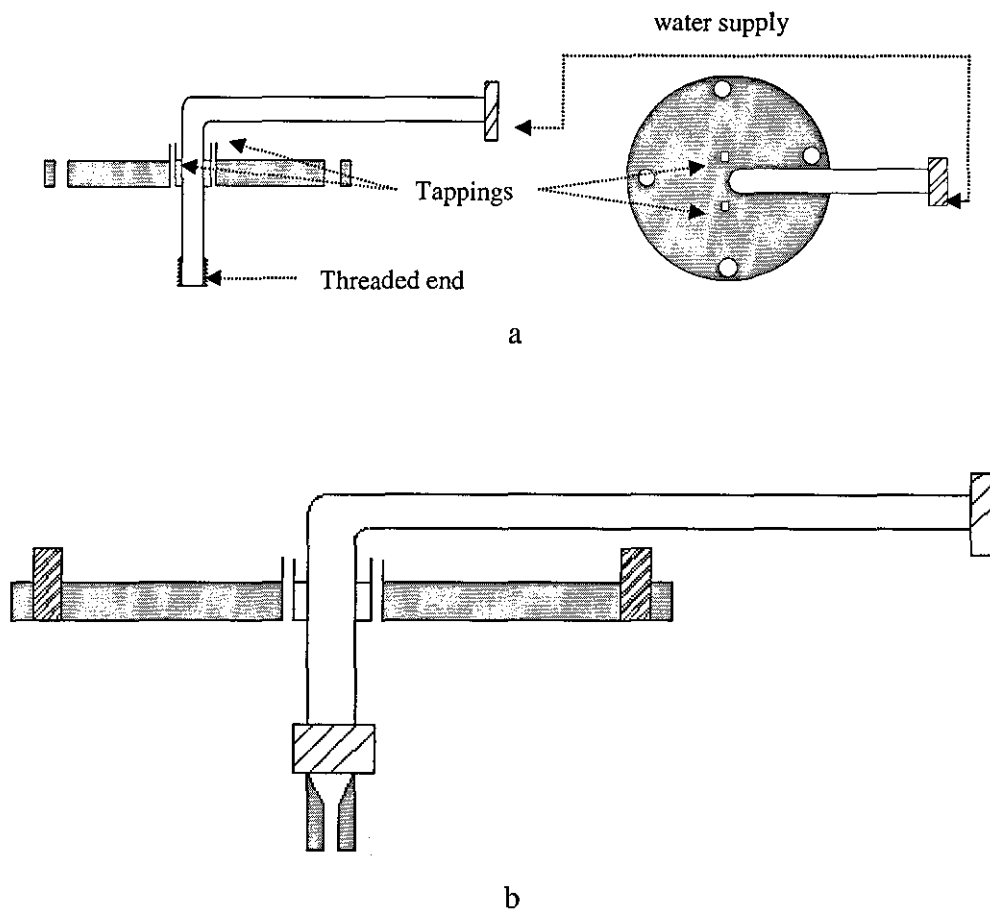


Figure 3.3 Schematic diagram of a) pipe and cover flange, and b) nozzle, pipe and cover flange connected together.

3.3.2 Supporting flanges design

Supporting flanges are permanent parts of the system. They are made to accommodate and support the confined tubes and nozzles with various diameters and lengths. As shown in Figure 3.4, this part comprises two hollow flanges one on top to hold the downcomer and cover flanges and a second flange, with slightly different configuration, is located below the first one. The hollow part must be greater than the largest downcomer diameter (in this case > 90 mm). Its role is to hold the downcomer column firmly during the run. As shown in Figure 3.4a, the top flange provides a place on which the downcomer is connected (screwed). The lower part of the supporting flange is

designed slightly differently from that of the upper part. As can be seen from Figure 3.4b, it has four adjustable plastic bolts that are spaced evenly and fitted horizontally. They are designed to accommodate a wide range of downcomer diameters and lengths. The main role of these bolts is to support the lower end of various downcomer configurations, which assures that the downcomer is not affected by the vibration. This way both of the downcomer ends are supported firmly, and thus the vibration is substantially reduced.

Figure 3.5 shows the two flanges are connected together by stainless steel rods

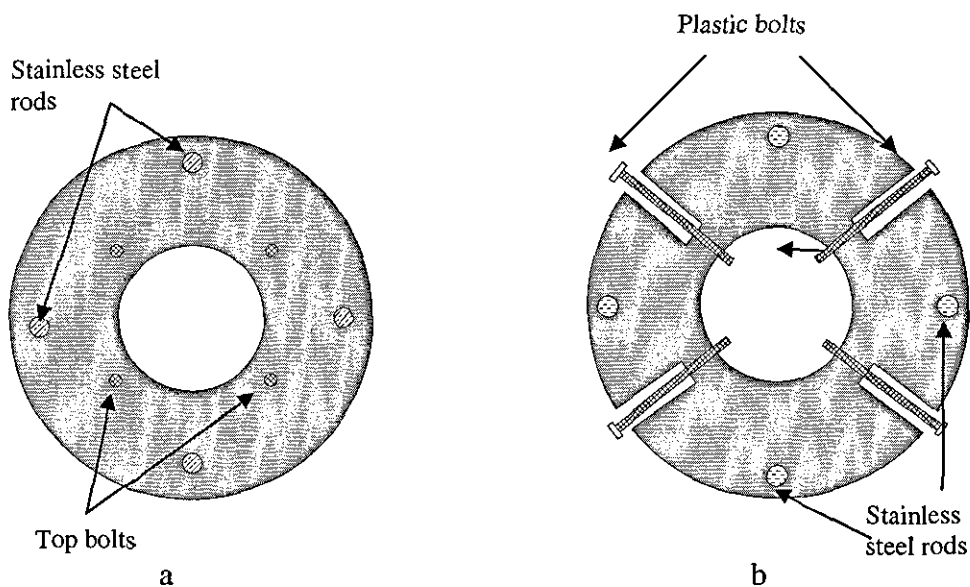


Figure 3.4 a) Top and b) lower parts for the supporting flanges.

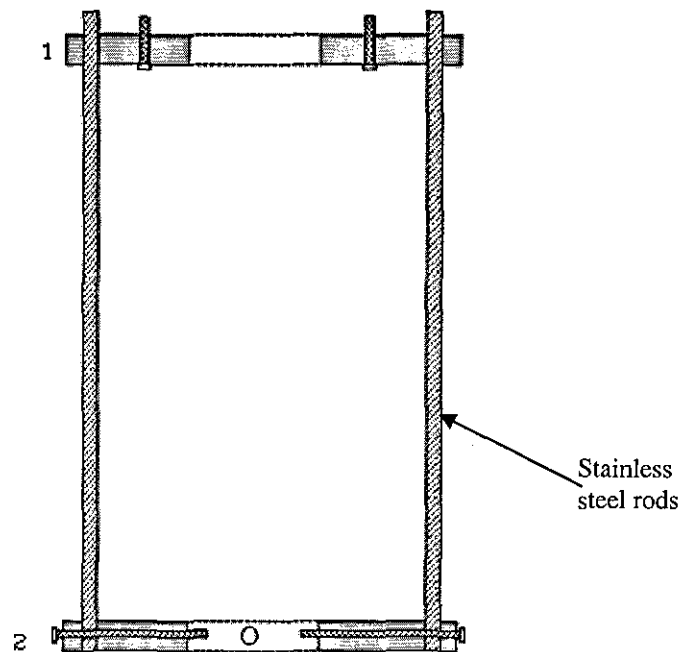


Figure 3.5 Complete set of the supporting flanges where 1 and 2 refer to top and lower flanges, respectively.

3.3.3 Downcomer design

This section provides a design for each downcomer so that it can be fitted and removed easily. The downcomer diameter varies from 23 mm to 89 mm, to accommodate this range of sizes three methods of support were used.

a) $50 \leq D_c \leq 89$ mm

Each downcomer is designed with the same collar or flange that fits the upper supporting flange (regardless of the diameter) and matches the cover disc flange shown in Figure 3.3b. This part is glued to the cylindrical part of the downcomer to form the final shape of the downcomer as shown in Figure 3.6. Each downcomer has four holes fixed on its flange that coincide with the bolts mounted on the upper part of the supporting flange (see Figure 3.4a). Here, the inside diameter range is limited because of the tapping for air and pressure measurements. Since the other end of the tapping must be opened to the

inside of the downcomer (headspace) for air supply and pressure drop measurements, the downcomer diameter must be greater than the distance between the two tappings.

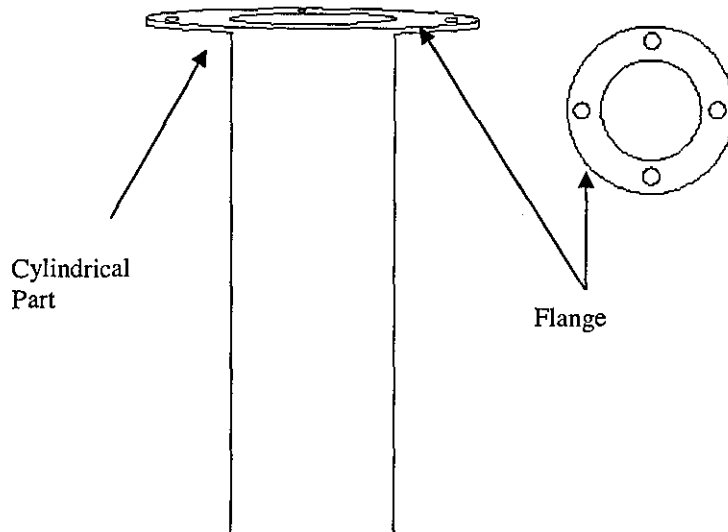


Figure 3.6 Final shape of the downcomers for $50 \leq D_c \leq 89$ mm.

b) $D_c = 50$ mm

In order to take advantage of the current design, this downcomer should have the following features;

- As shown in Figure 3.7a downcomer flange is connected to the cylindrical part through an extension (neck). The purpose of the extended neck is to accommodate the tappings.
- Alternatively, air and pressure tappings can be fixed at the top end of the downcomer (Figure 3.7b).

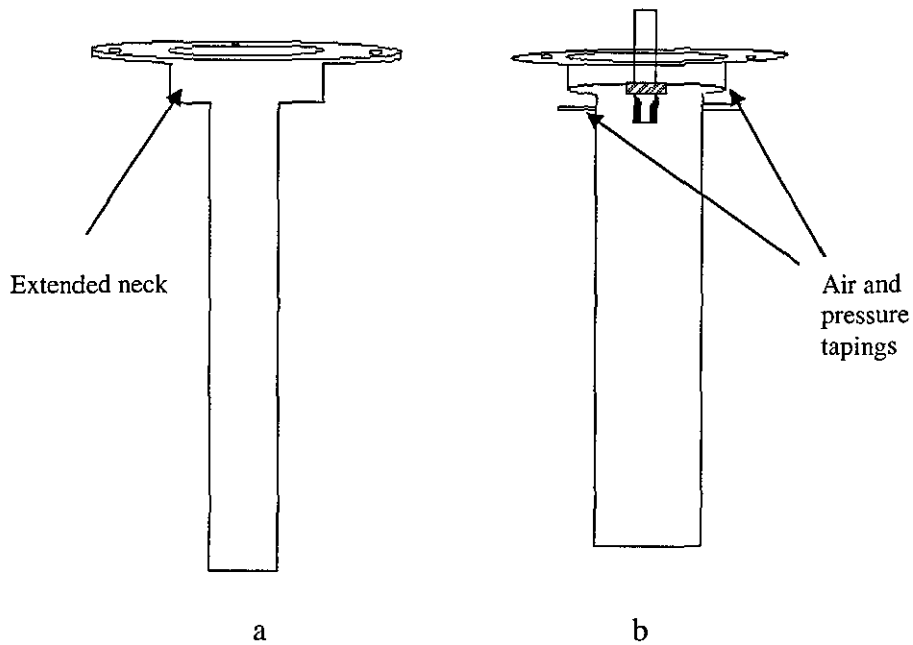


Figure 3.7 Downcomer with extended neck.

c) $D_c \leq 40$ mm

The last type of downcomer design is shown below in Figure 3.8, where the downcomer is directly connected to the nozzle cap through a reducer fitting. In this case less support is provided to the downcomer from the top flange. However since the downcomer is not heavy, the fitted reducer and the lower supporting flange provide sufficient support to stabilize it during the run. Tappings are also connected to the top end of the downcomer.

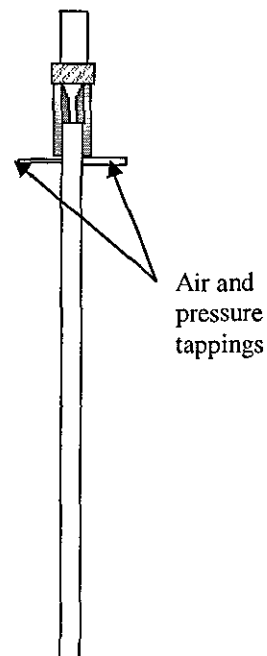


Figure 3.8 Downcomer fixed directly to the nozzle.

When all of the foregoing parts are put together, the final appearance of the new equipment utilized to make experimental measurements for air entrainment rate is shown in Figure 3.9 (AutoCAD design sketch of the equipment is in appendix V). The advantages of the new design are as follows;

- Parts can be swapped easily and in very short time (minutes).
- It is suitable for various ranges of downcomer and nozzle diameters, and lengths.
- It provides firm supports to the top and the bottom part of the downcomer and nozzle to avoid vibration during each run caused by the water pump, which could affect the results.
- It enables the researcher to see the whole process closely and clearly with naked eye (e.g. nozzle, jet length, impingement of the jet on the receiving pool, mechanisms..etc).

- It can be used to conduct confined and unconfined liquid plunging jet experiments for the sake of comparison. The above equipments can also be used to carry out air-lift column experiments utilizing a wide range of annuli.
- It is easy and cheap to maintain. Maintenance can be performed without emptying the reservoir.

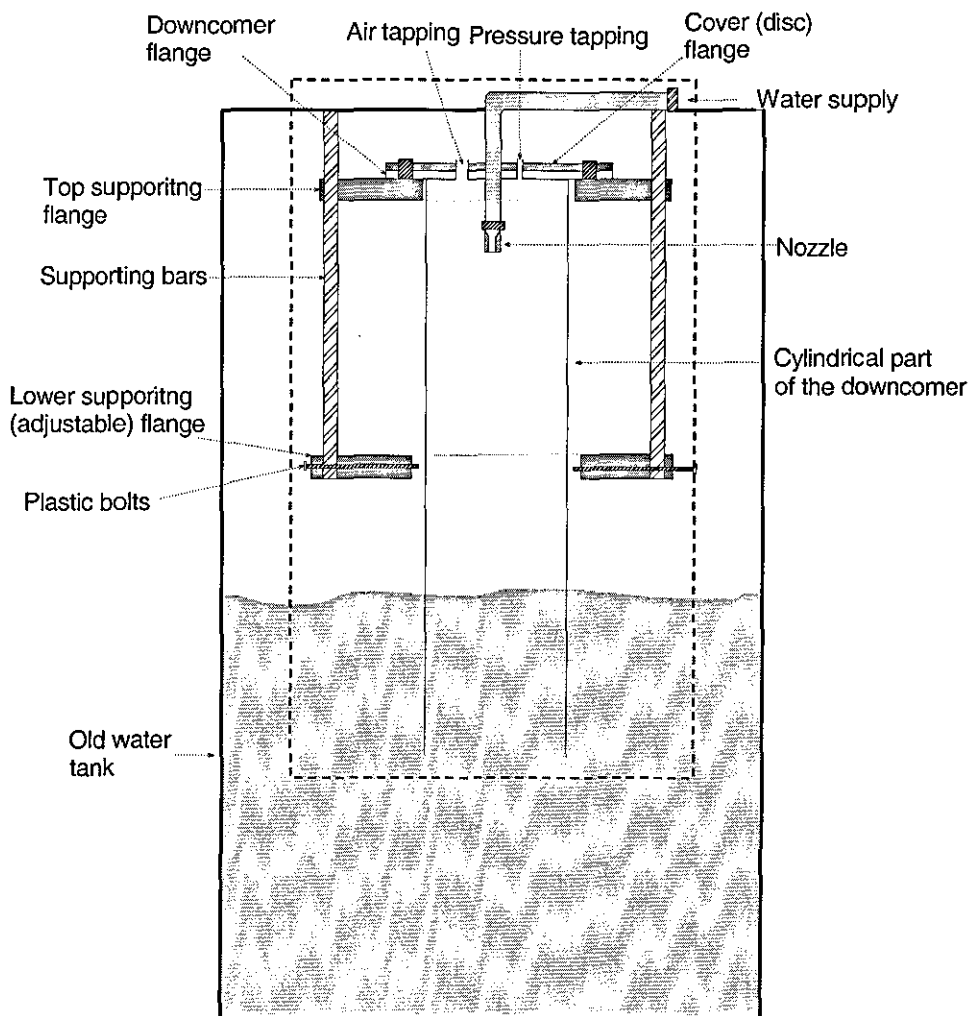


Figure 3.9 Schematic diagram of the new design equipments, marked off by the dotted line, used to make the measurements for air entrainment.

Table 3.1 Range of parameters used in the experiment.

Parameter	Dimensions
D_c (downcomer diameter, mm)	23, 38, 50.5, 71 and 89
L_j (jet length, mm)	200, 300 and 400
d_n (nozzle diameter, mm)	6, 8, 12 and 15
L_D (downcomer length, mm)	600, 800 and 1350
l/d_n	5
θ (defined in Figure 3.10)	20°

Conical nozzles are favoured for industrial designs because of their lower pressure drop characteristics (van de Donk, 1981). Therefore, it is of interest to investigate the pressure drop produced by these types of nozzles especially for CPLJR. Nozzle dimensions and geometry that were used in the current study is shown in Table 3.1 and Figure 3.10.

Losses due to gradual contractions pipes that are shown in Figure 3.10 were investigated in the present study. The resistance flow due to sudden contraction is approximated by (Crane Co., 1982),

$$\Delta P = \frac{1}{2} \rho K_1 V_j^2 \quad (3.5)$$

Where

$$K_1 = 0.5 \left(1 - \frac{d_n^2}{d^2} \right) C_c \quad (3.6)$$

Contraction coefficient C_c has been estimated and expressed according to the contraction angle (Crane Co., 1982) by,

$$C_c = 1.6 \sin \left(\frac{\theta}{2} \right) \quad \text{for } \theta \leq 45^\circ \quad (3.7)$$

$$C_c = \sqrt{\sin \frac{\theta}{2}} \quad \text{for } 45^\circ \leq \theta \leq 180^\circ \quad (3.8)$$

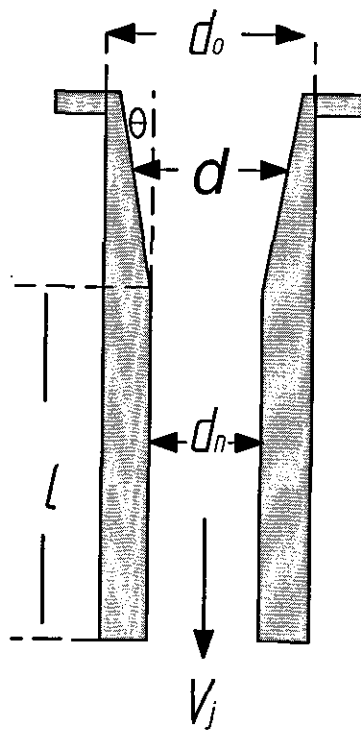


Figure 3.10 Gradual contraction for conical nozzle.

The final expression of the pressure drop in term of the down stream jet velocity (V_j), which accounts for the contraction losses, is:

$$\Delta P = \frac{1}{4} \rho V_j^2 \left(1 - \frac{d_n^2}{d^2} \right) C_c \quad (3.9)$$

Figure 3.11 shows that the pressure drop ratio ($\Delta P/\Delta P_k$) increases non-linearly as jet velocity increases. Where ΔP is the pressure drop (equation (3.5)) due to gradual contractions for wide range of contraction angles (θ), and ΔP_k is the pressure drop due to kinetic energy (across a simple pipe using Bernoulli's equation (3.10)):

$$\Delta P_k = \frac{1}{2} \rho V_j^2 \quad (3.10)$$

Figure 3.11 shows that θ has very small effect on the pressure drop. For example, the pressure drop ratio for $\theta = 30^\circ$ at $V_j = 10$ m/s is, approximately, equal to 0.08. Whereas the pressure drop ratio for $\theta = 75^\circ$ at the same jet velocity is equal to about 0.14. The difference in the pressure drop ratio from the 45° increase in the contraction angle is equal to 0.06, which is negligible.

Based on the above results a contraction angle (θ) equal to 20° was used for the conical nozzle in the present work as there is not a significant reduction in pressure drop by reducing the contraction angle further.

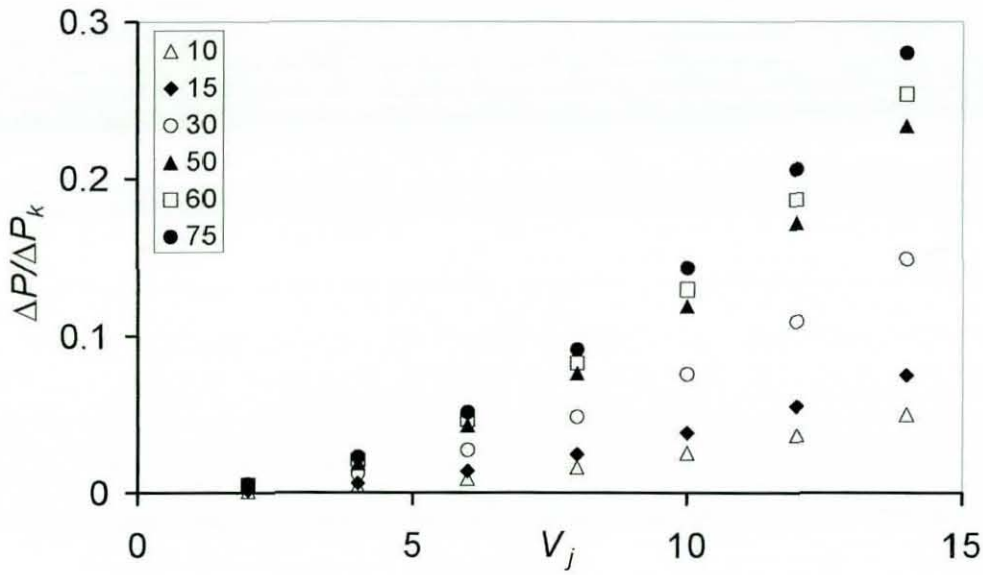


Figure 3.11 Pressure drop due to gradual contractions for various angles

Figure 3.12 shows the downcomer lengths (short ones = 600 mm) and diameters that were employed in the current work not including the longer ones with 800 and 1350 mm total length and 23 mm diameter.

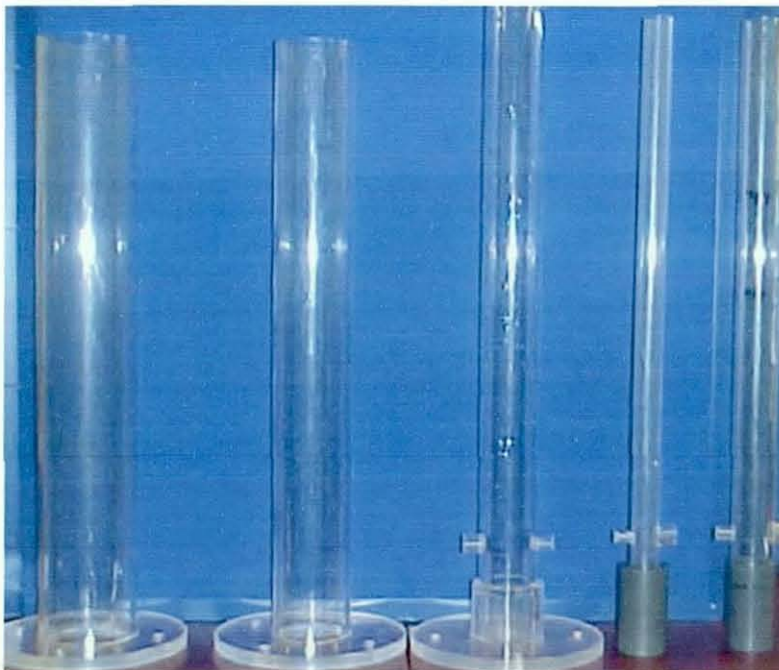


Figure 3.12 Downcomers utilized in the current work.

3.4 Modifications:

3.4.1 Soap bubble meter:

An extra tube with smaller air inlet tube connected to the side is used to obtain single bubbles (Figure 3.13). The lower part of the extended tube is connected to a spherical rubber bulb that can be squeezed to establish bubbles as needed. The side tube is open for ambient (or external) air, which is located above the soap level (it may be better if the smaller tube was connected at an angle). As the air flows through the side tube, the soap rises (squeezed as needed) and a single bubble is generated in the soap bubble meter, which is accurate enough to carry out the experiment.

One should design the side tube diameter to be greater than the tapping diameter (13 mm in this case).

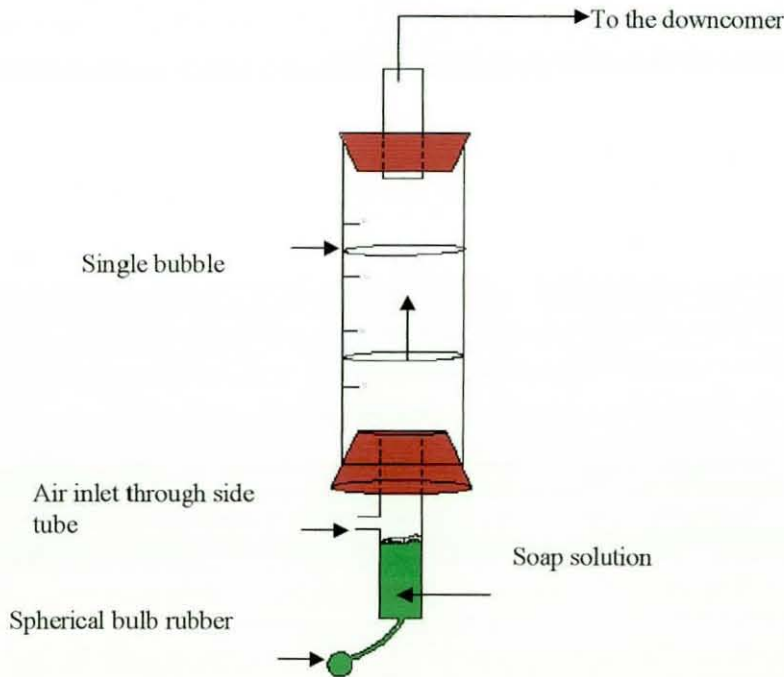


Figure 3.13 Bubble meter with slight modification.

3.5 Experimental Methodology

3.5.1 Air entrainment rate measurements

In this study, the air entrainment rate was measured as the *net* flow of gas removed by the jet from the headspace. It is important to clarify that some air may be entrained and then disentrained back into the headspace; only the *net* flow rate is measured by the soap bubble meter, *i.e.* the air flow rate leaving the bottom of the downcomer. This effect becomes more significant as the downcomer diameter and immersion depth increase and jet velocity decreases, since then disentrainment occurs to a greater degree.

Air entrainment rate was measured adopting the second method that was discussed in the literature for a confined column (air is measured as it is removed by the jet from the headspace). An air tapping located on the top of the downcomer is used to measure air entering the downcomer. The air tapping is connected all the way to the top of the bubble column meter through a soap trap (see Figure 3.1). The other end of the soap bubble meter is connected to a soap container and a side tube. As soon as the jet plunges through the headspace, a suction pressure is created inside the downcomer headspace. As shown in Figure 3.1, the loss is compensated for by an external pressurized air supply, which travels through the bubble column and then the trap before it reaches the headspace.

A stop watch was used to measure time, T , which is needed for the bubble to travel a certain vertical distance, of known volume and hence the volumetric flow rate of air was determined.

In some cases, external air was fed at very low pressure from a compressed supply, which allowed better control of the level liquid inside the downcomer. This air passed through the bubble meter before entering the downcomer headspace. A column of water was used to precisely set the pressure in the supply. For example: when water level rose inside the downcomer more external air was fed to push the level down. When water level decreased, inside the downcomer, below the initial value less external air was fed by closing the supply controlling valve (Figure 3.1, section § 3.2) in an attempt keep the level constant through out the runs. For some experiments to maintain a constant liquid level in the downcomer the pressure in the headspace was controlled to as much as 100 mm water gauge below atmospheric pressure.

3.6 Conclusions

The new designed equipment (used to make the measurements) has performed efficiently and provided good experimental results. Therefore, this design was used to carry out the future work regarding air-lift column and mass transfer rates (Chapters 7 and 9).

Utilizing external air can be beneficial when it is used to push down the level inside the downcomer to its initial state because entrainment occurs at a high gas pressure. However, this action is reversed when it is used the other way around when the pressure is reduced (to increase the level inside the downcomer or reduce penetration depth). The problem may be overcome by increasing the air tapping diameter from 12.5 mm to > 20 mm, which may minimize the use of an external air supply.

Chapter 4: Results and Discussions

4.1 Introduction

In this chapter a number of measurements, > 500, have been carried out utilizing the experimental apparatus described in Chapter 3. The results reported here investigate the effects of the jet velocity, jet length, nozzle diameter, and downcomer length and diameter on the volumetric rate of gas entrainment and mechanisms in a confined plunging liquid jet system.

4.2 Results and Discussion:

4.2.1 Effect of main variables

Jet Velocity (V_j):

Previous investigations have shown that entrainment rate increases as jet velocity increases. This relation is proportional with power law of V_j , where the index used for the jet velocity has three values depending on jet velocity (Ohkawa *et al.*, 1986a for unconfined systems). For confined system their results show that net entrainment rate increases linearly with jet velocity. In general, net air entrainment rate (Q_A) increases as jet velocity increases. Similar behaviour has been also described by Cumming *et al.* (2002), Ohkawa *et al.* (1986a) for confined systems and Yamagiwa *et al.*, (1990) for a downflow bubble column; however the relation between Q_A and V_j was not clearly specified for confined system. Also, bubble penetration depth increases as jet velocity increases (Ohkawa *et al.*, 1986a) to a certain value and then decreases at high jet velocity where jet diameter expands (before it breaks) due to air friction forces. Although the disrupted jets have less penetration depth, still a higher entrainment rate is achieved. There is a point where the jet breaks into droplets (Mckeogh and Ervine, 1981) where less entrainment rate and depth resulted.

Figure 4.1 and 4.2 were generated for the present study to show the effect of jet velocity on air entrainment rates (Q_A) for two different nozzle diameters and three jet lengths. McCarthy and Molloy (1974) and more recently Low (2003) have shown

that the jet roughness increases with increasing jet velocity (or jet Reynolds number) and that this is the controlling variable in the entrainment process. Surface instabilities, which give rise to the jet roughness, grow with distance from the nozzle until eventually the jet breaks up into liquid droplets. Figure 4.1 and Figure 4.2 also show that this effect caused greater entrained gas flowrates as the jet length was increased. (The jet lengths used here were all shorter than the breakup length, so that entrainment was always continuous.) Looking at Figure 4.1 and Figure 4.2 one can clearly see that entrainment rate increases in proportion with jet velocity to the power n , (V_j^n).

Since L_j , d_n and D_c are constant for a single run, thus air entrainment rate (Q_A) is directly proportional to the jet velocity to the n^{th} power;

The jet velocity index (n) was investigated using STATISTICA software by specifying the following function for constant d_n and D_c values:

$$Q_A = C * V_j^n \quad (4.1)$$

Since C changes for different geometries, certain conditions were specified. To illustrate this concept, $d_n = 6$ mm and $D_c = 23$ mm were chosen as a case study (L_j and V_j are changing). The results from regression method are summarized below in Table 4.1;

Table 4.1 Values of C and n by numerical and regression methods

d_n, L_j and D_c	Regression	
	C	n
6mm, 200mm and 23 mm	0.000012	1.409
6mm, 300mm and 23mm	0.00001	1.58
6mm, 400mm and 23mm	0.000011	1.59
6mm and 23mm for all of L_j	0.0000085	1.63

From Table 4.1, C and n for 300 and 400 mm jet lengths obtained by the regression method are the same. However, C and n values are slightly different for 200 mm jet length. This can also be seen from the trends shown in Figure 4.1 and 4.2. This may be attributed to the fact that with 300 and 400 mm jet lengths, and 23 mm downcomer diameter the external air was not introduced because there was no level increase or significant pressure drop ($\Delta h = 0-30$ mm) inside the column, despite the fact that the jet penetrated beneath the receiving pool surface by 50-100 mm (jet length increased). Whereas for the 200 mm jet length, external air was introduced from the beginning of the run in an attempt to control the jet length. Better control over the jet length was achieved, but at the cost of the pressure drop inside the column. Pressure drop head (Δh) inside the column reached 900 mm at the highest jet flow. This means that the air inside the column is at a pressure well below atmospheric. This low pressure may explain the reason why 200 mm data changes slope at high jet velocities (high pressure drop). The exponent n appears to be approximately constant with a value of about 1.5, which is in good agreement with Sene's (1988) theoretical model for high jet velocity

$$Q_g \propto \left(\frac{\mu_g}{\rho_l g \sin \alpha} \right)^{1/2} V_j^{3/2} d_n \quad (4.2)$$

Equations (2.4) and (4.3) (correlation produced by Ohkawa *et al.* (1986a)) indicate a power-law dependence of $Q_g \propto V_j^n$ with $n = 1.3$ to 2.0 and $n = 2.4$ for unconfined and confined systems respectively.

$$Q_g = 0.698 (V_j^3 d_n^2)^{0.8} \left(\frac{d_n}{D_c} \right)^{1.3} \left(\frac{D_c}{H_{ds}} \right) \quad (4.3)$$

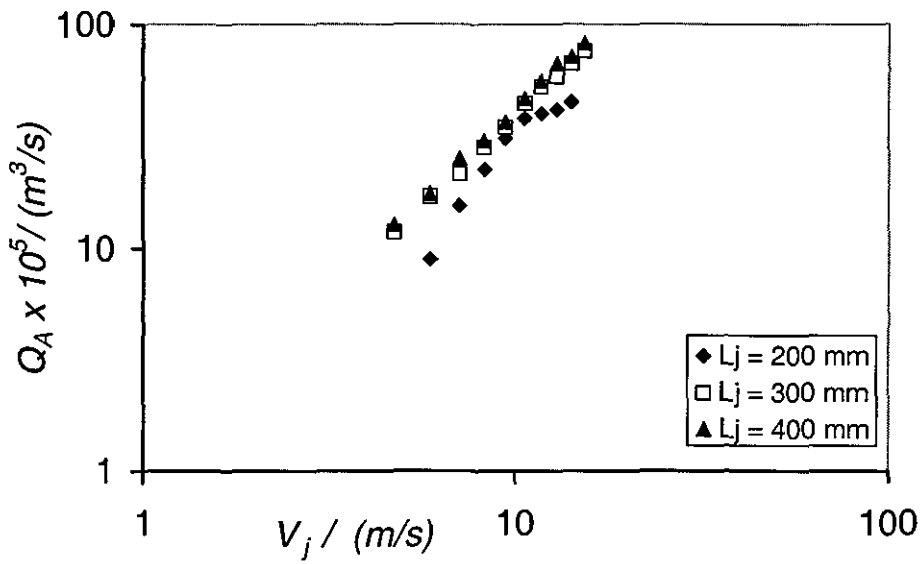


Figure 4.1 The effect of the liquid jet velocity and jet length on the entrainment air flow rate 600 mm downcomer length, $d_n = 6$ mm and $D_c = 23$ mm.

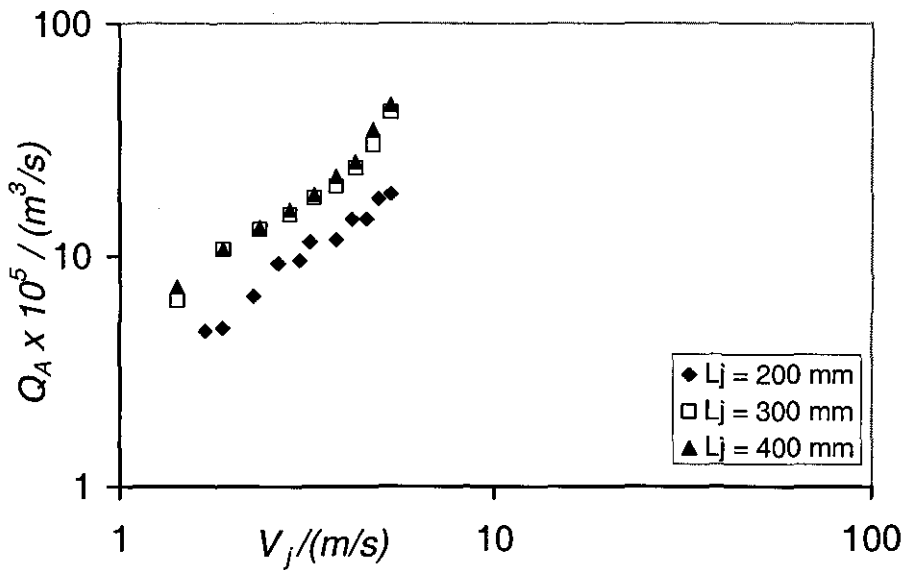


Figure 4.2 The effect of the liquid jet velocity and jet length on the entrainment air flow rate 600 mm downcomer length, $d_n = 15$ mm and $D_c = 23$ mm.

Jet length (L_j):

Generally, entrainment rate increases as jet length increases to certain value and then decreases when the jet starts to break into droplets. As described above, increasing the jet length, should increase the amplitude of the disturbances on the surface of a rough jet, since they have a longer time to grow since their inception at the nozzle exit. Hence increasing the jet length should increase the gas entrainment rate. Air entrainment ratio continues to increase until it reaches a maximum value where the entrainment ratio levels off and decreases. However, the break up point of the jet has not been reached for the current study. McKeogh and Ervine (1981) investigated this phenomenon experimentally where they showed that the jet break-up length is a function of the turbulence level within the jet, the jet diameter, and the nozzle geometry and velocity.

Present results shown by photos a and b in Figure 4.3, and Figures 4.4 and 4.5 show that *net* air entrainment rate (Q_A) increases with jet length (also, Ohkawa *et al.*, 1986; McKeogh and Ervine, 1981). Figure 4.3a shows that the submerged part of the downcomer is more than that shown in Figure 4.3b, which means that the jet length for this downcomer (Figure 4.3a) is shorter. Therefore, less air is entrained represented by fewer bubbles leaving the base of the downcomer for the same conditions. So far in the case shown in Figure 4.3b, the jet is behaving more like an unconfined jet and penetrates more deeply into the pool. This effect can also be seen from the trends plotted on Figures 4.4 and 4.5. Figure 4.4 and Figure 4.5 show such an effect, with the entrained gas flow rate increasing by about 40 - 50%, when the jet length is doubled from 200 to 400 mm, whilst keeping the jet velocity approximately constant. Similar results were obtained for other nozzle and column diameters; the effect is significant, although it is not large, probably because of the relative short lengths of jet used in this section of the study. However, the effect can still be seen from the current trends. By comparison, equations (2.2) and (2.4) predict about a 40% increase in entrainment rate for a two-fold increase in jet length, whereas equation (4.3) predicts no effect, which simply reflects that this variable did not appear to be

controlled or measured during Ohkawa *et al.*'s (1986a) experiments; in other studies the same group of workers showed that Q_A depended on the jet length.

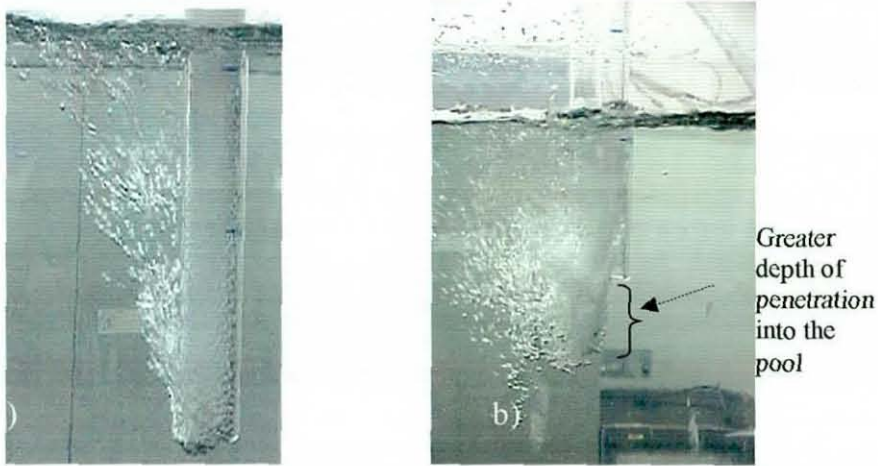


Figure 4.3 Air entrainment with same d_n , D_c , Q_j and a) $L_j = 300$ mm and b) $L_j = 400$ mm.

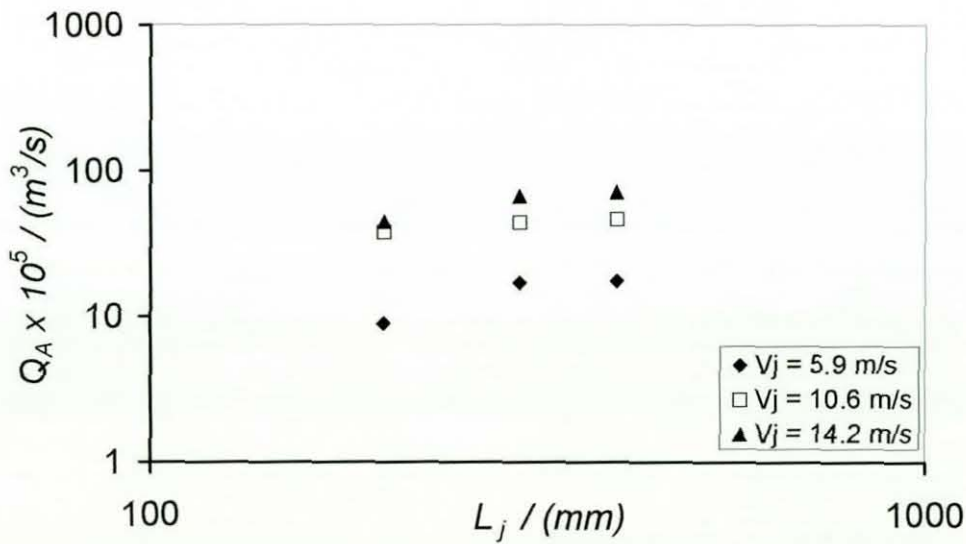


Figure 4.4 The effect of jet length and jet velocity on the entrained gas flow rate 600 mm downcomer length, $d_n = 6$ mm and $D_c = 23$ mm.

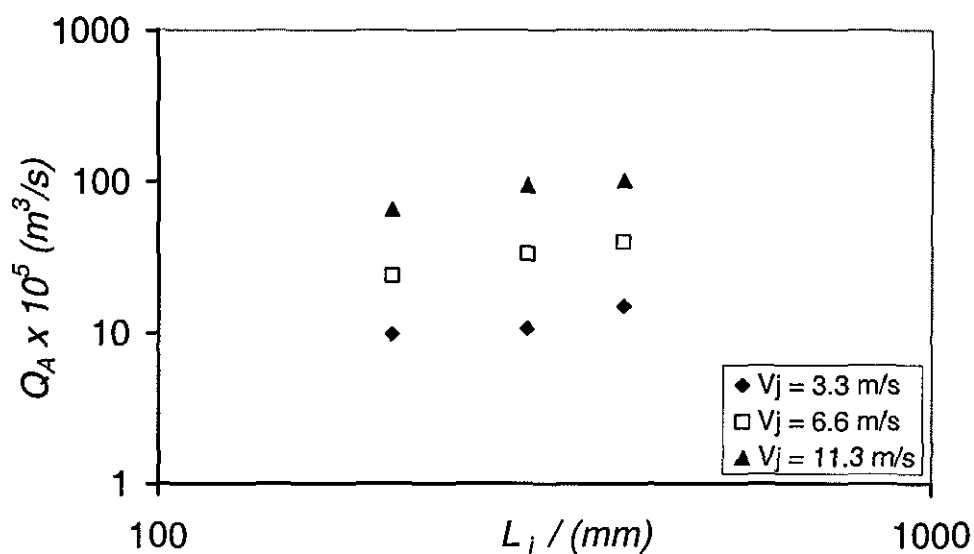
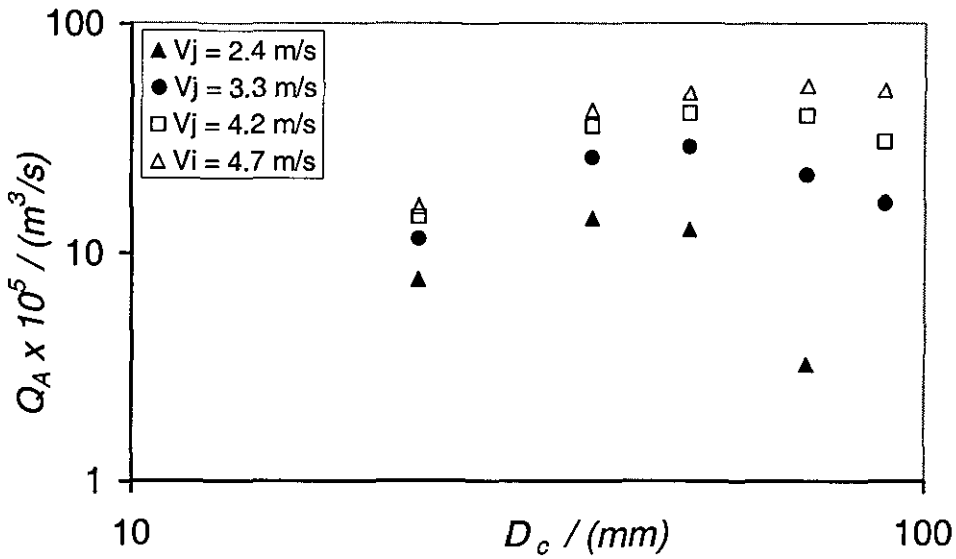


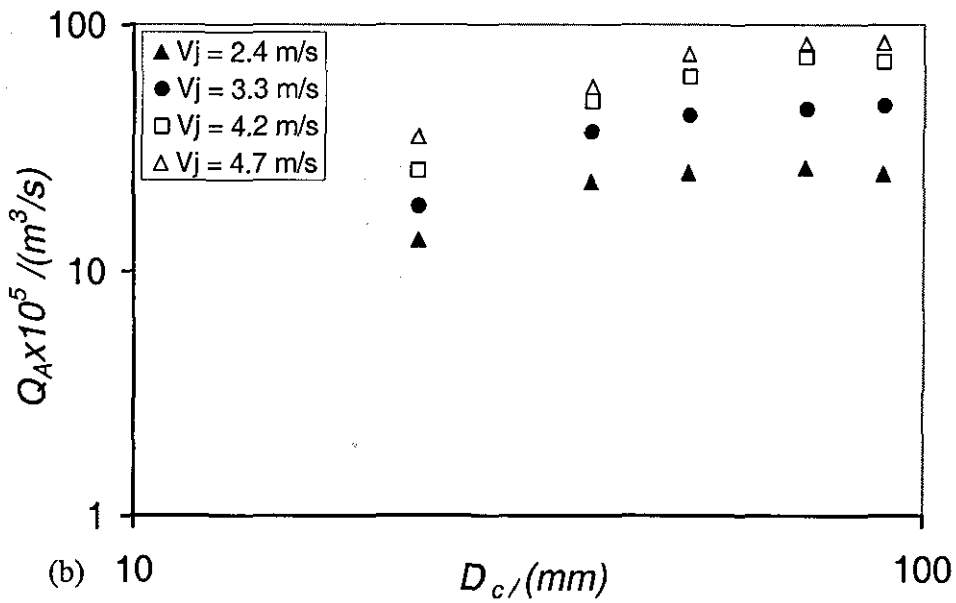
Figure 4.5 The effect of jet length and jet velocity on the entrained gas flowrate 600 mm downcomer length, $d_n = 8$ mm and $D_c = 38$ mm.

Downcomer Diameter (D_c):

This section of the report presents an investigation of the downcomer diameter (D_c) effect on air entrainment ratio. Figure 4.6, below, shows two representative sets of data for the 15 mm nozzle diameter and jet lengths of 200 and 400 mm, corresponding to downcomer immersions of 400 and 200 mm, respectively. Both sets of results show that the air entrainment rate increases with increasing downcomer diameter until it reaches a maximum and either decreases or levels off depending on the jet velocity. At low jet velocities and with larger downcomer diameters, the superficial liquid velocity in the downcomer is insufficient to carry all the entrained bubbles downwards and hence the *net* entrainment rate decreases; a significant fraction of the bubbles are entrained and then rise up in the recirculation eddy and disentrain at the free surface. In the regions where the gas entrainment rate decreases with increasing downcomer diameter, the liquid superficial velocity is less than about 0.20-0.25 m/s, which corresponds to a typical bubble terminal velocity. Thus a fraction of the entrained bubbles are able to rise against the downflowing liquid and are disentrained.



(a)



(b)

Figure 4.6 The effect of downcomer diameter and jet velocity on the entrained gas flow rate 600 mm downcomer length, $d_n = 15 \text{ mm}$ and (a) $L_j = 200 \text{ mm}$, $H_c = 400 \text{ mm}$ (b) $L_j = 400 \text{ mm}$, $H_c = 200 \text{ mm}$.

Comparison of Figures 4.6 (a) and (b), shows that the disentrainment phenomenon occurs to a greater extent with the longer immersion depth, H_{ds} . Therefore, the *net* entrainment rates are greater for the shorter downcomer immersion depth.

At the higher jet velocities, a plateau air entrainment value was reached when the downcomer diameter was about four to five times the nozzle diameter. In these cases the liquid superficial velocity in the downcomer exceeded the typical bubble terminal velocity. Low (2003) investigated gas entrainment using relatively large downcomers, with $D_c / d_n > 6$ and could find no effect of the downcomer diameter on the gas flowrate. He also measured the entrainment rate using the same nozzle and operating conditions for an unconfined plunging jet and found that lower values of Q_A were obtained, compared to the confined case. This agrees qualitatively with the results shown in Figure 4.6 in that the gas flowrate is insensitive to downcomer diameter for $D_c / d_n > 5$, at large jet velocities.

Nozzle Diameter (d_n):

Figure 4.7 shows the effect of nozzle diameter on air entrainment ratio behaviour for a 38 mm diameter downcomer and a jet length of 300 mm; similar results were obtained for other combinations of jet length and downcomer diameter. It is obvious from Figure 4.7 that for a given jet velocity, the entrainment rate increases significantly with increasing nozzle diameter. However, since the liquid volumetric flow rate produced by the pump is limited, then the highest jet velocities and hence some of the highest values of Q_A can only be obtained using the smaller nozzle diameters.

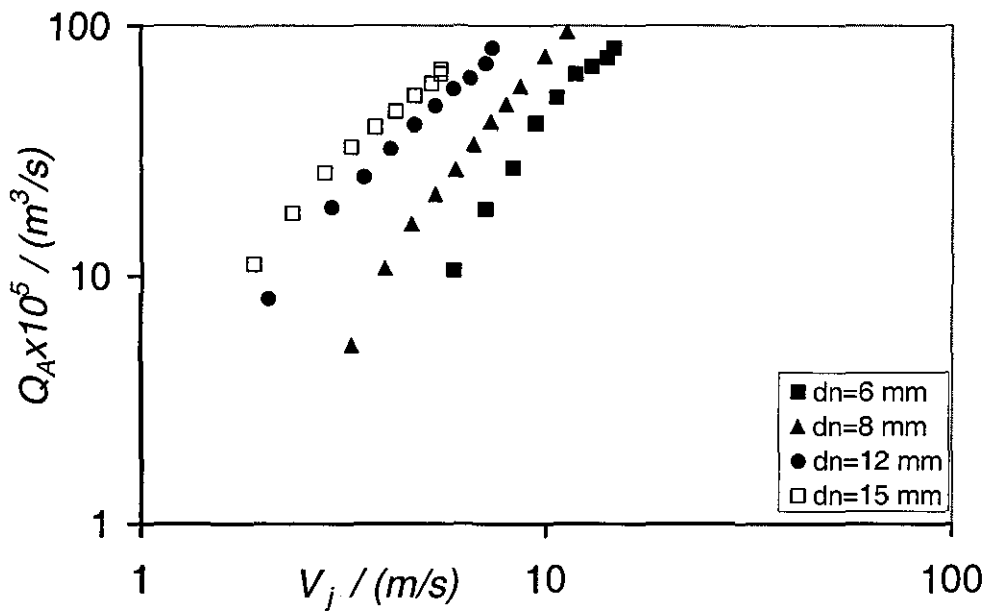


Figure 4.7 Effect of nozzle diameter on air entrainment rate.

All of the literature correlations, *e.g.* equations (2.1) to (2.4), indicate that the entrained gas rate should increase with increasing nozzle diameter. For a given jet velocity, increasing the nozzle and hence the jet diameter, produces a larger jet perimeter at the plunging point and hence more gas is entrained. On this basis, the entrainment rate may be expected to be approximately proportional to the nozzle diameter, but the correlations of equations (2.2) to (2.3) suggest a slightly larger exponent of 1.2 to 1.4. Power law regression of the data in Figure 4.7 gives an exponent of about 1.5 to 1.6 on the nozzle diameter.

Pump Effect:

Due to refurbishing of the pilot plant lab, the rig was moved to another area of the lab. Since the rig was dismantled, this was a good opportunity to replace the mono-pump with a centrifugal pump. Therefore, before proceeding any further a pump consistency test was performed on the new pump. This action was taken for two purposes; a) to achieve higher jet velocities, and b) to investigate pump effect on air entrainment rates through reducing the vibration that was caused by the mono-pump. Also, another test was performed to check the effect of implementing a baffle to stop air being sucked into the pump due to the high flow rates that could be achieved.

Pump consistency performance was checked by conducting several runs utilizing both pumps for the same operating conditions. The downcomer length (L_D) and the nozzle diameter (d_n) remained constant for all of the runs, whilst the jet length (L_j) and the downcomer diameter (D_c) were varied. Also, the same flow rates were used for both pumps so that the results would be directly compared.

Figure 4.8 and Figure 4.9 show that both pumps have almost the same results and trends. The old pump provided slightly higher entrainment ratios especially at higher jet velocities. This may be attributed to the fact that the old pump made the whole rig vibrate including the jet, which may have disturbed the jet and therefore increased the roughness of the jet surface. As a result higher air entrainment rates were measured especially at high jet velocities, where the vibration was more significant. Other (secondary) factors that may contribute to the small differences between the results were that the water levels inside the downcomer were very difficult to maintain constant. As a conclusion from the above investigation, one can see that pump effect on entrainment rate is not very significant.

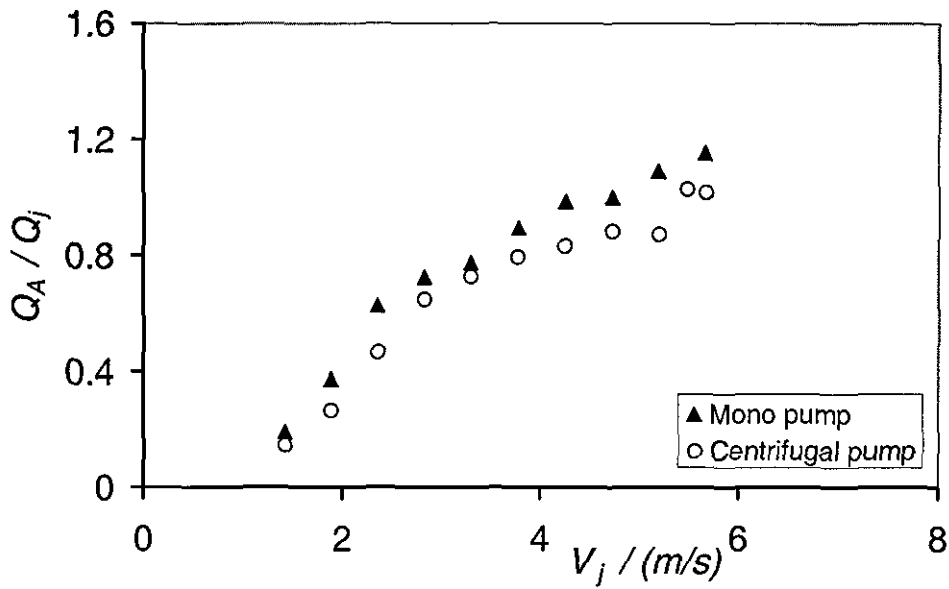


Figure 4.8 Air entrainment rate for both pumps with $D_c=71$ mm, $d_n=15$ mm and $L_j=400$ mm.

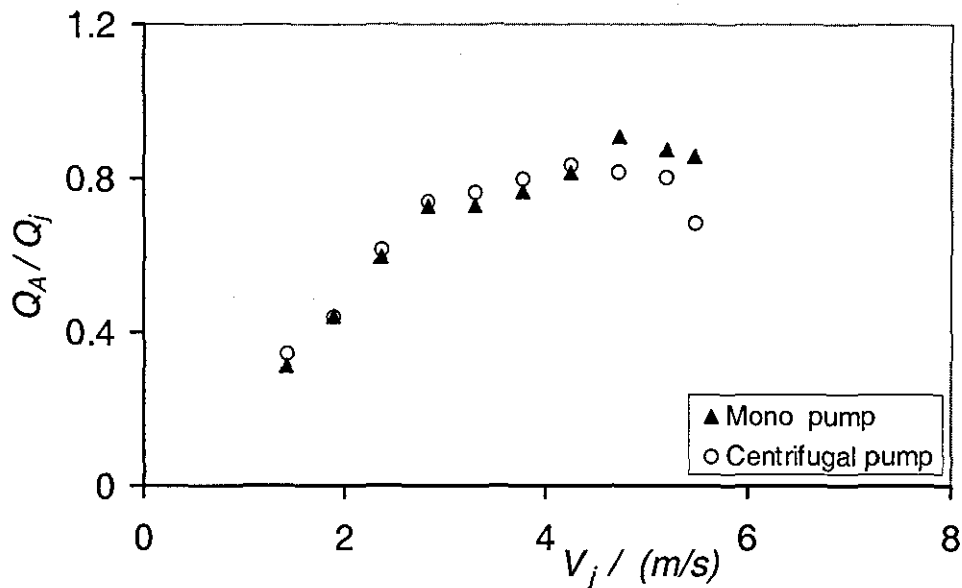


Figure 4.9 Air entrainment rate for both pumps with $D_c=50.5$ mm, $d_n=15$ mm and $L_j=400$ mm.

Unexpectedly, some of the bubbles leaving the base of the downcomer were drawn into the pump suction. This incident was not observed with the old pump. This

may be explained by the bubbles direction as they leave the base of the pump. With the old pump, the bubbles were shifted away from the suction point. Whereas for the new pump the situation is the opposite (bubbles were shifted towards the suction pump). As a result, a weir baffle was used to reduce the amount of air sucked into the pump.

Figure 4.10 was plotted using the results obtained from two runs that were carried out utilizing the new pump, which allowed air to be sucked by the pump. As shown in the figure, air that was drawn by the pump has very little effect with or without the baffles presence. This suggests that this amount of air did not have a significant effect on air entrainment ratio.

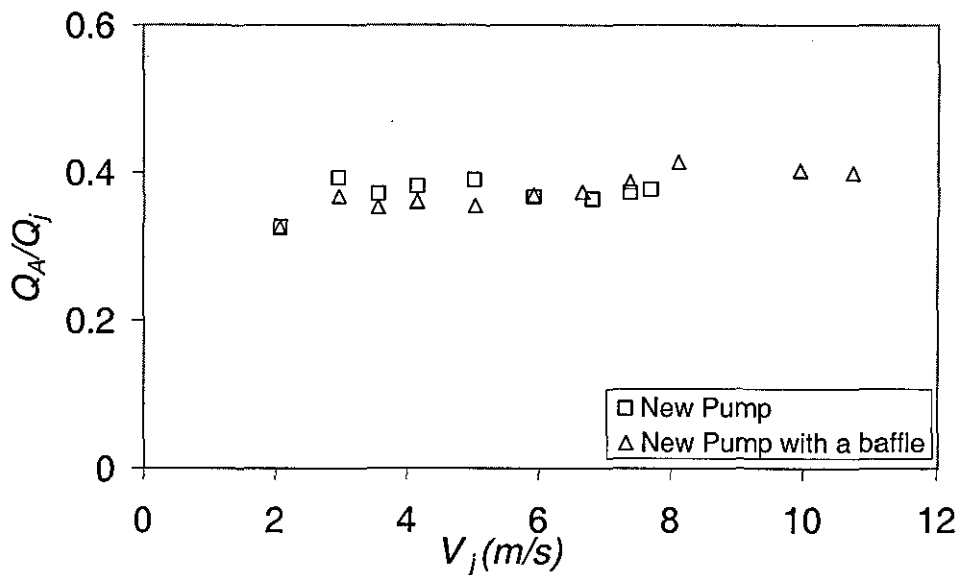


Figure 4.10 Air entrainment rate for the new pump with and without a baffle for $L_j = 400$ mm, $D_c = 23$ mm, $d_n = 12$ mm and $L_D = 1350$ mm.

Effect of Downcomer Submergence Length (H_{ds}):

From the literature there is a considerable disagreement over the effects of the immersed part of the downcomer length on the rate of gas entrainment in confined plunging jet systems. Cumming *et al.* (2002) found that downcomer length had a

negligible effect on the entrainment rate, whereas Ohkawa *et al.* (1986a) suggested otherwise (Q_A decreases with increasing H_{ds}). The immersed downcomer length is therefore the difference between the total length (L_D) and the jet length (L_j). As pointed out previously, short downcomer lengths (L_D) were used initially in the current work. The experiment conducted here used total downcomer lengths of 600 – 1350 mm and two different jet lengths to investigate their effect on the entrainment rate.

In Figure 4.11 and Figure 4.12 the entrainment rate ratio is plotted against the jet velocity for different jet and downcomer lengths (L_j and L_D respectively). Each plot is generated utilizing two downcomer lengths (600 and 1350 mm) keeping the rest of the variables constant (d_n , L_j and D_c). Figure 4.11 shows that at low jet velocities ($V_j < 2.5$ m/s), 400 mm jet length and 15 mm nozzle diameter, the same results were obtained for both downcomer lengths. When the jet velocity exceeds 2.5 m/s the shorter downcomer gave slightly higher entrainment ratios. For a jet velocity above 4.0 m/s the shorter downcomer gave a significant higher entrainment rate. This behaviour may be described by the proposed mechanisms shown in scenarios 1, 2 and 3 in Figure 4.11. Similar behaviour was described for a 12 mm nozzle and is shown in Figure 4.12. At low jet velocities (scenario 1), the downcomer submergence length (H_{ds}) has no effect on air entrainment ratios (Figure 4.11 and Figure 4.12) because the entrained air flow rate is relatively small and the closely packed bubbles (unbroken tiny bubbles) coalesced, and hence larger bubbles were formed, at short L_{im} below the water surface inside the downcomer for both cases due to loss of momentum as the jet penetrated downward. As a result some bubbles left the base of the downcomer, whilst the rest rose to the surface (due to buoyancy forces). These bubbles were disentrained and thus were not measured. As shown by scenario 1, this mechanism applies for both downcomers and hence the results were the same. Scenario 2 suggests that as the jet velocities increases, more air is entrained represented by longer penetration depth (L_{im}) of the unbroken bubbles (closely packed tiny bubbles) below the water surface to occupy most of the short downcomer submergence length (H_{ds}). Bubbles broke up at a deeper depth, which may have minimized the disentrainment of

the bubbles and therefore more air is measured than the previous case with the short downcomer. However, the situation is different with longer downcomer because the unbroken bubbles still occupied a small portion of the downcomer. Therefore, bubbles coalesced inside the downcomer before they left the bottom of the downcomer. The coalesced bubbles travelled a long way (in the downward direction) to leave the bottom of the downcomer, which increases the disentrainment flow rate and therefore less net air was measured than that of the short downcomer. As air entrainment ratio increased with higher jet velocities, the bubbles coalesced outside the short downcomer, which suggests that almost no disentrainment took place. With regards to the longer downcomer the bubbles coalesced at deeper distance than that of scenarios 1 and 2, however still inside the downcomer. This means that disentrainment phenomenon continued in the case of the longer downcomer and therefore reduced the amount of *net* air leaving the downcomer as bubbles.

The above suggestions may be further explained by carrying out runs with different variables, as shown below in Figure 4.14, such as a shorter jet length (200 mm), $d_n = 12$ mm and $D_c = 23$ mm. The results for both downcomers show almost the same values up to about $V_j = 7$ m/s, which is higher than the previous case ($V_j = 4.0$ m/s). This may be because the jet length is shorter in this case, and therefore the submerged part (H_{ds} , Figure 4.11) of the downcomer is longer than the previous case especially for the shorter downcomer. As a result it took higher jet velocities to drive the closely packed bubbles (unbroken bubbles) outside the short downcomer after which the two sets of the experimental data deviated from each other ($V_j > 7$ m/s, Figure 4.14). This may have affected air entrainment measurements for CPLJR.

Comparing Figure 4.12 and Figure 4.14, one can see that almost the same values of Q_A/Q_j were recorded for the longer downcomer (1350 mm) for both jet lengths. The highest air entrainment ratio value recorded for the longer downcomer, for both runs, was equal to 0.48. However, this was not the case for the shorter downcomer (600 mm) where the highest entrainment ratio dropped down from 0.7 to 0.5 as the jet length decreased (from 400 to 200 mm). This shows that the *net* air

entrainment rate was affected by downcomer submergence (H_{ds}) due to disentrainment.

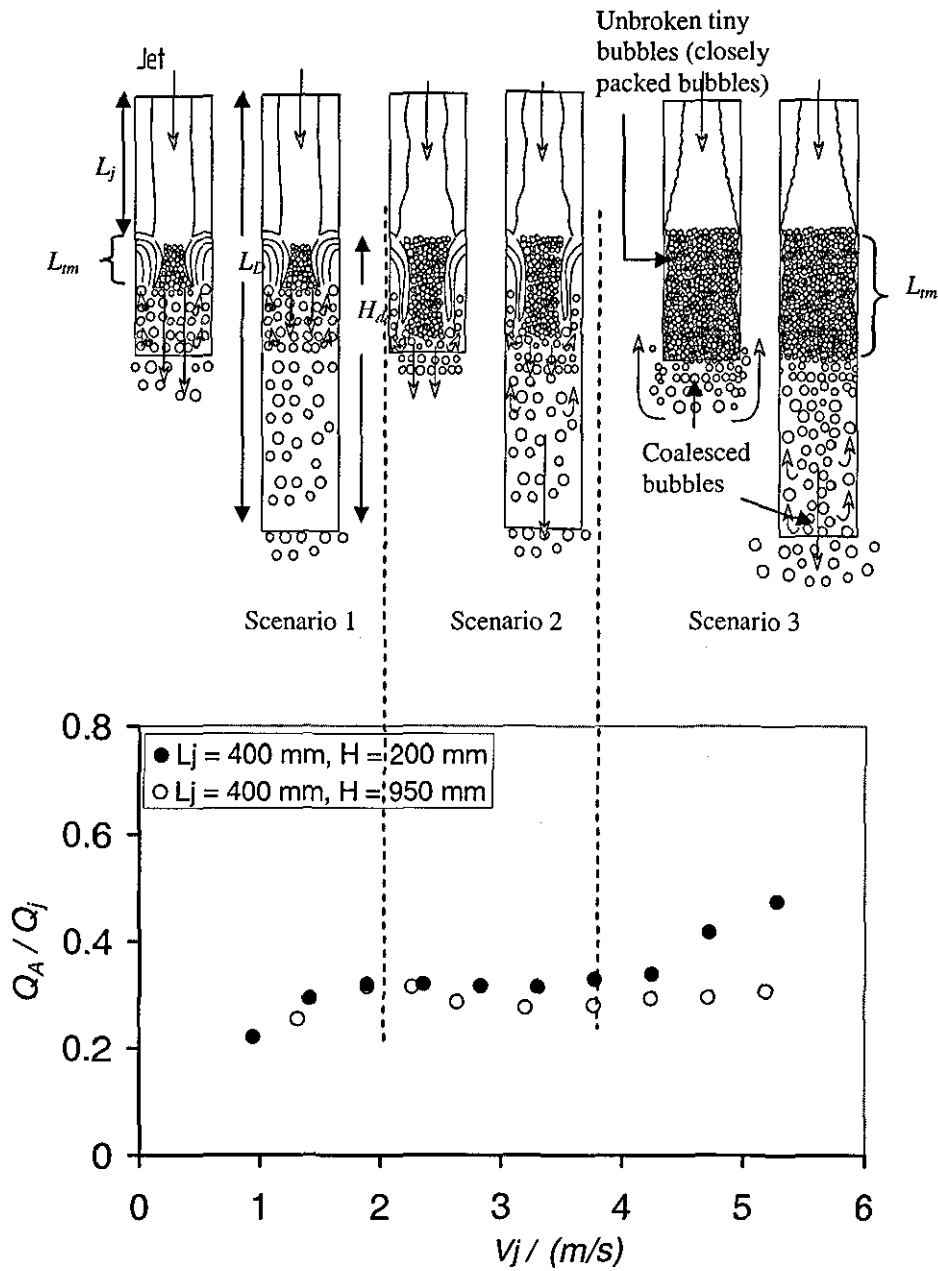


Figure 4.11 The effect of the downcomer length on the entrainment rate ratio $d_n = 15$ mm and $D_c = 23$ mm, filled symbols: 600 mm downcomer and open symbols: 1350 mm downcomer

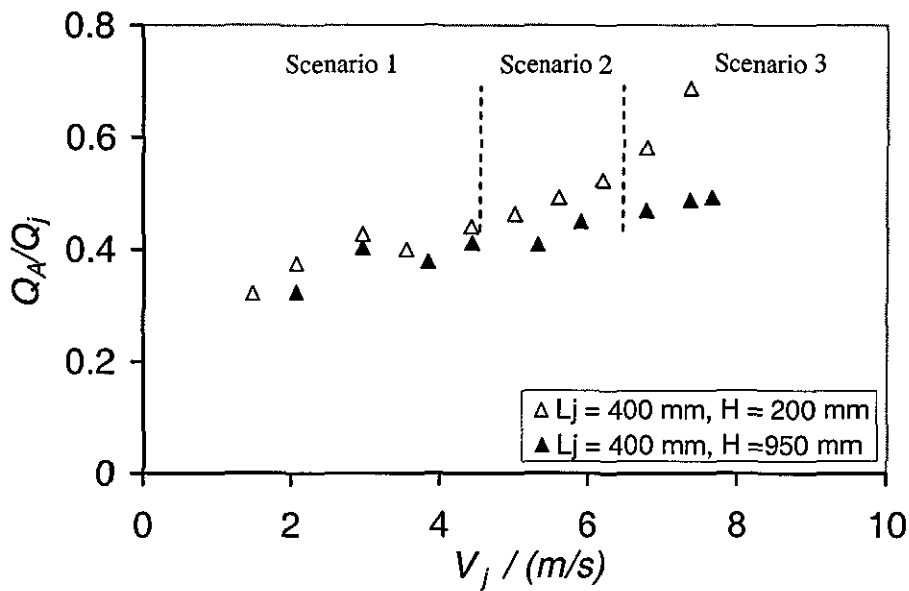


Figure 4.12 The effect of the downcomer length on the entrainment rate ratio $d_n = 12$ mm and $D_c = 23$ mm, filled symbols: 600 mm downcomer and open symbols: 1350 mm downcomer

Over much of the range of jet velocities investigated, Figure 4.12, shows that there is little difference in the entrained gas rate between the long and short downcomers. Some minor differences may be apparent at the lowest jet velocities, but here the entrainment rates are low and the measurements are subject to greater variability and error. However, at the highest jet velocities, the *net* entrainment rates for the shorter immersion depth are significantly and consistently greater than for the longer downcomer. This may be attributed to an effect of disentrainment with long immersion depths. This is illustrated in Figure 4.13 (a) which shows the expansion of a two phase submerged jet in a long downcomer; the eddy circulation region surrounding the jet is typically $3-5D_c$ long, corresponding to jet expansion angles of $10-20^\circ$ (Bayly *et al.*, 1992). Bubbles can disentrain by being advected upwards in the recirculation zone. In contrast, for shorter downcomers shown in Figure 4.13 (b), the jet is unable to expand to the wall before the exit from the confining tube and hence a larger proportion of the entrained bubbles are able to escape. Consequently the rate of gas disentrainment is reduced with shorter downcomers and therefore the *net*

entrainment rate is increased. This effect is most important at high jet velocities, where with a short downcomer, almost all of the bubbles entrained are swept out of the confining column, with very little disentrainment taking place. Over a wide range of conditions, however, there was no effect of the downcomer immersion depth on the entrained gas flowrate.

Ohkawa *et al.*'s (1986a) finding that the entrainment rate is inversely proportional to H_{ds} , equation (4.3), for long downcomers was not found to be the case here. However, in Ohkawa's experiments the jet length does not appear to have been controlled in these experiments and does not feature in equation (4.3). Thus, the effect of changing H_{ds} may have been misinterpreted as being due to a change in L_j .

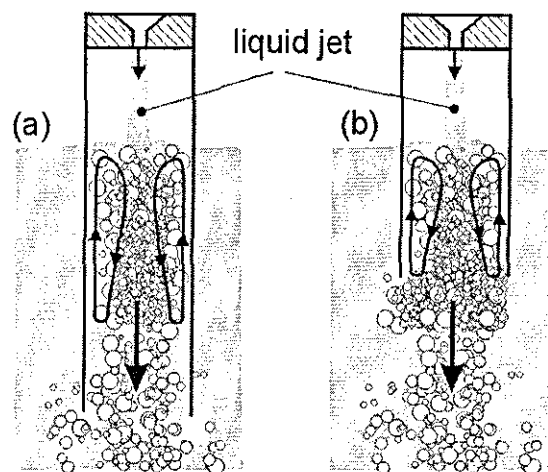


Figure 4.13 Expansion of the two-phase jet in (a) a long downcomer and (b) a short downcomer

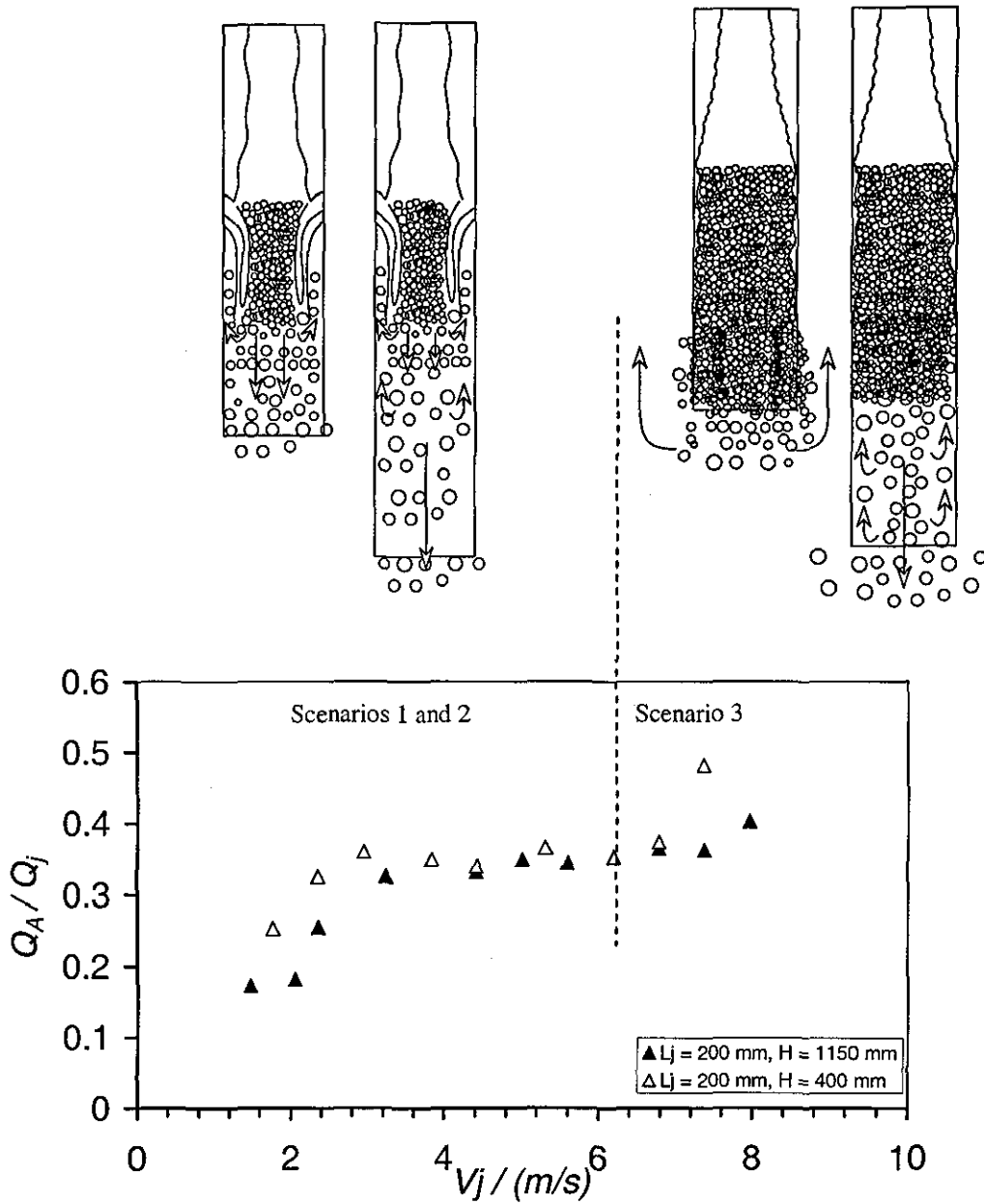


Figure 4.14 The effect of the downcomer length on the entrainment rate ratio $d_n = 12$ mm and $D_c = 23$ mm, filled symbols: 600 mm downcomer and open symbols: 1350 mm downcomer.

Figure 4.15 is generated for the smallest nozzle diameter (6 mm), a jet length of 200 mm and two downcomer submergences (H_{ds}). Results show that air entrainment measurements for both lengths are identical (except for the first two

readings). This could probably be attributed to the fact that with a smaller jet diameter, higher jet velocities were achieved (at the same jet flow rates) than the previous cases, that drove the unbroken bubbles (closely packed bubbles) outside both of the downcomers (scenario 3). Also, no contact was observed between the jet and the downcomer wall which may have affected the jet momentum (due to jet expansion). As shown in Figure 4.15, similar results were obtained at $V_j \geq 7$ m/s for both downcomers.

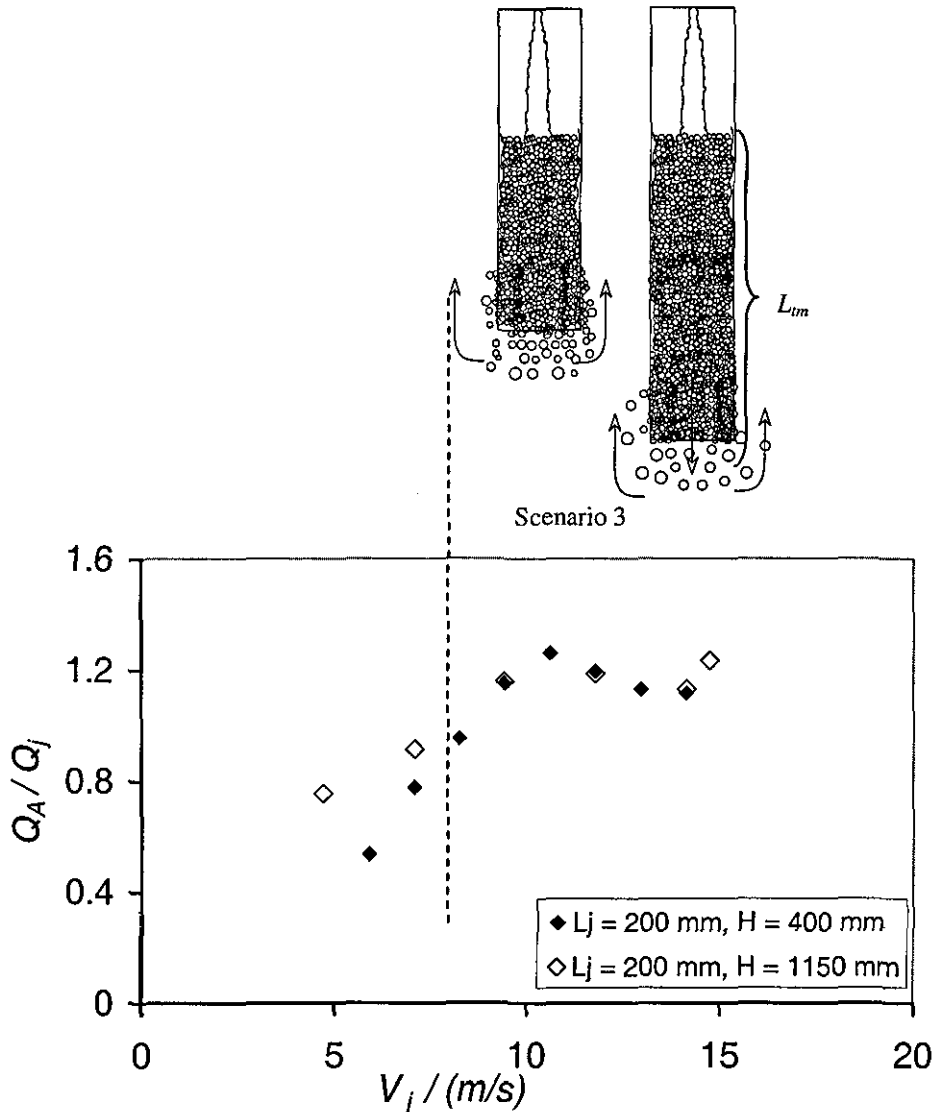


Figure 4.15 The effect of the downcomer length on the entrainment rate ratio $d_n = 6$ mm and $D_c = 23$ mm, filled symbols: 600 mm downcomer and open symbols: 1350 mm downcomer.

A mid-range (800 mm) downcomer length, with same diameters (23 mm) as the previous downcomers (600 mm and 1350 mm), was employed to investigate its effect on air entrainment ratios, and compare it with the previous cases. Results for the three downcomers are plotted in Figure 4.16, where the short downcomer data (600) were measured utilizing the old pump and the other downcomers (800 mm and 1350 mm) data were measured utilizing the new centrifugal pump. It is clear from Figure 4.16 that the difference is very small on air entrainment ratio obtained with various downcomer lengths (L_D) up to a jet velocity of 7 m/s.

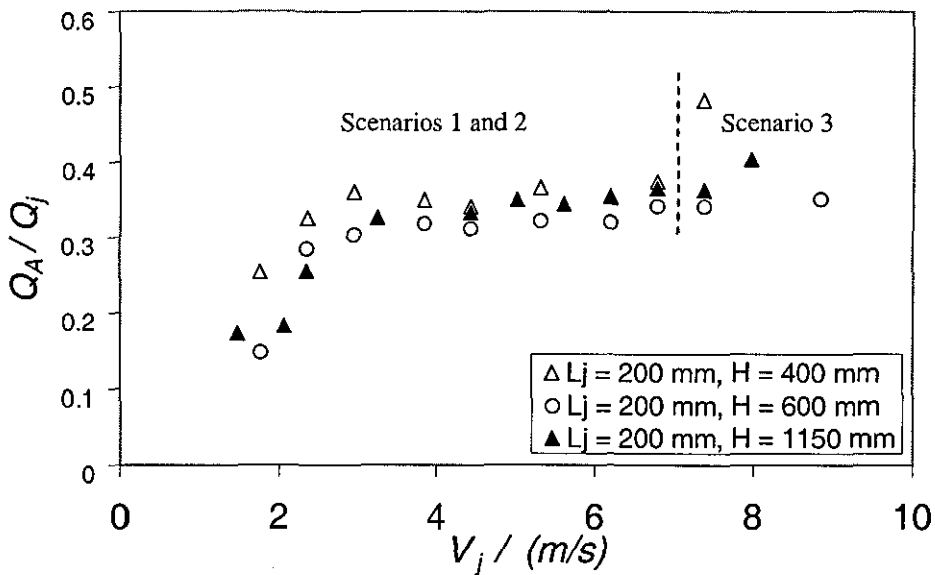


Figure 4.16 The effect of the downcomer length on the entrainment rate ratio $d_n = 12$ mm and $D_c = 23$ mm, square symbols: 600 mm downcomer, circle symbols: 800 mm downcomer and open symbols: 1350 mm downcomer.

4.3 Fitting the Data

The entire data set covering the individual effects of the nozzle diameter, jet length, jet velocity and downcomer diameter on the entrainment rate, comprises over 500 separate measurements. Figures 4.1 – 4.7 indicate that for a range of conditions the entrainment rate follows approximately a power-law dependence on the main

operating variables, which is the assumption behind many of the empirical correlations in the literature. The exception to this is the effect of the downcomer diameter on the entrainment rate, where there is evidence of a maximum; for large diameter downcomers, Q_A then decreases with increasing D_c , corresponding to low liquid superficial velocities in the downcomer, that are unable to carry down the larger gas bubbles. This is not a particularly satisfactory way to operate a confined plunging jet reactor and so this region of low liquid superficial velocities and large downcomer diameters is of little practical importance. Therefore data with a liquid superficial velocity of less than 0.2 m/s have been excluded from the regression analysis. In these cases, a power-law dependence of Q_A on D_c should suffice.

To quantify the effect of the main parameters (V_j , L_j , d_n and D_c) on the measured entrainment ratio, a correlation that relates air entrainment ratio to three dimensionless groups was investigated. The best way to determine the number of independent dimensionless parameters into which the variables are combined is by using Buckingham's pi theorem, which is described by the following equation:

$$i = n_v - r \quad (4.4)$$

where

i = the number of independent dimensionless groups.

n_v = the number of variables involved.

r = the rank of the dimensional matrix that is formed by tabulating the exponents of the fundamental dimensions.

Fundamental dimensions are L and T , which appear in each of the variable involved.

The first step was to prepare a list of the variables and their dimensions in terms of fundamental dimensions as follows,

Table 4.2 Variables in fundamental dimensions.

Variable	Symbol	Dimensions
Air entrainment rate	Q_A	L^3/T
Jet velocity	V_j	L/T
Kinematic Viscosity	ν	L^2/T
Nozzle diameter	d_n	L
Downcomer diameter	D_c	L

To solve for r , the following matrix is formed:

$$\begin{array}{rcccccc}
 & Q_A & V_j & d_n & D_c & \nu \\
 L & 3 & 1 & 1 & 1 & 2 \\
 T & -1 & -1 & 0 & 0 & -1
 \end{array}$$

Rank (r) in this case is equal to 2 (number of rows or columns in the largest non-zero determinant which can be formed from it). Therefore, the number of independent dimensionless groups that can be formed is equal to:

$$i = 5 - 2 = 3 \text{ groups}$$

Data regression was carried out using STATISTICA software, fitting the parameters in the following dimensionless correlation.

$$\frac{Q_A}{Q_j} = a (Re_j)^b \left(\frac{L_j}{d_n} \right)^c \left(\frac{d_n}{D_c} \right)^d$$

Measurements which exhibited significant amounts of disentrainment, for example with low liquid superficial velocities, or with very short immersion depths and high jet velocities were excluded from the analysis. The fitted parameters

obtained for the regression were (the additional figures are the 95% confidence intervals for the exponents): $a = 1.4 \times 10^{-4}$, $b = 0.56 \pm 0.07$, $c = 0.62 \pm 0.05$, $d = -0.38 \pm 0.05$ as shown below,

$$\frac{Q_A}{Q_j} = 1.37 \times 10^{-4} \text{Re}^{0.558} \left(\frac{L_j}{d_n}\right)^{0.617} \left(\frac{d_n}{D_c}\right)^{-0.383} \quad (4.5)$$

Where,

$$\text{Re} = \frac{d_n V_j}{\nu}$$

A comparison between the regressed correlation, equation (4.5) and the experimental measurements is given in Figure 4.17, which also shows an error band of $\pm 30\%$. Satisfactory agreement has been obtained, apart from at very low entrainment rate ratios.

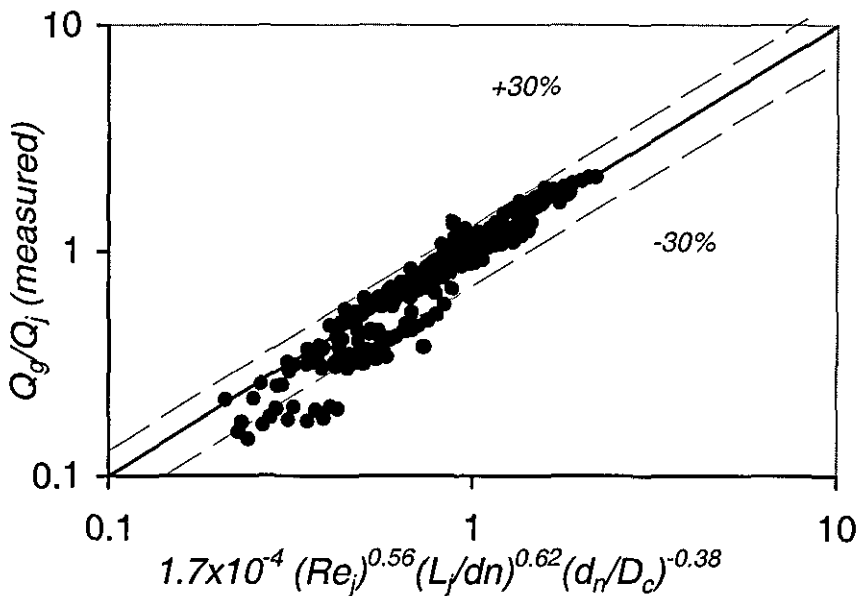


Figure 4.17 Comparison of the dimensionless correlation of equation (4.5) with the experimental data set, showing an error band of $\pm 30\%$.

4.4 Mechanisms

Most of the work regarding plunging jet mechanisms has been conducted with *unconfined plunging liquid jets*. So far there has not been discussion of the mechanisms, which describe the air entrainment for a confined plunging liquid jet reactor. With confined plunging jet reactors the situation is different because of the downcomer presence. Having an extra constraint, represented by the downcomer, may have a substantial effect on the mechanisms. For example air voidage fraction is greater for the confined systems than unconfined ones. Also, the downcomer wall can have an effect on air entrainment mechanisms especially for narrow downcomers and large nozzle diameters. This part of the report discusses mechanisms for confined plunging liquid jet reactor for the current conditions. The mechanisms can be divided into three categories based on the flow behaviour as follows:

4.4.1 Smooth (low velocity) jets

Smooth jets usually have very little entrainment rate (Figure 4.18). As shown in Figure 4.19 the jet surface is smooth and the jet diameter decreases along the jet length. This reduction in the jet diameter is shown in Figure 4.19. The amount of accompanying air is expected to be small. As soon as the jet impinges onto the pool surface a cavity is established slightly below the pool surface. Similar behaviour was observed by previous authors Bin (1993), McKeogh and Ervine (1981) and Davoust *et al.* (2002) for unconfined systems. However, in the present study the situation is different because a vortex (swirl) was established even at low velocity. Also the cavity caused by the jet appears to be more than that described by other authors for unconfined system, because of the downcomer presence. As the volume of the downcomer restricts the bubbles, the voidage for a confined jet is higher than that for the unconfined case.

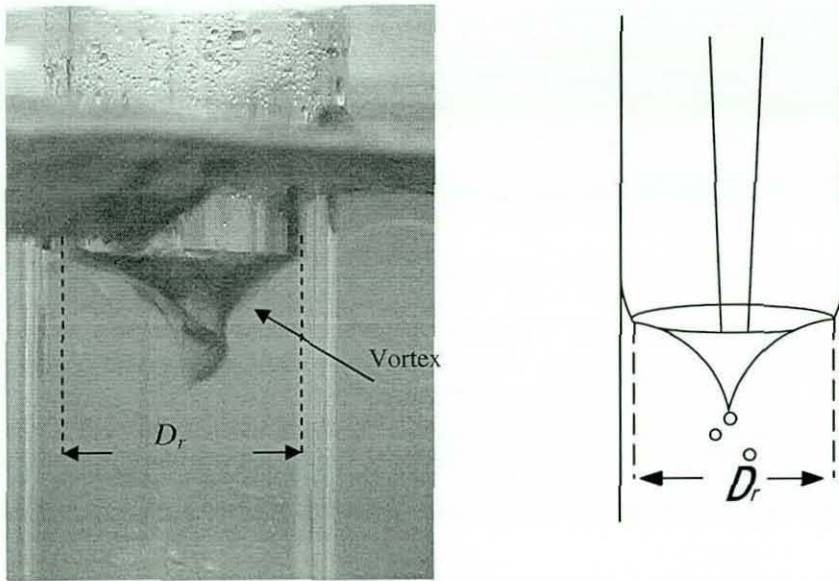


Figure 4.18 Cavity in a vortex manner inside the downcomer caused by smooth jet.

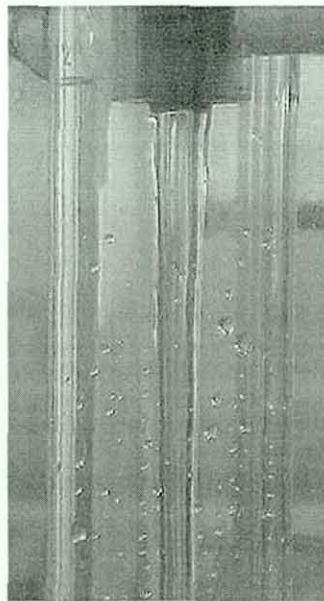


Figure 4.19 Smooth jet surface and a reduction on the jet diameter at low jet velocity.

4.4.2 Moderate velocity jets

This region starts, approximately, when the first bubble is entrained inside the downcomer (under the water surface) and continues until the turbulent flow is developed. At this stage, the jet characteristics are in transition between laminar and turbulent. Air entrainment is attributed to jet surface irregularity (roughness of jet surface). Air entrainment mechanisms in this case are clearer than that of the laminar flow.

Tiny bubbles are formed at the top part of the downcomer that move intermittently in a circular (toroidal) motion on both sides of the jet associated with vortex (swirl) phenomenon. Toroidal motion may be due to the jet momentum and downcomer diameter. Swirl motion may have resulted from several factors such as, the jet not being in the centre of the downcomer or due to the pump vibration causing the toroidal motion. These bubbles rotate around an axis. The rotation phenomenon slows down as the two-phase flow penetrates deeper inside the downcomer. At a certain depth, where the jet momentum slows down, bigger bubbles are formed due to coalescence of smaller bubbles. Also at this point the two-phase superficial velocity is slow comparison to the impingement point where the jet momentum was high. Larger bubbles soon rise back up and do not leave the downcomer.

4.4.3 Rough (high velocity) jets

4.4.3.1 Low rough jets

As the jet velocity (V_j) increases for certain conditions (jet length, downcomer diameter and nozzle diameter), and thus turbulence, the two-phase flow penetrates deeper in downward direction until the first bubble leaves the downcomer marking the first measured value of air entrainment rate. This velocity is defined as the minimum entrainment velocity (V_{em}) for a confined plunging liquid jet reactor.

At the top of the downcomer, continuous circular motions are also noticed defined as toroidal motion (Figure 4.20). Two types of bubbles are formed; primary and secondary bubbles. Very small (closely packed) bubbles form at the top of the downcomer and extend to L_{tm} distance below the pool surface. L_{tm} is defined as the length of the downcomer occupied by the toroidal motions, after which the bubbly flow forms as shown in Figure 4.20b. The closely packed bubbles move up and down in a toroidal motion due to the jet momentum. Larger bubbles, by coalescence, form below the small ones until they leave from the bottom of the downcomer. As shown in Figure 4.21 at this velocity the larger bubbles are sporadic and take the shape of ellipsoids.

Note that there are two separate motions occur simultaneously. A toroidal motion that starts at the pool surface and travels down to L_{tm} distance. This motion rotates a round an axis, which is perpendicular to the jet direction. The second one is known as the vortex (swirl) motion that also starts at the pool surface and penetrates down in a spiral manner. It spins around an axis that is parallel to the jet direction. Figure 4.22 shows a schematic of both motions.

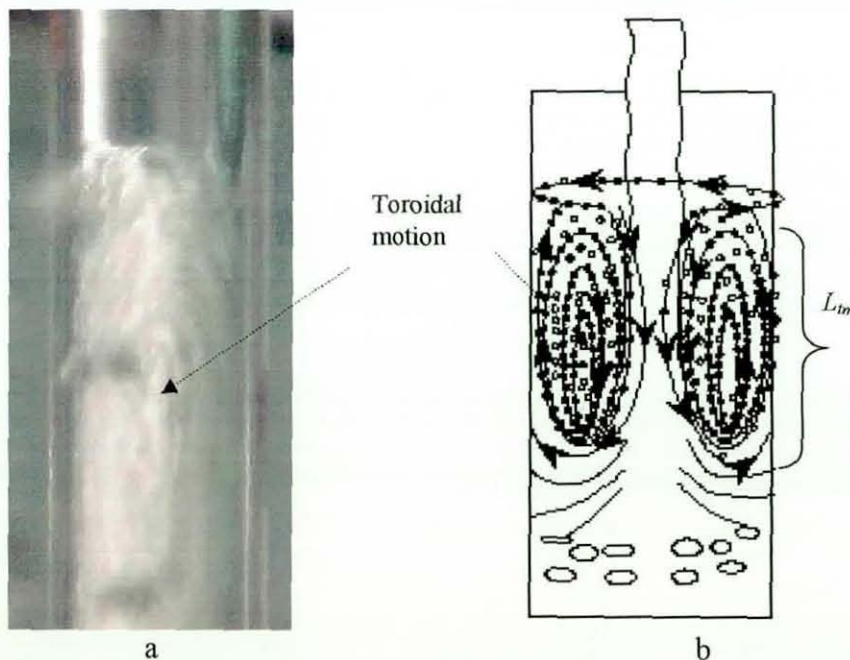


Figure 4.20 Top part of the 23 mm downcomer a) side and b) front view, where small bubbles can be barely seen.

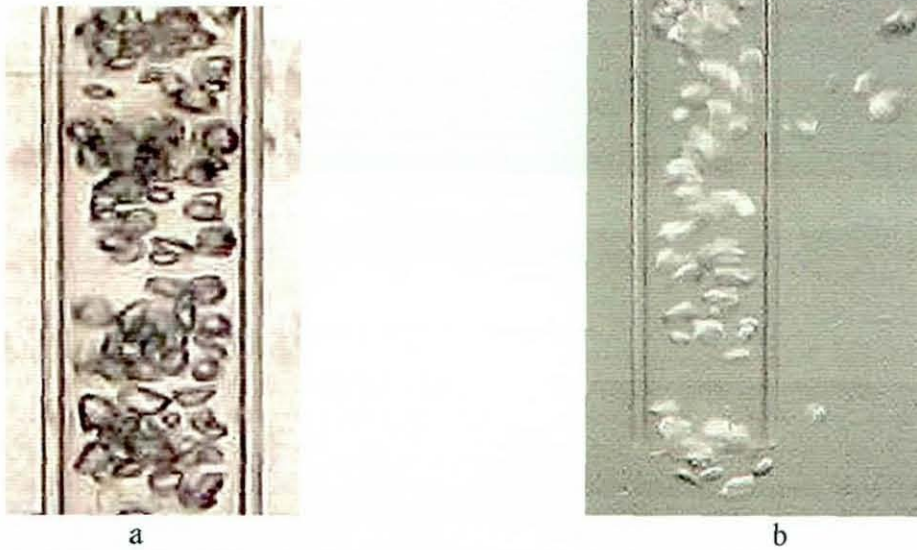


Figure 4.21 Sporadic (ellipsoidal) bubbles at the a) middle and b) bottom parts of the downcomer.

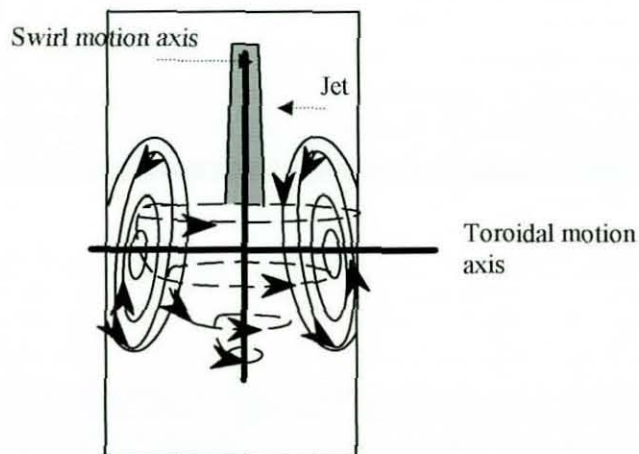


Figure 4.22 Circular and vortex motions axis.

4.4.3.2 Moderate rough jets

Similar behaviour was observed when the jet velocity increases beyond the minimum entrainment velocity. However, L_{tm} is increased (Figure 4.23a) and the bubbles are not sporadic anymore. Because of higher jet velocity, and thus more air

entrainment, the bubbles are overlapping, forming a train of bubbles that travel all the way to the bottom of the downcomer as shown in Figure 4.23b.

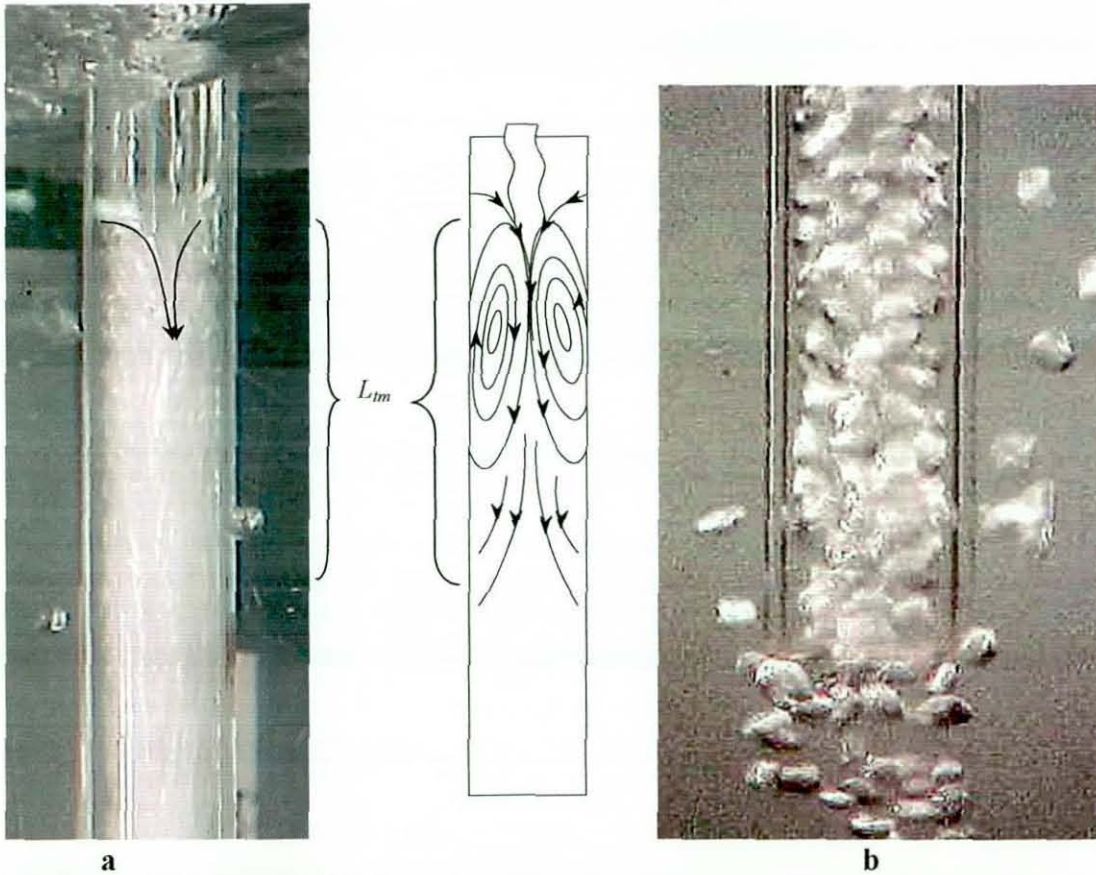


Figure 4.23 a) Top part that shows longer L_m and b) bottom part that shows train of bubbles of the downcomer at moderate jet velocity.

4.4.3.3 High rough jet

As the jet reaches high turbulent region by continuing to increase the jet velocity, the irregularity on the jet surface increases and the jet diameter expands due to air friction. Air entrainment at this stage is due to two factors: roughness on the jet surface and boundary layer. It is difficult to point out which factor dominates, however boundary layer effect can be seen at the impact point, where the cavity is

transformed into a depression or meniscus, which implies that there is an air ring associated with the jet. As shown in Figure 4.24a, the entrainment mechanisms are not clear at the top part of the downcomer. A dense stream of white cloud was noticed further down the downcomer, which comprises a two-phase flow. At this point, the size (or the shape) of the bubbles inside the downcomer cannot be determined with the naked eye because it was moving very fast.

As it can be seen from Figure 4.24c, a clear water ring was noticed around the white dense cloud. The ring thickness increases in the downward direction (for 15 mm nozzle). In other words the white stream diameter decreases in the direction of the flow (Figure 4.24c). As the jet velocity further increases, the water ring around the white stream disappears and the white stream occupies the whole space (for 8 mm nozzle, Figure 4.25). As shown in Figure 4.25, visible sporadic bubbles were observed outside the bottom of the downcomer where the high superficial velocity of the two-phase flow slows down abruptly and the two-phase stream (white cloud) surface curves upward due to the momentum of the down flowing liquid being dispersed in the pool.

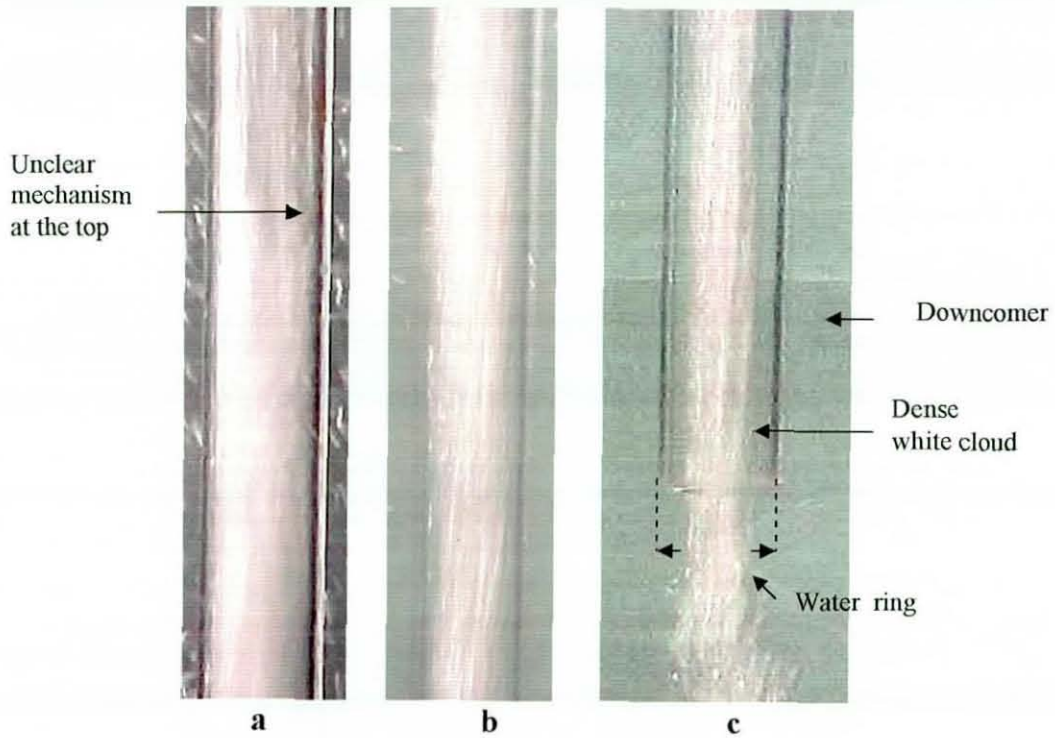


Figure 4.24 a) Top, b) middle and c) bottom parts of the downcomer that show the dense white cloud, of air and water, surrounded by water ring toward the end of the downcomer.



Figure 4.25 White cloud diameter did not change in the downward direction, and visible bubbles form outside the downcomer.

As a conclusion the mechanisms for high turbulent jet comprises of two mechanisms (Figure 4.25): the first one is for confined systems where bubbles and water in the form of white cloud, due to high superficial velocity inside the downcomer, were observed along the full length of the downcomer. The second mechanism is similar to unconfined systems where the high two-phase flow (white cloud) leaving the bottom of the downcomer mixed with the tank liquid.

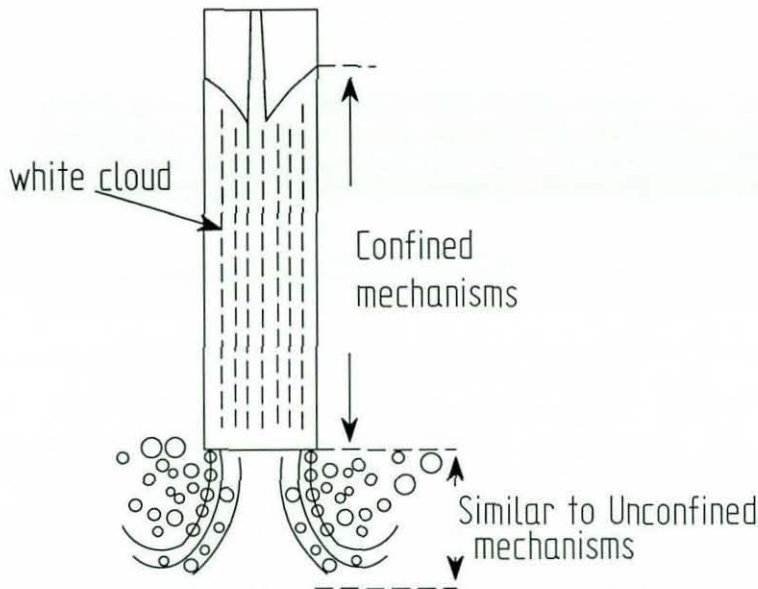


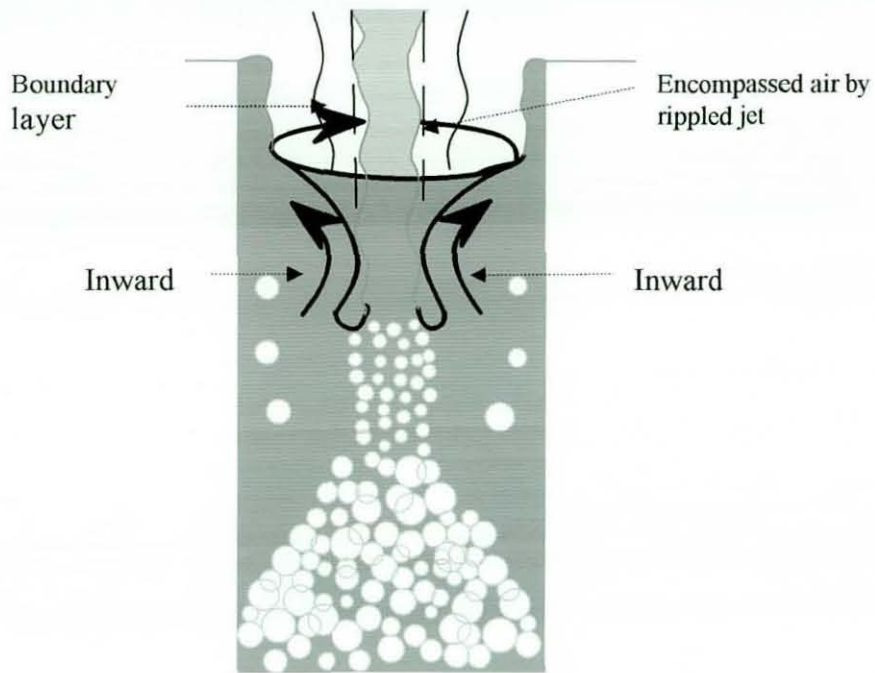
Figure 4.26 Schematic diagram of the mechanisms at high turbulent jet.

The appearance of the bubbles outside the downcomer may be attributed to the fact that the two-phase flow (white cloud) that was moving at high superficial velocity experienced a sudden diameter expansion where the downcomer diameter increased from D_c (23 mm in this case) to ∞ (reservoir diameter). This slowed down the superficial velocity dramatically and therefore allowing the coalescence phenomenon.

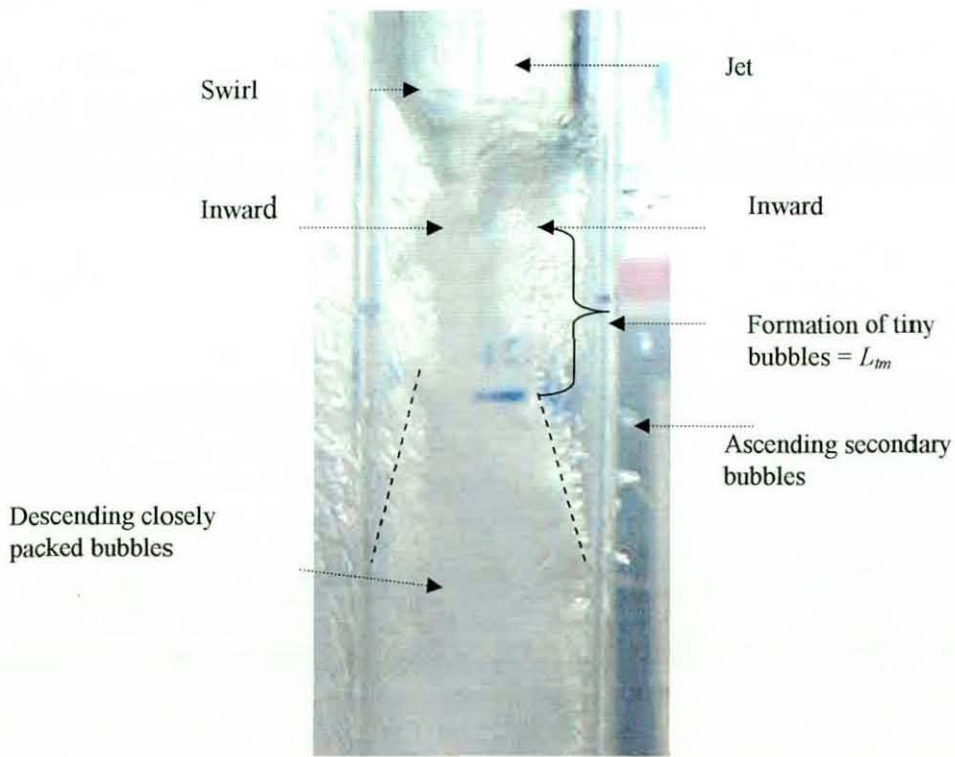
4.4.4 Bubble formation

It appears from the foregoing observations that there is a toroidal motion on both sides of the jet at the top of the downcomer. This motion is associated with a swirl type of motion that starts at the pool surface, where the impingement takes place. This phenomenon (swirl) is continuous for large diameter downcomers and intermittent for the small ones especially for large nozzle diameters, where the jet hits the downcomer wall. As a result the swirl motion is disturbed and does not continue. Swirl phenomenon dies down, in the form of spiral motion, as the jet loses its momentum by penetrating deeper down beneath the receiving pool surface.

Figure 4.27 shows a schematic and a photograph of the air entrainment mechanisms for large downcomers, where the swirl is continuous. It can be seen from Figure 4.27 that at high jet velocity (turbulent flow) the swirl is strong and the bubble form at the base of the vortex, where the jet splits into layers that curve upwards. This pushes the bottom of the swirl inward to form tiny (primary) bubbles with different sizes. Larger bubbles will be broken into smaller bubbles by jet momentum in the formation region. These bubbles move in a toroidal and swirl motion (dual action) due to the jet momentum. All of the bubbles are carried downwards by the dual motion that is caused by the jet, and released deeper down at the base of the swirl where the jet momentum effect disappears. At this point, visible bubbles start to appear. Where larger bubbles (secondary) rise back in spiral form, and the smaller (primary) bubbles leave the bottom of the downcomer. This phenomenon shows that for large downcomers in confined plunging system bubbles appear further down at the base of the swirl rather than under the pool surface.



a



b

Figure 4.27 a) Schematic and b) actual photograph of air entrainment mechanism for high jet velocity (Turbulent).

4.5 Conclusions

Current study shows that the air entrainment rate increases as the main parameters increase (jet velocity, jet length, nozzle diameter and downcomer diameter). Air entrainment rate is proportional to jet velocity raised to the power 1.6 for 300 and 400 mm jet lengths, and to the power 1.40 for 200 mm jet length. This small difference may be due to the use of low headspace pressure air in the case of 200 mm jet length. Air entrainment rate increases non-linearly with jet length. Air entrainment rate increases as downcomer diameter increases until it reaches maximum value when the downcomer diameter is about five times the nozzle diameter. Larger nozzles entrain more air than smaller ones, at the same jet velocity, due to higher surface area. However, nozzles with smaller diameter generate higher jet velocity, for the same jet volumetric flow rate, and therefore higher entrainment rate. A dimensionless equation was fitted to the entrainment data where the superficial velocity in the downcomer is greater than 0.2 m/s.

The following points can be concluded from the results presented here regarding the downcomer length and pump effects on air entrainment ratio. As shown in Figure 4.28, assuming same conditions apply, downcomer length does not affect the total air entrainment rate (Q_{TA}), which is equal to *net* air entrainment measured by CPLJR (Q_N) and disentrainment inside the downcomer (Q_{DS}). However, one can say that downcomer length affects *net* air entrainment rate measured by CPLJR when the closely packed bubbles break inside the downcomer and do not leave the downcomer. The small difference that was observed utilizing both pumps is negligible, and may be due to the pump mechanical nature. The amount of air drawn into the new pump and pumped back through the plunging jet had almost no effect on measured air entrainment ratios.

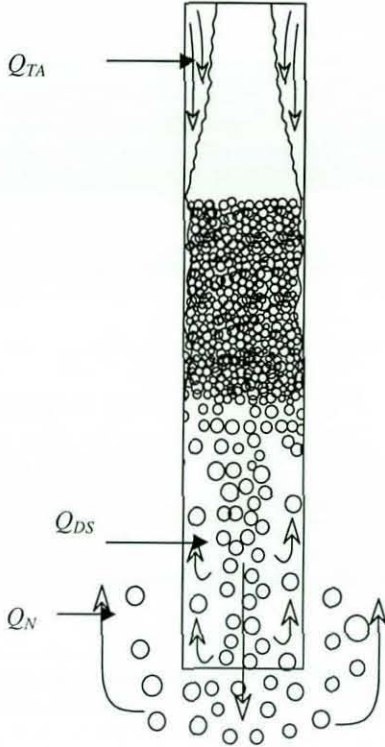


Figure 4.28 Schematic that shows Q_{TA} , Q_N and Q_{DS} .

**Chapter 5: Background of two phase flow
behaviour in Air-lift Column**

5.1 Air-Lift Column Literature Survey

5.1.1 Introduction

As shown previously in the air entrainment section, discussed in chapter 4, deeper bubble penetration was achieved utilizing a longer downcomer. As a result the contact time between the bubbles and the water in the downcomer increases. This will enhance oxygen mass transfer rate from the gas phase (air) to the water phase. Results obtained from chemical engineering department at Loughborough University (Whitehead, 2002) showed that the mass transfer in the downcomer was high and the gas-liquid stream leaving the base of the downcomer was almost saturated with oxygen (> 90%). This means that the closed annulus shown in Figure 2.10 (§ 2.2.3) will give no further mass transfer, and energy is expended without any further transfer of oxygen. In order to overcome this situation the configuration shown in Figure 5.1 is proposed. The idea is similar to that used in a jet loop or air-lift reactor. However, this approach is considered to be novel because it is the first time it has been combined with a plunging liquid jet system. This idea is being investigated in this project. As discussed earlier, the idea is to collect the gas-liquid flow leaving the bottom of the downcomer and to contact the bubbles with fresh water to enable further mass transfer. This can be achieved by having an annulus (external tube), number 10 in Figure 5.1, around the downcomer. The hydrostatic pressure gradient difference between the bubbly flow in the riser and the surrounding clear liquid (in the tank) caused by the density difference will induce a water flow from the bottom of the riser, which dilutes the gas-water stream leaving the base of the downcomer and thus restores the mass transfer driving force. This is expected to be done with no increase in the energy input costs. This is a new concept for the CPLJR so there is no available literature concerning air-lift column topic utilized in a CPLJR. However, there is a substantial body of literature that might be helpful from studies of air-lift columns such as an air lift column in a fermentation process (Fields *et al.*, 1984), air-lift in fluidised bed, gas dispersion into annulus (Yamashita, 1998) and airlift bioreactor

(Chisti, 1989). Although the application is different from CPLJR, the principles should be the same. Also, it is necessary to look at methods predicting gas hold-up and pressure drop in two-phase flow systems as this will be required to model the hydraulics of the reactor. This chapter reviews methods of calculating voidage and pressure drop in the annulus riser.

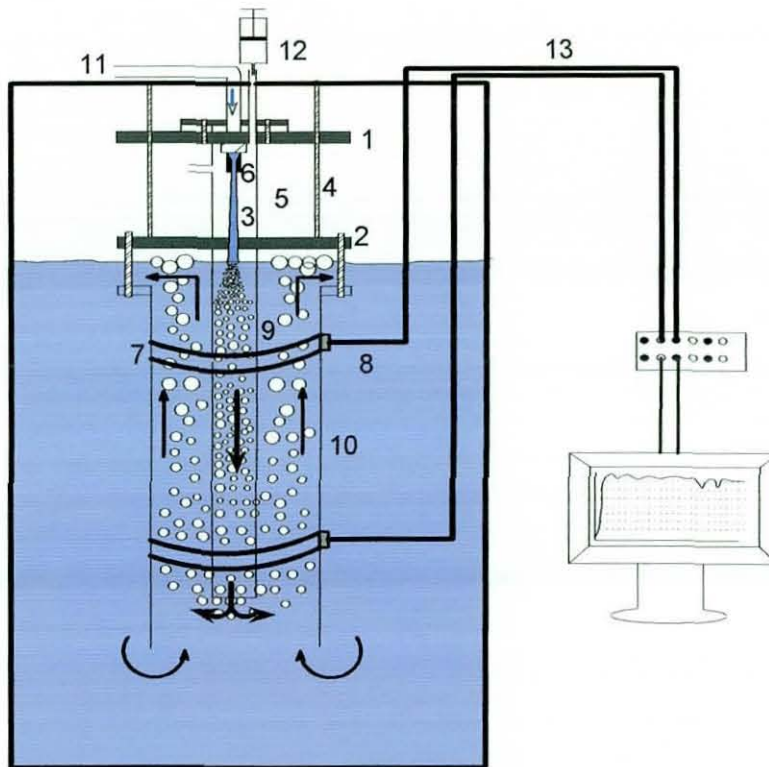


Figure 5.1 Apparatus of the CPLJR air-lift column used in the current study; 1-6, support for downcomer and annulus (the new equipment used in air entrainment rate experiment); 7, electrode rings; 8, 0.2 mm multi strand wires; 9, downcomer; 10, annular riser; 11, water supply; 12, salt injection point; 13 computer connection.

5.1.2 Void fraction calculation

It would be very helpful to briefly investigate the void fraction in vertical tubes or downcomers. To estimate the void fraction in the annular riser and the

downcomer standard theory is used to calculate the two-phase gas-liquid flow. For this process two types of flow occur, firstly co-current upflow in the annulus and secondly co-current downflow in the downcomer. The target is to arrive at a void fraction expression that can be used in a model to predict the amount of liquid flow rate entrained from the base of the annulus (Q_{le}).

Gas void fraction is not simply the gaseous fraction of the mixture ratio of the gas and liquid flow rates, this would only be true if there were no slip between the gas and liquid phases and if the effect of nonuniform flow and concentration across the duct is neglected. In practice the gas moves upwards faster than the liquid because of the buoyancy. Thereby, in the case of the downcomer the bubbles flow (gas) slower than the liquid in the downward direction, whereas bubbles flow faster than the liquid in the annulus and hence $\varepsilon \neq Q_g/(Q_g+Q_l)$. In order to provide a better estimation for void fraction one must consider the effect of the relative local (slip) velocity between the gas and liquid phases and the effect of the nonuniform flow and concentration distribution across the duct as pointed out by Zuber and Findlay (1965). The first attempt to predict the bubble velocity in a bubbly mixture, considering slip velocity effect and ignoring the nonuniform flow and concentration distribution across the duct, was proposed by Behringer in 1936 (Zuber and Findlay, 1965):

$$v_A = \frac{Q_A}{A} + \frac{Q_l}{A} + V_\infty \quad (5.1)$$

Griffith and Wallis in 1961 (Zuber and Findlay, 1965) provide an expression that predicts the terminal bubble rise velocity for slug flow

$$V_\infty = 0.35 \left[\frac{g \Delta \rho d_t}{\rho_l} \right]^{1/2} \quad (5.2)$$

Hewitt (1978) provided an expression to calculate V_∞ for slug regime in tubes that are not of small diameter

$$V_{\infty} = 0.345\sqrt{gd_t}$$

Two groups of authors, Nicklin *et al.* (1962) and Neal (1963) (Zuber and Findlay, 1965), modified equation (5.1) to consider the effect of nonuniform flow on the volumetric concentration in the slug flow by introducing constant C_0 as shown below

$$v_A = C_0 \frac{Q_l + Q_A}{A} + 0.35 \left[\frac{g\Delta\rho d_t}{\rho_l} \right]^{1/2} \quad (5.3)$$

However, they differ in the definition of v_A , Nicklin *et al.* (1962) defines v_A as the actual velocity of the vapour slug, whereas Neal (1963) defines it as the total cross-sectional average gas velocity.

Zuber and Findlay (1965) have provided what is considered to be the most acceptable expression for the weighted mean velocity of the gas not only for slug regime flow but also for churn –turbulent bubbly regime flow considering the effect of both factors C_0 and slip velocity as the following

$$\bar{V}_A = C_0 \langle j \rangle + 0.35 \left[\frac{g\Delta\rho d_t}{\rho_l} \right]^{1/2} \quad (5.4)$$

for slug flow regime and

$$\bar{V}_A = C_0 \langle j \rangle + 1.53 \left[\frac{\sigma g \Delta\rho}{\rho_l^2} \right]^{1/4} \quad (5.5)$$

for churn-turbulent bubbly flow, where $\langle j \rangle$ is the average superficial velocity (or as defined by Zuber and Findlay volumetric flux density) of the mixture and it is equal to

$$\langle j \rangle = \langle j_A + j_l \rangle = \frac{Q_A + Q_l}{A} \quad (5.6)$$

Equation (5.6) has been used by many recent authors to predict gas void fraction for two-phase flow. Clark and Flemmer (1984) used the Zuber and Findlay equation to predict the voidage in the downcomer as shown by the equation below:

$$\frac{j_{Ad}}{\varepsilon_d} = C_0 (j_{Ad} + j_{jd}) - V_\infty \quad (5.7)$$

The voidage in the downcomer can be calculated as

$$\varepsilon_d = \frac{Q_A}{C_0 (Q_A + Q_j) - V_\infty A_d} \quad (5.8)$$

whilst voidage in the annulus can be calculated as

$$\varepsilon_a = \frac{Q_A}{C_0 (Q_A + Q_j) + V_\infty A_a} \quad (5.9)$$

Previous works show that C_0 values vary. $C_0 = 1.2$ was approximated initially by Nicklin *et al.* (1962) based on the fact that the ratio of the maximum to the average flow velocity in turbulent flow is equal to approximately 1.2. Zuber and Findlay (1965), showed that the distribution parameter C_0 varies between 1 (for flat profiles) and 1.5 (for peaked profiles). Clark and Flemmer (1984, 1985) have used 1.16 for C_0 and have shown that this value is valid for up and downflow.

Clark and Flemmer (1984) have also used 0.25 m/s for terminal rise velocity of a bubble (V_{∞}).

A correlation to fit experimental measurements to holdup (ϵ_g) was developed by Akita *et al.* (1988) utilizing an air-lift column for a batch process as shown in Figure 5.2. It consists of two columns (riser and downcomer), a multiple-orifice nozzle sparger, two glass-pipe pressure taps and orifice flowmeter. Data were generated by monitoring the effect of liquid circulation velocities on gas holdups. Liquid velocities were controlled through varying opening ratios of the gate valve (G , Figure 5.2). Results show that gas holdup decreases as opening ratio increases due to the increase of the liquid velocity in comparison with the gas velocity.

$$\epsilon_g (1 - \epsilon_g)^{-4} = 0.20 \left(\frac{gD_c^2 \rho_l}{\sigma} \right)^{1/8} \left(\frac{gD_c^3}{kv_l^2} \right)^{1/12} \left(\frac{j_{gl}}{(gD_c)^{1/2}} \right) \quad (5.10)$$

A useful study conducted by Yamashita (1998) that covers the effect of different types of gas sparger, diameter and length of the draft tube, lower clearance and clear liquid height on gas holdup in bubble column with a draft tube in the case of gas dispersion into the annulus. They showed that at low superficial gas velocities as the size of the holes in the sparger increased the hold-up decreased. But at high superficial gas velocities the hold-up became independent of the gas sparger design.

The apparatus described in Figure 5.3 was utilized by Jones (1985) to study the effect of gas flow rate and draft-tube diameter on liquid circulation velocity. Measured results show that draft-tube gas voidage increased with increasing air flow rate. Gas voidage also increases as the area ratio (ratio of annulus: draft-tube cross-sectional areas) was increased.

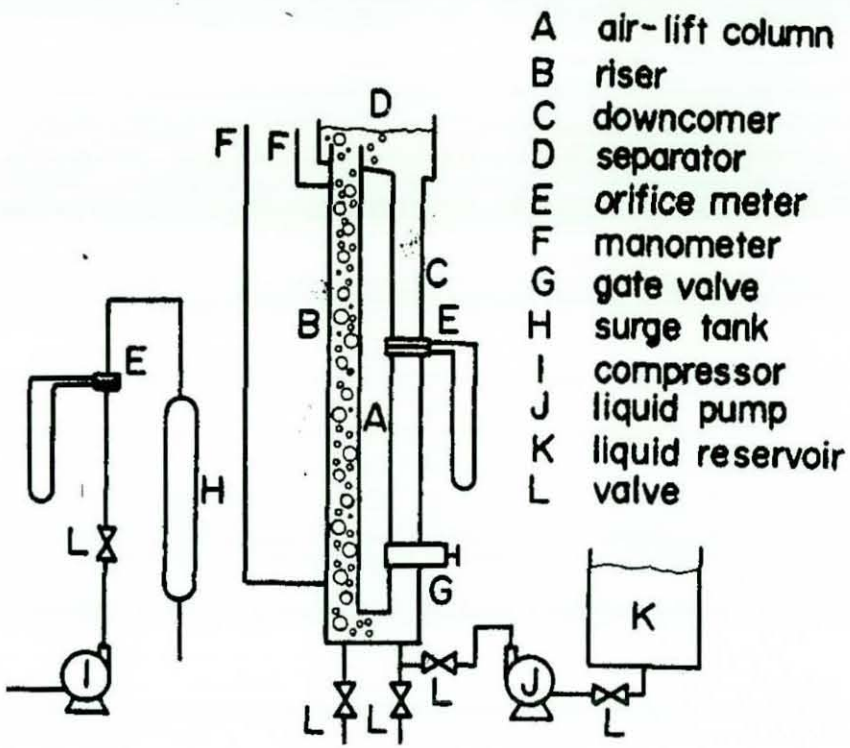


Figure 5.2 Experimental apparatus utilized by Akita *et al.* (1988).

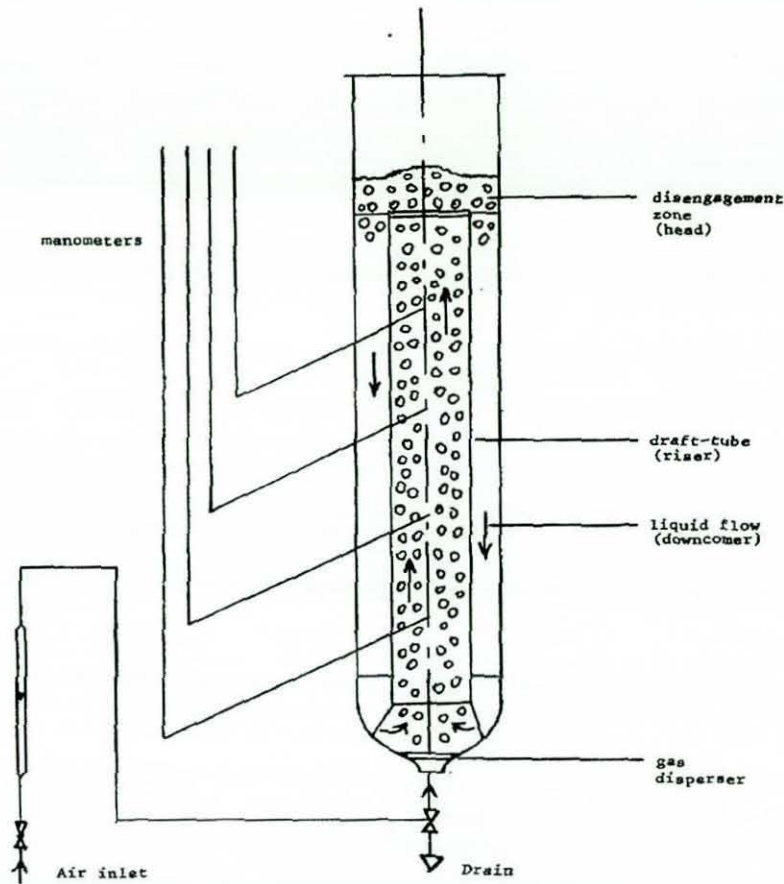


Figure 5.3 Schematic diagram of the apparatus used by Jones (1985).

Majumder *et al.* (2006) investigated the bubble distribution in a modified column reactor. They showed that the bubble size decreases with increasing superficial liquid velocity, whereas the bubble size increases with increasing nozzle diameter. Also the rate of coalescence increases as the gas flow rate increases, and hence the gas holdup increases.

5.2 Velocity in Air-Lift Column

Determination of liquid velocity in gas-liquid mixture is of great importance for various purposes depending on the applications. Since it is difficult to segregate

between the two phases, the only way is to treat the two-phase flow mixture as one stream. In the case of air-lift columns the velocity in the riser has been measured and predicted by various authors adopting different methods. The observations of a few are described in this section.

The effect of pseudoplastic non-Newtonian fluid on the hydrodynamic behaviour and mixing has been investigated by Fields *et al.* (1983). They have used a concentric tube air-lift fermenter along with improved radio-pill system to make the measurements. As shown in Figure 5.4, fermenter configuration comprises an air source at the base of the fermenter, external and draft tubes, energising and receiving coils, shielding metal and radio-pill. The data were measured by receiving a radio pulses as the pill passes along the downcomer close to the aerial. Series of pulses are picked up by the aerial and transmitted to a PDP 11/45 computer to calculate the times between successive signals, which are stored for actual analysis. The method used to detect the pulse (radio-pill), in their study, has the problem that the pill can be easily lost or damaged in the process.

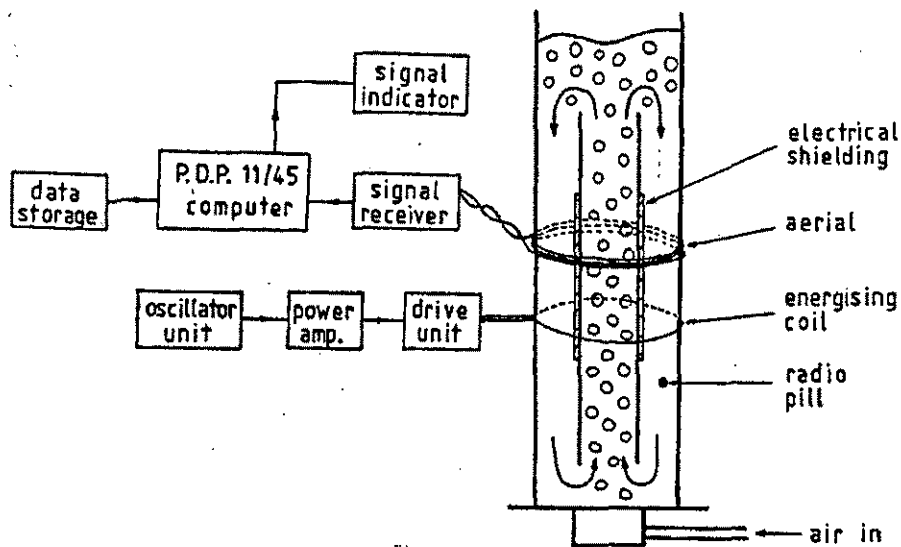


Figure 5.4 Schematic diagram of fermenter configuration and electronic units (Fields *et al.*, 1983).

Fields *et al.* (1983) showed that the mean liquid circulation times decrease as air flow rate increases due to voidage increase in the riser. Increasing the voidage of the liquid by the addition of the xanthan gum has a complex effect on circulation time. As the xanthan gum increased beyond a critical concentration, the voidage began to decrease due to air slug formations in the riser. Their study differs from the current one because air flowrate is the only variable changing and the system was closed with no additional entrainment of liquid unlike the CPLJR.

In a paper by Yamashita (1998) it was shown that the effect of the clearance, between the lower end of the draft tube and the bottom of the bubble column, on the gas hold up depends on the superficial velocity. For higher superficial velocity the gas hold up increases with the clearance until it reaches maximum value then decreases until it reaches critical value and levels off for the rest of the clearance values.

An investigation concerning the effect of gas flow rate and draft-tube diameter on liquid circulation velocity and flow rate was carried out by Jones (1985) (Figure 5.3). Highest liquid velocity, not volumetric flow rate, was obtained with largest draft-tube diameter. Liquid volumetric flow rate increased with increasing air flow rate. Maximum volumetric flow rate of the liquid was achieved at diameter ratio (ratio of draft-tube diameter to internal diameter of the column) equal to 0.5. He claimed that the model prediction for annular liquid velocities was satisfactory for small draft-tubes at low gas flow rates despite the fact that there was a significant deviation between the proposed models and the experimental data for all of the draft-tube sizes and gas flow rates.

However, in the current study the situation is different because the process is an open system and therefore there is an extra factor represented by entrainment of fresh water through the bottom of the annulus (Q_{le}) (see Figure 5.1).

5.3 Prediction of Air-Lift Reactor Performance

Since the device shown in Figure 5.1 is novel there is no available analysis in the literature to describe its behaviour. Cumming *et al.* (2002) proposed an expression for a closed loop plunging jet reactor derived from a force balance to predict the depth in the downcomer (z) for CPLJR without an air-lift column

$$H_{ds} = \frac{\rho_l j_{ld} (V_{ld} - V_j) - \rho_l j_{la} V_{la} + z \rho_a g + (-dp/dz) z + P_{sa} - P_{sd}}{\rho_d g - (-dp/dz)} \quad (5.11)$$

Chisti (1989) published a book on bioreactors and the use of various airlift columns configurations as a closed system. He derived an expression for the liquid circulation model based on energy balances as follows:

Rate of energy input into reactor = rate of energy dissipation

Or

$$E = E_R + E_D + E_B + E_T + E_F$$

Where,

E = Energy input due to isothermal gas expansion

E_R = Energy dissipation due to wakes behind bubbles in the rise

E_D = Energy loss due to stagnant gas in the downcomer

E_B = Energy loss due to friction and fluid turn-around at the bottom of reactor

E_T = Energy loss due to friction and fluid turn-around at the top of the reactor

E_F = Energy loss due to friction in the riser and downcomer

After working out all of the terms, the final expression of the liquid circulation in terms of the superficial velocity:

$$j_{la} = \left[\frac{2gH(\epsilon_a - \epsilon_d)}{\frac{C_f}{(1-\epsilon_a)^2} - \left(\frac{A_a}{A_d}\right)^2 \frac{1}{(1-\epsilon_d)^2}} \right]^{0.5} \quad (5.12)$$

This is still cannot be applied to the current study because the above expression predicts the superficial velocity in the annulus for closed airlift reactors at certain conditions. Whereas in the current study, the system is not closed and therefore an extra important factor that needs to be included is the clear water entrainment flowrate (Q_{le}) induced from the base of the annulus. This phenomenon affects the mechanisms as well as the energy losses expressed by equations (5.12) or any model developed for closed system. Therefore a model predicting Q_{le} , and thus Q_{la} , must be sought. To enable this, the frictional loss in the system needs to be determined by calculation. The model for the induced water flow in the annulus is described in details in chapter 7.

5.3.1 Frictional pressure gradient

An important term in the energy balance is the pressure loss due to friction pressure gradient. The frictional pressure gradient of two-phase flow is approximated utilizing several alternatives correlations presented in the literature. Here, three correlations are investigated to predict the frictional pressure gradient, they are homogenous model (Kay and Nedderman, 1988; Holland and Bragg, 1995), two-phase multiplier cited by Holland and Bragg and Akita's empirical correlation for a batch process (1988).

From fluid flow for chemical engineering text book by F. Holland and. Brag, the friction factor for two-phase flow can be approximated by three approaches (1995);

(i) Simply by using a common constant value such as $C_f = 0.007$, however this approach is the least satisfactory.

(ii) Calculating friction factor as a single phase flow using mean viscosity for Reynolds number;

$$Re = \frac{Gd_e}{\mu}$$

where friction factor for turbulent flow in smooth pipe is equal to Blasius equation,

$$C_f = 0.079 Re^{-0.25}$$

$$d_e = D_a - D_{co}$$

which is valid for $3000 \leq Re \leq 10^5$. Mean viscosity is estimated using the following equation

$$\bar{\mu} = w\mu_g + (1 - w)\mu_l, \quad \text{by Cicchitti } et al. (1960)$$

There are similar equations that can be used to estimate the mean viscosity, such as

$$\frac{1}{\bar{\mu}} = \frac{w}{\mu_g} + \frac{(1 - w)}{\mu_l}, \quad \text{by McAdams } et al. (1942)$$

$$\bar{\mu} = \bar{\rho} [wVL_g\mu_g + (1 - w)VL\mu_l] = \frac{j_g\mu_g + j_l\mu_l}{j}, \quad \text{by Dukler } et al. (1964)$$

where

$$w = \frac{M_g}{M_g + M_l}$$

(iii) Calculating a friction factor as a single-phase flow.

As far as the frictional pressure concerned, the author presented two approaches to calculate the frictional pressure gradient; homogenous model and two-phase multiplier.

1. For homogenous model the frictional component of the pressure gradient can be approximated based on:

$$\left(\frac{dp}{dl}\right)_f = \frac{\bar{V}}{VL} \left(\frac{dp}{dl}\right)_{lo} = \left[1 + w \left(\frac{VG}{VL} - 1\right)\right] \left(\frac{dp}{dl}\right)_{lo} \quad (5.13)$$

where

$$-\left(\frac{dp}{dl}\right)_f = \frac{2C_f G^2 \bar{V}}{d_e} \quad (5.14)$$

For actual two-phase flow.

$$-\left(\frac{dp}{dl}\right)_{lo} = \frac{2C_{f_{lo}} G^2 VL}{d_e} \quad (5.15)$$

If the whole of the two-phase mixture is treated as a single liquid. Where

$$G = \frac{M_g + M_l}{A_a} \quad (5.16)$$

and $C_{f_{lo}}$ is evaluated for the Reynolds number given by

$$\text{Re}_{lo} = \frac{Gd_e}{\mu_l} \quad (5.17)$$

The subscript lo stands for the hypothetical single-phase flow of liquid instead of the actual two-phase flow. In order to calculate the frictional pressure gradient for two-phase mixture, the friction factor of the two-phase mixture must be approximated. In

this case the friction factor of the two-phase flow is assumed to equal that of the hypothetical liquid that relates the frictional pressure gradient for both flows.

2. For separated flow model two phase multiplier (ϕ_R^2) is used to calculate the frictional component of the pressure gradient. It is the relation between the frictional pressure gradient of the two phase flow mixture and that of the single-phase flow (whole liquid or whole gas).

$$\left(\frac{dp}{dl}\right)_f = \phi_R^2 \left(\frac{dp}{dl}\right)_R \quad (5.18)$$

When the reference flow is only liquid in the two-phase flow the friction pressure gradient can be estimated by

$$-\left(\frac{dp}{dl}\right)_l = \frac{2C_{fl}(1-w)^2 G^2 VL}{d_e} \quad (5.19)$$

The above equation differs from the previous ones because it predicts the friction pressure gradient based on the liquid flow only in the two-phase not the total flow of the two-phase. Once the frictional pressure gradient for liquid as reference is evaluated, the two-phase multiplier frictional pressure gradient is then calculated by

$$\left(\frac{dp}{dl}\right)_f = \phi_l^2 \left(\frac{dp}{dl}\right)_l \quad (5.20)$$

where C_{fl} is evaluated for

$$\text{Re}_l = \frac{(1-w)Gd_e}{\mu_l}$$

Similarly, if the gas phase is taken as the reference flow, the frictional pressure gradient looks like

$$-\left(\frac{dp}{dl}\right)_g = \frac{2C_{fg} w^2 G^2 VG}{d_e} \quad (5.21)$$

where C_{fg} is evaluated for

$$Re_g = \frac{wGd_e}{\mu_g} \quad (5.22)$$

and the two-phase frictional pressure gradient can be predicted by;

$$\left(\frac{dp}{dl}\right)_f = \phi_g^2 \left(\frac{dp}{dl}\right)_g \quad (5.23)$$

The two-phase multiplier for both reference flows, ϕ_i^2 and ϕ_g^2 , are calculated by Lockhart and Martinelli (1949) as shown below,

$$\phi_i^2 = 1 + \frac{C}{X} + \frac{1}{X^2} \quad (5.24)$$

where

$$X^2 = \frac{\left(\frac{dp}{dl}\right)_i}{\left(\frac{dp}{dl}\right)_g} \quad (5.25)$$

and C value for various cases are shown in Table 5.1 (Holland and Bragg, 1995),

Table 5.1 Values of constant C for various flow combinations.

	liquid	gas	C
(tt)	turbulent (t)	turbulent (t)	20
(vt)	viscous (v)	turbulent (t)	12
(tv)	turbulent (t)	viscous (v)	10
(vv)	viscous (v)	viscous (v)	5

The last frictional pressure gradient model presented in this section is developed by Akita (1988) for batchwise process. Friction factor was calculated by summing the forces, on the y direction, exerted on a small part of the riser (cylindrical shape) that holds two-phase flow. Friction factor for two-phase fluids is larger than that of a single phase due to the increase of the shear stress with increasing gas holdup. Below is his final expression that predicts the frictional factor C_f for continuous parallel gas-liquid flow (equation (5.27)). He did not write the frictional pressure gradient term directly, instead he wrote it in shear stress term as shown below,

$$\tau_w = \frac{C_f G^2}{2\rho} \quad (5.26)$$

where

$$C_f = 0.0468 \left(\frac{j_l}{gD_c^{1/2}} \right)^{-1.1} \varepsilon_g \quad (5.27)$$

from fluid mechanics books, the relation between the frictional pressure gradient and the shear stress is given by

$$\left(\frac{dp}{dl}\right)_f = \frac{4\tau_w}{D_c} \quad (5.28)$$

Mechanistic models have been developed by Caetano *et. al.* (1992) for an upward vertical two-phase flow through annulus for bubble flow, dispersed bubble flow, slug flow and annular flow. They used the homogenous model reported in Holland and Brag (1995) to estimate the friction pressure gradient component, equation 5.14. The models were tested against experimental data for average liquid hold-up and total pressure gradient and showed good agreement, except for the annular pattern, where the agreement was fair.

5.4 Decisions and Conclusions

In this chapter the focus was on the theoretical background to enable the calculation of the flow in the annular riser. The two-phase stream flowing inside the annulus comprises the gas-liquid stream from the base of the downcomer (Q_j and Q_g) and fresh water entrained from the bottom of the annulus from the surrounding water in the tank (Q_{le}). It was decided that the best technique that suits the determinations of the water flow rate in the annulus is electrodes. Electrodes designs are different based on the applications. The most common probes are the regular (finger type) and ring electrodes. Since in the current thesis a lot of bubbles are generated, the regular probes may not provide an accurate reading due to a small contact surface between the electrodes and the tracer. As an alternative, electrode rings are more efficient and provide better reading due to a wide contact surface between the electrodes and the salt tracer, which measures average of salt concentration. This technique is tested in chapter 6 in a small column to establish its ease of use. However, electrode rings technique has never been used in Chemical Engineering Department at Loughborough

University, it is better to test this technique before employing it in CPLJR air-lift column experiments. Thus, a new rig was designed and assembled by the author to assess electrode rings by varying the air flow rate and salt concentration. After approving the technique, it is used to determine the velocity of the liquid in the annular riser. The electrodes are designed to measure the time delay of a tracer by measuring the conductivity as it passes through the bottom and top pair of electrode rings (experimental section). This will give an indication of how fast the liquid going through the annulus and thereby the flow of the liquid. The raw data recorded by the electrode rings are used to estimate the convective time through a dispersion model.

**Chapter 6: Conductance Measurements Utilising
Electrode Rings**

6.1 Introduction

The reactor being investigated in this thesis comprises a central downcomer surrounded by an annular riser in which entrained air and liquid are flowing upwards (Figure 5.1). To measure water flow rate in two-phase mixture would be valuable measurement, which could be used to test the modeling of the hydraulic flows in the device.

It was decided to measure flow utilizing ring electrodes shown in Figure 6.1.

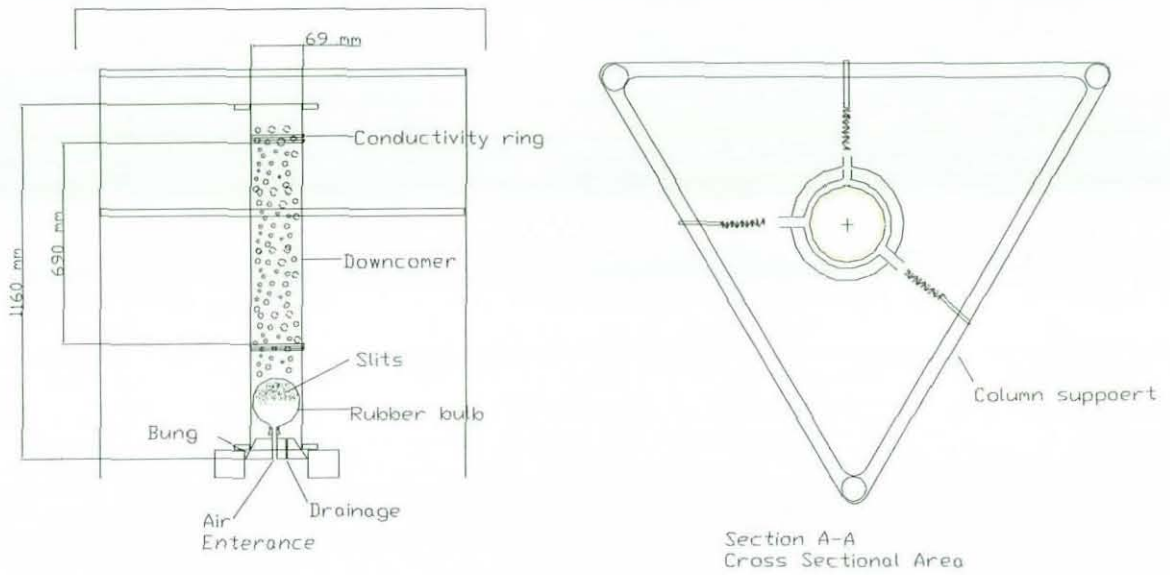
6.2 Experimental Apparatus

The two-phase flow experiment was set up to test the conductivity measuring system for future application in the annular air –lift column. The test apparatus shown in Figure 6.1 was assembled in the laboratory (by the author) to carry out the experimental measurements. It comprises 1160 mm length and 69 mm diameter Perspex column that was positioned vertically utilizing a triangular support as shown in Figure 6.1. Four electrode rings coated with thin layer of conductive paint were mounted on the inside wall of the column. Two electrode rings were at the top and two at the bottom. The ring width was 4.5 mm and the rings were 20.3 mm apart. Top and bottom rings were 740 mm apart. These rings were connected to PC through wires via a conductivity meter. The conductivity meter gave a voltage output which was analysed using HP VEE software that worked in conjunction with a data acquisition card. The output was displayed on the PC monitor. An air sparger was made from a pipette bulb with slits cut on the top half as shown in Figure 6.1. The Perspex tube was sealed at the bottom with a larger bung with two holes, one for the air feed tube and the other as a drainage line. Using a spherical bulb has advantages; slits opened up as the air flow was increased and yet produced fairly consistent bubbles. Also, after shutting off the air, these holes closed down and therefore the

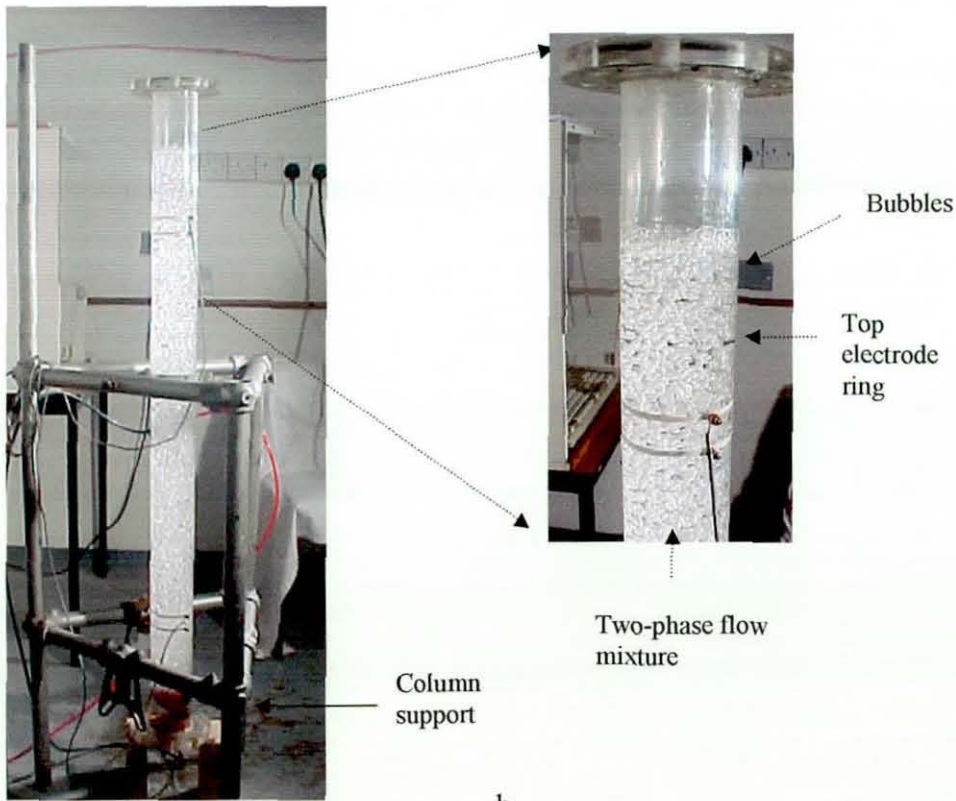
device is self cleaning during operation. As mentioned earlier, a special triangular stand was used to support the mid part of the column during the measurements. The tube was raised on wooden blocks that were placed under the lower flange of the tube to give space for air tube and drainage. Figure 6.1 shows the final assembled shape of the apparatus designed by the author.

6.3 Experimental Methodology

The Perspex tube was filled with tap water to cover the top electrode rings. The air flow, supplied to the system, was controlled by a needle valve. Air flow entered from the bottom of the tube through the slotted bulb into the Perspex tube. As the air passed through the bulb the surface expanded due to air pressure and the slotted holes open up allowing air to pass into the column as bubbles (Figure 6.2). As shown in Figure 6.2, bubbles travel upward establishing a two-phase mixture. The signal detected by the electrode rings, as the mixture passes the two electrode rings, measures the impedance between them. The impedance will change as a function of voltage, which is displayed on PC screen. The main test that was carried out to assess the electrode rings performance was the ability to measure salt concentration and hence be used as a flow measuring device.



a



b

Figure 6.1 Apparatus used to make voidage measurements.

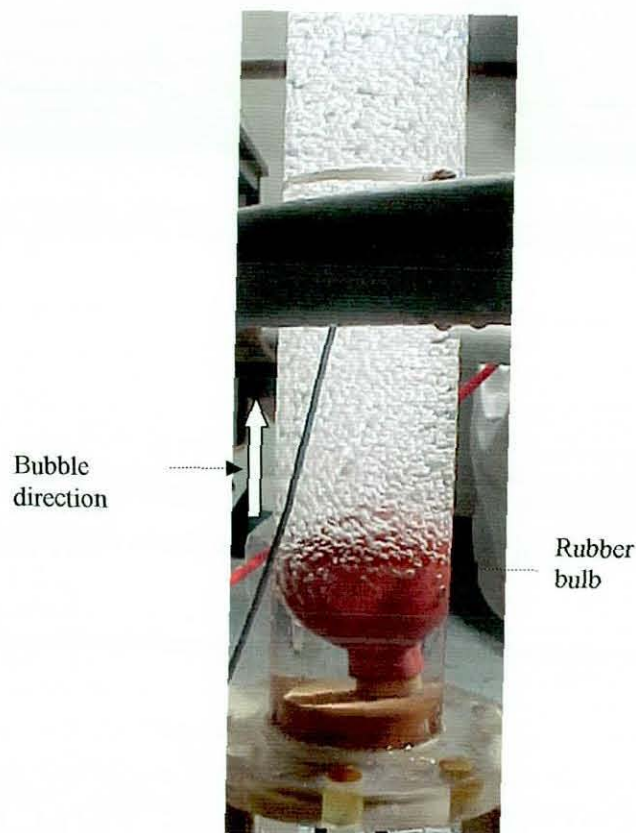


Figure 6.2 Bubbles as they leave the pipette filler (Sparger).

6.4 Results and Discussion

6.4.1 Concentration of salt measurement

The advantage of using a ring electrode would be that it should be less dependant on local variations of salt concentration compared to point electrodes. If this measurement was successful, the electrodes measurement could be used in the annular riser to detect the passage of salt tracer.

20 ml salt solutions at concentrations ranged from 0.0056 to 0.0224 mg/ml were used into the top of the Perspex tube. Figure 6.3 shows the voltage responses measured by electrode rings before and after adding salt solutions. The passage of salt

sinking down the tube can be seen as, it passes the top and bottom electrodes, by the changing voltage measurement in Figure 6.3.

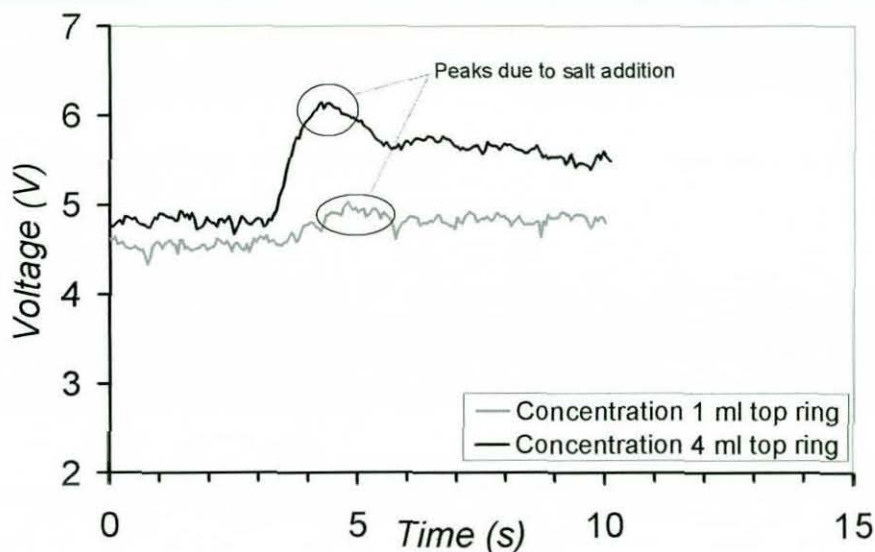


Figure 6.3 Electrode rings responses for different salt concentrations.

The use of salt was further investigated by varying the salt concentration inside the column for two runs. One with constant voidage and the other one with no air flow in a well mixed solution. In the case of the constant voidage the salt was added and given some time for the solution to reach equilibrium throughout the column and voltage output was recorded. As for the other experiment, since there was no air flowing, the solution is mixed after adding the salt for some time and then the air was completely turned off for the data to be collected. Figure 6.4 shows that for both runs the concentration is linear to just above 0.05 mg/ml, above this the data converges. It is noticeable that for the two phase mixture (air-water) the data is more scattered, this is probably due to the difficulty in controlling the voidage.

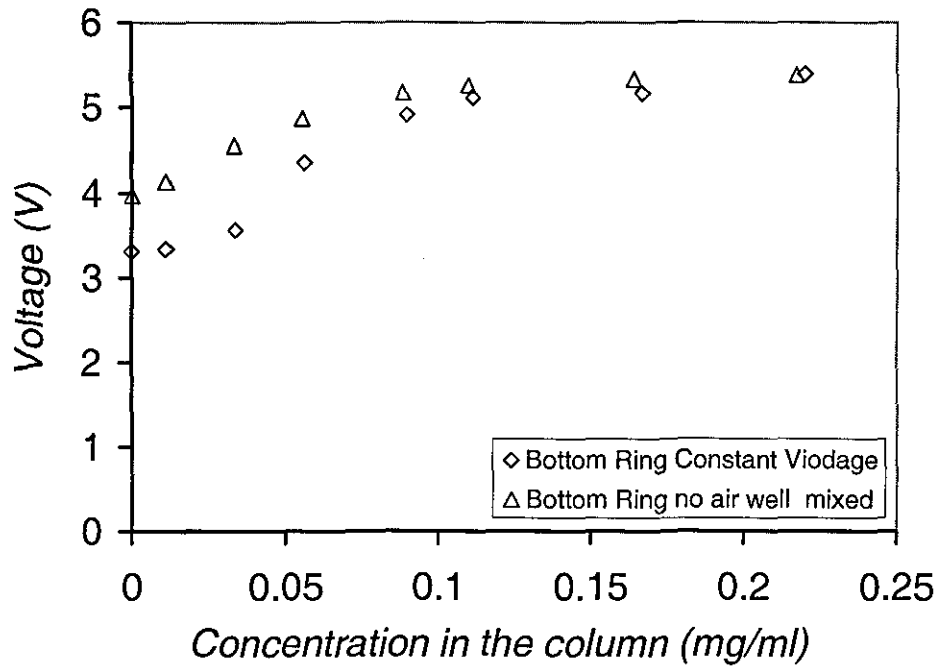


Figure 6.4 Voltage responses by the probes as salt concentration increases.

6.5 Conclusions

The use of rings has proved to be a good method of measuring salt concentration up to concentration just above 0.05 mg/ml. This technique will therefore be used for measuring the flow of the liquid in the annulus by using salt as a tracer.

**Chapter 7: Air-Lift Column Model Development and
Experimental work**

Figure 7.1 shows the flows in the device. The central downcomer carries the water-air mixture with a water flow of Q_{ld} and an air flow of Q_{Ad} . It is assumed that at the bottom of the downcomer both air and water flows stop moving downwards, this distance is controlled by the jet velocity and bubble buoyancy, and both then flow up the annulus. The density of the air-flow mixture in the annulus is lower than that in the tank. This density difference generates a hydrostatic force causing water from the tank to flow up the annulus (Q_{le}).

7.2.1 Entrained liquid flow rate

7.2.1.1 Downcomer (Concentric Tube)

At present the downcomer is not included in the model. For completeness the downcomer is included in this description, but is not included in the model predicting the water flow in the annulus.

The control volume in this case is the downcomer as shown in Figure 7.2. Therefore, the material balance is taken around the downcomer. Material balance for each phase is performed separately to solve for the voidage ϵ_d in the downcomer.

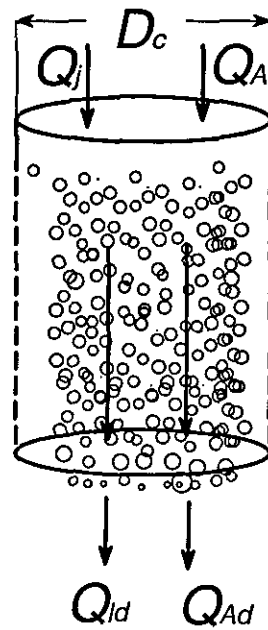


Figure 7.2 Schematic of the downcomer.

(i) Liquid Phase

Jet flow rate is the same as the water flow rate inside the downcomer, thus

$$Q_j = Q_{ld} = A_d j_{ld} \quad (7.1)$$

cross sectional area of the downcomer is

$$A_d = \frac{\pi D_c^2}{4} \quad (7.2)$$

So the water superficial velocity inside the downcomer is equal to

$$j_{ld} = \frac{4Q_j}{\pi D_c^2} \quad (7.3)$$

(ii) Gas Phase

A similar approach is applied here to derive the superficial velocity for the gas phase inside the downcomer,

$$Q_{Ad} = Q_A = A_d j_{Ad} \quad (7.4)$$

gas superficial velocity in the downcomer is

$$j_{Ad} = \frac{4Q_A}{\pi D_c^2} \quad (7.5)$$

7.2.1.2 Annulus (Annular Riser)

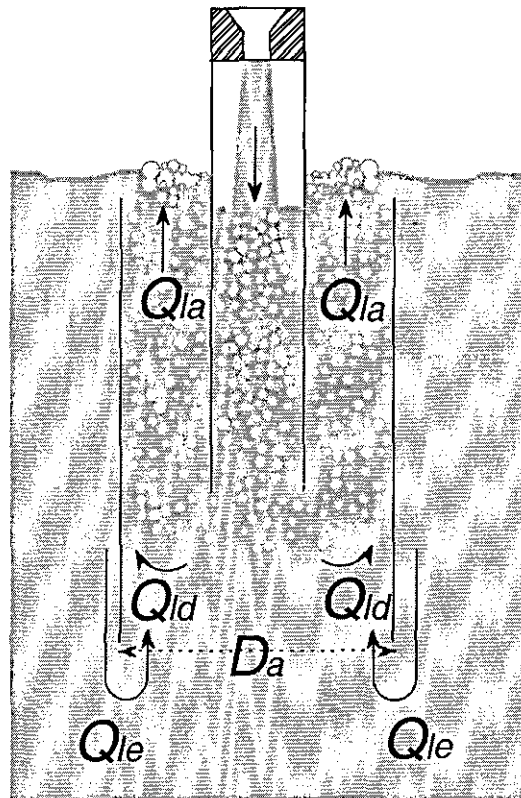


Figure 7.3 Schematic of the annulus as a control volume.

(i) Liquid Phase

From Figure 7.3, liquid flowrate in the annulus comprises the new liquid entrainment rate induced from the bottom of the annulus (Q_{le}) and the liquid flowrate from the downcomer ($Q_{ld} = Q_j$)

$$Q_{le} + Q_{ld} = Q_{la} \quad (7.6)$$

and cross sectional area of the annulus is

$$A_a = \frac{\pi(D_a^2 - D_{co}^2)}{4} \quad (7.7)$$

$$Q_{le} + Q_j = \frac{\pi(D_a^2 - D_{co}^2)}{4} j_{la} \quad (7.8)$$

since $Q_{ld} = Q_j$, superficial velocity of the liquid in the annulus is described by

$$j_{la} = \frac{4(Q_{le} + Q_j)}{\pi(D_a^2 - D_{co}^2)} \quad (7.9)$$

(ii) Gas Phase

The same method is applied on the gas phase, however it is worth pointing out that in the case of the gas there is no gas being generated elsewhere. Therefore, the same amount of gas flowing down the downcomer is also flowing in the annulus. Thus,

$$Q_A = A_a j_{Aa} \quad (7.10)$$

where j_{Aa} is the superficial velocity of the gas in the annulus

7.3 Void Fraction

Generally, void fraction can be described in the literature (Kay and Nedderman, 1988) by equations that relates the mean velocities ($\overline{V}_A, \overline{V}_l$) of the gas and liquid to the superficial velocities as shown below,

$$j_A = \varepsilon \overline{V}_A \quad (7.11)$$

$$j_l = (1 - \varepsilon) \overline{V}_l \quad (7.12)$$

7.3.1 Downcomer

Recall Figure 7.2, the void fraction inside the downcomer can be described as

$$\varepsilon_d = \frac{j_{Ad}}{\overline{V}_{Ad}} \quad (7.13)$$

and mean gas velocity (Zuber and Findlay, 1965),

$$\overline{V}_{Ad} = C_0 (j_{Ad} + j_{ld}) - V_{\infty d} \quad (7.14)$$

From literature (Hewitt, 1978), the terminal rise velocity of a bubble in a slug flow is found experimentally to be given by

$$V_{\infty d} = 0.35 \sqrt{gd_t} \quad (7.15)$$

which agrees with the theoretical prediction of Dumitrescu (1943).

and for churn-bubble flow

$$V_{\infty d} = 1.53 \left[\frac{\sigma g}{\rho_l} \right]^{1/4} \quad (7.16)$$

Where, $\Delta\rho = \rho_l$

Therefore, final expression that predicts voidage in the downcomer for slug flow regime

$$\varepsilon_d = \frac{j_{Ad}}{C_0(j_{Ad} + j_{ld}) - V_{\infty d}} = \frac{Q_A}{C_0(Q_A + Q_j) - V_{\infty d} A_d} \quad (7.17)$$

7.3.2 Annulus (Annular riser)

The same procedure is followed to derive an expression for void fraction inside the annulus including the new liquid entrainment flowrate (Q_{le}). Here, the material balance is performed around the annulus (control volume) excluding the downcomer (recall Figure 7.3),

$$\varepsilon_a = \frac{j_{Ad}}{V_{Aa}} \quad (7.18)$$

$$\overline{V_{Aa}} = C_0(j_{Aa} + j_{la}) + V_{\infty a} \quad (7.19)$$

replacing the superficial velocities in equation (7.19) with the corresponding flow rates, yields

$$\overline{V_{Aa}} = C_0 \left[\frac{4Q_A}{\pi(D_a^2 - D_c^2)} + \frac{4(Q_{le} + Q_j)}{\pi(D_a^2 - D_c^2)} \right] + V_{\infty a} \quad (7.20)$$

Or

$$\overline{V_{Aa}} = \frac{C_0}{A_a} (Q_A + Q_{le} + Q_j) + V_{\infty a} \quad (7.21)$$

the final expression that estimates the voidage in the annulus is,

$$\varepsilon_a = \frac{Q_A}{C_0(Q_A + Q_{le} + Q_j) + V_{\infty a} A_a} = \frac{Q_A}{C_0(Q_A + Q_{la}) + V_{\infty a} A_a} \quad (7.22)$$

Again

For slug flow

$$V_{\infty a} = 0.35\sqrt{gd_i} \quad (7.23)$$

For churn-bubble flow

$$V_{\infty a} = 1.53 \left[\frac{\sigma_g}{\rho_l} \right]^{1/4} \quad (7.24)$$

7.4 Pressure Drop (Energy Balance):

In order to calculate water entrainment rate (Q_{le}) and therefore water flowrate inside the annulus (Q_{la}), a complete energy balance must be carried out for the whole system at points 0, 1 and 2 as shown in Figure 7.4, which is a schematic that describes the motion of the two-phase mixture as it leaves the downcomer, indicated by velocities, and also shows the points where the energy balance should be performed.

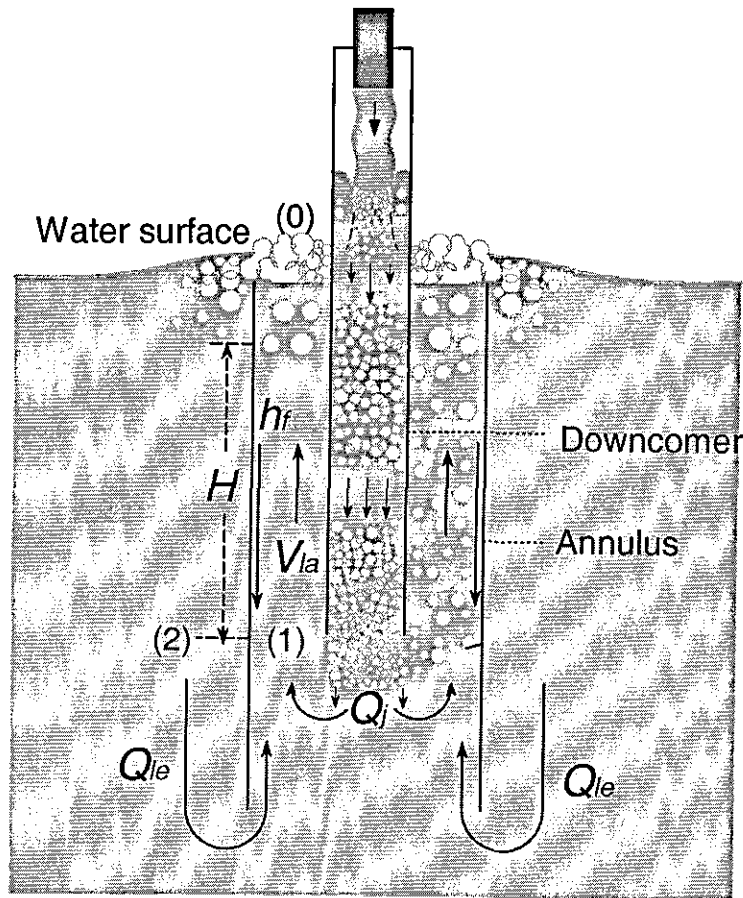


Figure 7.4 Schematic of the air-lift column utilized in CPLJR.

7.4.1 Energy Balance at 1

The energy associated with the two-phase mixture leaving the base of the downcomer is dissipated as the flow is brought to a halt by the bubble buoyancy and the induction of water flow into the annulus from the tank. The depth that the bubbles will travel below the downcomer is controlled by the jet velocity and the bubble buoyancy. Considering these terms, the energy at point 1 can be predicted by the following equation,

$$E_1 = \rho_1 \frac{\bar{V}_{la1}^2}{2} + P_1 + P_0 \quad (7.25)$$

The effect of the flow path when the two-phase flow changes direction is ignored.

Where P_0 is the atmospheric pressure above the water level and P_1 is made up of the following elements:

- (i) Hydrostatic head of the liquid above it (the hydrostatic component of the pressure gradient, which is $\left(\frac{dp}{dl}\right)_H = \epsilon_a \rho_g g + (1 - \epsilon_a) \rho_l g$.

The first term, head due to air bubbles, is negligible because air density is very small.

- (ii) Frictional pressure gradient in the annulus $\left(\frac{dp}{dl}\right)_f$ or the pressure

loss due to the friction $P_f = h_f g \rho_l$.

Combining equations from i and ii, gives

$$P_1 = \underbrace{h_f g \rho_l}_{ii} + \underbrace{Hg(1 - \epsilon_a)}_i \rho_l \quad (7.26)$$

and therefore from equations (7.25) and (7.26) the energy balance at point 1 is given by

$$E_1 = \underbrace{\rho_1 \frac{\bar{V}_{la1}^2}{2}}_{\text{Kinetic energy}} + \underbrace{h_f g \rho_l}_{\text{Frictional pressure}} + \underbrace{Hg(1 - \epsilon_a)}_{\text{Hydrostatic pressure}} + \underbrace{P_0}_{\text{Atmospheric pressure}} \quad (7.27)$$

which describes energy balance at point 1.

7.4.2 Energy Balance at 2

Since the water outside the annulus is assumed to be stagnant, then the kinetic energy at this point is negligible ($v \approx 0$). Therefore, energy due to the hydrostatic head outside the annulus (clear water) is equal to

$$E_2 = P_2 = H \rho_l g + P_0 \quad (7.28)$$

Assuming that ϵ_a is constant throughout the annulus in both, vertical and radial directions, which probably depends on voidage and annulus diameter, and equating both energies at 1 and 2 (equations (7.27) and (7.28)) and solving for \overline{V}_{la} , yields

$$\underbrace{\rho_l \frac{\overline{V}_{la}^2}{2} + h_f g \rho_l + H g \rho_l (1 - \epsilon_a) + P_0}_{E_1} = \underbrace{H \rho_l g + P_0}_{E_2}$$

Solving for the velocity in the annulus,

$$\overline{V}_{la} = \sqrt{2g(H\epsilon_a - h_f)} \quad (7.29)$$

where head loss due to friction (h_f) is evaluated by the following equation

$$h_f = \left(\frac{dp}{dl} \right)_f \frac{H}{\rho_l g}$$

and $\left(\frac{dp}{dl} \right)_f$ can be estimated using the two-phase multiplier frictional pressure gradient model discussed in chapter 5.

Using equations (7.22) and (7.29) and the appropriate head loss equation, the induced flow Q_{la} in the annulus can be calculated.

7.5 Experimental Work

7.5.1 Apparatus

As shown in Figure 7.7, the air-lift column in CPLJR consists of two major parts; the equipment that were used to measure air entrainment rate data and the new air-lift column equipment, represented by an annulus inserted around the downcomer. Air entrainment rate equipment including modified support for the annulus and the downcomer are numbered from 1-17 in Figure 7.7. The new air-lift column equipment comprises three annuli with different diameters 74, 94 and 144 mm with ring electrodes and wires, amplifier box and a PC as shown in Figure 7.7 numbered from 18-23. The annulus height (L_a) of 1350 mm was used for all the experiments. Two pairs of ring electrodes (probes), upstream probe (input) and downstream probe (output) were mounted on the inside wall of the annulus. The probes were separated by a fixed distance (H) of 825 mm common for all of the annuluses. The electrodes were made of a double sided stainless steel shim (Figure 7.6a). They were tinned after they pass through the Perspex wall and connected to cable by a soft solder. The wires were connected to an amplifier box and then to PC (see § 7.5.2).

An injection point 23 was used to introduce the tracer to the system through a tapping that opened to the head space inside the downcomer. A salt solution volume of 15 - 20 ml with a concentration of 100 - 200 mg/ml used as a tracer. A 20 ml syringe was used to inject the salt into the system. Salt tracer impedance was measured by the electrodes connected to an amplifier box and then to PC. Salt tracer signals measured by the electrodes were analysed using HP VEE software (a data acquisition program that controls and communicates with a test piece over a General Purpose Interface Bus (GPIB)), it allows for electronic capture of data from an experiment (www.doe.caleton.ca/~jaguire/appontes.html). After collecting the raw data in the form of voltage the mean liquid phase velocity from tracer tests was estimated by calculating the time between the tracer peaks (convective time scale or correlation time) using equation (7.34) (§ 7.6).

7.5.2 Air-lift column design details

One of the air-lift columns used in the current study is shown as photograph in Figure 7.5. A flange with four holes was used to support all annuluses. Three of the annuluses, with diameters ranging from 74-144 mm, have the same flange and therefore the same pitch circle for the four holes. One of the annulus has wider flanges because of its diameter that exceeded the range made previously. Thus, four new holes were made on the supporting lower flange to accommodate the new annulus. The holes in the flanges coincide with those, recently made, on the supporting lower flange. Four long stainless steel rods go through the flange part of the annulus and were used to mount the annulus to the lower flange of the new equipment. The long rods also were used to adjust the jet length to the desired level. These rods provided a firm support to the annulus and were used to centralize the downcomer. As shown in Figure 7.6b and Figure 7.7 two pair of stainless steel rings were mounted to the annulus wall that serves as electrode probes. Spacing between each pair of electrode was 22 mm and the thickness and width of each electrode was 0.1 mm and 6.5 mm respectively (AutoCAD design sketch of the equipment is in appendix V). These dimensions remain the same for all of the probes. One of them located at the bottom of the annulus gave an input signal and another one at the top gave an output signal as the tracer passed them. The probes were separated by fixed distance H of 825 mm from the centre line of each probe. Two 2-meter 16 multi strand wires with 0.2 mm were connected to the electrodes. These wires were connected to the converter box 21 through a connection point 20 that connects the signal detected by the probes to the PC. This point simplifies the removing and reconnecting various annuluses (Figure 7.6a).

Unfortunately, the stainless steel shim tended to peel off, which would affect the readings. This may be attributed to the ring diameter being less than the annulus diameter, which imposes stress on the stainless steel shim before it dries allowing it to peel. Therefore, it was necessary to hold the rings in place for a long time until the glue on the tape dries. However, it is not easy to find a device that holds the ring

periphery symmetrically at the same time for different diameters. So, a good trick was used here for this purpose utilising a balloon (Figure 7.6b). After connecting the rings, a balloon was inflated inside the downcomer to hold the probes in place until the glue dried up. This was a simple and effective method of supporting the ring electrode, which is suitable for all diameters and easy to remove afterwards.

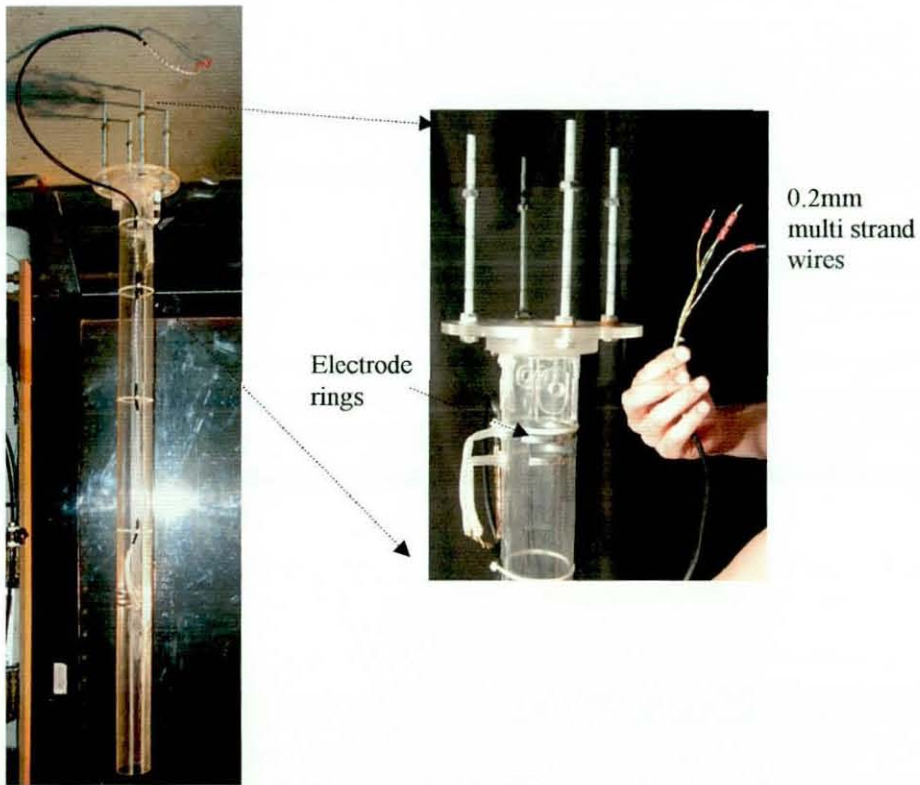


Figure 7.5 One of the annuli (74 mm) used in the work.

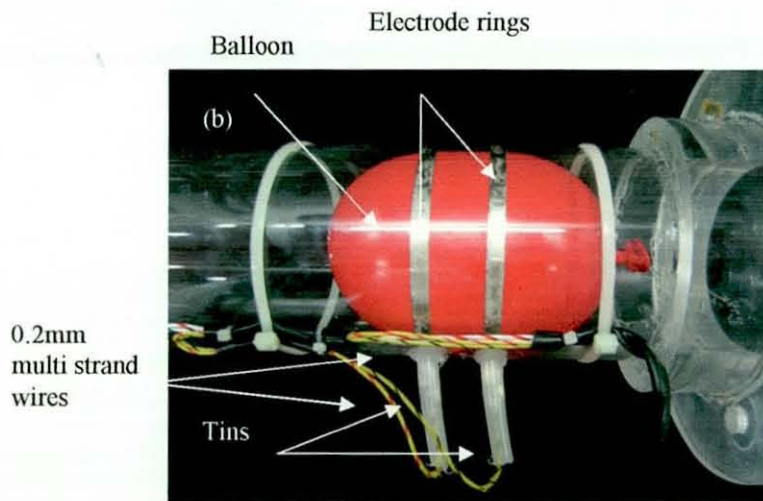
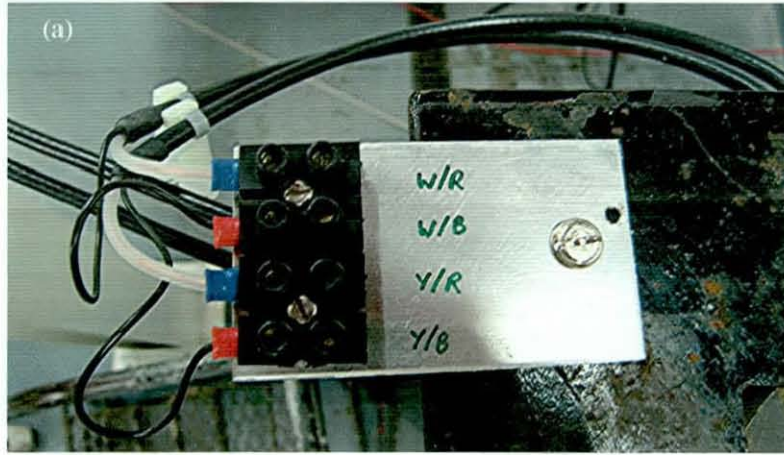


Figure 7.6 (a) Connection point between the annulus and the PC, and (b) Top part of the annulus that shows the strand wire, electrode rings and the balloon.

7.5.3 Experimental methodology

Air-lift measurements comprised two experiments carried out simultaneously; air entrainment rate and induced liquid flow measurements. Air entrainment rate measurements follow the same procedure that was carried out in chapter 3, however this time the difference was the presence of annulus around the downcomer. The set of measurements were carried out utilising the rig shown in Figure 7.7. The second type of experiments was carried out in parallel with air entrainment rate utilising ring electrodes to detect salt traces injected into the system via a tapping located at the top of the downcomer. Tap water was used as liquid and ambient air as gas. Air entrainment measurements follow exactly the same procedure in chapter 3. Air entrainment rate was measured first then the conductance. Salt tracer was injected two to four times for each air entrainment rate reading. Each response was saved for each measured air entrainment flow. After that the mean liquid velocity was estimated using an axial dispersion model discussed in the next section. Then Q_{le} and Q_{la} were calculated to represent the experimental measurements. These results were compared against the theoretical ones obtained from the air-lift model and reported later in chapter 8.

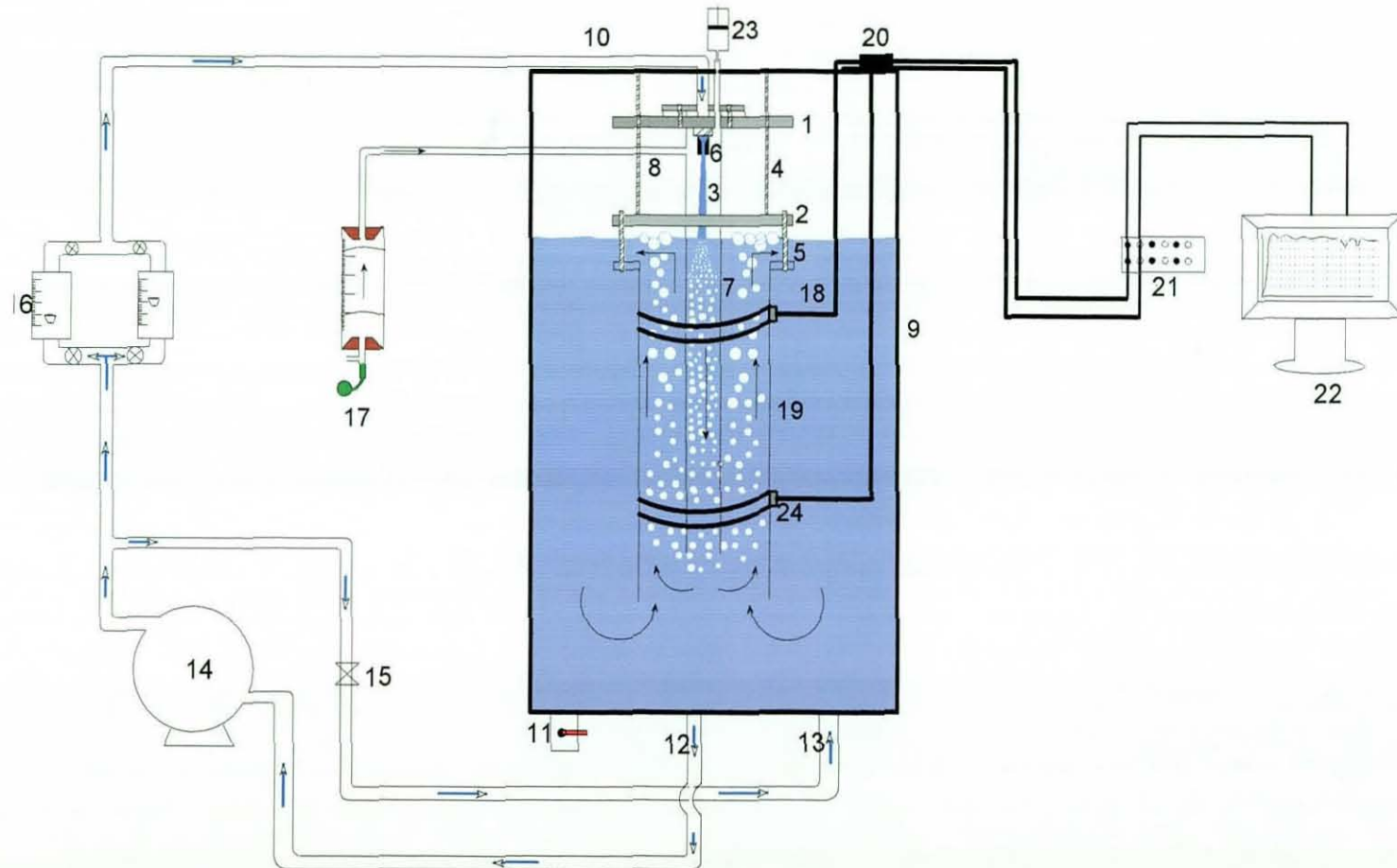


Figure 7.7 Schematic diagram of the air-lift column in the CPLJR used in the current study. 1, top flange; 2, bottom flange; 3, liquid jet; 4, rods; 5 riser rods; 6, nozzle; 7, downcomer; 8, air tapping; 9, water tank; 10, water supply; 11, drain; 12, recycled water; 13, bypass; 14, pump; 15, valve; 16, rotameter; 17, bubble meter; 18, wires; 19, annulus; 20, connection point; 21, amplifier; 22, PC; 23, injecting salt by syringe; electrode rings.

7.6 Estimation of Liquid velocity and Axial Dispersion in the Annulus

The conductivity ring method (described in chapter 6) has proven to be a valid method for the current experiment to determine the induced liquid flow in the air-lift column. The procedure was similar to the one used in chapter 6 (conductance measurements) except for two facts; a) a tracer was introduced into the system through one of the tappings as the jet plunges through the headspace (§7.5.1), and b) the tracer will be diluted (dispersed) before it passed through the upstream ring electrode (first electrode). The second point is very important because it explains the difference in the concentration time history (response) between the two probes (upstream and downstream ones). As the tracer moved upward vertically it disperses due to mixing. This explains why the concentration time history detected by the top probe (downstream one) is distorted in comparison with the upstream probe (bottom ring electrode). Figure 7.8 depicts the concentration histories for the up stream and downstream electrodes obtained from the current study of air-lift column experiment.

After collecting the data experimentally in the form of voltage out put (raw data), the mean liquid phase velocity and axial dispersion coefficient from tracer tests were estimated by calculating the time between the tracer spikes (convective time scale or correlation time) $t_{corr.} = H / \bar{V}$ and other parameters such as Peclet number (Pe) and peak to peak time. From the literature, Peclet number can be obtained by dividing correlation time (convective time) over dispersive time scale as shown below

$$Pe = \frac{\text{convective time}}{\text{dispersive time}} = \frac{H / \bar{V}}{H^2 / D_{dis}} = \frac{D_{dis}}{\bar{V}H} \quad (7.30)$$

From equation (7.26), one can see that Peclet number relates the dispersive to convective effects, and compares the mixing patterns measured with that of the dispersion model.

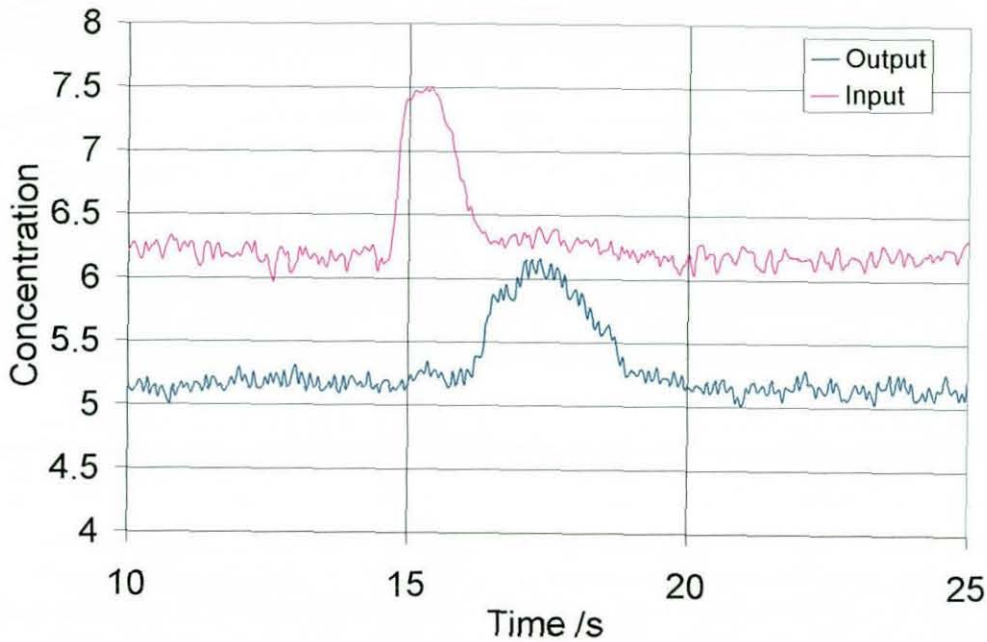


Figure 7.8 Typical concentration (dimensionless) time histories for input and output probe locations in a two-phase upflow recorded in the current study.

7.6.1 Theory

This section presents a brief background of how the model was implemented to estimate the mean liquid velocity and local liquid dispersion coefficient. Axial dispersion model is described in the literature (Taylor; 1953, 1954) by

$$\frac{\partial C^*}{\partial \theta} = \frac{D_{dis}}{V_{la}H} \frac{\partial^2 C^*}{\partial z^{*2}} - \frac{\partial C^*}{\partial z^*} \quad (7.31)$$

In order to use this model one should assume that the above model may be applied to any section of a flow. C^* , z and θ are dimensionless and equal to

$$C^* = \frac{(C - C_i)}{(C_\infty - C_i)} \quad (7.32)$$

$$z^* = \frac{z}{H} \quad (7.33)$$

$$\theta = \frac{t}{t_{corr.}} \quad (7.34)$$

equation (7.28) normalises the step –change experimental response by calculating dimensionless concentration for step-change experiment in an open-open system. The normalisation of the dimensionless concentration C^* for pulse experiment is given by

$$C^* = \frac{(C - C_i)}{\int_0^\infty (C - C_i)dt} \quad (7.35)$$

Axial dispersion is indicated by Peclet number, which expresses the degree of axial mixing for a certain section as the liquid flows through it. Levenspiel (1982) has shown that when $Pe > 0.01$ the flow is shifting away from plug flow, otherwise the flow is behaving like a plug flow (when $Pe < 0.01$).

Levenspiel and Smith (1957) provided a solution for the differential equation (7.31) assuming open-open system and therefore applied the corresponding boundary conditions. The solution is expressed as following:

$$C^*(\theta) = \frac{1}{\sqrt{4\pi\theta(D_{dis} / \bar{V}_{la} H)}} \exp\left[-\frac{(1-\theta)^2}{4\theta(D_{dis} / \bar{V}_{la} H)}\right] \quad (7.36)$$

Imperfect pulse technique is implemented to investigate the liquid velocities and dispersion coefficient for desired section of the flow. A set of data obtained by measuring two points, upstream and downstream points, which are separated by a

distance H , are compared. As shown in the literature, the output response for a linear system ($C_1^*(\theta)$) can be predicted by integrating the inlet ($C_0^*(\theta)$) and the system mass transfer function $M(\theta)$ as shown below

$$C_1^*(\theta) = \int_0^{\infty} M(\theta)C_0^*(\theta - \theta')d\theta' \quad (7.37)$$

Figure 7.8 is an example from the current study for the input and output responses of the foregoing system. Once the system transfer function is known, the output signal can be predicted for any input signal. Predicted results from equation (7.33) are fitted to match the output concentration time history by adjusting the Peclet (Pe) number and correlation (convective) time ($t_{corr.}$). Mean liquid velocity and dispersion coefficient for the best-fit can be estimated by,

$$\overline{V}_{la} = \frac{H}{t_{corr.}} \quad (7.38)$$

$$D_{dis} = Pe \frac{H^2}{t_{corr.}} \quad (7.39)$$

As presented in the literature (Fahim and Wakao, 1992; Obradovic *et al.*, 1997), there are four techniques used to evaluate Pe and $t_{corr.}$. However, some of them are not accurate such as the Laplace transfer domain analysis, whilst others such as the time domain analysis are (Obradovic *et al.*, 1997; Verlaan *et al.*, 1989). Figure 7.9 presents a flow chart, by Rielly (2006), of the algorithm that is chosen as estimation method of the model parameters, where parameter designated with an overbar sign indicates Fourier transfer in the frequency space, f . After solving for $C_0^*(\theta)$ through normalisation of the input signal of a certain tracer, the Fourier transform of this signal is estimated by the Fast Fourier Transformation method (FFT).

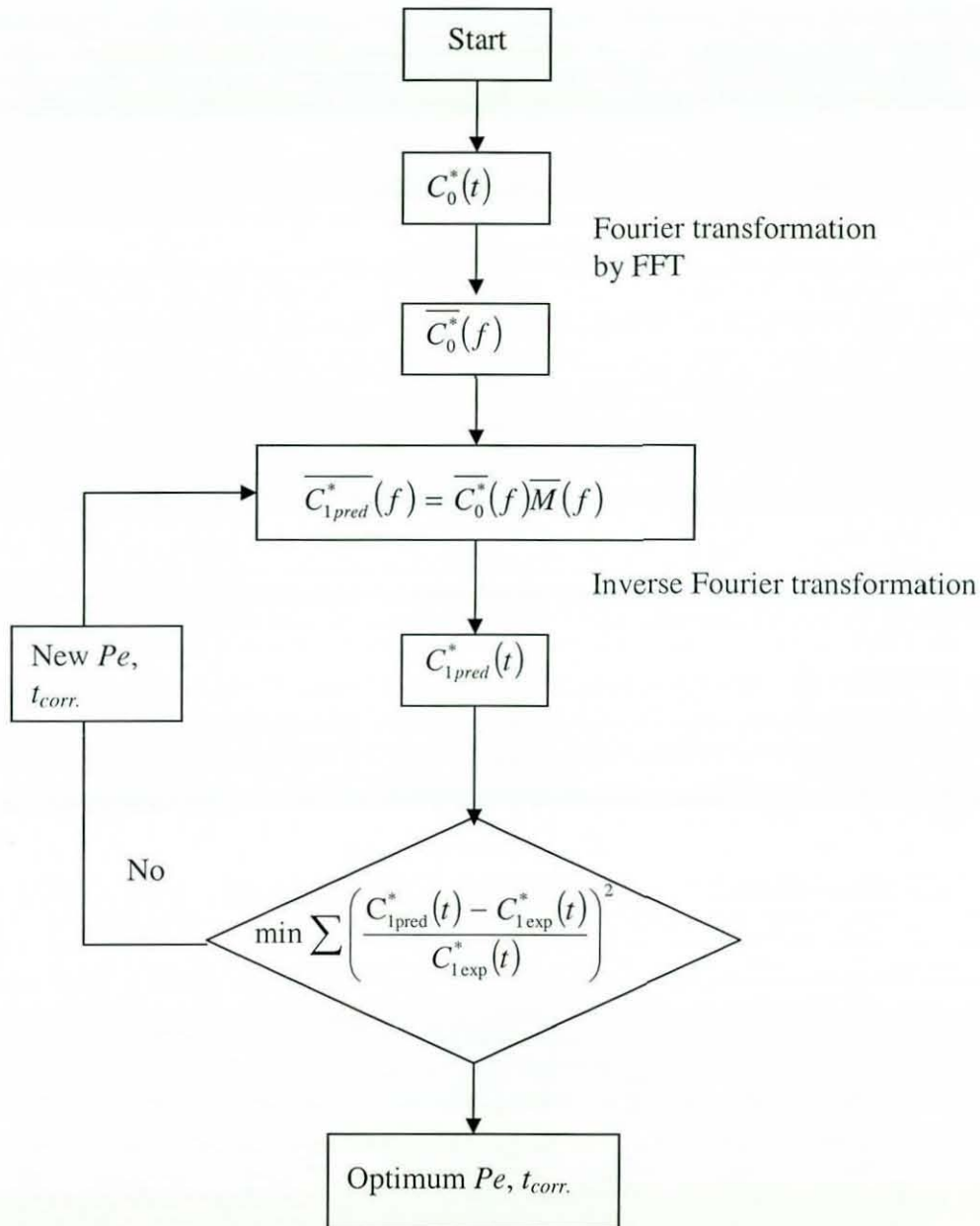


Figure 7.9 Algorithm for the parameter estimation method (Rielly, 2006).

The best-fit parameters of the model are determined using a written FORTRAN program based on the algorithm shown in Figure 7.9, however this is beyond the interest of the current study.

Figure 7.10 shows concentration time histories of three trends input probe, output probe and the best fit convoluted response to the input signal determined by the program. Also appendix I shows an excel sheet of the program used to calculate the model parameters for the best fit.

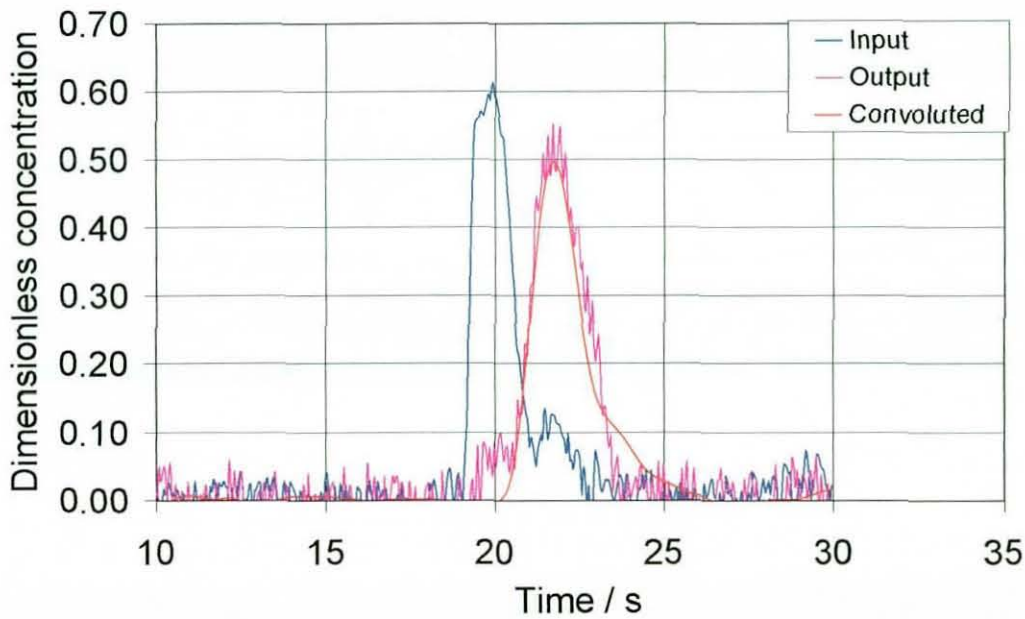


Figure 7.10 Typical concentration histories, obtained in the current study, for the input and out put probe locations in an upflow bubble column. The best fit convoluted response is also shown.

7.7 Solving for Air-Lift Column Variables

After calculating the mean velocity from equation (7.34), which is obtained from the dispersion model, then the rest of the parameters can be determined by equations developed earlier in the Air-lift model section and they are

$$j_{la} = \overline{V}_{la}(1 - \varepsilon_a) \quad (7.40)$$

$$Q_{la} = j_{la}A_{la} = Q_{le} + Q_j \quad (7.41)$$

$$Q_{le} = Q_{la} - Q_j \quad (7.42)$$

Void fraction in the annular riser, ε_a , is predicted by the drift-flux model (equation (7.22)) developed in the current study (Chapter 7)

$$\varepsilon_a = \frac{Q_A}{C_0(Q_A + Q_{le} + Q_j) + V_{\infty a}A_a} \quad (7.22)$$

Substituting equation (7.38) into equation (7.22) and solving for ε_a yields

$$C_0\overline{V}_{la}\varepsilon_a^2 - (C_0j_A + C_0\overline{V}_{la} + V_{\infty a})\varepsilon_a + j_A = 0 \quad (7.43)$$

which is a quadratic equation that can be solved by obtaining the roots either by Excel solver command or calculating a , b and c for quadratic solution

$$a\varepsilon_a^2 - b\varepsilon_a - c = 0 \quad (7.44)$$

$$\varepsilon_a = \frac{-b \pm \sqrt{b^2 - 4ac}}{2a} \quad (7.45)$$

where

$$a = C_0 \overline{V_{la}}$$

$$b = C_0 j_G + C_0 \overline{V_{la}} + V_{\infty a}$$

$$c = j_g$$

where $0 \leq \varepsilon_a \leq 1$ void fractions range is accepted. An example of the Excel spread sheet used to calculate the experimentally measured induced flow is shown in appendix I.

Chapter 8: Air-Lift Column Results and Discussions

8.1 Results and Discussion

8.1.1 Introduction

This chapter investigates the effect of the nozzle diameter and annulus diameter on water flow rate (Q_{la}) that carries the gas-mixture up the riser utilizing the air-lift column surrounding the downcomer in the plunging liquid jet reactor. The results comprise two sets of data; a) the ones measured experimentally using a salt tracer technique described in chapter 7 that is used to estimate the water flow rate in the annular riser by dispersion method, and b) the ones predicted theoretically by the new hydraulic model developed in the previous chapter (chapter 7). This model is tested against experimental data over a range of liquid flow rate, nozzle diameter and annulus diameter. The objective of validating the measurements of induced water against the prediction of the model is to determine if it might be used as a design procedure for the device.

8.1.2 Experimental measurements and discussions of induced Flow

8.1.2.1 Effect of annulus diameter (D_a) on water flow rate (Q_{la})

In this section the effect of the annulus diameter on water flow rate is considered. Figure 8.1 to Figure 8.3 show the water flow rate measured experimentally for different annulus diameters (74 mm – 144 mm) and different nozzle diameters (6 mm - 12 mm). All of the figures show that the water flow rate inside the annulus increases substantially as the annulus diameter increases, for the same nozzle. Figure 8.2 shows such an effect, when the annulus diameter is increased from 74 to 144 mm, the water flow rate measured by 144 mm annulus is 2.6 times that of 74 mm annulus, whilst keeping the nozzle diameter and jet flow rate constant.

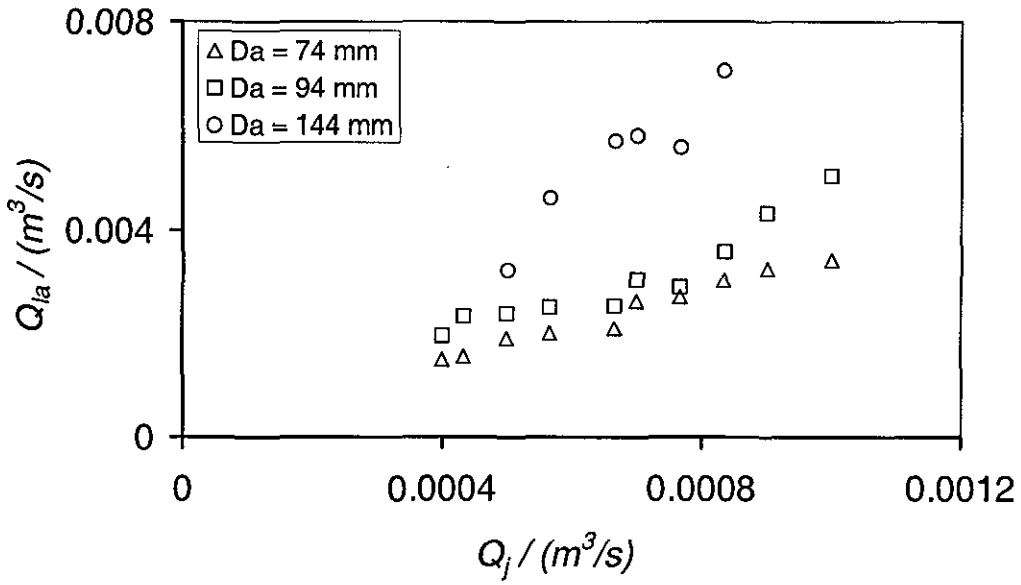


Figure 8.1 Effect of annulus diameter on Q_{la} for 12 mm nozzle.

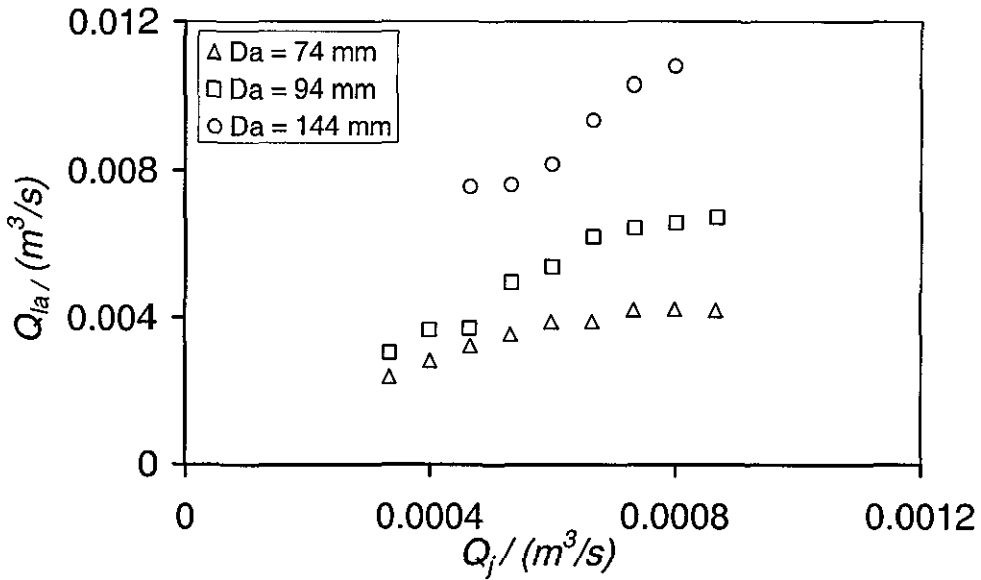


Figure 8.2 Effect of annulus diameter on Q_{la} for 8 mm nozzle.

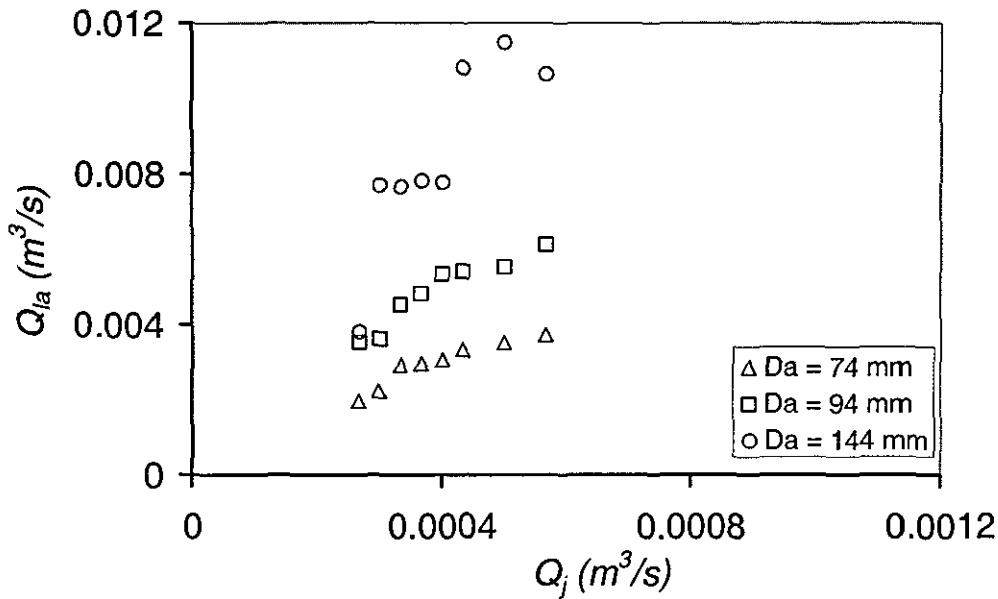


Figure 8.3 Effect of annulus diameter on Q_{la} for 6 mm nozzle.

8.1.2.2 Effect of nozzle diameter (d_n) on water flow rate in the annulus (Q_{la})

Figure 8.4 shows results of the effect of various nozzle diameters (6 – 15 mm) for 94 mm annulus on water flow rate up the riser (Q_{la}). The water flow rate (Q_{la}) increases significantly with decreasing nozzle diameter. Decreasing the nozzle diameter increases the jet velocity and hence high values of entrained gas flow rate are obtained. This increases the gas voidage in the riser, which increases the hydrostatic pressure difference between the bubbly flow in the riser and the surrounding clear liquid (in the tank) and thus more water is induced from the base of the annulus.

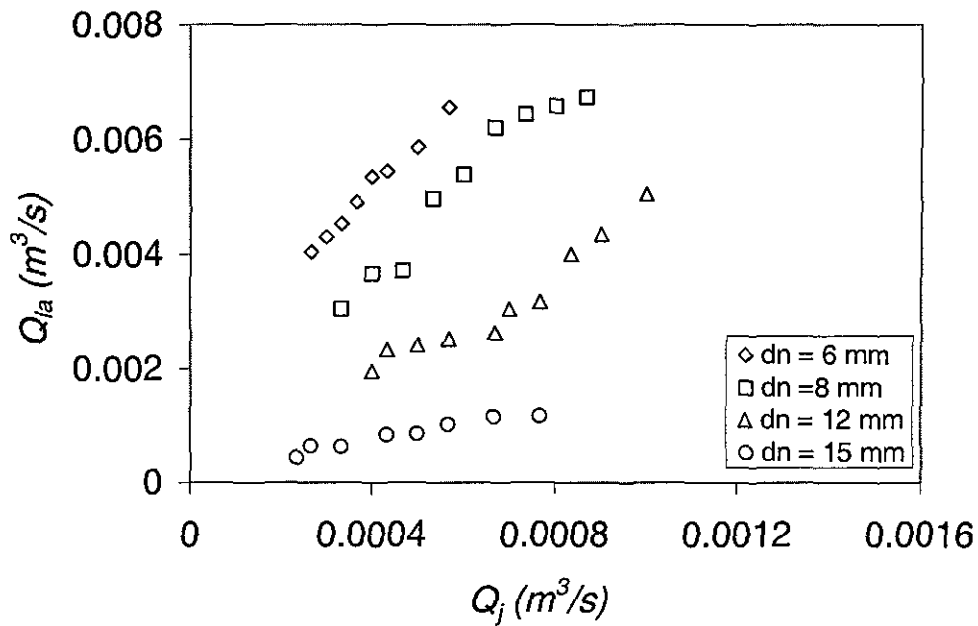


Figure 8.4 Effect of various nozzle diameters (d_n) on water flow rate up the riser (Q_{la}) for 94 mm annulus as jet flow rate (Q_j) increases.

8.1.2.3 Effect of annulus diameter on air entrainment rate (Q_A)

This section shows the effect of the annulus diameter on air entrainment ratios measured for a given conditions (same d_n , L_j and D_c). Figure 8.5 and Figure 8.6 show the air entrainment ratios measured for all of the annuli (74-144 mm) utilising 6 mm and 8 mm nozzles respectively. This shows that the effect of the annulus diameter on the air entrainment ratio is negligible. This suggests that air entrainment rate measured by a given nozzle is required to be done only once for any of the annuli regardless of its diameter if the conditions in the downcomer are fixed.

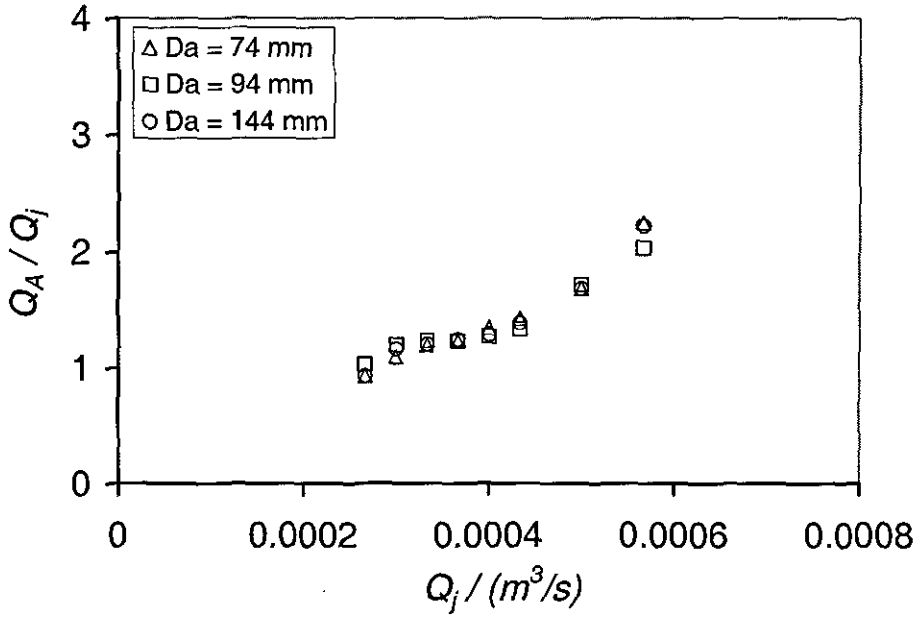


Figure 8.5 Air entrainment measured by three different annuluses and 6 mm for a given conditions.

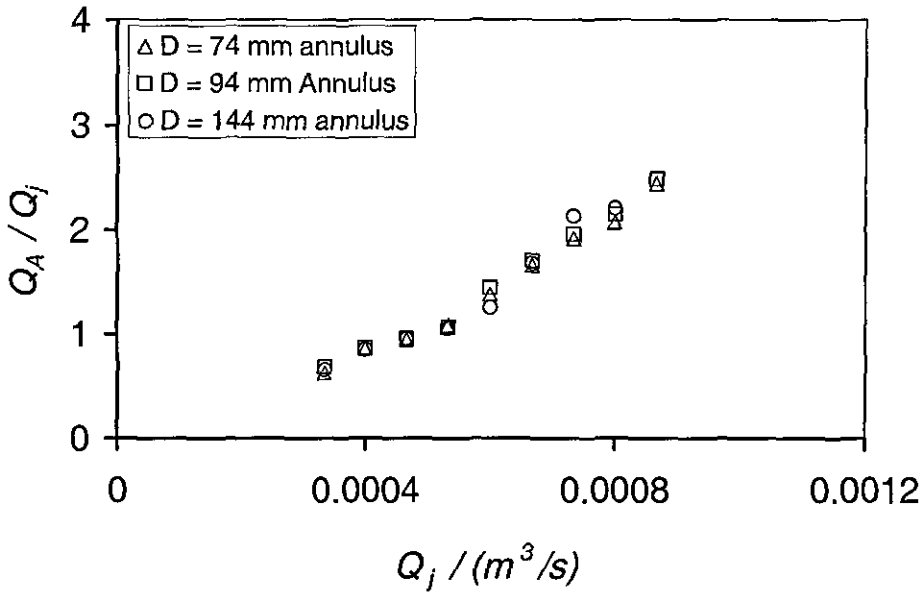


Figure 8.6 Air entrainment measured by three different annuluses and 8 mm for a given conditions.

8.1.2.4 *Effect of the noise and dilution on the response of water flow rate measurements*

(i) Effect of nozzle diameter

Some difficulties were encountered in measuring induced flow rate for large annuli and high jet velocities. Here, the disturbances and the noise displayed using the axial dispersion method to measure the induced flow are investigated. As shown in Figure 8.7a the system worked well at low jet flow using the same 74 mm annulus (6 mm nozzle and 16 L/min flow rate). At higher jet flow rates using the 74 mm annulus (e.g. 6 mm and 30 L/min) the signal becomes much noisier but was still adequate to make the flow measurements and thus be analysed by the dispersion method (Figure 8.7b). The increase of noise may be due to the increase of the voidage around the electrodes. Induced liquid flow rate also increased with the voidage, which diluted the tracer and thus reduced the conductivity signal in comparison with that measured for low jet flow rate.

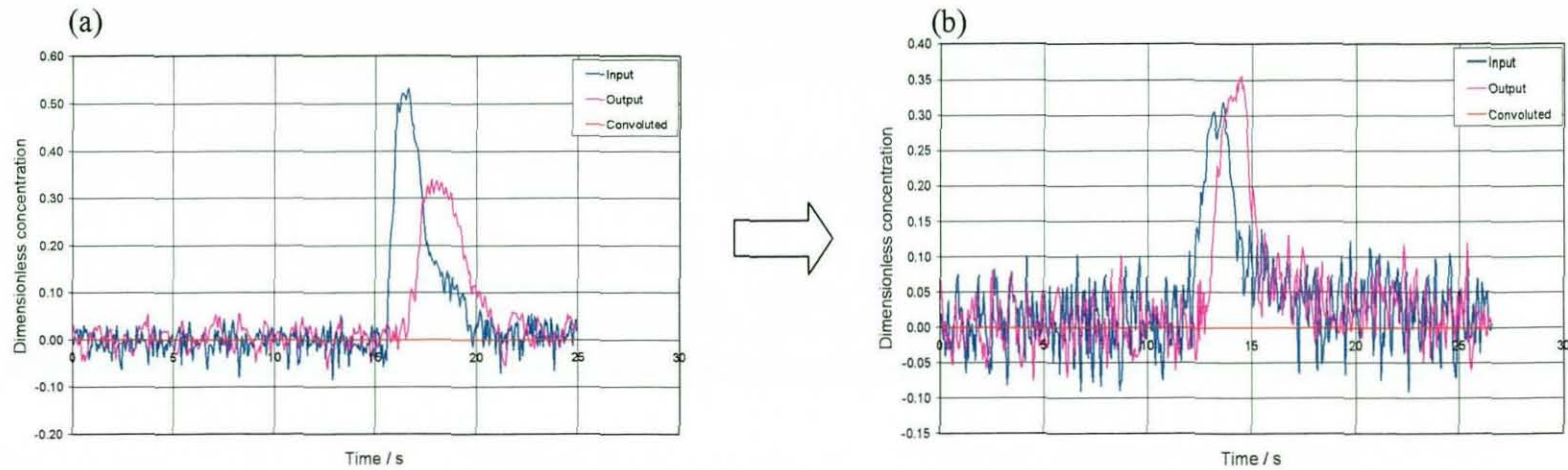


Figure 8.7 Concentration time histories of injected tracer detected by electrode rings mounted on the wall of the air-lift column for 6 mm as the jet flow rate increases from 16 L/min to 30 L/min for the 74 mm Annulus.

(ii) Effect of annulus diameter

Figure 8.8 depicts the responses obtained from air-lift column system for the same conditions but using different annulus diameters. The responses worsened as the annulus diameter is increased for the same volume of salt tracer injected. This is due to the dilution of the salt tracer up the riser. As shown previously, as the annulus diameter increases the water flow inside the annulus increases due to the increase of induced flow. This dilutes the salt tracer even more to the extent of making it difficult to be detected by the probes. Figure 8.8c shows that the dispersion and dilution has become so large that the signal can not be detected. This affects the accuracy of the correlation (convective) time ($t_{corr.}$) value predicted by the dispersion method, which is used to estimate water flow rate up the annulus (Q_{la}). An attempt was made to overcome this problem by increasing (doubling) the concentration as well as the volume of the injected salt (15 – 20 ml), which gave some improvements. Figure 8.9 shows the concentration time histories and delay times responses for tracers before and after the increase of salt concentration and dosage volume. Results show that clearer peaks are obtained however still a lot of noise is associated with the readings, which affected, in some cases, the measured water flow rate up the annulus results.

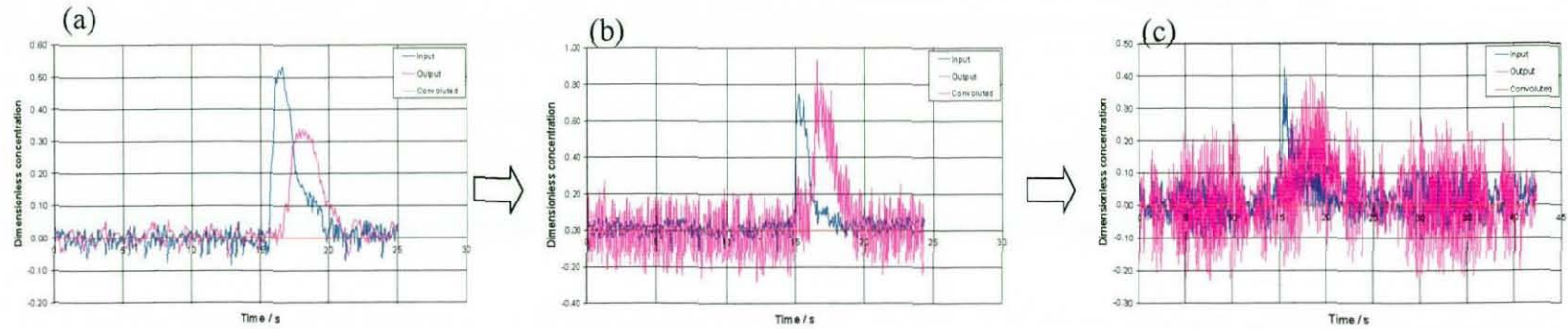


Figure 8.8 Concentration time histories of injected tracer detected by electrode rings for 6 mm nozzle and 16 L/min as the annulus diameter increases from 74 mm to 144 mm.

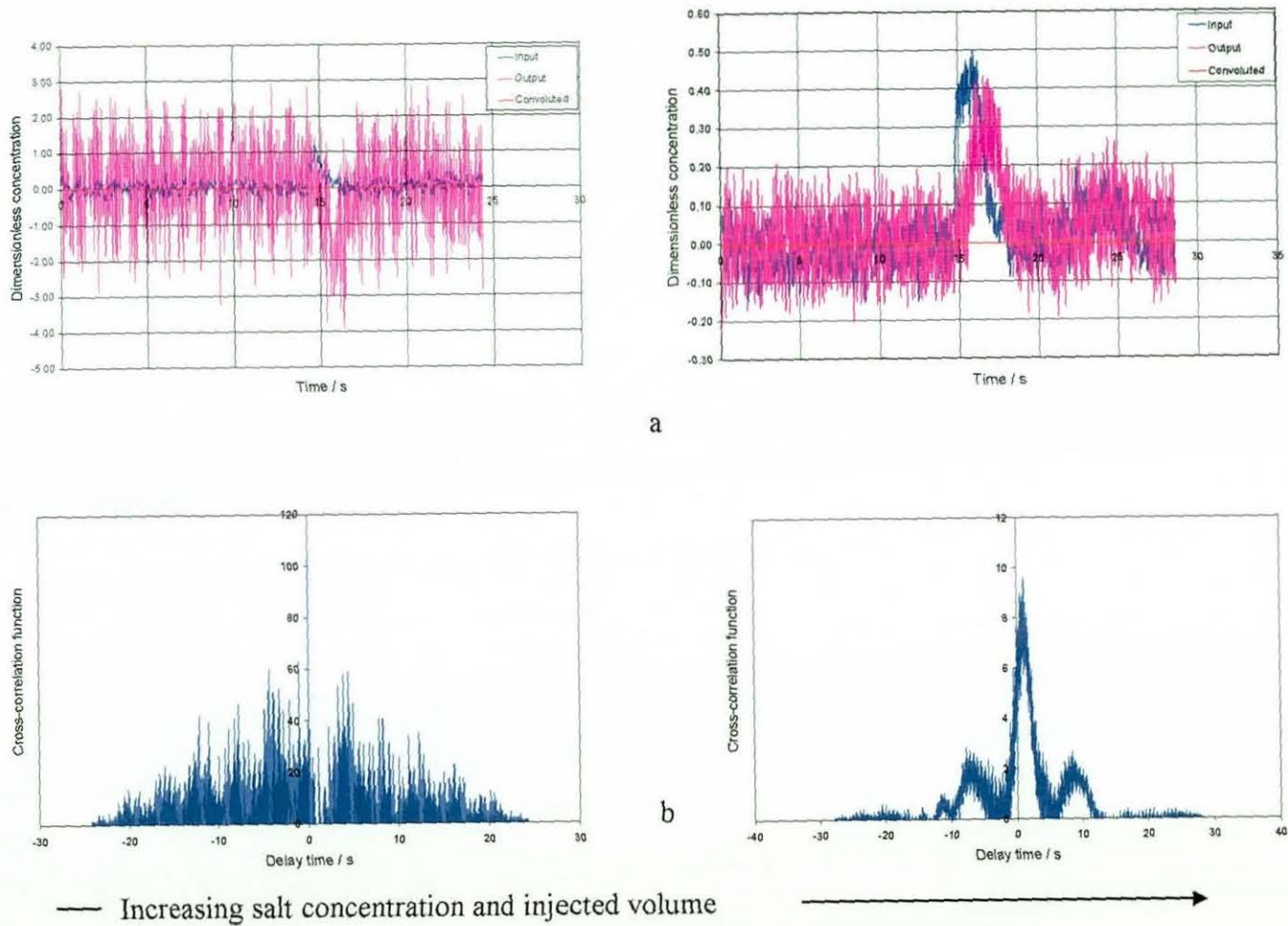


Figure 8.9 a) Concentration time histories and b) delay time responses for tracers before and after the increase of salt concentration and dosage volume for 144 mm Annulus.

8.1.3 Comparison between the model and experimental measurements

8.1.3.1 Nozzle effect

As mentioned in the experimental section nozzle diameter range 6-15 mm was used to make air-lift column measurements, whereas the rest of variables jet length (L_j), annulus (D_a) and downcomer (D_c) diameters remain constant for each run. The present section investigates the effect of nozzle diameter on the agreement between the theoretical and experimental approaches for water flow rate in the annulus (Q_{la}).

Results for all the nozzles utilizing two annulus diameters (74 mm and 94 mm) are summarized in Figure 8.11 and Figure 8.12. They show that water flow rate in the annulus for the largest nozzle (15 mm), is over estimated by the correlation by a factor of 3.5 that decreases to 1.3 at high jet flow rate, however it has the same trend as the one obtained by plotting experimental data. This is a good indication because the theoretical model does not only predict the values but also the behaviour (trend). Figure 8.11 and Figure 8.12 show that decreasing nozzle diameter improves the agreement between the developed model and experimental results. For the smaller nozzle diameter the ratio of gas entrainment to the jet flow increases significantly compared with that for larger nozzles. This effect suggests why the liquid jet flow has an effect on the entrained flow in the annulus. When the model was developed the voidage ε_a throughout the annulus was also assumed to be constant, which is not the case in reality especially at low liquid superficial velocity. Impressions of the voidage variation are shown on Figure 8.10a and Figure 8.10b for the same annulus and different nozzle diameters. Underneath the base of the downcomer the escaping two-phase stream contacts the freshly induced water (Q_{le}) forming a mixing zone of two-phase mixture that penetrates to a certain depth controlled by liquid superficial velocity and the buoyancy in the downcomer (Figures 8.10a and c, and Figures 8.10b and d). The mixing intensity as well as the bubble penetration depth affects the voidage distribution in this zone, and hence up the riser. Since large nozzle diameter gives lower liquid superficial velocity and gas entrainment rate in the downcomer, the

bubble penetration depth is shorter and the mixing intensity is lower which causes the bubble to rise up the annulus soon after leaving the downcomer, and thus the bubbles experience little mixing and may not be distributed uniformly throughout the annulus. In contrast, the two-phase mixture established by the smaller nozzle diameter comprises a higher liquid superficial velocity and gas entrainment rate that penetrates deep down before it rises back up the annulus. It is also characterised with extreme rapid mixing. The foregoing two factors enhance the bubble distribution up the riser reducing voidage variation, which is one of the model assumptions.

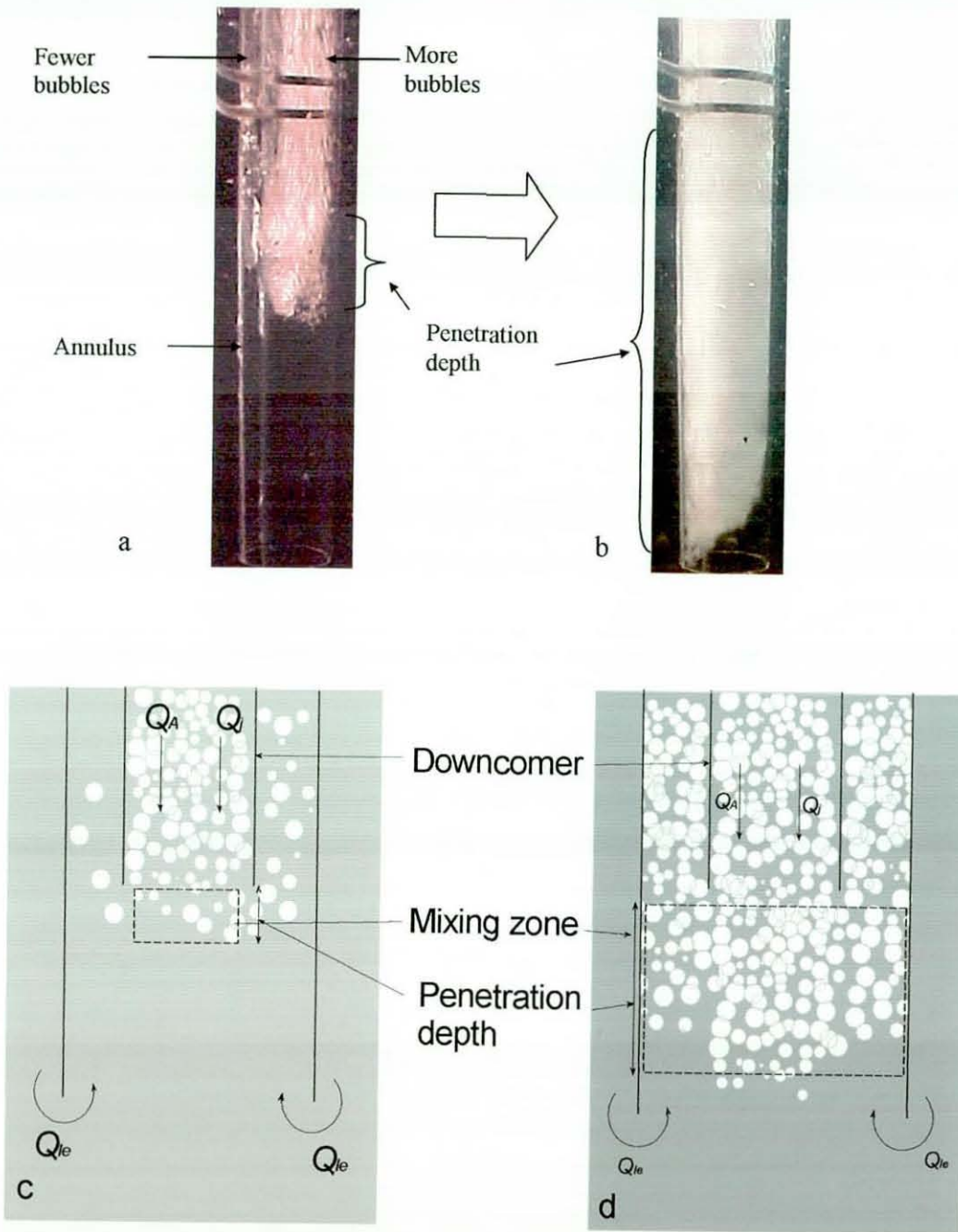


Figure 8.10 Bubbles distribution inside 74 mm annulus for a) and c) moderate V_j where most of the bubbles are located in one side of the annulus, and b) and d) high V_j where the two phase flow occupies all of the annulus.

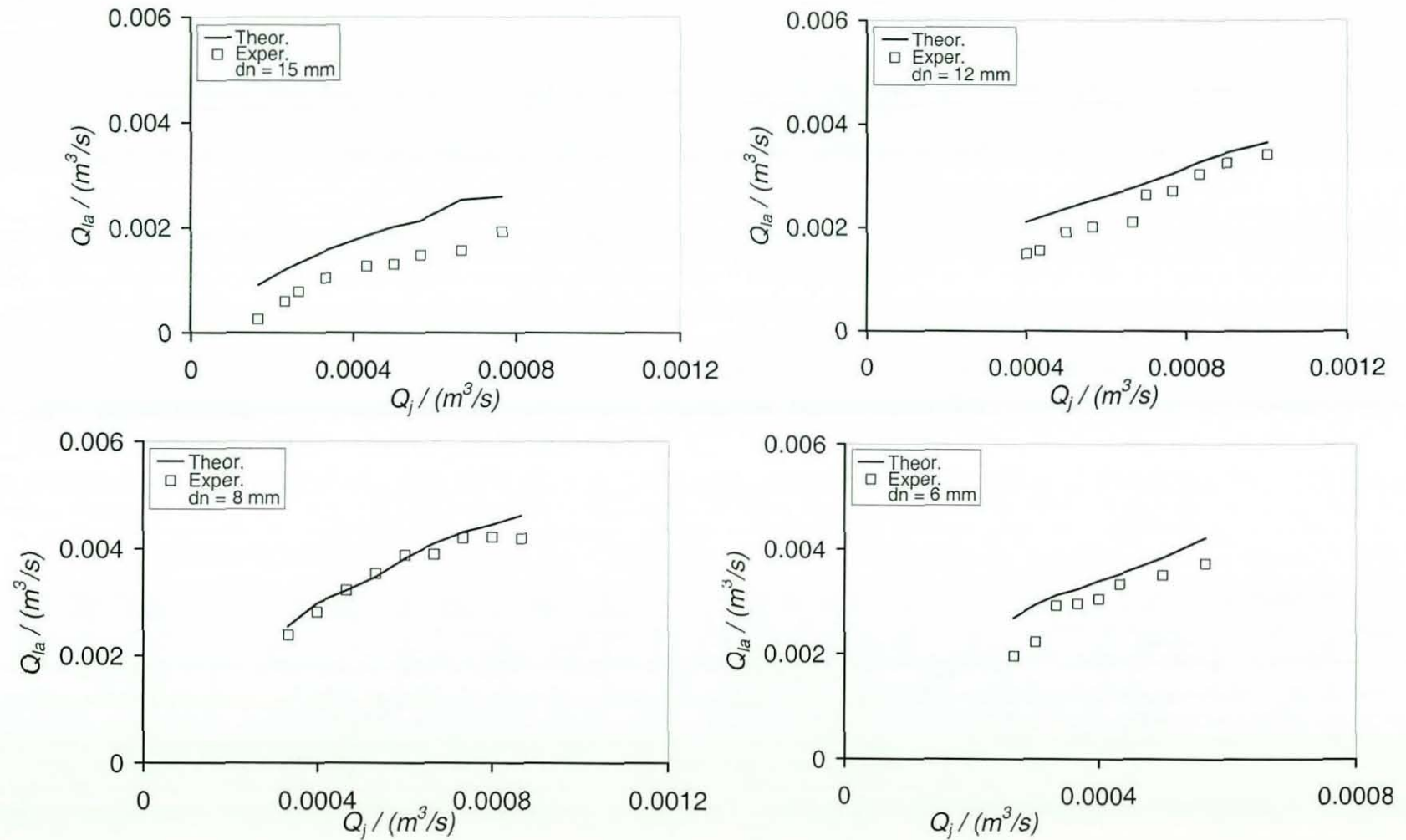


Figure 8.11 Experimental and theoretical results for all nozzles and 74 mm annulus diameter.

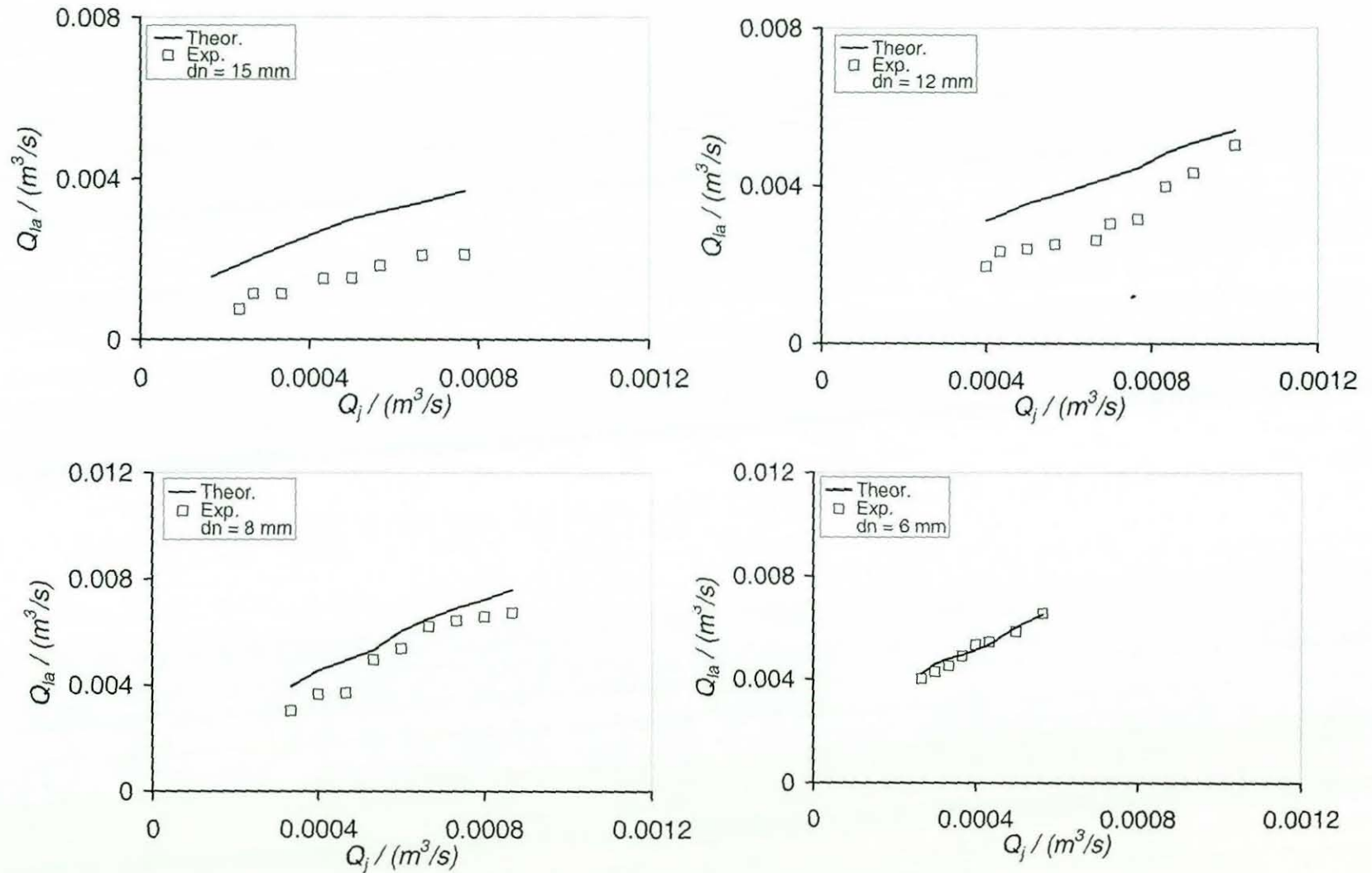


Figure 8.12 Experimental and theoretical results for all nozzles and 94 mm annulus diameter.

Experimental and theoretical results of the induced water flow in the 74 mm riser were plotted against the air entrainment rate for all of the nozzles used as shown in Figure 8.13. This demonstrates that the induced flow is controlled by the air flowing into the riser regardless of the nozzle diameter or jet flow rate. The figure again shows that the model predicts the annular induced flow well.

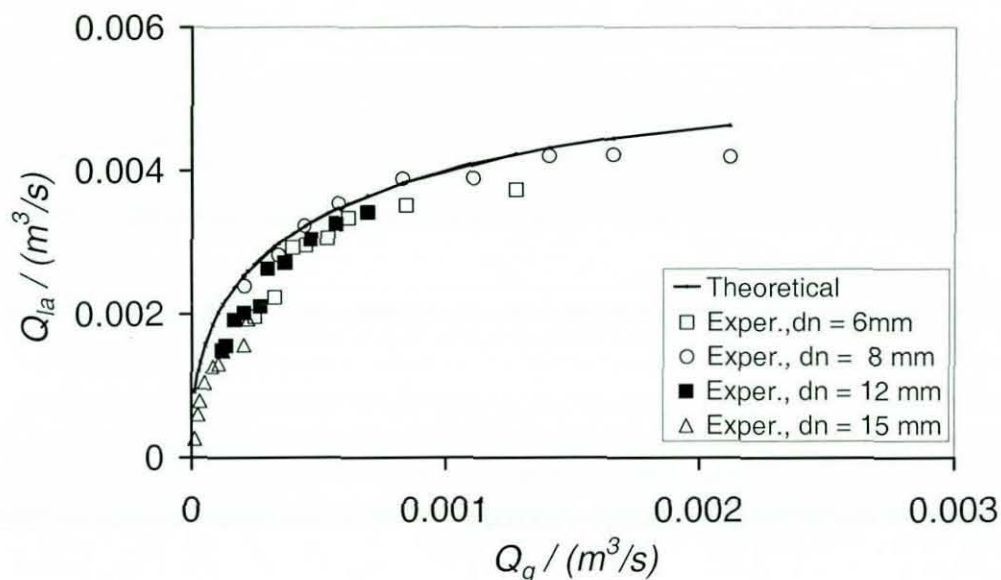


Figure 8.13 Comparison between the experimental and theoretical results for all of the nozzles and the 74 mm annulus.

8.1.3.2 Annulus diameter (D_a) effect

The effect of D_a on the agreement between the theoretical and experimental values is investigated here and shown in Figure 8.14 to Figure 8.16, which depict the water flow rate inside the annulus for model and experimental results for annulus diameter ranges from 74 -144 mm utilizing an 8 mm nozzle diameter. It is obvious from the figures that the agreement between model and experiment slightly worsens with increasing D_a . This is attributed to the velocity profile inside the annulus, where the distribution of the bubbles up the riser is better with a smaller annular riser. This can be further explained by the time history responses shown in Figure 8.17a and

Figure 8.17b generated by 94 and 144 mm annuli respectively. Figure 8.17b shows that the time history recorded for the 144 mm annulus displays two peaks, which suggests the tracer on one side of the annulus moves faster than the rest of the entrained liquid and hence water flow rate up the riser (Q_{la}) is not uniformly distributed around the annulus due to voidage variation. However, the 94 mm annulus (Figure 8.17a) shows one clear peak and hence a better voidage distribution than the previous case. The improvement of bubble distribution established by smaller annuli can be attributed to the annulus wall proximity that restricts the flows. Also, deeper penetration depth is achieved with smaller annuli, which reduces voidage variation through the annulus. Therefore, the model predicts the data produced by the smaller annuli better because they provide better bubble distribution than larger ones.

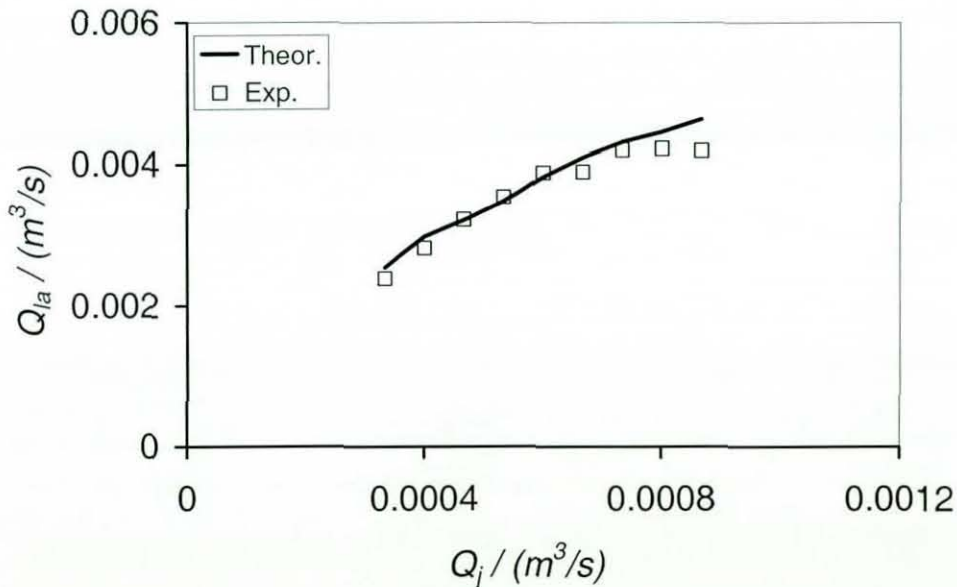


Figure 8.14 Experimental and theoretical results for 74 mm annulus and 8 mm nozzle.

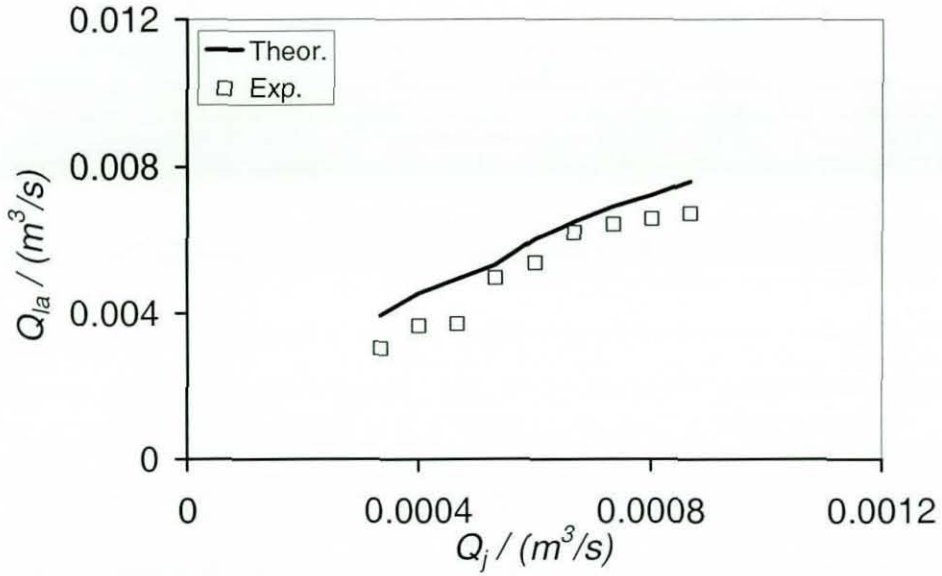


Figure 8.15 Experimental and theoretical results for larger annulus, 94 mm, and 8 mm nozzle.

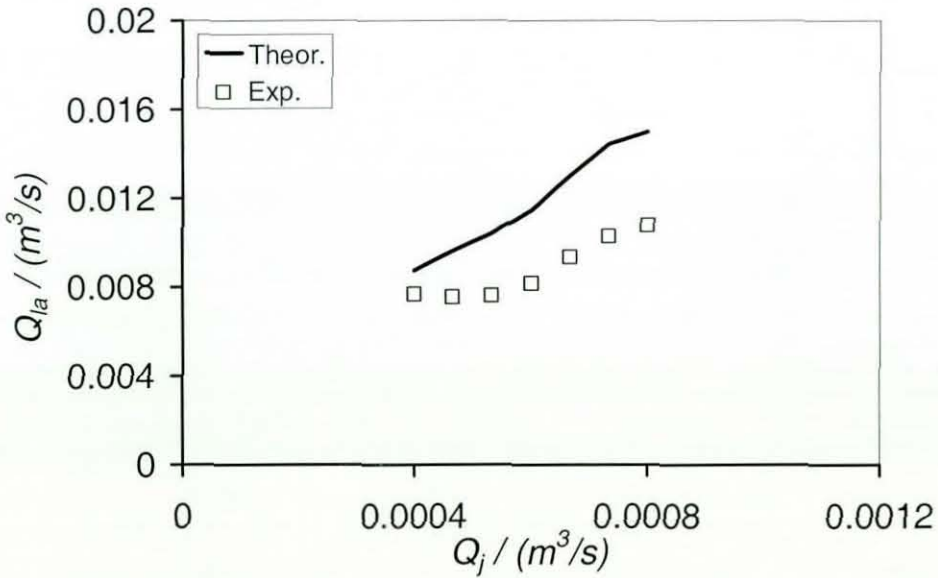


Figure 8.16 Experimental and theoretical results for largest annulus, 144 mm, and 8 mm nozzle.

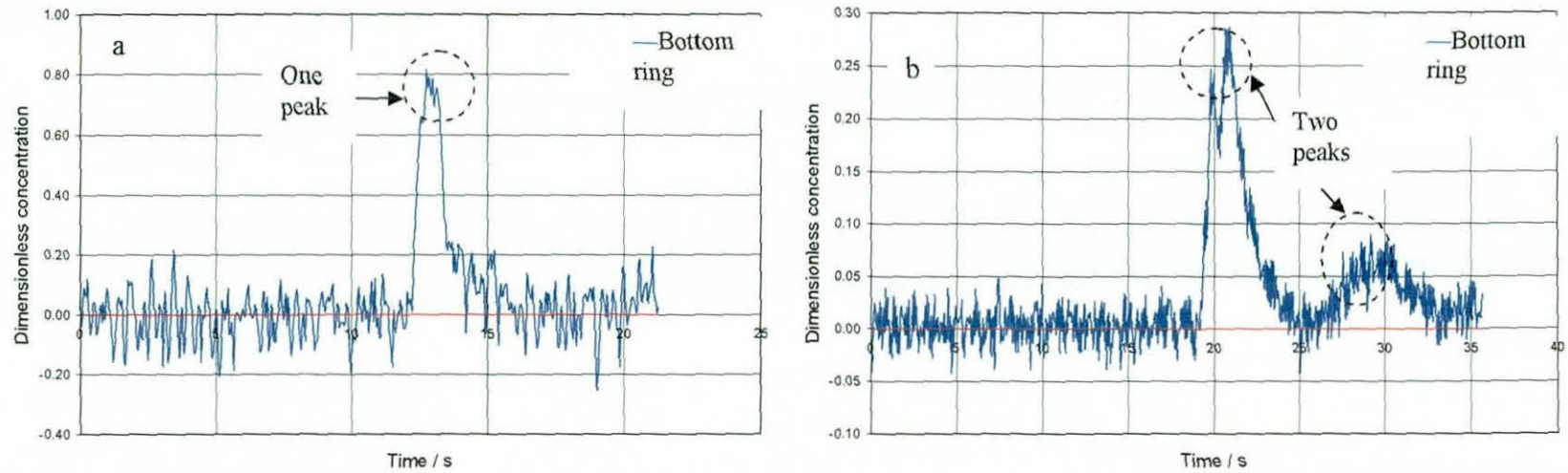


Figure 8.17 Time history generated by $d_n = 8$ mm and $Q_j = 36$ l/min for $D_a =$ a) 94 with one peak and b) 144 mm with two peaks respectively.

8.1.4 Prediction of frictional pressure gradient $(dp/dl)_f$

In chapter 7 the frictional loss term was determined by several possible two-phase models. Three frictional pressure correlations are selected homogenous model (Kay and Nedderman, 1988; Holland and Bragg, 1995), two-phase multiplier (Holland and Bragg, 1995) and Akita's (1988). An Excel spreadsheet was used to solve all of the equations to calculate all of the variables in the theoretical model such as, voidage ε_a , water entrainment rate Q_{le} and water flow rate in the annulus Q_{la} . Figure 8.18 shows the layout of one of the calculations using the Excel spreadsheet.

A comparison between the data obtained by the theoretical models including the frictional pressure gradient models and the experimental data is shown in Figure 8.19 to Figure 8.22 for 74 mm annular riser and for each nozzle separately, where the values for C_0 and C are 1.2 and 20 respectively.

Water entrainment rate flow in the Annulus using two-phase multiplier in the model to predict the frictional pressure gradient

Input Data

D	0.075
d	0.03
C ₀	1.2
d _n	0.006
g	9.81
V _{c-d}	0.25045581
A _s	0.00371101
H	0.825
μ _l	1.01E-03
μ _g	1.77E-05
C	20
	15 0.1001
	20 0.10018
V _{specific volun}	18 0.00100148 m ³ /kg

Recalculate

Output

Q _g /m ³ /s	Q _g /m ³ /s	ε _α	j _j /m/s	j _g /m/s	j _{la} /m/s	h _r /m	j _{lat} /m/s	J _{le} /m/s	Q _{le} /m ³ /s	Δ	Q _{lecalc} /m ³ /s	Q _{lecalc} /m ³ /s	Re	C _f	
0.000266667	0.00024847	0.054709183	0.071858316	0.066953611	0.743999538	0.013562105	0.744174366	0.67231605	0.002494969	-0.000174828	0.00249432	0.002781636	0.002203132	3.31E+04	5.86E-03
0.0003	0.00032799	0.066357373	0.080840606	0.088383838	0.81264029	0.016131583	0.812850471	0.732009865	0.002716493	-0.000210182	0.002715713	0.003016493	0.002509304	3.61E+04	5.73E-03
0.000333333	0.00039857	0.075913644	0.089822896	0.107403145	0.862896464	0.01818679	0.862889416	0.77306652	0.002868855	7.04822E-06	0.002868881	0.003202188	0.003286638	3.84E+04	5.64E-03
0.000366667	0.00045276	0.082850765	0.098805185	0.122004357	0.89644977	0.019658167	0.89643225	0.797627065	0.002959999	1.75206E-05	0.002960064	0.003328666	0.003330564	3.99E+04	5.59E-03
0.0004	0.00053616	0.092984124	0.107787475	0.144478844	0.941686811	0.021772467	0.941642323	0.833854848	0.003094441	4.44874E-05	0.003094606	0.003494441	0.00344305	4.19E+04	5.52E-03
0.000433333	0.00061646	0.102220581	0.116769764	0.166115773	0.979480037	0.023664929	0.979397464	0.862627699	0.003201217	8.25735E-05	0.003201523	0.00363465	0.003766533	4.36E+04	5.47E-03
0.0005	0.00084396	0.126271543	0.134734343	0.227420403	1.065025038	0.028444073	1.064735095	0.930000752	0.003451239	0.000289943	0.003452315	0.003951239	0.003978827	4.74E+04	5.36E-03
0.000566667	0.00127573	0.165933368	0.152698922	0.343769184	1.173963058	0.035921307	1.173959549	1.021260626	0.003789905	3.50934E-06	0.003789918	0.004356571	0.004250589	5.22E+04	5.23E-03

M _g	M _{la}	w	μ	G/kg/s.m ²	(dp/dx) _l	(dp/dx) _g	Re _g	0.1	X	φ _l	φ _g	(dp/dx) _f	(dp/dx) _f _g	ΔP/pa
					holland/pa/							holland/pa/		
					m							m		
0.000298158	2.75611251	0.000108169	1.01E-03	742.7663619	143.8164244	0.005096963	2.04E+02	2.09E-02	167.9931437	1.057869515	177.7148255	160.943222	160.943222	132.7781582
0.000393592	3.01046025	0.000130724	1.01E-03	811.3308309	167.8432022	0.008284635	2.70E+02	1.95E-02	142.3361431	1.067970884	152.0108565	191.4355462	191.4355462	157.9343256
0.000478289	3.1957837	0.00014964	1.01E-03	861.2925206	186.3428609	0.011652004	3.28E+02	1.86E-02	126.4608424	1.076203629	136.0976176	215.8249573	215.8249573	178.0655898
0.000543311	3.32001241	0.00016362	1.01E-03	894.7857905	199.2055305	0.014563901	3.72E+02	1.80E-02	116.953127	1.082165325	126.5626187	233.2859694	233.2859694	192.4609248
0.000643394	3.48745173	0.000184454	1.01E-03	939.9324131	217.1216096	0.019578451	4.41E+02	1.72E-02	105.3082425	1.090875259	114.8781563	258.3766326	258.3766326	213.1607219
0.000739748	3.62728108	0.000203899	1.01E-03	977.6380076	232.5879137	0.024994237	5.07E+02	1.67E-02	96.46585685	1.098833337	105.9998994	280.8347185	280.8347185	231.6886427
0.00101275	3.94333619	0.00025676	1.01E-03	1062.878529	269.2147836	0.043308422	6.94E+02	1.54E-02	78.84302382	1.119745273	88.28410322	337.5494311	337.5494311	278.4782807
0.001530876	4.34785817	0.000351975	1.01E-03	1172.024153	319.4112174	0.089245847	1.05E+03	1.39E-02	59.82477491	1.155244158	69.11222173	426.2827178	426.2827178	351.6832422

Figure 8.18 Layout of the theoretical model used to calculate Q_{la} and other variables.

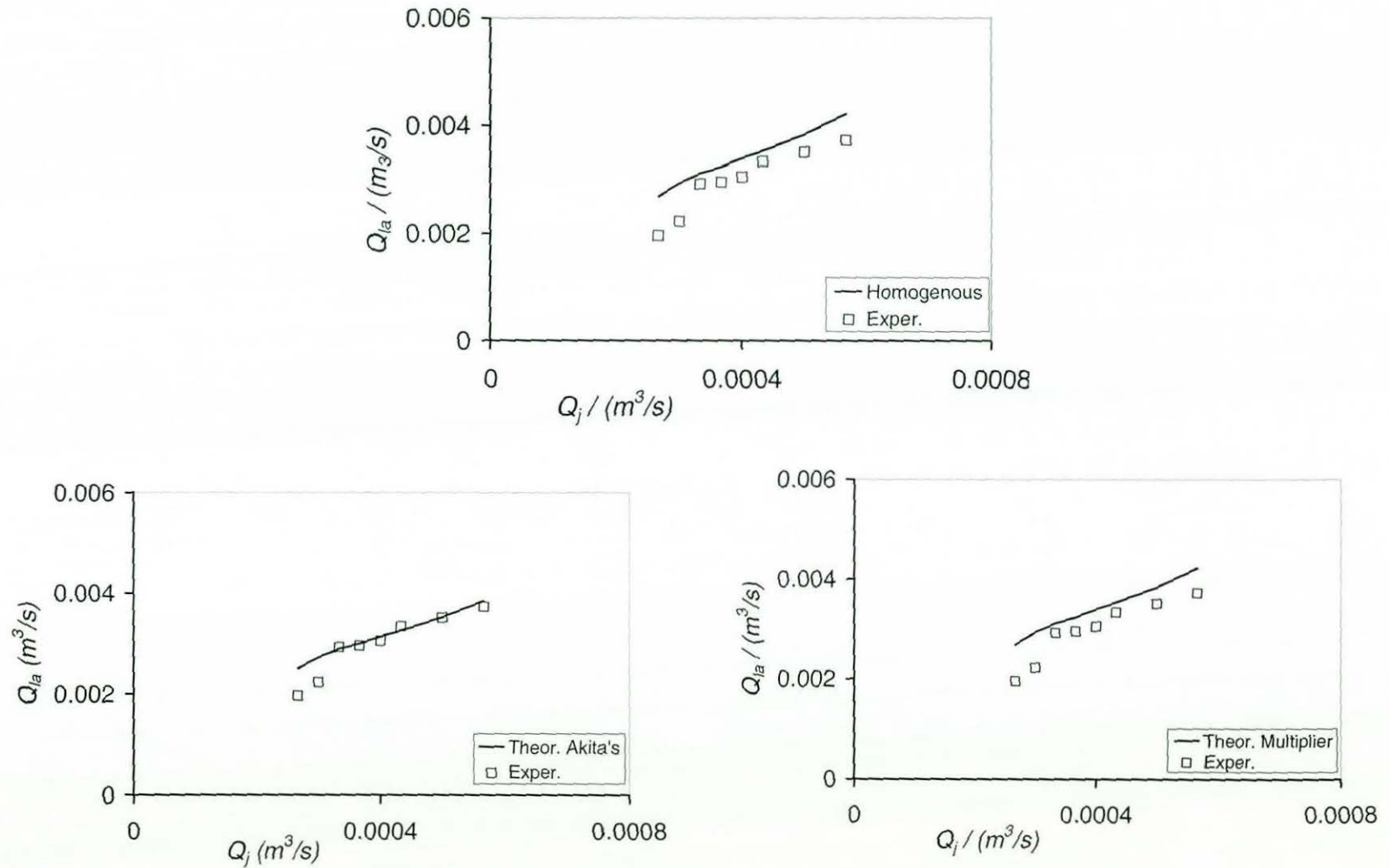


Figure 8.19 Theoretical and experimental results, using different models, for 6 mm nozzle and 74 mm annulus.

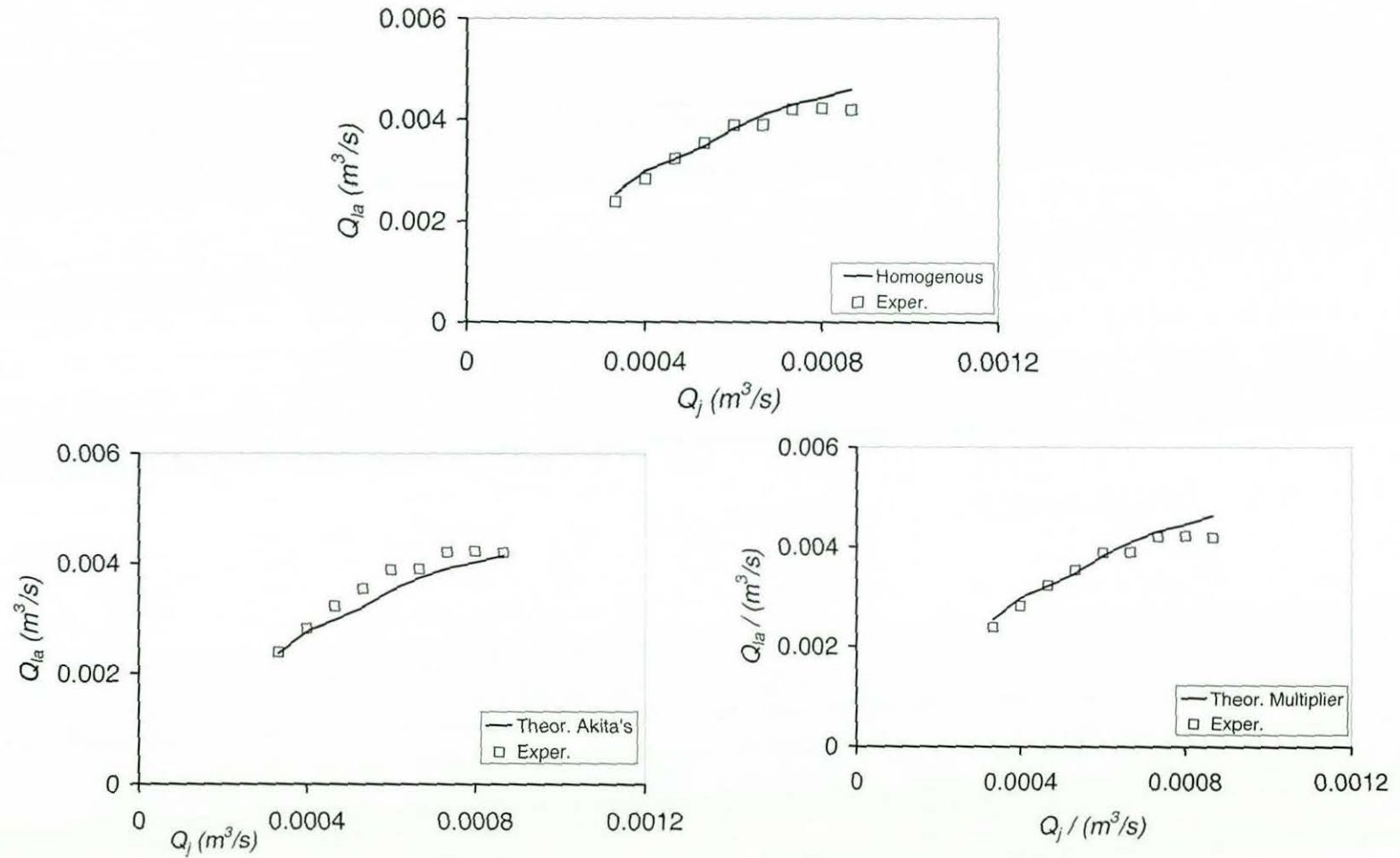


Figure 8.20 Theoretical and experimental results, using different models, for 8 mm nozzle and 74 mm annulus.

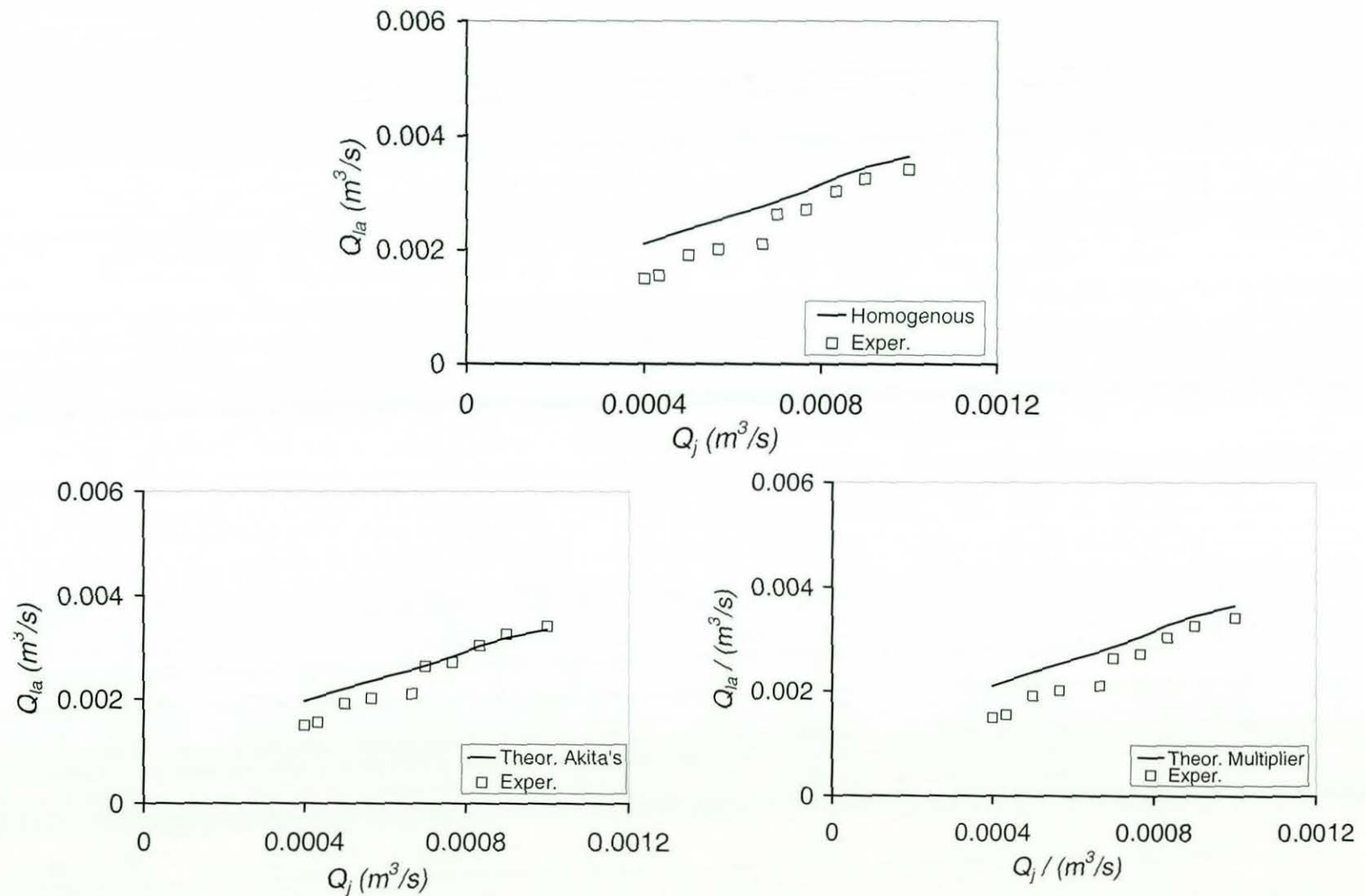


Figure 8.21 Theoretical and experimental results, using different models, for 12 mm nozzle and 74 mm annulus.

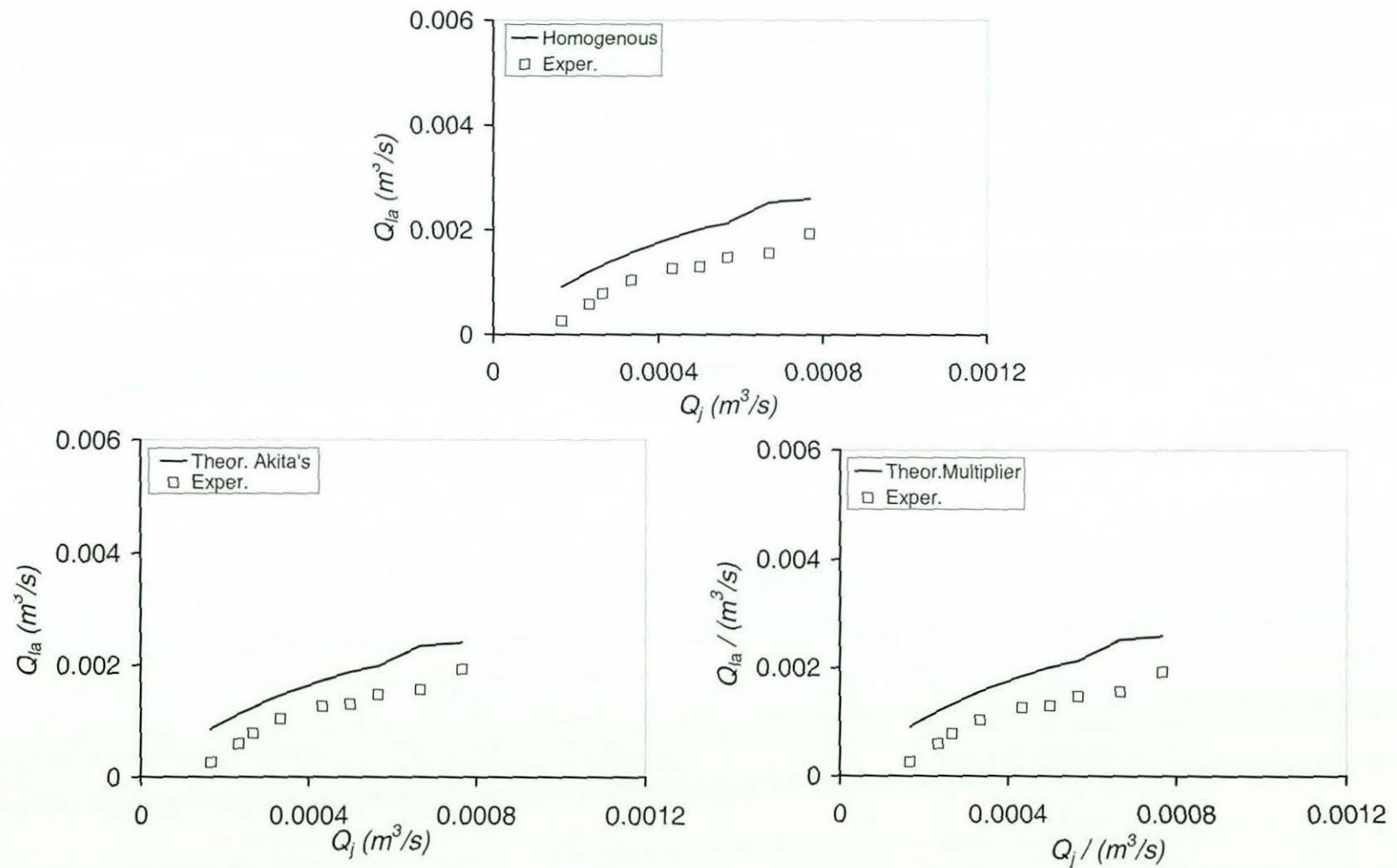


Figure 8.22 Theoretical and experimental results, using different models, for 15 mm nozzle and 74 mm annulus.

Foregoing figures indicate that all of the correlations give good agreement with experimental results for different nozzle diameters (except for large nozzle, 15 mm) and same annulus diameter of 74 mm. To see this better two more plots are generated as shown in Figure 8.23 and Figure 8.24, where all of the correlations are plotted on the same graph for the same conditions. Both plots have the same annulus diameter of 74 mm and different nozzle diameters of 6 mm and 12 mm respectively. From these figures one can clearly see that all of the correlations give the same Q_{la} prediction except Akita's correlation. This is attributed to the fact that Akita's correlation is developed by fitting experimental data. It is valid for batch process and a limited range of $0 < j_{la}/(gd_e)^{0.5} < 1.0$. The actual value of $j_{la}/(gd_e)^{0.5}$ for the current case ranges from 1.0 to 1.79 depends on the nozzle diameter, which exceeds Akita's limit. The frictional pressure gradient models and Akita's correlation were further investigated in more detailed by generating another plot shown in Figure 8.25. This plot enables the reader to see the small changes that the other figures could not show. Figure 8.25 shows that homogenous and two-multiplier models give the same results.

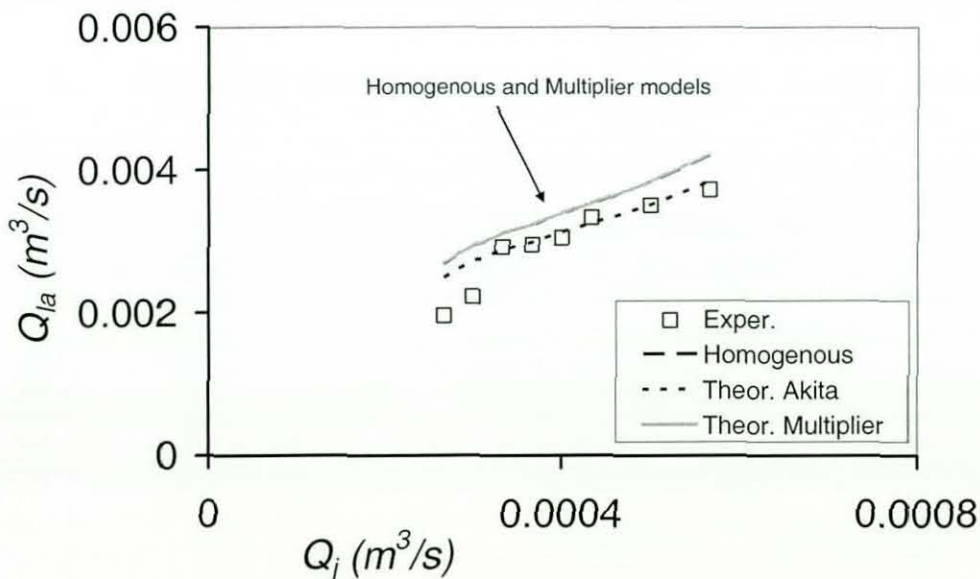


Figure 8.23 Effect of using different frictional pressure gradient correlations on the theoretical model for 6 mm nozzle and 74 mm annulus.

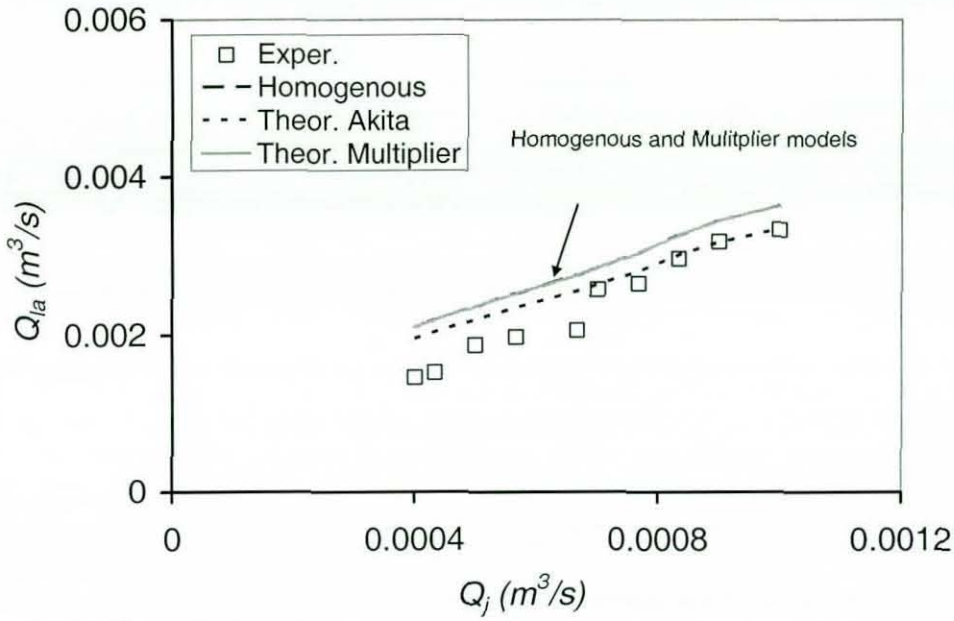


Figure 8.24 Effect of using different frictional pressure gradient correlations on the theoretical model for 12 mm nozzle and 74 mm annulus.

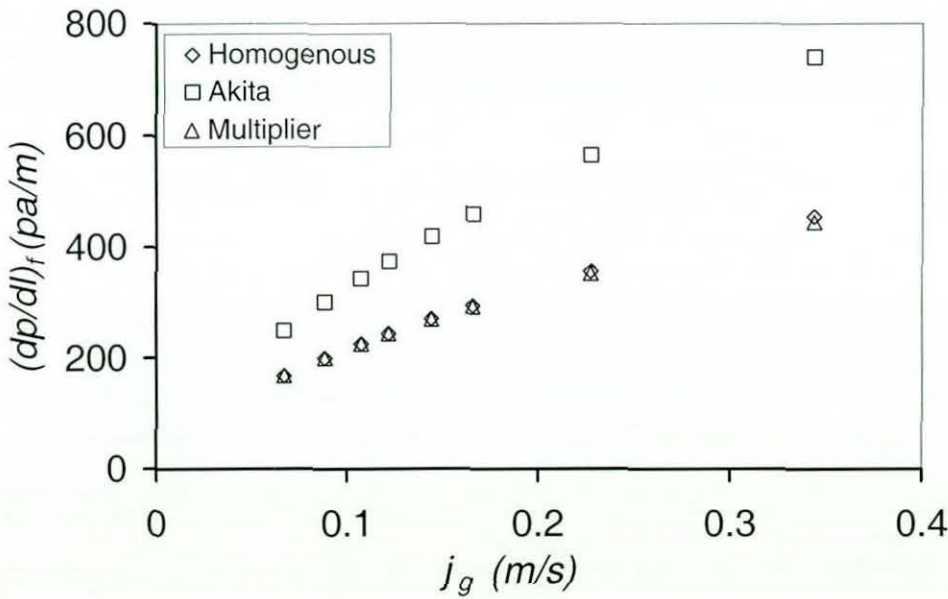


Figure 8.25 Differences between the correlations that are used to predict pressure frictional gradient $(dp/dl)_f$.

Based on the previous investigation one can choose any of the three models to predict the frictional pressure loss in the annulus to be used in the energy model to calculate the theoretical results. For the current study the two-phase multiplier frictional pressure gradient model has been used to calculate the theoretical data.

8.1.5 Sensitivity analysis

Here, sensitivity test is performed on the theoretical model by checking the assumptions and terms provided in the literature such as distribution factor C_0 , bubble rise velocity V_∞ , frictional pressure gradient $(dp/dl)_f$ and pressure drop due to change of direction and sudden contraction.

Effect of C_0 and V_∞

Arbitrary C_0 and V_∞ values were chosen to study their effect on the model. Figure 8.26 is generated by plotting experimental and theoretical results for water flowrate in the annulus (Q_{la}). Then the theoretical values were tested by increasing distribution factor from 1.2 to 1.7 and bubble rise velocity from 0.25 to 0.75 m/s. As shown in Figure 8.26, to get almost the same effect from the bubble rise velocity as that of the distribution factor, the bubble velocity is increased three times whilst the distribution factor is increased only 1.42 times. This shows clearly that the model is more sensitive to distribution factor (C_0) than to bubble rise velocity (V_∞). This result is very important because it shows that the model is less sensitive to V_∞ than C_0 . Distribution factor (C_0) and terminal velocity (V_∞) affect the theoretical model by affecting the voidage inside annulus, which is incorporated into the theoretical model expression. As can be seen from the voidage expression developed for the annulus in air-lift column experiment (equation (7.20)) C_0 has a significant effect on voidage in comparison with the terminal velocity of the bubble because the distribution factor is multiplied into the two-mixture superficial velocities ($j_g + j_{la}$), which is changing for

different flow experiments, whereas V_∞ is multiplied by the annulus cross sectional area that is constant throughout the run for the same annulus and downcomer. Still this effect is considered to be small in comparison to the other energy terms involved in the theoretical model (e.g. kinetic and hydrostatic energies).

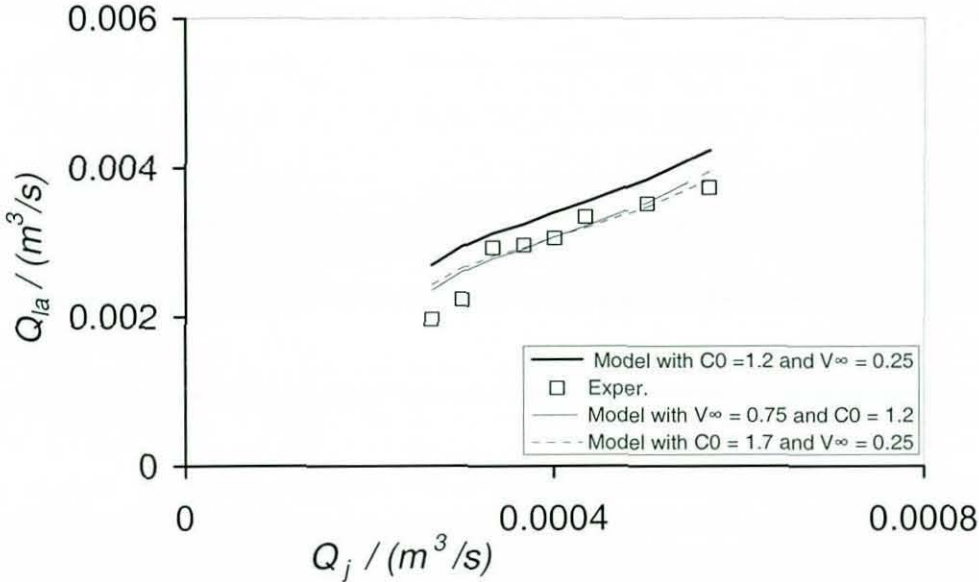


Figure 8.26 Effect of V_∞ and C_0 on the theoretical model.

8.1.5.1 Effect of frictional pressure gradient loss

This part of the section investigates the effect of the frictional pressure gradient on the theoretical model. This is done simply by removing the frictional pressure gradient $(dp/dl)_f$ term in the model, and keeping the rest of the terms in the model the same. Then, theoretical water flowrate in the annulus (Q_{la}) is recalculated. Figure 8.27 shows the results of Q_{la} for theoretical and experimental approaches, as the theoretical results comprise two lines solid line that accounts for $(dp/dl)_f$ effect and dotted line that does not account for $(dp/dl)_f$ effect. This figure shows that when the friction pressure gradient term is removed the model over predicts Q_{la} , however it is

not as significant as the other pressure terms in the energy model (kinetic and hydrostatic terms).

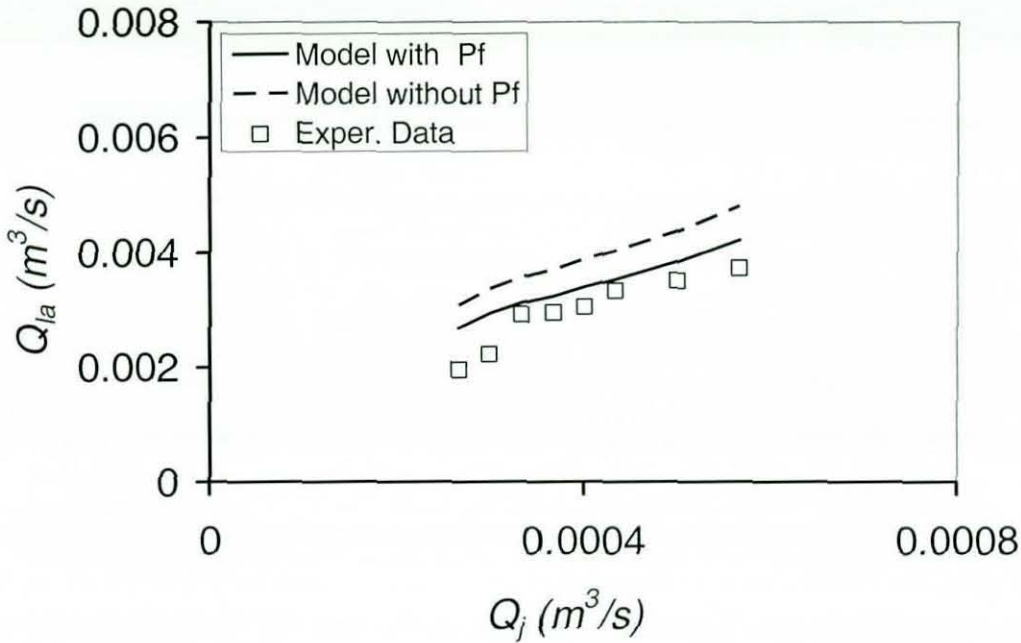


Figure 8.27 Effect of the frictional pressure gradient on the theoretical model ($d_n = 6\text{mm}$ and $D_a \approx 74\text{mm}$).

8.1.5.2 Using a constant to account for energy loss

So far, only the pressure drop in straight downcomer has been considered. There is another term of the pressure drop as the clear water is induced from the bottom of the base or the two-phase mixture leaves the bottom of the downcomer a change of direction from downward to upward occurs (energy due to fluid turn-around at the bottom of the reactor). A constant of 1.4 is used in front of the energy term to account for the pressure loss due to sudden change of direction. After that water flow rate in the annulus is recalculated for new values considering this effect.

8.1.5.3 *Accounting for kinetic energy loss in pressure gradient*

This type of pressure drop is due to a sudden expansion or sudden contraction. Since the cross sectional area in the present study decreases from the annulus diameter D_a to the difference between the annulus diameter and the downcomer diameter ($D_a - D_c$), it can be assumed as a sudden contraction. Hence, the following equations can be applied to account for the pressure drop due to a sudden contraction

$$P_f = h_f g \rho + \Delta P_c \quad (8.1)$$

Where

$$\Delta P_c = K \left(\frac{\overline{\rho V_{ta}^2}}{2} \right)$$

and

$$K_1 = 0.4 \left[1.25 - \left(\frac{D_a - D_{co}}{D_a} \right)^2 \right] \quad \text{when} \quad \frac{(D_a - D_{co})^2}{D_a^2} < 0.715$$

Figure 8.28 shows the effect of both losses, pressure drop due to a contraction and change of direction, on the predicted water flow rate in the annulus (Q_{ta}).

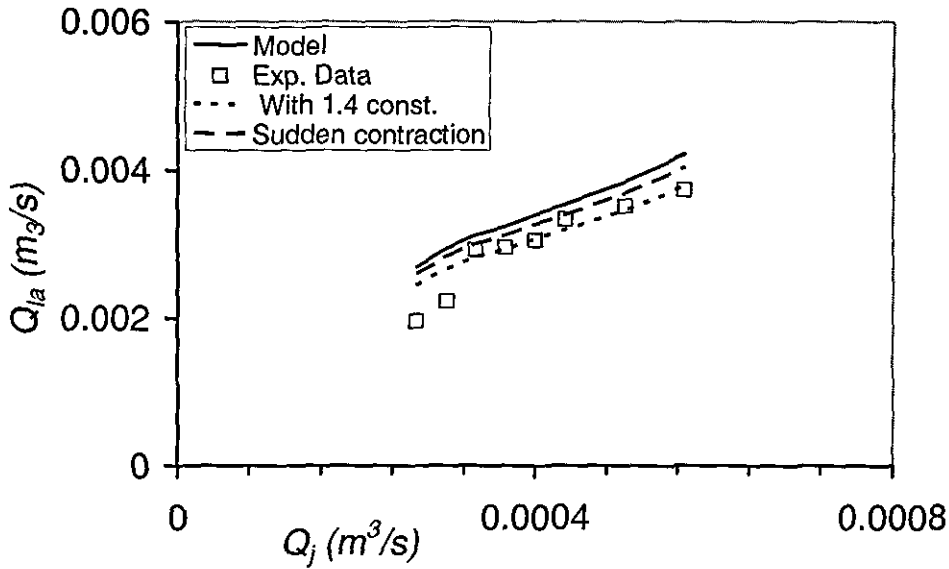


Figure 8.28 Effect of change of direction and sudden contraction on the theoretical model ($d_n = 6$ mm and $D_a = 74$ mm).

It is clear from the figure above that sudden contraction has less effect than that of the constant value, however both of these effects are not significant and can be neglected at this stage.

8.1.6 Phenomena

Since the concept of employing air-lift column in CPLJR is novel, some interesting phenomena were observed during the course of measuring water flow rate in the annulus. The observations can be divided into two-phase penetration depth and fountain from the top of the annulus.

8.1.6.1 Two-phase mixture penetration depth

Figure 8.29 represents a series of photographs for the bottom part of the annulus where, as expected, the penetration depth of the two-phase mixture flow

increases with the jet flow rate for 74 mm annulus. Penetration depth is controlled by the jet flow rate, bubble buoyancy and induced water flow rate (Q_{te}). Bubble distribution up the riser improves as penetration depth increases.

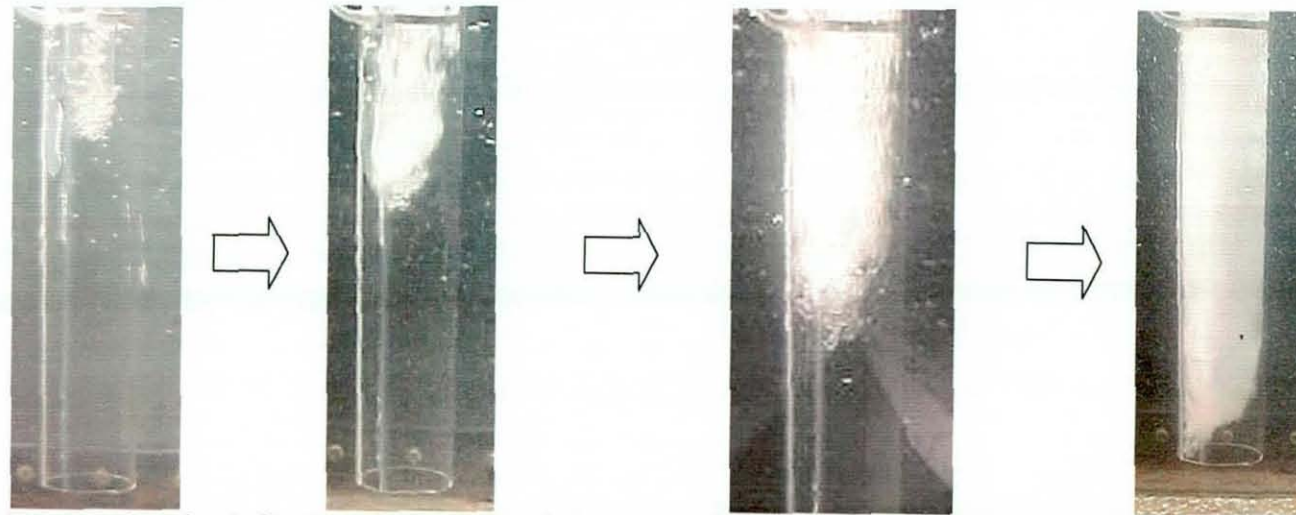


Figure 8.29 Penetration depth for two-phase mixture increases as the jet flow rate increases for a given conditions.

8.1.6.2 *Fountain*

As the voidage increases in the annulus the water flow rate (Q_{la}) also increases due to the increase of the hydrostatic pressure gradient difference between the surrounding water in the tank (voidage is zero) and the two-phase mixture inside the annulus (bubbly flow). As two-phase mixture leaves the annulus through the top, it shoots upward above the water level establishing fountain on top of the annulus. The fountain height depends on water flowrate out of the annulus, which depends on the voidage generated by jet velocity for a given condition. Figure 8.30 comprises series of impressions that show fountain behaviour as jet velocity increases for the same annulus. The energy from the two-phase mixture is dissipated elevating the water above the water level.

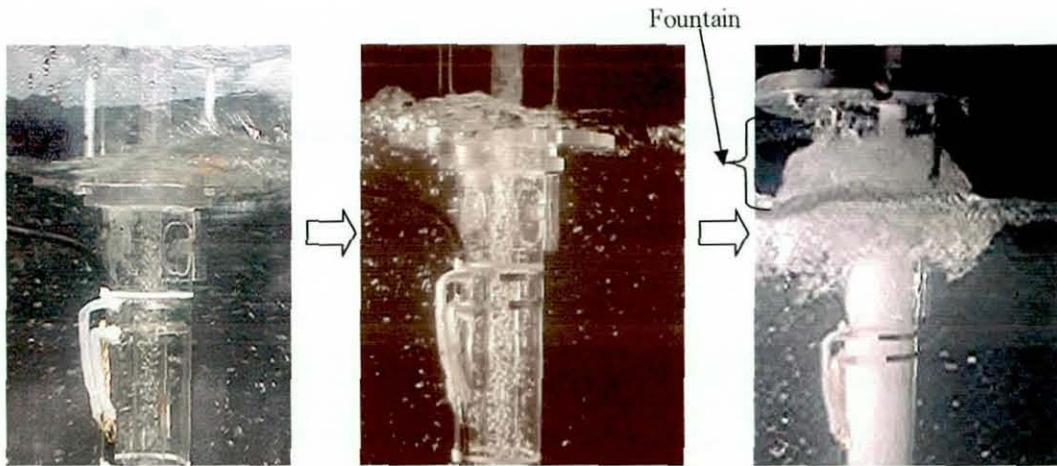


Figure 8.30 Fountain head increases as the jet velocity for a given condition increases.

8.2 Conclusions

A number of measurements have been reported on the effects of the nozzle diameter and annulus diameter on induced water flow rate up the riser in an air-lift column surrounding a confined plunging jet system. The use of an annular column surrounding a concentric tube (downcomer) in a confined system produces a large water flow rate induced from the bottom of the annulus. The water flow rate up the annulus (Q_{la}) varies depending on the nozzle and annulus diameters, for example the induced flow rate (Q_{le}) for an 8 mm nozzle and 94 mm annulus is between 4 to 13 times jet flow rate (Q_j) over a reasonable range of water flow rate up the riser (Q_{la}). Water flow rate (Q_{la}) increases with decreasing nozzle diameter, since this entrains more gas, which increases the hydrostatic pressure difference between the two-phase flow in the riser and the surrounding clear liquid, causing more fresh water to be entrained from the base of the annulus. Increasing annulus diameter increases the cross sectional area and hence increases water flow rate up the annulus (Q_{la}). The controlling variable for the induced water flow rate is air entrainment rate. Experimental data were compared against the theoretical model that predicts water flow rate (Q_{la}). Results show that the agreement between the model and the measured values improves with decreasing nozzle diameter, since this increases the penetration depth of the two-phase stream and entrains more gas, which gives a better voidage distribution. Current results also show that the model predicts the measurements obtained by smaller annuli better, which may be due to better voidage distribution. This model has limitations because it is developed for certain simplifying assumptions so it would be good to investigate this model to further improve it, which would require further experimental investigations. Finally the result shown here illustrate that annulus diameter (D_a) does not affect air entrainment rate for the same jet conditions.

Chapter 9: Mass Transfer

9.1 Introduction

This chapter investigates the mass transfer of a plunging liquid jet, issuing into an air-lift column surrounding a confined receiving pool, over a range of jet operating conditions and annulus diameters. Mass transfer performance of a plunging jet has been expressed in the literature as an overall mass transfer coefficient K_La and oxygen transfer efficiency OE . In the present work emphasis is on use of OE because the system is not well mixed and therefore it is not accurate to express mass transfer by K_La without a satisfactory model of the process. A plunging liquid jet reactor (confined and unconfined) is characterised by plug flow, where the concentration changes as gas liquid mixture flow downwards together. van de Sande and Smith (1975) divided the unconfined system into two volumes (Figure 9.1)

- (i) Bubble cloud volume that contains two sub-regions; a) at the top of the cone where the air is in close contact with a fresh surface of the surrounding liquid and b) inside the bubble cone where small bubbles are dispersed in an intense turbulent field. Extremely rapid mass transfer is likely to occur in this zone, so the water in the zone can be assumed to be nearly saturated.
- (ii) Volume of the rest of liquid in the tank where larger bubbles are escaping from the cone and ascending towards the pool surface.

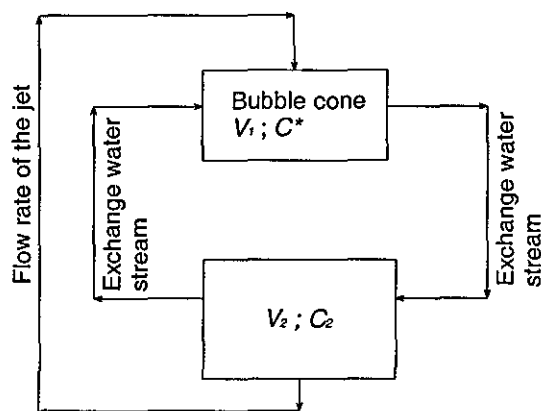


Figure 9.1 Proposed model for the flow rates in the pool liquid (van de Sande and Smith, 1975).

In a confined plunging liquid jet, the submerged region can be divided into two different zones as described by Evans and Machniewski (1999) and Evans *et al.* (2001) (Figure 9.2)

- (i) Mixing zone located underneath the impingement point, where entrained gas is broken into fine bubbles. Turbulence intensity in this region is high.
- (ii) Pipe flow, which is below the mixing zone. It is characterised with larger bubbles and the turbulence level is significantly lower.

Evans *et al.* (2001) concluded that using CO_2 as the entrained gas after the mixing zone, the liquid was more than 70% saturated with CO_2 gas suggesting that the pipe flow zone contribution is less important in the case of physical absorption. However, it is insufficient to treat the mixing zone as one, uniform, ideally mixed unit because they found some degree of backmixing in the pipe flow zone during concentration profiles measurement, which might have affected $K_L a$ values. Also, assuming the flow pattern in the contactor and the mixing model influences the driving force for the mass transfer and thus the volumetric mass transfer coefficient. Therefore, to avoid the uncertainty about the actual flow pattern and mixing of the phases in CPLJR, Evans *et al.* (2001) measured average volumetric mass transfer

coefficient in the absorber. This shows that it is inaccurate to assume that the liquid inside the tank is well mixed especially for confined systems due to downcomer presence that has a concentration change along its length and also separates the two-phase mixture from the rest of the tank.

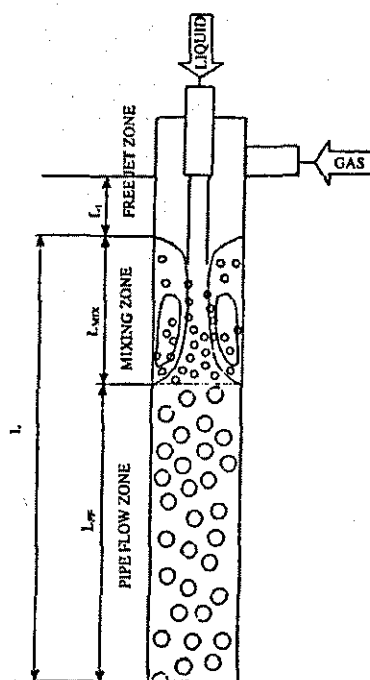


Figure 9.2 Schematic of the plunging liquid jet reactor used by Evans and Machniewski (1999) and Evans *et al.* (2001).

Low (2003) evaluated the overall liquid mass transfer coefficient $K_L a$ adopting the model shown Figure 9.3, which is an improved method of Moppett *et al.*'s (1996) model. Other authors calculated $K_L a$ for confined plunging liquid jet by assuming that the liquid phase in the main tank for closed systems is perfectly mixed with plug flow in the circulation line (Tojo and Miyanami, 1982; Maalej *et al.*, 1999). A number of papers model the downflow column as a stirred reactor (e.g. Fakeeha *et al.*, 1999 and Sotiriadis *et al.*, 2005), which is not a very realistic model of the flow behaviour.

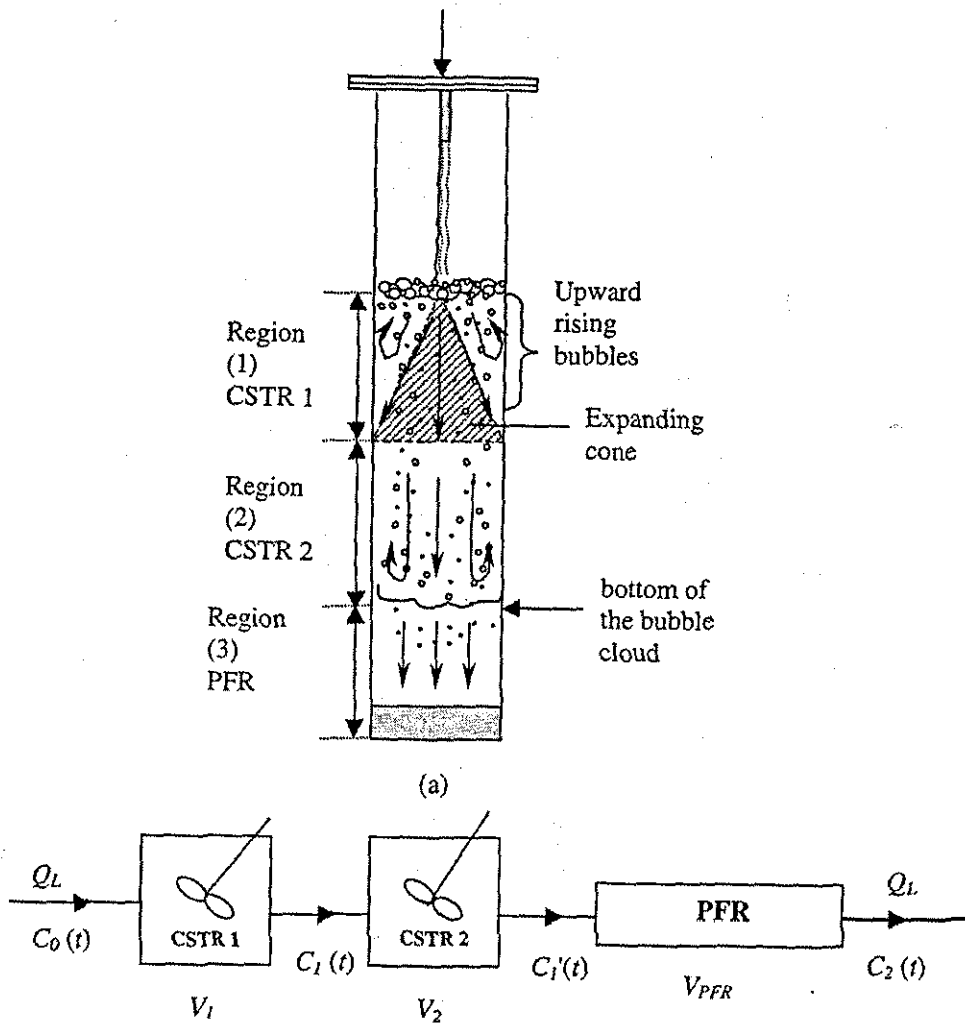


Figure 9.3 Schematic of the model proposed by Low (2003).

Figure 9.4 shows possible efficiency limits for OE that could be achieved by a typical plunging liquid jet reactor. It is generated from multiplying the jet flow rate by the saturation concentration of the oxygen which represents the maximum amount of O_2 that can be absorbed in a confined plunging jet system. This also shows why all plunging jet devices decline in performance with increasing jet power and increasing jet velocity.

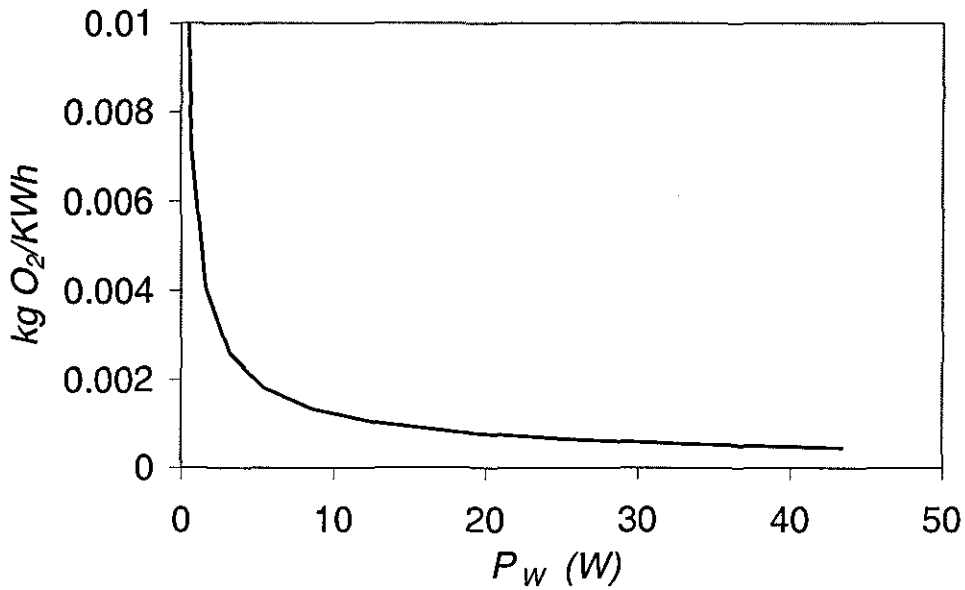


Figure 9.4 Limits of Overall Efficiency OE .

In the present study the case is more complex due to the novel technique represented by an annulus surrounding the confined system, which is an additional zone that must be considered when measuring mass transfer as K_{La} . Oxygen concentration is not only changing in downward direction inside the downcomer but also up the riser where fresh water has been induced. This would require a lot of additional measurements to understand mass transfer performance and the flow regimes inside the downcomer and the annulus need to be characterised as well as the use of a number of submerged oxygen probes located at key points in the rig to determine oxygen concentrations where flows change so as to determine the K_{La} values in different sections of the process.

The objective of this chapter is to assess the performance of the current apparatus from the practical and economical point of views. However, as indicated by Ohkawa *et al.* (1986b) and van de Sande and Smith (1975), there is no absolute criterion for comparing various contactors, and hence in order to provide some basis for comparison, oxygenation capacity (the oxygen uptake per kilo-watt hour) was used as a criterion.

From the above reasons it became clear that in order to get accurate mass transfer measurements and compare the present results with previous ones employing different techniques would be difficult, it is more meaningful to measure oxygen mass transfer as *OE*. *OE* is the overall efficiency of the device that measures the amount of dissolved oxygen per unit of the jet power ($\text{kg O}_2/\text{kWh}$) and from the economical point of view this parameter can be used as an operating costs indicator of the oxygenation devices.

9.1.1 Oxygenation efficiency (*OE*)

Here, mass transfer was measured by employing a new device represented by an air-lift column surrounding a confined plunging jet downcomer. There is no available literature concerning mass transfer for an air-lift column combined with CPLJR. However, there is a body of literature that describes oxygen efficiency achieved by plunging liquid jet reactors as unconfined and confined devices. As discussed in the literature by van de Sande and Smith (1975) and Bin (1977) oxygen mass transfer can occur in plunging liquid jet reactors in three different regions

- (i) From the headspace to the liquid jet as it plunges through the surrounding air.
- (ii) From the headspace to the receiving liquid pool especially at the impingement point or as the liquid pool surface gets rougher.
- (iii) From the bubbles cloud as they travel downward.

A new region that contributes to the mass transfer when using air lift column is

- (iv) From the bubbles flowing upward inside the riser.

van de Sande and Smith (1975) and Bin (1977 and 1993) showed that the mass transfer caused by the first two regions is negligible because the surface area of the jet

and the pool is small relative to that of the bubble swarm, and hence the mass transfer is mainly due to the bubbles. It is favourable to have high OE values by dissolving as much oxygen as possible for the lowest energy input. However, this is not as simple as it sounds because there are limiting factors associated with each device or aeration process.

Below is a brief review of some of the previous work that has been conducted by various authors to measure OE utilizing unconfined and confined jet reactors,

9.1.2 Unconfined Systems

Sneath (1978) investigated the treatment of slurry utilizing a plunging jet passing through a 178 mm diameter shroud. He used large nozzles ranging from 38 mm to 68 mm and jet length of 1.5 m to measure oxygenation efficiency OE . Oxygenation efficiency up to 4 kg O_2 /kWh was recorded. He also proposed a correlation of OE as a function of jet power P_w :

$$OE = 1.48P_w^{-0.533}$$

van de Donk (1981) studied the oxygenation efficiency OE for small and large diameters utilizing unconfined system. He showed that OE decreases with jet velocity and diameter, whereas jet length has little effect on OE for both small and large diameter jets. He proposed an empirical correlation for large diameter conical nozzles $30 < d_n < 100$ mm (for air-water system):

$$OE = 1.1V_j^{-0.6}d_n^{-0.4}$$

Yamagiwa *et al.* (1991) also showed a decreasing performance for OE with increasing jet velocity using a plunging jet bioreactor for low jet velocities (1 – 5 m/s) as a continuous biological treatment. OE values they obtained ranged from 2.0 to 4.6 kg O_2 /kWh.

9.1.3 Confined Systems

Oxygenation efficiency OE was also measured by Ohkawa *et al.* (1986b) using an inclined short nozzles. They used conical nozzles with different lengths with inside diameters of 0.008 – 0.020 m, jet length ranged from 0.03 to 0.15 m and three jet inclination angles of 30°, 45° and 60°. From OE vs. V_j plot, the measured OE lies between 0.7 to 6.0 kgO₂/kWh. Results revealed that this system gives higher oxygenation efficiency at low jet velocities than that of conventional devices.

Low (2003) used confined system to measure OE for air-water system with nozzle diameter ranged from 0.006 to 0.015 m and jet power P_w from about 1.25 to 17 W. L_j/d_n value used in his thesis was equal to 15. The OE found, falls within the range of 0.5 to as high as 4 kgO₂/kWh. His results revealed that OE decreases with jet power (W), whereas OE was independent of L_j/d_n over the range investigated. An empirical correlation for OE in terms of P_w and d_n , for the above experimental conditions and a confined column D_c of 0.10 m, was found:

$$OE = 273.2P_w^{-0.406} d_n^{0.927}$$

From literature (van De Sande and Smith, 1975; Ohkawa *et al.*, 1986b) OE for various conventional aerators fall between 1.0 and 3.0 kg O₂/kWh. A summary of oxygenation efficiency values in kg O₂/kWh for conventional surface aerators including plunging liquid jet systems is provided in Table 9.1 (Horan, 1990; Low, 2003; Takahara, 1990; Backhurst *et al.*, 1988; Yamagiwa *et al.*, 1991). It can be seen from this table apart from the deep shaft device (with a very long contact time) and the devices using pure oxygen the typical best performance achieved by the different reactors is ≈ 2 kg O₂ /kwh. The high efficiencies quoted for plunging jet devices is for jets operating at low power input which will actually put quite low actual mass of oxygen into the water.

Table 9.1 Oxygenation efficiency values of various aerators

<i>Aerator Type</i>		<i>OE (kg O₂/kWh)</i>
Diffused Air ^a	Fine bubble	1.2 – 2.0
	Coarse bubble	0.6 – 1.2
	Submerged jet	1.2 – 2.4
	Deep shaft ^c	3.0 – 6.0
	Static mixer ^d	1.22 – 1.83
Pure Oxygen ^a	UNOX	2.4 – 3.8
	VITOX	2.8 – 4.2
Mechanical ^a	Simcar surface aerator	2.1 – 2.4
	Turbine aerator	2.1 – 3.2
	Simple cone	2.0 – 2.6
Oxidation brushes ^a	Kessener brush	2.4 – 3.2
	Cage rotor	1.4 – 3.0
Plunging jet (air – water) ^b	Unconfined systems	0.7 – 8.0
	Confined systems	0.3 – 2.5
	Bioreactor ^e	2.0 – 4.6

^aHoran (1990).

^bLow (2003).

^cTakahar (1980).

^dBackhurst *et al.* (1988).

^eYamagiwa *et al.* (1991)

9.2 Experimental Work

9.2.1 Apparatus

The rig used to measure oxygen absorption (mass transfer rig) is shown in Figure 9.5. It comprises the same equipment that was used to measure air entrainment rate and induced water flow rate up the riser. A Clark-type polar-graphic oxygen probe, that senses oxygen in water and other aqueous solutions, is immersed inside the riser at its top part to measure oxygen concentration in the liquid leaving the top of the riser. The oxygen probe is connected to a chart recorder through a WPA-0T4 oxygen meter. The measured oxygen concentration is displayed on a chart recorder. The top part of the tank is sealed with a thick plastic sheet to prevent any air from entering the

system during oxygen removal by supplying nitrogen to the jet head space. Nitrogen is supplied to the headspace from a compressed cylinder through a 4 mm diameter nitrogen tapping. Ambient air is supplied to the system through an air tapping (12.5 mm in diameter). Two risers 94 and 144 mm diameter, two nozzles 8 and 12 mm diameter and a downcomer of 23 mm diameter were used when making the absorption measurements. Riser and downcomer lengths are 1350 mm. The submerged part of the downcomer is 950 mm (H_{ds}). An extra rotameter that reads a maximum of 100 l/min is fitted in the nitrogen supply line to measure the nitrogen flow rate. Tap water is used as liquid and air as the oxygen source.

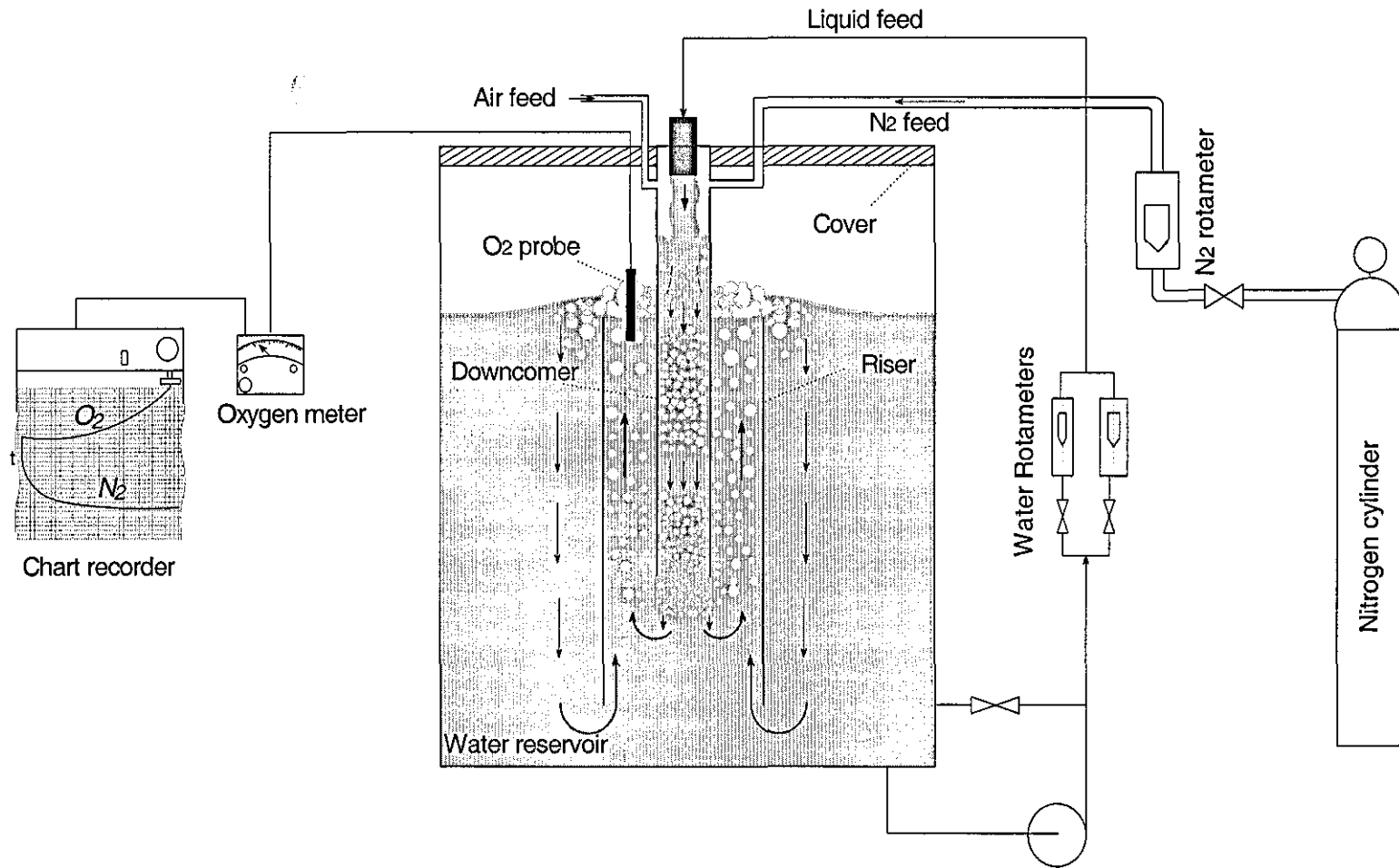


Figure 9.5 Schematic of air-lift column apparatus combined with confined jet to measure *OE*.

9.3 Theory

Nitrogen is fed to the system until almost all of the oxygen is removed (Figure 9.6), and then nitrogen supply is cut off at same time air is introduced. Air is supplied only from the air tapping so that the previous air entrainment and thus induced water measurements can be used to calculate oxygenation efficiency. This continues until the chart displays 100% oxygen concentration (Figure 9.7).

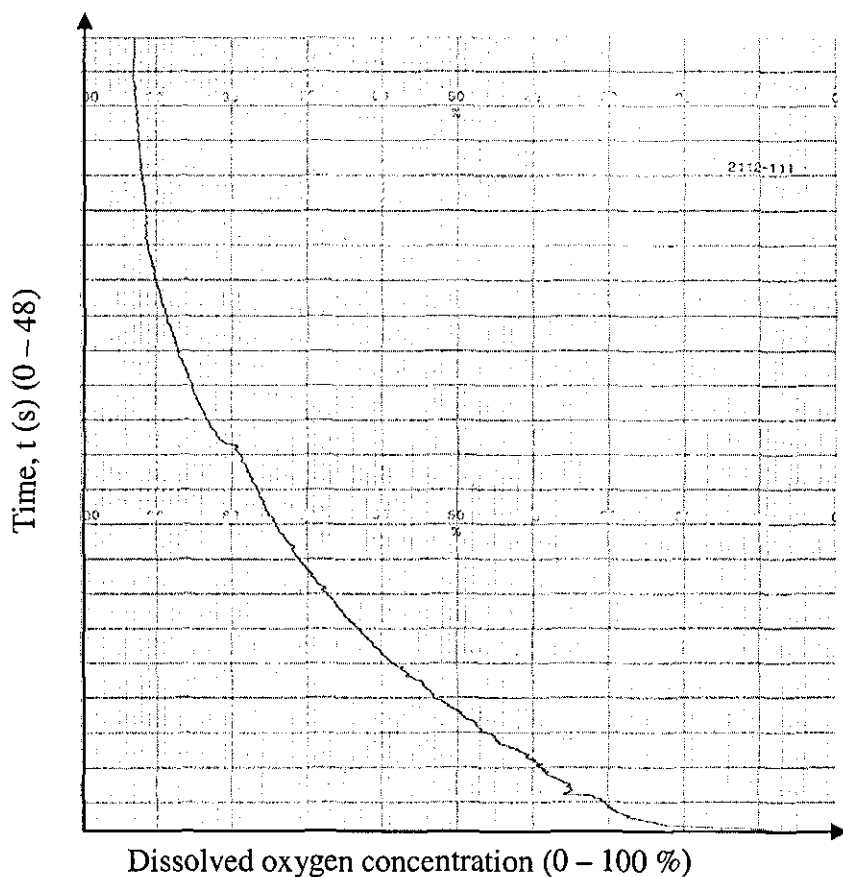


Figure 9.6 Oxygen removal by introducing nitrogen.

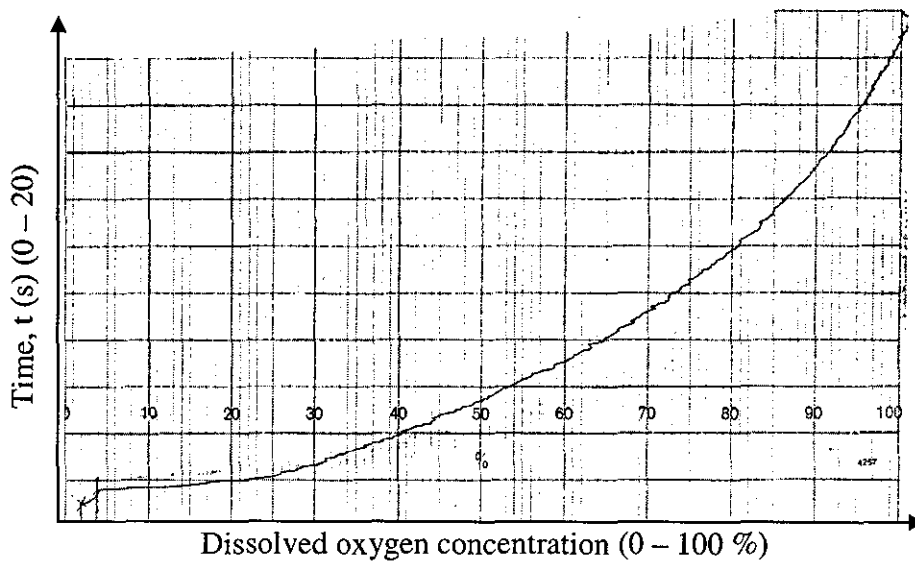


Figure 9.7 An example of aeration carried out in the current work

The oxygen probe has a time delay between a change in the oxygen content of the water and the measured value. This means that the concentration measured by the oxygen probe does not give the true oxygen content of the liquid at the top of the riser. The effect of this is shown in Figure 9.8 an idealized graph showing the discrepancy between the actual and the measured oxygen concentration. When the air supply is turned on there will be delay whilst the oxygenated liquid travels down the downcomer and back up the riser. The oxygen content should then remain at a constant value until the freshly oxygenated water travels down to the base of the tank and enters the riser again (as shown in Figure 9.5). After that the oxygen content of the liquid at the top of the riser should steadily increase. A method has therefore been developed to estimate the time dependency of the oxygen content of the liquid in the tank. The probe response can be fitted by a first order differential equation (9.1), which is used to describe the probe behaviour.

$$C_f - C_p = \tau \frac{dC_p}{dt} \quad (9.1)$$

where,

τ = probe time constant

C_f = actual concentration at the probe

C_p = measured concentration

After integration and applying the following boundary conditions,

at $t = 0$, $C_p = 0$

at $t = t$, $C_p = C$

the general solution for the above differential equation response to a step input yields

$$\frac{C}{C_f} = 1 - e^{\left(\frac{-t}{\tau}\right)} \quad (9.2)$$

where C/C_f is a fractional response.

The probe time constant (τ) is calculated experimentally by analysing the probe response to a step change in oxygen concentration (Figure 9.11), this is achieved by immersing the probe in sodium sulphite solution until all of the oxygen is removed and then exposing it to the ambient air to give a change in the oxygen concentration.

$$\frac{C}{C_f} = \frac{\text{Chart reading at time } t - \text{Initial chart reading}}{\text{Final chart reading} - \text{Initial chart reading}} = \frac{R(t) - R(0)}{R(\infty) - R(0)} \quad (9.3)$$

From equation (9.3) when the time t equals the time constant τ , the value of C/C_f is equal to 0.632, using this the value of τ can be estimated.

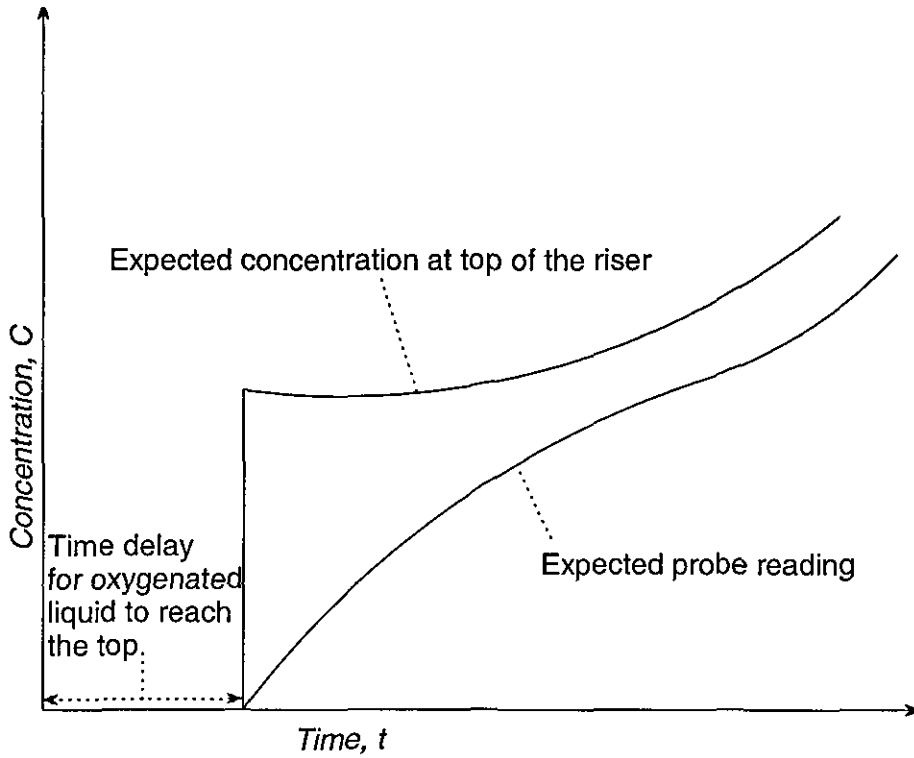


Figure 9.8 Idealized performance of plunging jet reactor.

Actual dissolved oxygen concentration at the probe C_f can be estimated by equation below,

$$C_f = C_p + \tau \frac{dC_p}{dt}$$

The measured concentration gradient dC_p/dt is approximated by a Taylor expansion series as follows,

$$C_p(t + \Delta t) = C_p + \frac{\Delta t}{1!} \frac{dC_p}{dt} + \frac{\Delta t^2}{2!} \frac{d^2 C_p}{dt^2} \quad (9.4)$$

$$C_p(t - \Delta t) = C_p - \frac{\Delta t}{1!} \frac{dC_p}{dt} + \frac{\Delta t^2}{2!} \frac{d^2 C_p}{dt^2} \quad (9.5)$$

Subtracting the above two equations, yields

$$\frac{dC_p}{dt} = \frac{C_p(t + \Delta t) - C_p(t - \Delta t)}{2\Delta t} \quad (9.6)$$

When the oxygen content for the liquid reaching the top of the riser has been determined it is used to calculate the Oxygen Efficiency (*OE*) as shown below,

$$\text{Chart Scale or Overall } O_2 = R(\infty) - R(0)$$

where $R(0)$ is read directly from the chart when air is introduced (Figure 9.9). Oxygen concentration is calculated below,

$$O_2 \text{ Conc.} = O_{2 \max} \times \frac{R(t) - R(0)}{R(\infty) - R(0)}$$

where $O_{2 \max}$ is the maximum amount of oxygen that water can hold at 20° C and it has a value of 9.09 ppm (www.lagoonsoline.com/aerationmain.htm, 2002)

$$\text{Oxygen Uptake} = Q_{la} \times O_2 \text{ Conc. (kg/hr)}$$

$$P_w = Q_j \Delta P$$

where P_w is the power consumed by the jet and ΔP is the pressure drop across the nozzle. P_w is equal to the kinetic energy of the jet at the point of the discharge ignoring other energy terms of energies (e.g. the potential energy due to difference in level between the nozzle and the pool surface and all friction losses in the circulating loop), and hence

$$\Delta P = \frac{\rho_l V_j^2}{2}$$

Solving power in terms of jet flow rate, gives

$$P_w = \frac{8\rho_l Q_j^3}{\pi^2 d_n^4}$$

Finally, oxygenation efficiency is calculated below,

$$OE \text{ (Oxygen Efficiency)} = \frac{\text{Oxygen Uptake}}{P_w} \quad (9.7)$$

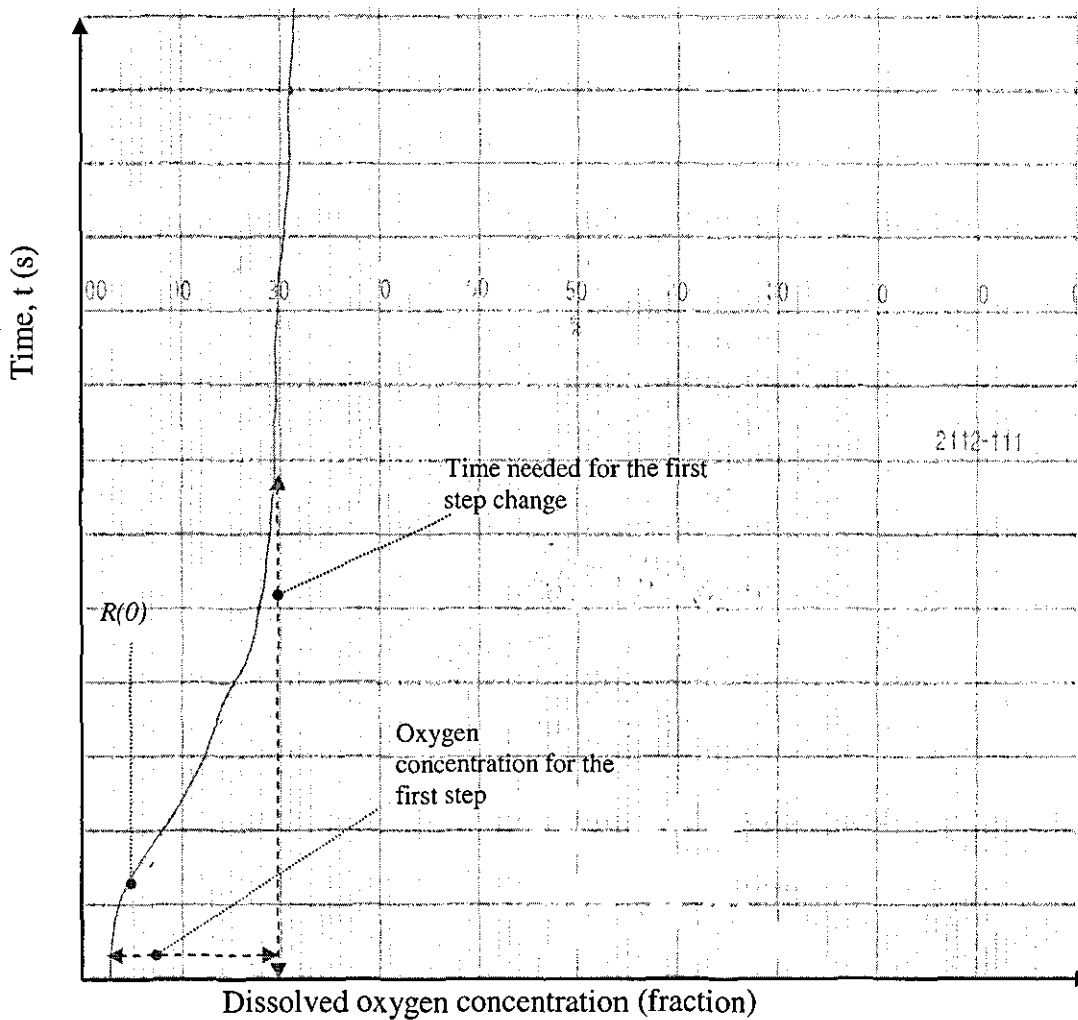


Figure 9.9 First step response of the concentration generated experimentally.

Figure 9.10 is an example of the estimated oxygen content of the water utilising the oxygen probe measurement.

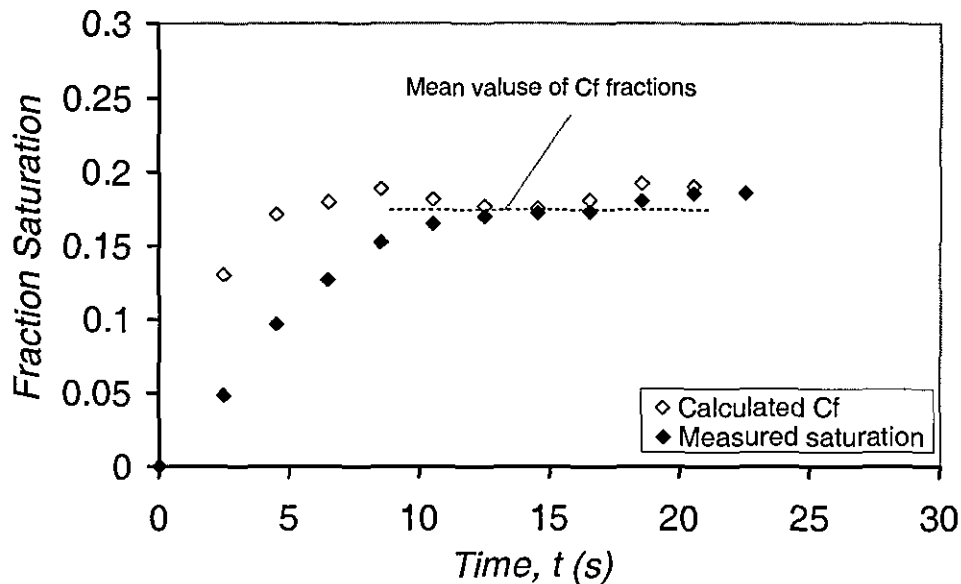


Figure 9.10 Adjusted oxygen reading.

9.4 Results and Discussions

9.4.1 Evaluating time constant and oxygen efficiency

Figure 9.11 depicts the probe response generated by the probe before conducting a run. Time constant τ needed to evaluate the probe response is obtained from Figure 9.12 adapting the methodology described earlier. After carrying out the calculations obtained from the measured data (see appendix III for more details) a time constant of 3.8 was found and was then used to estimate the time dependency of the oxygen content of the water in the current study.

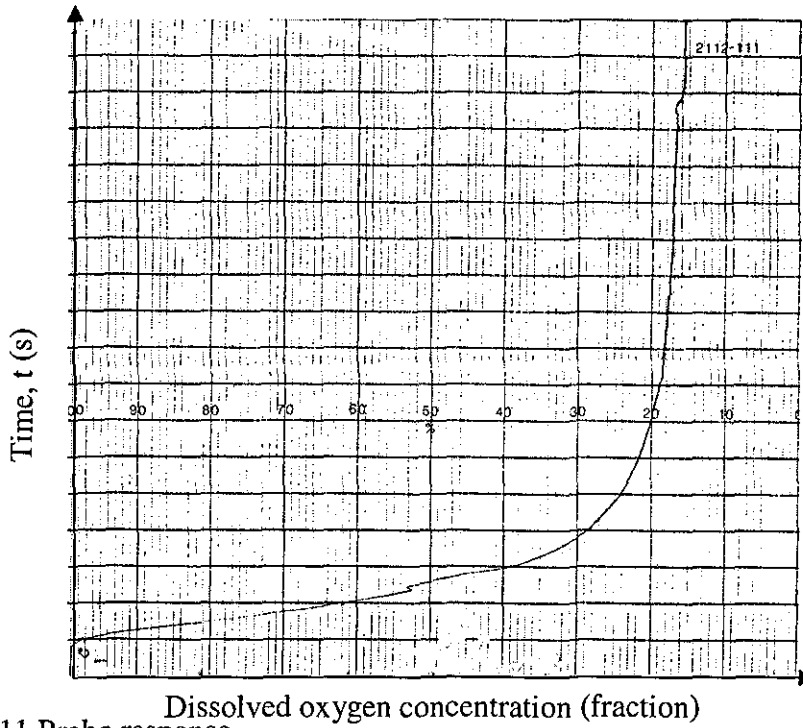


Figure 9.11 Probe response.

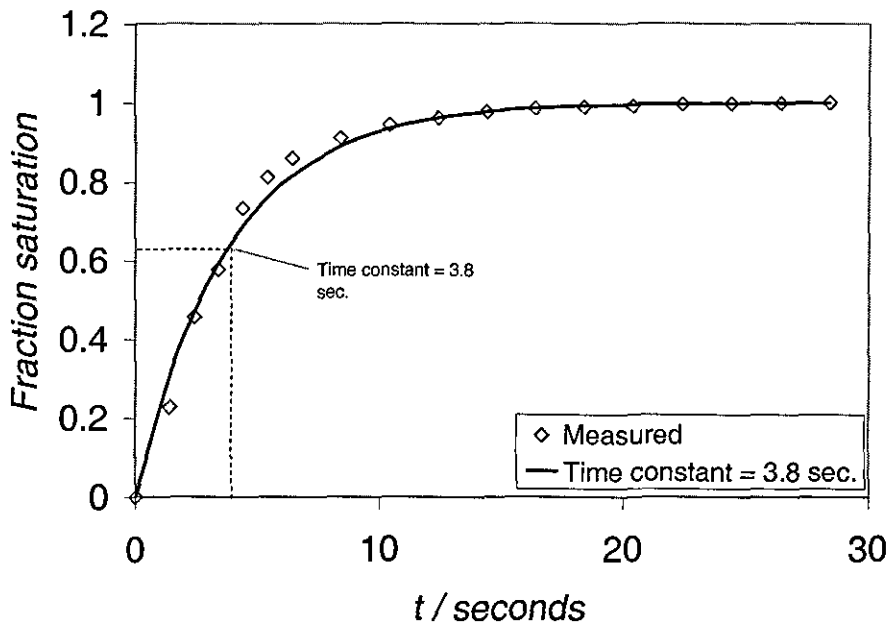


Figure 9.12 Probe response for measured and theoretical data.

It is clear from Figure 9.12 that the agreement between the measured and fitted approach is very good. This means that the time constant used is a good estimate and can be used to calculate dissolved oxygen concentration and thus oxygenation efficiency for all of the runs.

Several mass transfer experiments were carried out utilizing two riser diameters, two nozzle diameters and one downcomer diameter. For each run a chart is generated for a given condition. Figure 9.13 shows an example of one of the charts during oxygenation of the system. From this chart oxygen concentration is determined to measure the oxygen efficiency in kgO_2/kWh as described in theory section (see appendix III). Effect of the system variables are discussed in the following sections. Oxygenation efficiency results for 94 and 144 mm annuluses utilizing 8 and 12 mm nozzle diameters are summarized in Table 9.2. It is obvious from Table 9.2 that the last point, measured by 12 mm nozzle and 144 mm, does not agree with the rest. This attributed to the difficulties of measuring the water flow up the riser (Q_{la}) at very high induced flowrate (Q_{le}) as discussed previously in chapter 8.

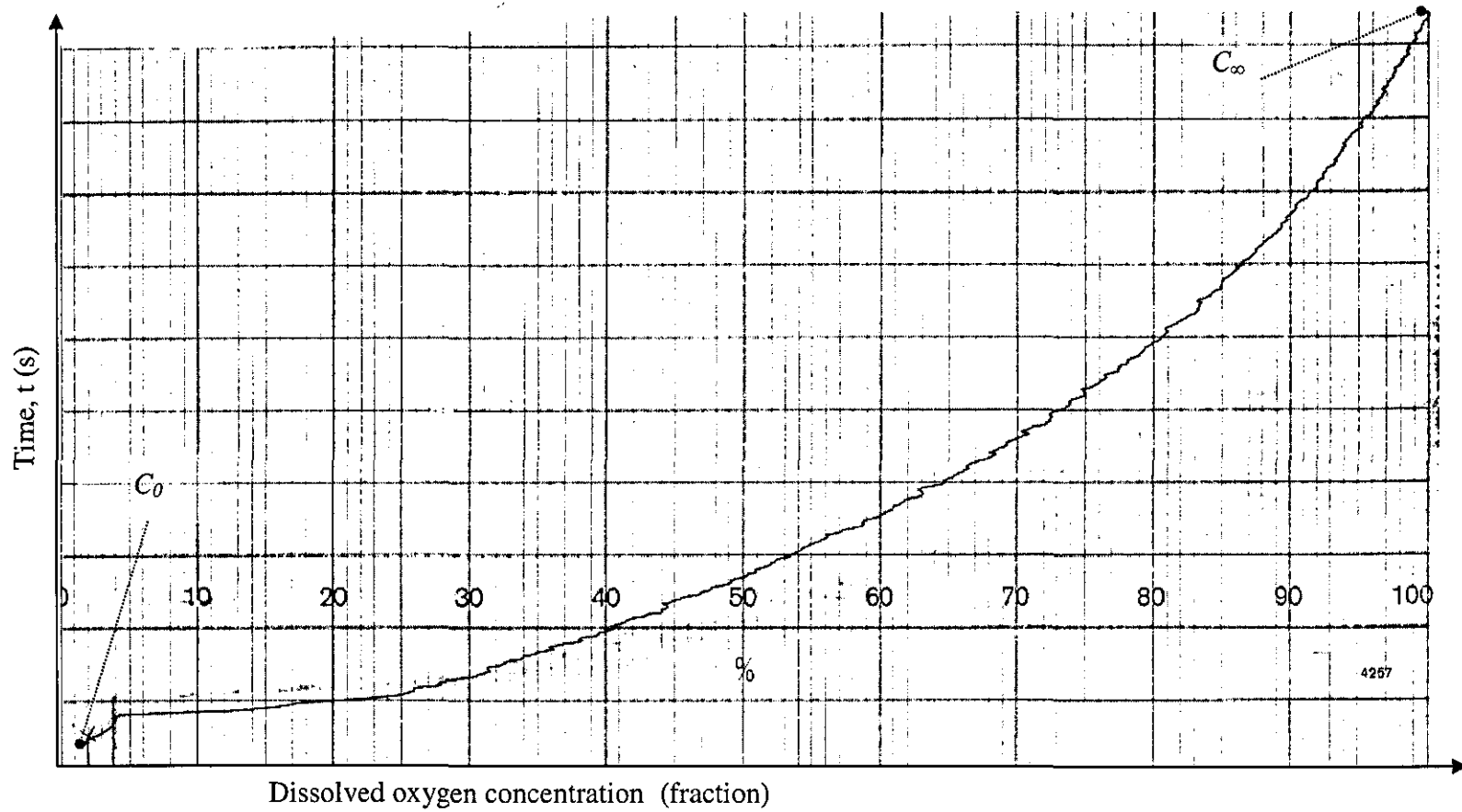


Figure 9.13 Dissolved oxygen concentrations measured in the current work.

Table 9.2 Oxygenation efficiency results utilizing air-lift column in CPLJR

d_n (mm)	Q_{la} (m ³ /s)	Oxygen Uptake, OE (kgO ₂ /kWhr)	D_a (mm)
8	0.0004	2.275606	94
	0.0006	1.111074	94
	0.0008	0.822697	94
	0.0004	3.21627	144
	0.0006	1.235346	144
	0.0008	1.010461	144
12	0.0005	3.650749	94
	0.000667	2.01658	94
	0.000767	1.742328	94
	0.001	1.308339	94
	0.0005	6.24199	144
	0.000667	3.046629	144
	0.000767	2.273038	144
0.001	2.411081	144	

9.4.2 Nozzle effect on mass transfer

Results plotted in Figure 9.14 and Figure 9.15 show that oxygen efficiency (OE) decreases as jet flow rate increases, however it increases with nozzle diameter. This is attributed to the fact that more power is consumed, proportional to the square of a jet velocity, which reduces OE despite higher oxygen concentration levels obtained. Thus it is not economically feasible to work at very high flow rates. Similar decreasing behaviour was observed by previous authors, except van de Donk (1981) who showed an opposite effect of nozzle diameter on OE (OE decreases with larger nozzles).

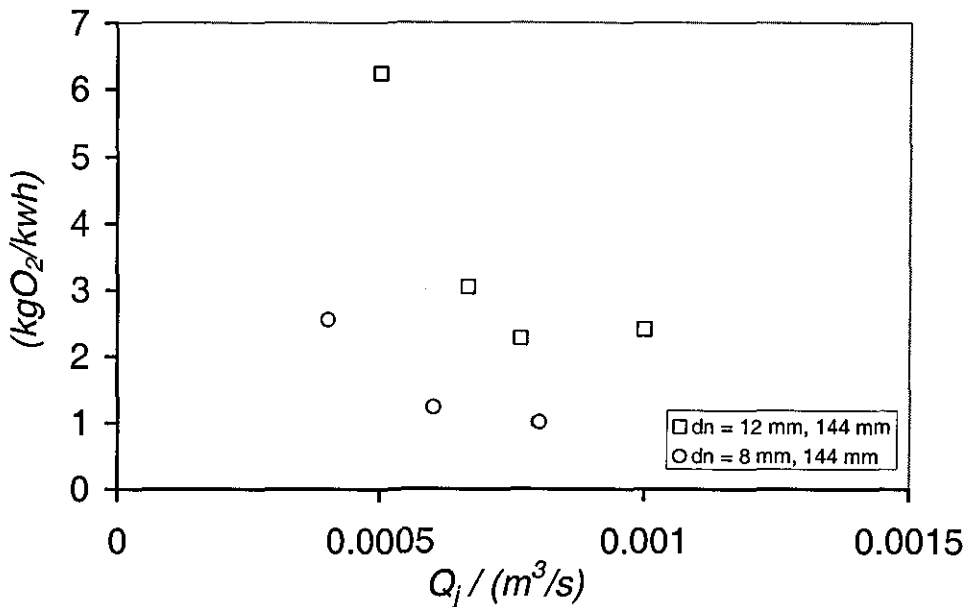


Figure 9.14 Oxygenation efficiency measured by different nozzles and larger riser

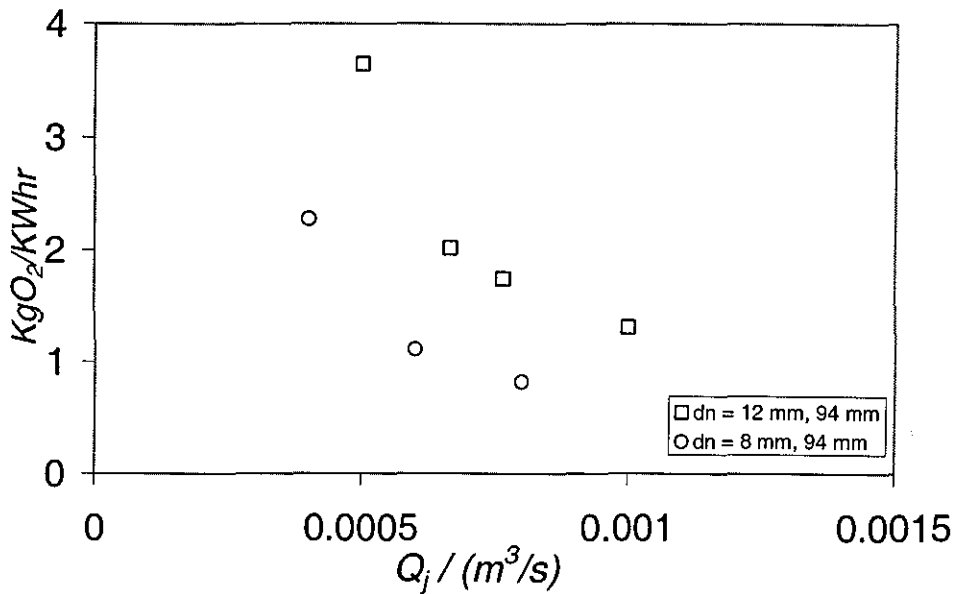


Figure 9.15 Oxygenation efficiency measured by different nozzles and smaller riser.

9.4.3 Riser effect on mass transfer

For similar conditions (same nozzle diameter and water flowrates) a larger riser enhances OE as shown in Figure 9.16 and Figure 9.17 by inducing higher flowrates up the riser. Larger risers could enhance mass transfer in two ways a) hindering bubble coalescence by providing a larger volume for the bubbles to spread out, and b) decreasing liquid superficial velocity up the annulus, which increases residence time between the bubble and liquid. All of the above factors enhance oxygen mass transfer by diluting the saturated stream leaving the base of the downcomer, and hence restoring oxygen concentration gradient.

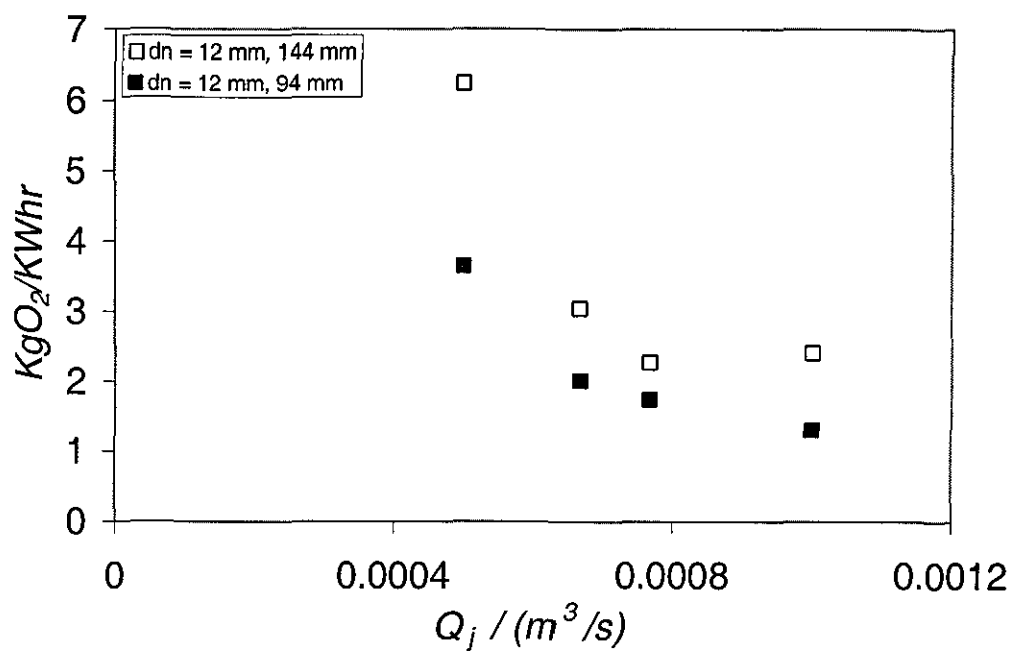


Figure 9.16 Effect of riser diameter on OE for larger nozzle.

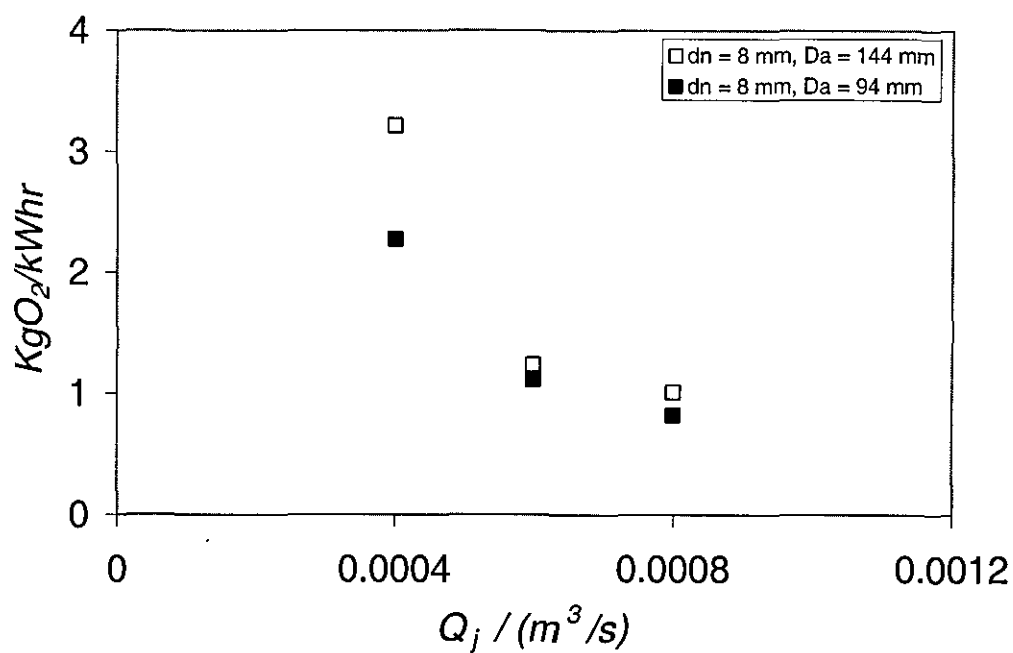


Figure 9.17 Effect of riser diameter on OE for smaller nozzle.

9.4.4 Comparison of oxygenation efficiency (OE) with literature

Figure 9.18 depicts OE behaviour with P_w for both of the results measured by Low (2003) using a confined system and those obtained in the current study. It is clear that OE values measured by the air-lift column device are higher than those measured by simple confined system at low and high power inputs. For example at 11.6 W the oxygenation efficiency (OE) values measured by Low (2003) is equal to 1.29 and 1.74 kg O_2 /kWh, whilst for the same dissipated energy and nozzle diameter the values measured in the current work are almost double (2.617 kg O_2 /kWh for 94 mm riser and 3.05 kg O_2 /kWh for 144 riser).

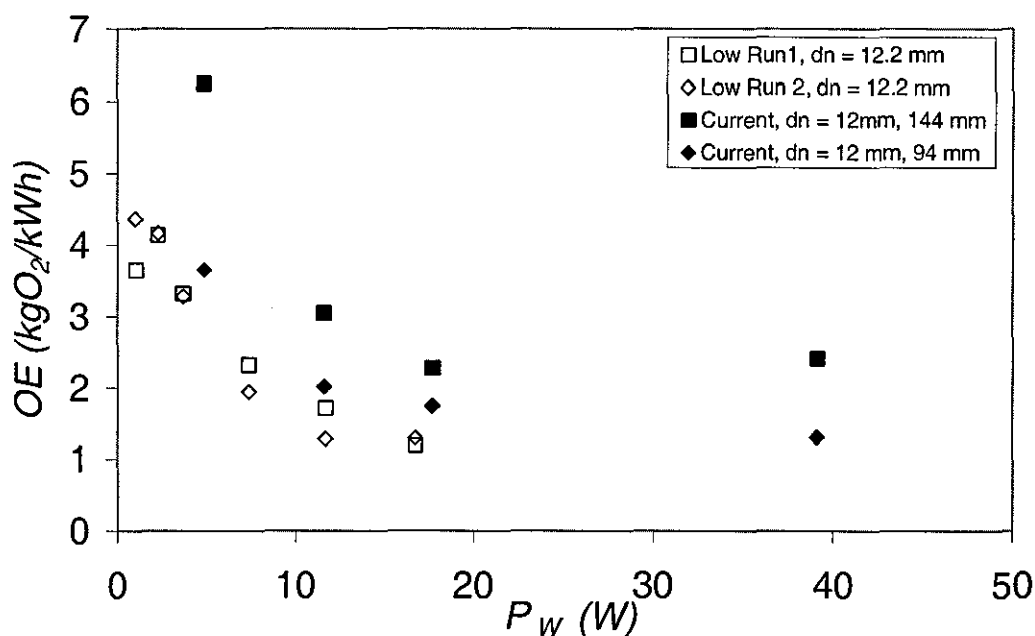


Figure 9.18 OE results measured by Low (2003) and current work for 12 mm nozzle.

The current results are also compared against those measured by unconfined system employed by van De Sande and Smith (1975) and van De donk (1981). Both authors measured OE at low jet velocity where high values of OE are expected.

Oxygenation efficiency values obtained by both authors and current work are shown in Figure 9.19 – Figure 9.21. The comparison, consistently, revealed that air-lift column device provides higher *OE* than various unconfined systems for wide range of jet velocity.

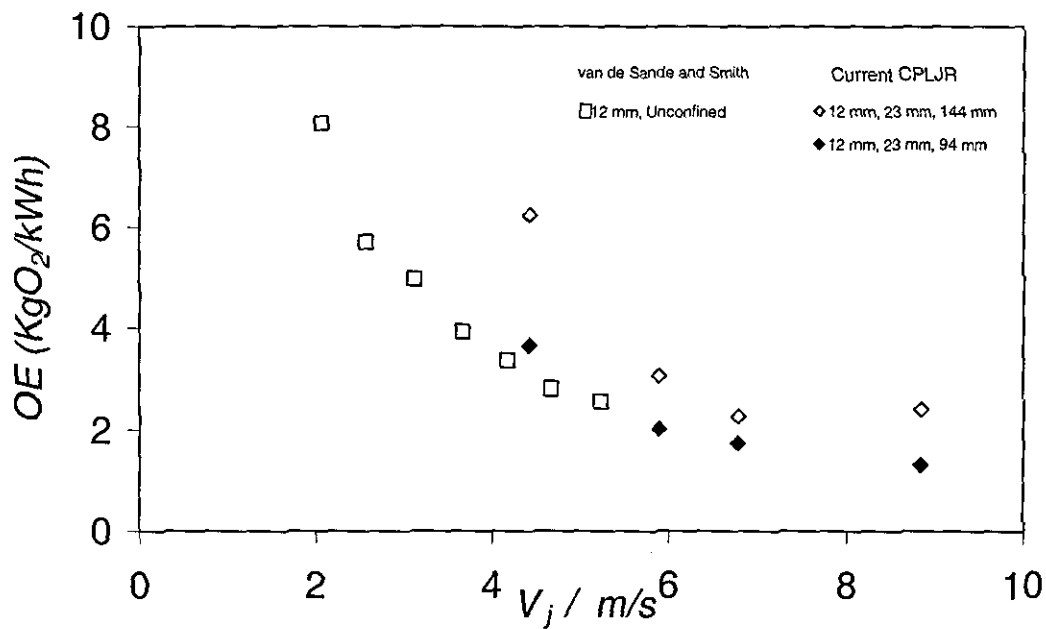


Figure 9.19 *OE* results measured by van de Sande (1975) and current work for 12 mm nozzle.

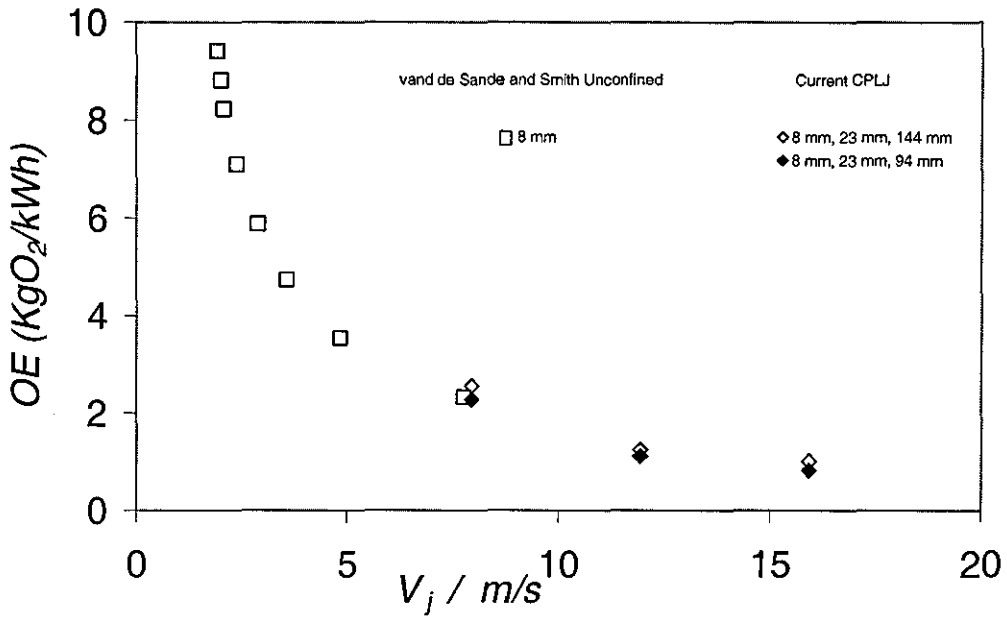


Figure 9.20 OE results measured by van de Sande (1975) and current work for 8 mm nozzle.

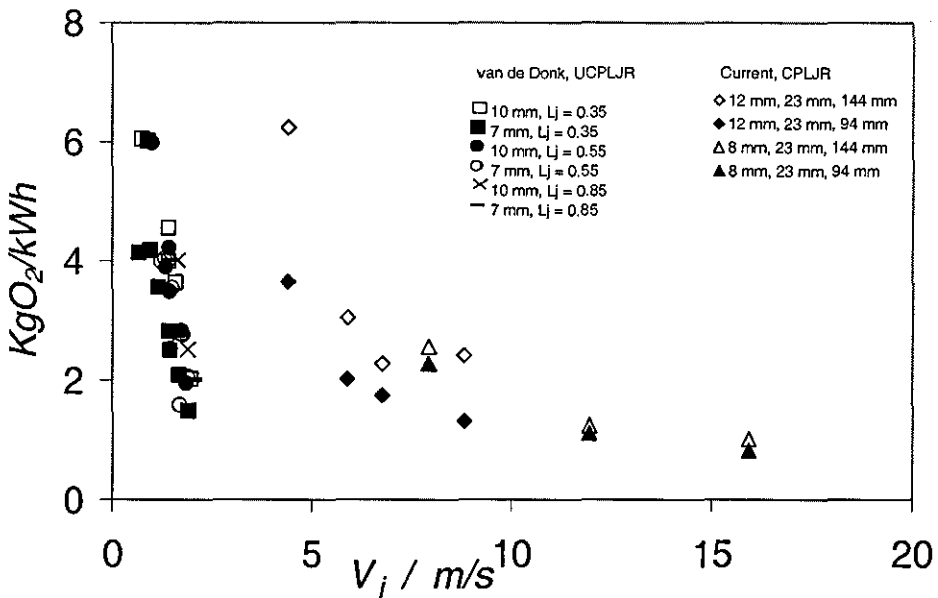


Figure 9.21 OE results measured by van de Donk (1981) and current work for different nozzles.

9.4.5 Correlation

The current data represent the results of experimental runs measuring mass transfer as oxygenation efficiency utilising an air-lift column with confined plunging liquid jet reactor described in previous chapters. Oxygen mass transfer was measured employing different nozzles and risers. To quantify the effect of the main variables (V_j , d_n and D_a) on the measured mass transfer, a correlation that relates oxygen efficiency to the main variables was sought. Data regression was carried out using STATISTICA software, which gives

$$OE = 2.57 P_W^{-0.058} d_n^{-1.1} D_a^{0.8} V_j^{-1.64} \quad (9.8)$$

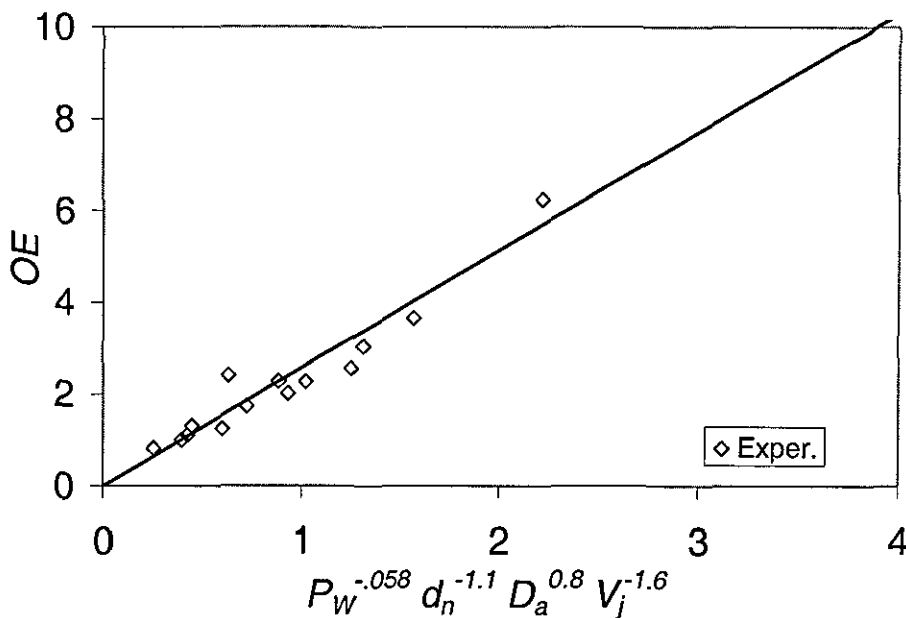


Figure 9.22 Correlation for the present work.

A comparison between the regressed correlation, equation (9.8) and the experimental measurements is given in Figure 9.22, which shows a satisfactory agreement

9.5 Conclusions

Oxygenation efficiency OE values in $\text{kg O}_2/\text{kWh}$ were measured in the present work for air-water system employing air-lift column in CPLJR. OE depends on jet kinetic energy and nozzle diameter. High OE were collected at low jet velocity and hence power input. Similar behaviour was reported by previous authors utilizing various PLJR (i.e. confined and unconfined systems). However, the values obtained in the current work exceeded those of other PLJR system. This is mainly due to the usage of new air-lift column in CPLJR, which induced fresh water up the annulus. This diluted the two-phase flow mixture leaving the base of the downcomer restoring oxygen gradient, and thus restoring driving force. Subsequently, more oxygen is transferred to the surrounding liquid. The device also recycles liquid within the tank very efficiently as liquid is continuously pulled into the base of the tube and discharged at its top. Possible development of the device is to recycle the oxygen entrained by the plunging jet giving us a much higher driving force and hence OE could be improved by a factor of 4.

Figures 9.19 – 9.21 show that there is a low limit for the jet velocities due to two reasons a) it was difficult to measure low jet velocities for large annulus, 144 mm, accurately due to the dilution of the salt tracer up the riser and b) for smaller annulus, 94 mm, the system collapsed at low jet velocity (water level inside the downcomer rose up to the nozzle exit). This can be avoided by increasing the jet length for a given conditions.

Chapter 10: Conclusions and Recommendations

10.1 Conclusions

The new designed equipment (used to make the measurements) has performed efficiently and consistently and provided good experimental results. This design enabled the researcher to use a wide range of downcomer lengths and diameters, nozzle diameters and annulus diameters in relatively short time. Results show that air entrainment rate increases as the main parameters increase (V_j , L_j , d_n and D_c). A number of measurements have been reported on the effects of the jet velocity, jet length, nozzle diameter and downcomer diameter on the volumetric rate of gas entrainment (Q_g) in a confined plunging jet system. Clearly the use of a confining column allows much greater bubble penetration depths to be achieved. The entrainment rate increases with increasing jet velocity (or jet Reynolds number), since this produces rougher jets, which trap gas as they plunge through the liquid pool surface. Similarly, increasing the length of the free jet above the receiving pool increases the surface roughness and hence increases Q_g . Increasing the nozzle diameter increases the diameter of the jet at the plunging jet point and therefore gas is entrained over a longer perimeter, again giving an increase in Q_g . The results shown in this thesis illustrate that the dependence of Q_g on the downcomer diameter is not a simple monotonic effect. For small downcomer diameters, Q_g increases to a maximum with increasing D_c ; as D_c continues to increase, the liquid superficial velocity in the downcomer can become so low that the larger bubbles are able to rise upwards; the rising bubbles can then disentrain into the downcomer headspace. Thus the *net* entrainment rate decreases with further increase in D_c . A dimensionless correlation has been proposed to predict the gas entrainment rate from the main operating variables for a confined plunging jet reactor. The correlation represents the data to within $\pm 30\%$, apart from a few cases where the confined plunging jet system did not operate satisfactorily because of excessive amounts of disentrainment into the downcomer headspace.

Disentrainment was found to be prevented by using short downcomer lengths, but this defeats the purpose of increasing the gas-liquid contact time using a confining

column. Downcomer length does not affect the total air entrainment rate (Q_{TA}), which is equal to net air entrainment measured by CPLJR (Q_N) and disentrainment inside the downcomer (Q_{DS}).

Interesting results were obtained from air entrainment rate measurements, which are different from previous work in some areas such as: mechanisms at the top of the downcomer that include the simultaneous dual action of toroidal and swirl motions (§ 4.4.3.1) and the continuous and intermittent vortices for wide and narrow downcomers respectively (§ 4.4.4). Current study shows that for large downcomers in a confined system fine (primary) bubbles appear further down at the base of the swirl rather than beneath the pool surface (§ 4.4.4). Also a water ring has been observed around the two-phase mixture for long downcomer at high rough jet (§ 4.4.3.3). Water ring width increases along the downcomer length.

Downcomer with electrodes rings, as probes, to measure salt traces in the solution have been tested for salt concentrations. Results show that these kind of probes responded well for variation of salt concentration in the solution slightly above 0.05 mg/ml. Then this method was used successfully to measure volumetric water flow rate up the riser (Q_{la}) by detecting a tracer carried by the liquid from one ring to the next inside the annular riser.

A number of measurements have been reported on the effects of the nozzle diameter and annulus diameter on water flow rate up the riser in an air-lift column surrounding a confined plunging jet system. The use of an annular column surrounding a concentric tube (downcomer) in a confined system allows much greater water flow rate to be induced from the bottom of the annulus. Water flow rate (Q_{la}) increases with decreasing nozzle diameter, since this entrains more air, which increases the hydrostatic pressure difference between the two-phase flow in the riser and the surrounding clear liquid, causing more fresh water to be entrained from the base of the annulus. Whereas, increasing annulus diameter increases the cross sectional area and hence increases water flow rate (Q_{la}). The induced flow is controlled only by the air flowing into the riser

regardless of the nozzle diameter or jet flow rate. Experimental data were compared against a model that predicts water flow rate (Q_{la}). Results show that the agreement between the model and the measured values improves with decreasing nozzle diameter, since this increases the penetration depth of the two-phase stream and entrains more gas, which gives a better voidage distribution. Current results also show that the model gives better prediction of the measurements obtained by smaller annuli, this is believed to be due to a better voidage distribution across the annulus. Finally the result shown here illustrate that annulus diameter (D_a) does not affect air entrainment rate.

Oxygenation efficiency (OE) values in $\text{Kg O}_2/\text{kWh}$ were measured in the present work for air-water system employing an air-lift column in CPLJR. OE depends on jet kinetic energy and nozzle diameter. High OE were measured at low jet velocity and hence power input. Similar behaviour was reported by previous authors utilizing various PLJR (i.e. confined and unconfined systems). However, the values obtained in the current work exceeded those of other PLJR system. For the same dissipated energy the oxygenation efficiency (OE) measured by the current system is almost double that of confined system. This increase could reach up to 5 folds of (OE) measured for unconfined system for the same jet velocity (V_j). This is mainly due to the usage of new air-lift column in CPLJR, which induced fresh water up the annulus. This diluted the two-phase flow mixture leaving the base of the downcomer restoring oxygen concentration gradient, and thus driving force. Subsequently, more oxygen is transferred to the surrounding liquid. The device also recycles liquid within the tank very efficiently as liquid is continuously pulled into the base of the tube and discharged at its top.

10.2 Recommendations

As shown previously in the literature, the air entrainment rate increases as the main variables increase (V_j , L_j , d_n and D_c). Deeper bubble penetration was achieved by longer

downcomer. The purpose of achieving deep bubble penetration is to enhance the mass transfer rate with no extra cost in the energy input. However, the amount of the water that is aerated in narrow downcomer is small relative to the amount of water in the reservoir. This can limit the amount of oxygen transferred to the water inside the downcomer. The surrounding water (outside of the downcomer) is not being aerated efficiently due to possible saturation of the stream leaving the downcomer base which is an inefficient use of energy. Also the bubbles that leave the downcomer may not spread far to cover all of the surrounding water (especially the bottom part). As a result, some ideas are proposed to try to improve this situation for the future work. One of them has been already employed that is the air-lift column. A higher oxygen transfer could have been achieved at high jet velocities by employing a longer concentric downcomer in air-lift column device. Another idea is to design a wider downcomer to accommodate larger amount of water and reduce the disentrainment rate (bubble coalescence) may worth trying. Some of the ideas are shown below:

10.2.1 Downcomer with longitudinal baffles and sieve

This design may enable the bubbles to achieve deeper depth. As shown in Figure 10.1a, having longitudinal baffles may interfere with the toroidal and swirl motions that occur inside the downcomer. This may reduce the disentrainment of the bubbles and therefore more net entrainment rate. It is not a simple design because baffle height, numbers, locations and dimensions must be investigated carefully to get the optimum results. Another way is to design the downcomer with horizontal sieve inside the downcomer at a certain depth (Figure 10.1b). This may affect the mixture momentum and increase pressure drop (Figure 10.1b), however it will hinder coalescence by breaking air bubbles into smaller bubbles reducing their terminal velocity, which increases bubble penetration depth and hence mass transfer with no extra cost. Also sieve dimensions (thickness, hole size and location of the sieve) must be studied carefully.

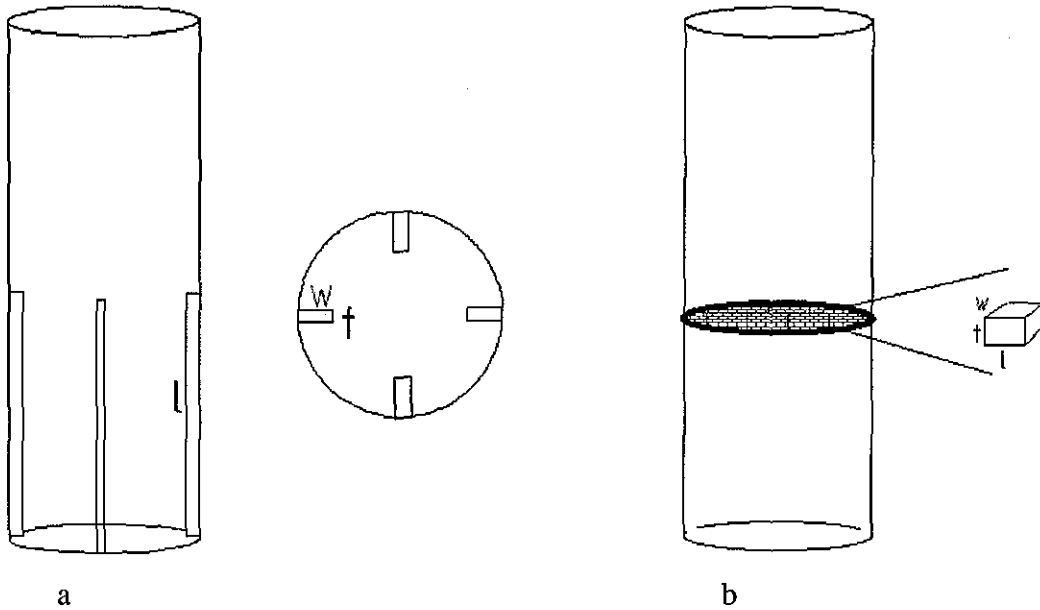


Figure 10.1 Downcomers featuring a) longitudinal baffles and b) sieve.

10.2.2 Downcomer with arms

Another way of aerating the water efficiently may be achieved by employing the design that is shown in Figure 10.2. A downcomer with arms that allow fresh water to flow inside the downcomer and dilute the two-phase mixture and restore the driving force. Mass transfer rate can be measured before and after the arms (before and after the dilution). Again, this needs to be tested first under various conditions.

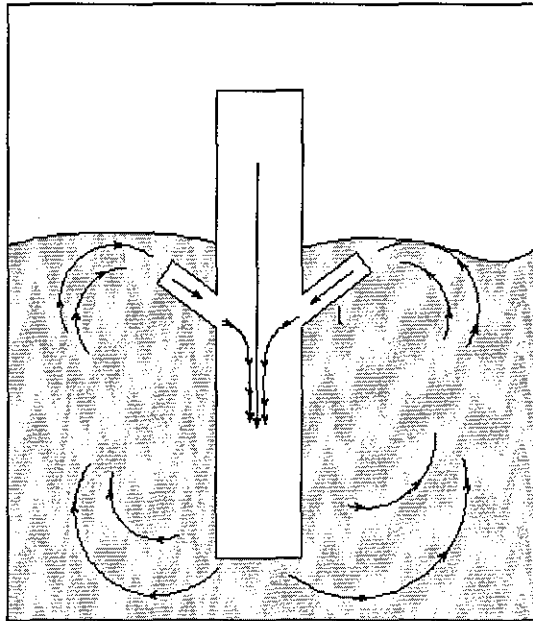


Figure 10.2 Downcomer with extended arms.

10.2.3 Downcomer as a bubble distributor

To aerate the whole tank efficiently a downcomer bubble distributor may be the best choice. The design is shown in Figure 10.3, however a larger place may be needed to carry out this type of experiments. Mass transfer rate can be measured at the saturation point (base of the downcomer) and at different places in the tank. However this will increase pressure drop.

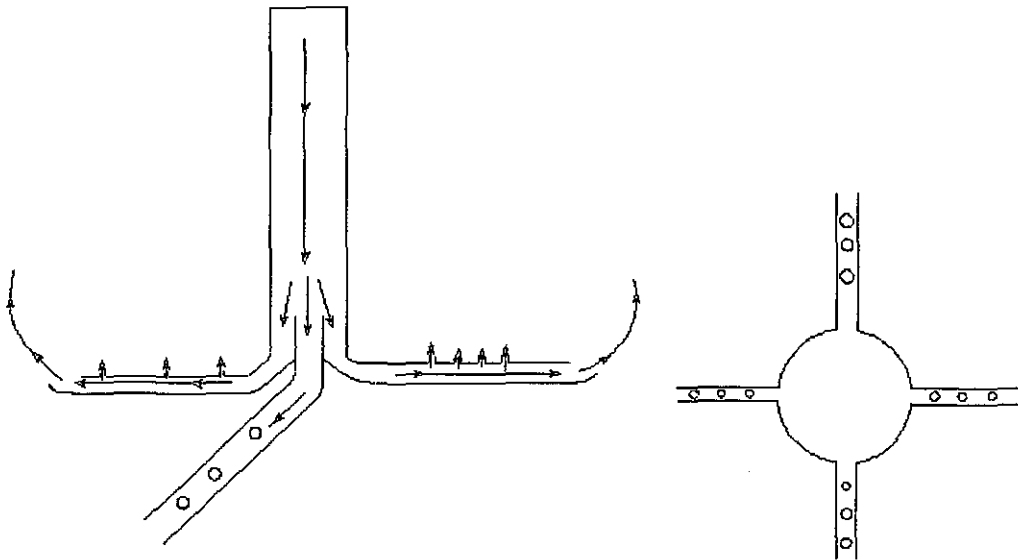


Figure 10.3 Downcomer (as a bubble distributor) with pipe network.

10.2.4 Total, measured and dis- entrainment apparatus

It would be interesting to measure the disentrainment rate caused by the bubbles rising up inside the downcomer along with the measured and total air entrainment rate. Knowing the disentrainment rate is significant because it will help to understand many facts. This may be achieved by employing the new design shown in Figure 10.4. This may lead to more results and new developments regarding the mechanisms and new correlation, which may reveal for the first time which of the two systems (unconfined or confined) gives higher air entrainment rate. This may also help to develop an important model that relates total entrainment rate (Q_{TA}) to disentrainment rate (Q_{DS}) and net entrainment rate (Q_N) as shown below,

$$Q_{TA} = Q_N f(V_j, L_j, D_C \text{ \& } d_n) + Q_D f(V_j, L_j, D_C \text{ \& } d_n) \quad (10.1)$$

Where

Q_N = any of the correlations developed up until now as a function of V_j , L_j , d_n and D_c (Al-Anzi's *et al.*, Bin's...etc).

Q_{DS} = correlation meant to be developed by the proposed design in figure 10.4 V_j , L_j , d_n and D_c .

Once this is done an optimization model can be applied by increasing the net entrainment rate through minimizing the disenitainment rate.

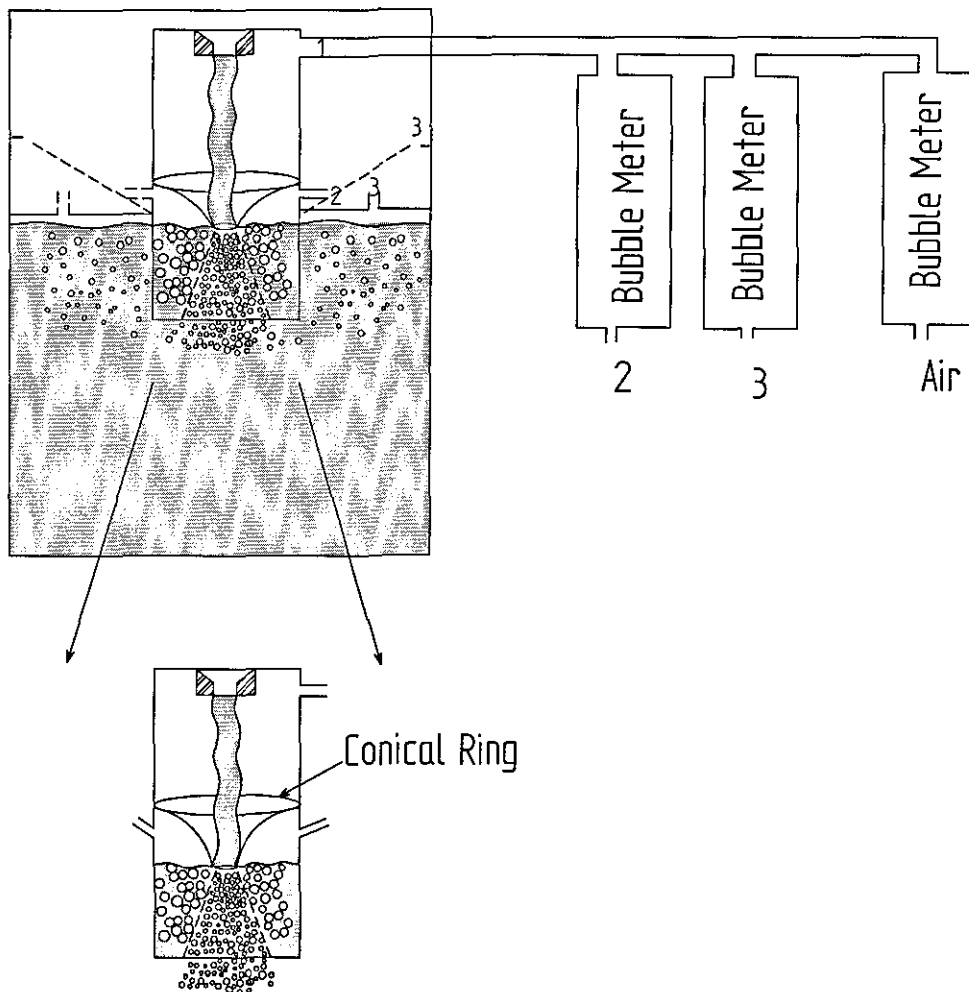


Figure 10.4 A system to measure total, measured and dis- air entrained flow rate in the same run.

10.2.5 Recycling of oxygen in CPJR

Possible development of the device is to use pure oxygen instead of air, which can improve concentration driving force by $1/0.21 = 4.7$ times and the oxygen can be recycled utilizing the rig shown in figure 10.5. In Figure 10.5, the mass transfer performance can be improved by installing a hood over the top of the annulus, where two-phase mixture leaves as a fountain, to collect the entrained gas (nitrogen or oxygen) released by the bubbles and reuse it efficiently through recycling it back into the system. This will minimize the consumption of fresh gas from the cylinder and thus the cost.

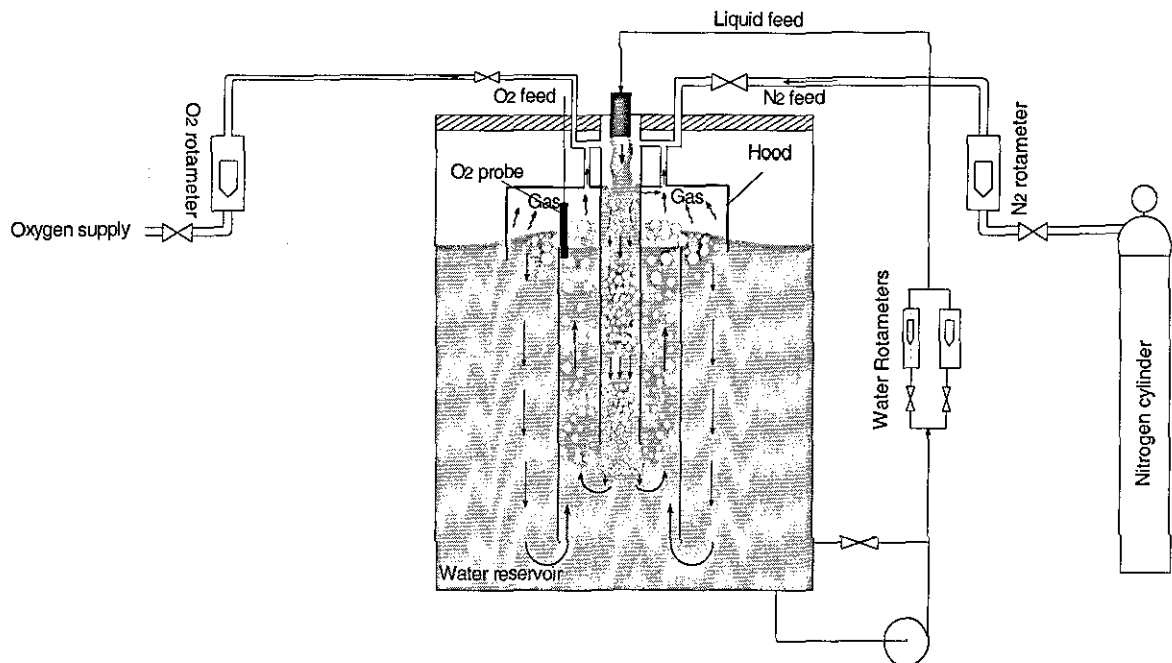


Figure 10.5 Reuse of the feed gas by installing a hood on top of the annular riser.

References

Akita, K., Okazaki, T. & Koyama, H., 1988. Gas holdups and friction factors of gas-liquid two-phase flow in an air-lift bubble column. *Journal of Chemical Engineering of Japan*, **21**, 476-482.

Al-Anzi, B., Cumming, I.W., & Rielly, C.D., 2006. Air entrainment rates in a confined plunging jet reactor. *10th International Conference on Multiphase Flow Industrial Plant*, Italy, 71-82.

Backhurst, J.R., Haker, J.H. & Kaul, S.N., 1988. The characteristics of aerators for the oxygenation of activated sludge, *Asian Environment*, **10**, 65 – 72.

Bayly, A.E., Rielly, C.D., Evans, G.M., & Hazell, M., 1992. The rate of expansion of a confined submerged jet, *CHEMECA '92*, Canberra, Australia, 119-2 – 126-2.

Behringer, H., 1936. The flow of liquid gas mixture in vertical tubes. *Zeit. Ges. Kälte-Ind.*, **43**, 55-58. Also AEC-Translation No. 1777. O. T. S. Department of Commerce, Washington, D. C.

Bin, A.K., 1977. Mass transfer in a plunging jet absorber. *Inz Chem (Polish)*, **7**, 275 – 291; *Trans IChemE Part A*, **19**, 227 – 235.

Bin, A.K., 1984. Air entrainment by plunging liquid jet. *In Proceeding of the Symposium on Scale effects in Modelling Hydrolic Structure*, Esslingen, Paper 5.5, 1-6.

Bin, A.K., 1988a. Minimum air entrainment velocity of vertical plunging liquid jets. *Chemical Engineering Science.*, **43**, 379-389.

Bin, A.K., 1988b. Gas entrainment by plunging liquid jets. *VDI-Forschungsh.* **648**, 1-36.

Bin, A.K., 1993. Gas entrainment by plunging liquid jets. *Chemical Engineering Science*, **48**, 3585-3630.

Burgess, J.M., Molloy, N.A. & McCarthy, M.J., 1972. A note on the plunging liquid jet reactor. *Chemical Engineering Science*, **27**, 442-445.

Caetano, E. F., Shoham, O. & Brill, J. P., 1992. Upward vertical two-phase flow through an annular-part II: modeling bubble, slug and annular flow. *Transaction of ASME*, **114**, 14 – 30.

Chisit, M. Y., 1989. *Airlift Bioreactor. (Chapter V in advances in hydrodynamics)* Elsevier, London and New York, 203 – 206.

Cicchitti, A., Lombardi, C., Silvestri, M., Soldaini, G., & Zavattarelli, R., 1960. Two-phase cooling experiments-pressure drop, heat transfer and burnout measurements. *Energia Nucleare*, **7**, 407-425.

Ciborowski, J. Bin, A., 1972. Minimum entrainment velocity for free liquid jets. *Inz Chem. (Polish)* **2**, 453-469.

Clark, N.N & Flemmer, R. L. C., 1984. On vertical downward two phase flow. *Chemical Engineering Science*, **39**, 170-173.

Clark, N.N & Flemmer, R. L. C., 1985. Predicting the holdup in two-phase bubble upflow and downflow using the Zuber and Findlay drift-flux model. *AIChE Journal*, **31**, 500-503.

Crane Co., 1982. Physical properties of fluids and flow characteristics of valves, fitting, and pipe. Manual.

Cumming, I.W. & Rielly, C.D., 2004. Confined plunging liquid jet reactors for oxygen transfer handout. *Department of Chemical Engineering, Loughborough University, Handout*, 1-7.

Cumming I. W., Rielly C. D. & Mason A. j., 2002. Hydraulic performance of an annular plunging jet reactor. *Trans IChemE Part A*, **80**, 543-549.

Davoust, L., Achard, J.L. & El Hammoumi, M., 2002. Air entrainment by a plunging jet: the dynamical roughness concept and its estimation by a light absorption technique. *Internationa Journal of Multiphase Flow*, **28**, 1541-1564.

Dukler, A. E., Wicks III, M., & Cleveland, R. G., 1964. Pressure drop and hold-up in two-phase flow, *AIChE Journal*, **10**, pp. 38-51.

Dumitrescu, Z. Angew., 1943. Strömung an einer Luftblase im senkrechten Rohr. *Mathematical Technique*, **23**, 139.

Evans, G.M. & Jameson, G.J., 1995. Hydrodynamics of a plunging liquid jet bubble column. *Trans IChemE Part A*, **73**, 679-684.

Evans, G.M & Machniewski 1999. Mass transfer in a confined plunging liquid jet bubble column, *Chemical Engineering Science*, **54**, 4981-4990.

Evans, G.M., Bin, A.K. & Machniewski, 2001. Performance of confined plunging liquid jet bubble column as a gas-liquid reactor. *Chemical Engineering Science*, **56**, 1151 – 1157.

Evans, G.M., Jamson, G.J. & Rielly, C.D., 1996. Free jet expansion and gas entrainment characteristics of a plunging liquid jet. *Experimental Thermal and Fluid Science*, **12**, 142-149.

- Fahim, M. A. & Wakao, N., 1992. Parameter estimation from tracer response measurements. *Chemical Engineering Journal*, **25**, 1-8
- Fakeeha, A.H., Jibril, B.Y., Ibrahim, G. & Abasaheed, A.E., 1999. Medium effects on oxygen mass transfer in a plunging jet loop reactor with a downcomer. *Chemical Engineering Science*, **38**, 259 – 265.
- Fields, P.R., Mitchell, F.R.G. & Slater, N.K.H., 1983. Studies of mixing in a concentric tube air-lift reactor containing xthanthan gum by means of an improved flow follower. *Chemical Engineering Communications*, **25**(1-6), 93-104.
- Griffith, P. & Wallis, G. B., 1961. Two-phase slug flow. *Journal of Heat Transfer, Trans ASME, Series C*, **83**, 307-320.
- Henderson, J. B., McCarthy, M. J. and Molloy, N. A., 1970. Entrainment by plunging jets. *In Proceeding of Chemeca '70*, Melbourne, **2**, 86-100.
- Hewitt, G. F. 1978. Measurements of two phase flow parameters. (*Chapter 1 in Introduction to two phase flow*), London: Academic press, 1-18.
- Holland, F. A. & Bragg, R., 1995. Fluid flow for chemical engineers. Edward Arnold. (*Chapter 7 in Gas-liquid two-phase flow*), 2nd Edition, 4-17.
- Horan, N.J., 1990. Biological wastewater treatment system: Theory and operation. John Wiley and Sons, 60.
- Jones, A.G., 1985. Liquid circulation in a draft-tube bubble column. *Chemical Engineering Science*, **40** (3), 449-462.

Kay, J. M. & Nedderman, R. M., 1988. Fluid mechanics and transfer processes. (*Chapter 19 in two phase flow*), Cambridge University Press, 499-516.

Levenspiel, O. & Smith, W. K., 1957. Notes on the diffusion-type for the longitudinal mixing of fluids in flow. *Chemical Engineering Science*, **6**, 227-233.

Levenspiel, O., Chemical engineering reaction. *Wiley International Edition*, 1982.

Lienhard, J. H., 1968. Capillary action in small jets impinging on liquid surfaces. *Journal of Basic Engineering*. Transaction of ASME, **90**, 137-138.

Lin, T. J. & Donnelly, H. G., 1969. Gas bubble entrainment by plunging laminar liquid jets. *AIChE Journal*, **12**, 563-571.

Lockhart, R.W., & Martinelli, R.C., 1949. Proposed correlation of data for isothermal two-phase, two-component flow in pipes. *Chemical Engineering Progress*, **45**, 39-46.

Low, K.C., 2003. Hydrodynamics and mass transfe studies of a confined plunging jet. *PhD thesis*, Department of Chemical Engineering, Loughborough University, UK.

Maalej, S., Benadda, B., Dabaliz, A. & Otterbein, M., 1999. Experimental study on a co-current gas-liquid downflow contactor with gas entrainment by liquid jet. *Chemical Engineering Technology*, **22**, 1043 – 1049.

McAdams, W.H., Woods, W.K., & Heroman, L.C., 1942. Vaporization inside horizontal tubes-II-Benzene-oil mixtures. *Transactions of ASME*, **64**, 193-200.

Majumder, S.K., Kundu, G. & Mukherjee, D., 2006. Bubble size distribution and gas-liquid interfacial area in a modified downflow bubble column, *Chemical Engineering Journal*, **122**, 1-10.

- McCabe, W.L. , Smith, J.C. & Harriot, P., 1993. *Unit Operations of Chemical Engineering*, 5th Edition, McGraw-Hill, Inc., NY.
- McCarthy, M.J. & Molloy, N.A. 1974. Review of stability of liquid jets and the influence of nozzle design. *Chemical Engineering Journal*, **7**, 7-20.
- Mckeogh, E.J. & Ervine, D.A., 1981. Air entrainment rate and diffusion pattern of plunging liquid jets. *Chemical Engineering Science*, **36**, 1161-1171.
- Moppet, G.D. 1996. Gas entrainment and mass transfer in a plunging jet bubble column. *PhD thesis*, Department of Chemical Engineering, University of Cambridge UK.
- Neal, L. G., 1963. An analysis of slip in gas-liquid flow applicable to the bubble and slug flow regimes. *Report KR-62, Kjeller Research Establishment, Kjeller, Norway*.
- Nicklin, D. J., Wilkes, J. O. & Davidson, J. F., 1962. Two-phase flow in vertical tubes. *Transactions of IChemE*, **40**, 61.
- Obradovic, B., Dudukovic, A. & Vunjak-Novakovic, G., 1997. Response data analysis of a tree phase airlift reactor. *Trans IChemE Part A*, **75**, 473-479.
- Ohkawa, A., Kusabiraki, D., Kawai, Y. & Sakai, N., 1986a. Some flow characteristics of a vertical liquid jet system having downcomers. *Chemical Engineering Science*, **41**, 2347-2361.
- Ohkawa, A., Kusabiraki, D., Shiokawa, Y., Sakai, N. & Fujii, M., 1986b. Flow and oxygen transfer in a plunging water system using inclined short nozzles and performance characteristics of its system in aerobic treatment of wastewater. *Biotechnology and Bioengineering*, **28**, 1845 – 1856.

- Ohkawa, A., Kusabiraki, D., & Sakai, N., 1987. Effect of nozzle length on gas entrainment characteristics of vertical liquid jet. *Journal of Chemical Engineering Japan*, **20**, 295-300.
- Ohl, C.D., Oguz, H.N. & Prosperetti, A., 2000. Mechanism of air entrainment by a disturbed liquid jet. *Physics of Fluids*, **12**, 1710-1714.
- Perry, R. T., 1967. Fluid mechanics of entrainment through liquid-liquid and solid-solid junctures. *PhD thesis*, University of Minnesota, USA.
- Rielly, C.D., 2006. A method to estimate the liquid phase velocity and axial dispersion coefficient from tracer tests. Department of Chemical Engineering, Loughborough, Handout, 1-8.
- Sene, K.J. (1988). Air entrainment by plunging jets. *Chemical Engineering Science*, **43**, 2615-2623.
- Sneath, R.W., 1978. The performance of a plunging liquid jet aerator and aerobic treatment of pig slurry. *Water Pollution Control*, **77**, 408 – 420.
- Sotiriadis, A.A., Thorpe, R.B. & Smith, J.M., 2005. Bubble size and mass transfer characteristics of sparged downwards two-phase flow. *Chemical Engineering Science*, **60**, 5917 – 5929.
- Suciu, G. D., & Smigelschi, O. 1976. Size of the submerged biphasic region in plunging jet systems. *Chemical Engineering Science*, **31**, 1217-1220.
- Takahara, Y., 1980. Haisui no seibutsusyori, Tikyusya, Toyo, Japan, 72.

Taylor G.I., 1953. Dispersion of Soluble matter in solvent flowing slowly through a tube. *Proceedings of the Royal Society of London. Series A, Mathematical and Physical Sciences*, (London) **219A**, 186

Taylor G.I., 1954, Conditions under which dispersion of a solute in a stream of solvent can be used to measure molecular diffusion. *Proceedings of the Royal Society of London. Series A, Mathematical and Physical Sciences* , (London) **225A**, 473 and **223A**, 446.

Tojo, K. & Miyanami, K., 1982. Oxygen transfer in jet mixers. *Chemical Engineering Journal*, **24**, 89 – 97.

van de Donk, J. A., 1981. Water aeration with plunging jets. *PhD thesis*, University of Technology Delft, Holland.

van de Donk, J.A.C., van Der Lans, R.G.J.M. & Smith, J.M., 1979. The effect of contaminants on the oxygen transfer rate achieved with a plunging jet contractor. *Third European Conference on Mixing*, 289-302.

van de Sande, E. & Smith, J.M., 1975. Mass transfer from plunging water jets. *Chemical Engineering Journal*, **10**, 225 – 233.

van de Sande, E., 1974. Air entrainment by plunging water jets, *PhD thesis*, University of Technology Delft, Holland.

verlaan, P., van Eijs, A. M. M., Tremper, J., va't Riet K. & Luyban, K., 1989. Estimation of axial dispersion in individual sections of an airlift-loop reactor. *Chemical Engineering Science*, **44**, 1139-1146.

Wallis, G.B., 1974. One-dimensional two-phase flow. New York, McGraw-Hill Book Company Inc.

Whitehead, A., 2002. PDP project report. Department of Chemical Engineering, Loughborough University, UK.

www.doe.carleton.ca/~jaguirre/appnotes.html, 2007. "Hp Vee program info page". Accessed on 13/02/2007.

www.lagoonsoline.com/aerationmain.htm, 2002. "Fundamental of Lagoon Aeration". Accessed on 07/12/2006.

Welty, J.R., Wicks, C.E. & Wilson, R.E., 1984. Fundamentals of momentum, heat, and mass transfer. Third Edition. Canada: John Wiley & Sons, Inc.

Yamagiwa, K., Kusabiraki, D. & Ohkawa, A., 1990. Gas holdup and gas entrainment rate in downflow bubble column with gas entrainment by liquid jet operating at high throughput. *Journal of Chemical Engineering of Japan*, **23**, 343-348.

Yamagiwa, K., Ohmae, Y., Dhlan, M.H. & Ohkawa, A., 1991. Activated sludge treatment of small scale waste water by a plunging liquid jet bioreactor with cross flow filtration. *Bioresource Technology*, **37**, 215 – 222.

Yamashita, F., 1998. Gas holdup in bubble column with draft tube for gas dispersion into annulus. *Journal of Chemical Engineering of Japan*, **31**, 289-294.

Zuber, N. & Findlay, J. A., 1965. Average volumetric concentration in two-phase flow systems. *Journal of Heat Transfer*, **87**, 453 - 468.

Appendices

Appendix I Example of an Induced Air Calculations

AI.1 Layout of the axial dispersion model used to predict t_{corr} and therefore Q_{la} , ϵ_a and Q_{le} .

Analysis of file:

Actual run with 16.txt

File C:\WINDOWS\Desktop\Bader\Actual Runs\Actual run with 16 .txt
 Date Thu 23/Feb/2006 10:44:08
 Dd / (mm) 35
 Twater (deg C) 14
 Troom (deg C) 16
 Qwater / (litre/min) 16
 Qair / (m³/s) 0.000248465
 D_{probe} / m 0.825
 Surfactant Conc (ppm) 0
 Dn / mm 10
 Lj / (m) 0.1
 Da / mm 90
 Comment Gain b:2
 Comment offset b: 4.80
 Comment

Raw experimental data

input signal	
Time (s)	Dimensionless Concentration
0	5.307617188
0.050003052	5.17578125
0.100006104	4.946289063
0.150009155	5.297851563
0.200012207	5.317382813
0.250015259	5.234375
0.300018311	5.229492188
0.350021362	5.146484375
0.400024414	5.249023438
0.450027466	5.1171875
0.500030518	5.185546875
0.550033569	5.29296875
0.600036621	5.258789063
0.700042725	5.239257813

Output signal	
Time (s)	Dimensionless Concentration
0	4.819335938
0.050003052	4.721679688
0.100006104	4.731445313
0.150009155	4.697265625
0.200012207	4.643554688
0.250015259	4.658203125
0.300018311	4.594726563
0.350021362	4.633789063
0.400024414	4.638671875
0.450027466	4.653320313
0.500030518	4.619140625
0.550033569	4.482421875
0.600036621	4.458007813
0.700042725	4.4921875

Calculations complete

Experiment type
 Step response
 Pulse response

Model type
 Axial dispersion
 Tanks in series

Baseline correction
 Initial no. points 30
 Final no. points 30

Data selection
 Start time 0
 End time 0

Calculations
 Load data
 Smoothing filter
 Spike filter
 Time delay
 Dispersion

[Click here to run macro](#)

Results

Model delay time 0.00E+00 s
 Correlation time 1.40E+00 s
 Peak to peak time 1.18E+00 s
 Peclet number 0.00E+00
 Sum sq errors 0.00E+00

C_D	1.2	Distribution coefficient
V_∞	0.250455805 m/s	Bubble terminal velocity
A_a	0.00352 m ²	Annulus CSA
Q_{ga}	2.48E-04 m ³ /s	Gas flowrate
j_{gs}	7.05E-02 m/s	Gas superficial velocity
a	0.990	a quadratic coefficient
b	-1.460	b quadratic coefficient
c	0.099	c quadratic coefficient
ϵ_a	0.0712	Annulus void fraction
j_{ls}	0.546 m/s	Liquid superficial velocity
Q_{la}	0.001924709 m ³ /s	Liquid flowrate in annulus
Q_{le}	0.001658042 m ³ /s	Entrained liquid flowrate

Appendix II Air Entrainment System

AII.1 Air entrainment rate measurements

This section presents the means of calculating the air entrainment ratio measurements

$$Q_A = \left(\frac{H}{T}\right)A_A \quad (\text{A.1})$$

Where,

$$A_A = \pi \left(\frac{d_A}{2}\right)^2 \quad (\text{A.2})$$

An air entrainment ratio is calculated by dividing air entrainment flow rate by jet flow rate (Q_j). Jet volumetric flow rate is measure in L/min utilizing two rotameters. Jet velocity in m/s is calculated as follows,

$$V_j = \frac{Q_j}{\pi \left(\frac{d_n}{2}\right)^2} \quad (\text{A.3})$$

From previous equations, air entrainment ratio can be simplified to,

$$\frac{Q_A}{Q_j} = \left(\frac{Hd_A^2}{TV_j d_n^2}\right) = \left(\frac{H}{TV_j}\right)\left(\frac{d_A}{d_n}\right)^2 \quad (\text{A.4})$$

AII.2 Calibration of rotameter meter

The jet flow rate was measured utilizing two rotameters. The rotameters combined together measure a maximum flow rate of 62 L/min. The rotameter calibrations were checked using a large bucket, which is marked up at 10 litre intervals. A stop watch was used to measure the time. The results are tabulated and plotted below:

Table A.1 Calibration results for rotameter.

Trials (s)	1	2	3	Error%
	Seconds (litre)	Seconds (litre)	Seconds (litre)	
Flow rate (L/min.)				
10	67 (10L)	59.44 (10L)	-	0.9
20	31 (10 L)	29.85(1 L)	59(20L)	0.5
30	18.50 (10L)	18.40 (10L)	-	7.5
40	29 (20 L)	28.6(20L)	28.8(20L)	3.3
50	24.28 (20L)	24.43 (20L)	24.31 (20L)	-1.167
60	20 (20 L)	31(30L)	40(40L)	0

As shown above, the percentage error in the rotameter calibration is very small, and can be neglected.

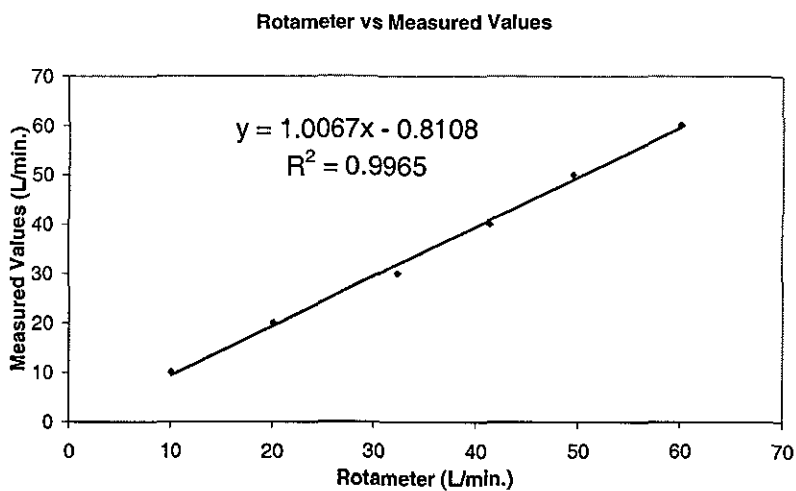


Figure A.1 Rotamemter calibration.

AII.3 Orifice calibration

An orifice was calibrated against two rotameters that were fixed on the rig. The orifice was connected to voltmeter through transducer. The results were collected by reading the values displayed by the voltmeter that correspond to those measured by the rotameters. Initial voltmeter reading was taken down before the run started defined as the offset. The final value was obtained by taking the square root of the measured value subtracted from it the offset value.

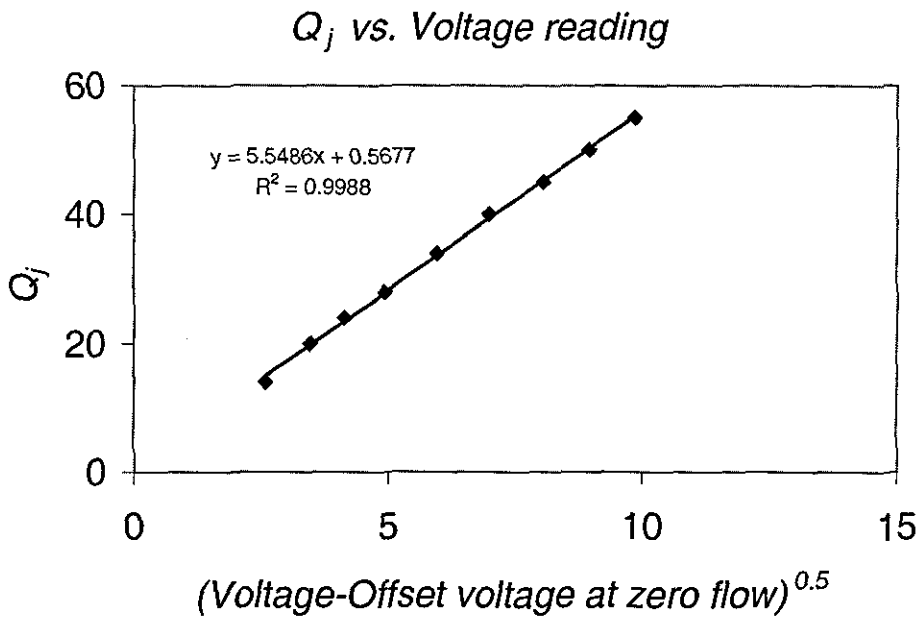


Figure A.2 Orifice calibration.

AII.4 Tapping design

Table A.2 presents a summary of tapping design results for various values of air entrainment ratio.

Table A.2 Air tapping results

Q_A/Q_j	V_j	Fr_j	Q_j	Q_A	$d_A(m)$	$d_A(mm)$
0.191877	2	27.21088	0.000353	6.78238E-05	0.001864831	1.864831
0.302175	4	108.8435	0.000707	0.000213623	0.002950839	2.950839
0.394125	6	244.898	0.00106	0.00041794	0.003859509	3.859509
0.475876	8	435.3741	0.001414	0.00067284	0.004669296	4.669296
0.550794	10	680.2721	0.001767	0.000973459	0.005412696	5.412696
0.620681	12	979.5918	0.002121	0.001316371	0.006107141	6.107141
0.686645	14	1333.333	0.002474	0.001698982	0.006763353	6.763353
0.749425	16	1741.497	0.002828	0.002119224	0.007388519	7.388519
0.809549	18	2204.082	0.003181	0.0025754	0.00798775	7.98775
0.867409	20	2721.088	0.003535	0.003066072	0.008564846	8.564846
0.923303	22	3292.517	0.003888	0.003590009	0.00912273	9.12273
0.97747	24	3918.367	0.004242	0.004146133	0.00966371	9.66371
1.0301	26	4598.639	0.004595	0.00473349	0.010189648	10.18965
1.081351	28	5333.333	0.004949	0.005351229	0.010702076	10.70208
1.131354	30	6122.449	0.005302	0.005998583	0.011202271	11.20227
1.18022	32	6965.986	0.005656	0.006674855	0.011691314	11.69131
1.228044	34	7863.946	0.006009	0.007379407	0.012170129	12.17013
1.274906	36	8816.327	0.006363	0.008111655	0.012639514	12.63951
1.320879	38	9823.129	0.006716	0.008871057	0.013100165	13.10016
1.366025	40	10884.35	0.00707	0.009657112	0.01355269	13.55269
1.410398	42	12000	0.007423	0.010469352	0.01399763	13.99763
1.454049	44	13170.07	0.007776	0.01130734	0.014435465	14.43546
1.497021	46	14394.56	0.00813	0.012170666	0.014866623	14.86662
1.539353	48	15673.47	0.008483	0.013058944	0.015291491	15.29149
1.581081	50	17006.8	0.008837	0.013971812	0.015710416	15.71042
1.622237	52	18394.56	0.00919	0.014908924	0.016123715	16.12372
1.662851	54	19836.73	0.009544	0.015869956	0.016531676	16.53168
1.702949	56	21333.33	0.009897	0.016854598	0.016934562	16.93456
1.742557	58	22884.35	0.010251	0.017862555	0.017332613	17.33261
1.781696	60	24489.8	0.010604	0.018893548	0.017726052	17.72605
1.820388	62	26149.66	0.010958	0.019947308	0.018115083	18.11508

Appendix III Mass Transfer Calculations

Oxygen electrode response - Measured by Bader 14/11/06

Time	Chart	Time	saturation	Ln (sat)	$1-\exp(-t/\tau)$
-0.4	0.01	0	0	#NAME?	0
1	1.9	1.4	0.227437	-1.48088	0.308174
2	3.8	2.4	0.456077	-0.78509	0.468248
3	4.8	3.4	0.576414	-0.55093	0.591285
4	6.1	4.4	0.732852	-0.31081	0.685853
5	6.75	5.4	0.811071	-0.2094	0.75854
6	7.15	6.4	0.859206	-0.15175	0.814409
8	7.58	8.4	0.910951	-0.09327	0.890357
10	7.85	10.4	0.943442	-0.05822	0.935225
12	8	12.4	0.961492	-0.03927	0.961733
14	8.13	14.4	0.977136	-0.02313	0.977393
16	8.2	16.4	0.98556	-0.01455	0.986644
18	8.23	18.4	0.98917	-0.01089	0.99211
20	8.25	20.4	0.991576	-0.00846	0.995339
22	8.29	22.4	0.99639	-0.00362	0.997246
24	8.3	24.4	0.997593	-0.00241	0.998373
26	8.3	26.4	0.997593	-0.00241	0.999039
28	8.32	28.4	1	0	0.999432

Chart scale 8.31 τ 3.8 3.830537

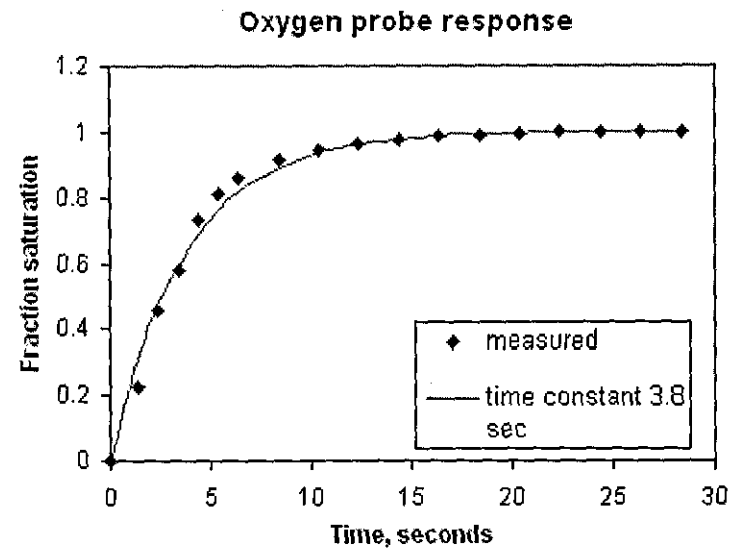


Figure A.3 Oxygen probe response.

An example of C_f estimation utilizing the chart

D_a 94 mm
 d_n 12 mm
 Q_f 60 l/min

Time	reading/From the chart	adjusted reading	fraction	time	dC_p/dt	C_f	C_{fmean}	0.287462
-0.8	0.7	0	0	0		0		
2	1.74	1.04	0.111828	2.8	0.03853	0.258244		
4	2.42	1.72	0.184946	4.8	0.028495	0.293226		
6	2.8	2.1	0.225806	6.8	0.014247	0.279946		
8	2.95	2.25	0.241935	8.8	0.009946	0.279731		
10	3.17	2.47	0.265591	10.8	0.007796	0.295215		
12	3.24	2.54	0.273118	12.8	0.004839	0.291505		
14	3.35	2.65	0.284946	14.8	0.004301	0.30129		
16	3.4	2.7	0.290323	16.8	0.002688	0.300538		
18	3.45	2.75	0.295699	18.8	0.002688	0.305914		
20	3.5	2.8	0.301075	20.8	0.004032	0.316398		
22	3.6	2.9	0.311828	22.8	0.003763	0.326129		
24	3.64	2.94	0.316129	24.8	0.005914	0.338602		
26	3.82	3.12	0.335484	26.8	0.001344	0.340591		
28	3.69	2.99	0.321505	28.8	-0.00323	0.309247		
30	3.7	3	0.322581	30.8				

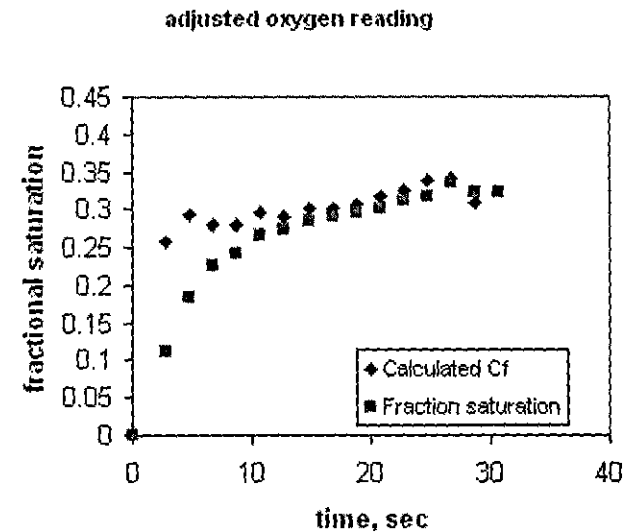


Figure A.4 Adjusted oxygen reading

An example of over all efficiency (*OE*) calculations

Mass transfer Experiment for 144 mm

Low

Q_j	0.0004 m ³ /s	d_n	0.008 m						24
Q_{la}	0.007686 m ³ /s	D_c	0.023 m						
V_T	0.435708	L_r	1.47 m						
D_a	0.144669	W_r	0.78 m						
L_a	1.35 m	t_r	0.38 m						
V_a	0.022191 m ³	L_{sub}	1.06 m						
V_c	0.00044 m ³	D_{co}	0.03 m						
V_{co}	0.000749	O_2	9.09 ppm						
X_1	0.025 cm	X_2	0.22 cm						
X_f	1	ρ	1000 kg/m ³						
t_c / s	t_a / s	t_{tank} / s	$\Delta X / cm$	<i>Overall</i> _{O₂}	<i>Conc.</i> _{O₂}	<i>O</i> _{2uptake}	<i>Power</i>	<i>O</i> _{2uptake}	
				/ cm	(mg/l)	kg/hr	W	kg/KW hr	
1.10101	2.789835	53.804	0.195	0.975	1.472249	0.040735	12.66515	3.21627	
			0.157915						

Moderate 1

Q_j	0.0006 m ³ /s	d_n	0.008 m						36
Q_{la}	0.008174 m ³ /s	D_c	0.023 m						
V_T	0.435708	L_r	1.47 m						
D_a	0.144669	W_r	0.78 m						
L_a	1.35 m	t_r	0.38 m						
V_a	0.022191 m ³	L_{sub}	1.06 m						
V_c	0.00044 m ³	D_{co}	0.03 m						
V_{co}	0.000749	O_2	9.09 ppm						
X_1	0.01 cm	X_2	0.3 cm						
X_f	1	ρ	1000 kg/m ³						
t_c / s	t_a / s	t_{tank} / s	$\Delta X / cm$	<i>Overall</i> _{O₂}	<i>Conc.</i> _{O₂}	<i>O</i> _{2uptake}	<i>Power</i>	<i>O</i> _{2uptake}	
				/ cm	(mg/l)	kg/hr	W	kg/KW hr	
0.734007	2.623045	50.58733	0.29	0.99	1.794396	0.052805	42.74487	1.235346	
			0.195429						

High

Q_j	0.0008 m ³ /s	d_n	0.008 m						
Q_{la}	0.010798 m ³ /s	D_c	0.023 m						
V_T	0.435708	L_r	1.47 m						
D_a	0.144669	W_r	0.78 m						
L_a	1.35 m	t_r	0.38 m						
V_a	0.022191 m ³	L_{sub}	1.06 m						
V_c	0.00044 m ³	D_{co}	0.03 m						
V_{co}	0.000749	O_2	9.09 ppm						
X_1	0.061 cm	X_2	0.4 cm						
X_f	1	ρ	1000 kg/m ³						
t_c / s	t_a / s	t_{tank} / s	$\Delta X / cm$	<i>Overall</i> _{O₂}	<i>Conc.</i> _{O₂}	<i>O</i> _{2uptake}	<i>Power</i>	<i>O</i> _{2uptake}	
				/ cm	(mg/l)	kg/hr	W	kg/KW hr	
0.550505	1.985638	38.29448	0.339	0.939	2.633661	0.102381	101.3212	1.010461	
			0.272058						

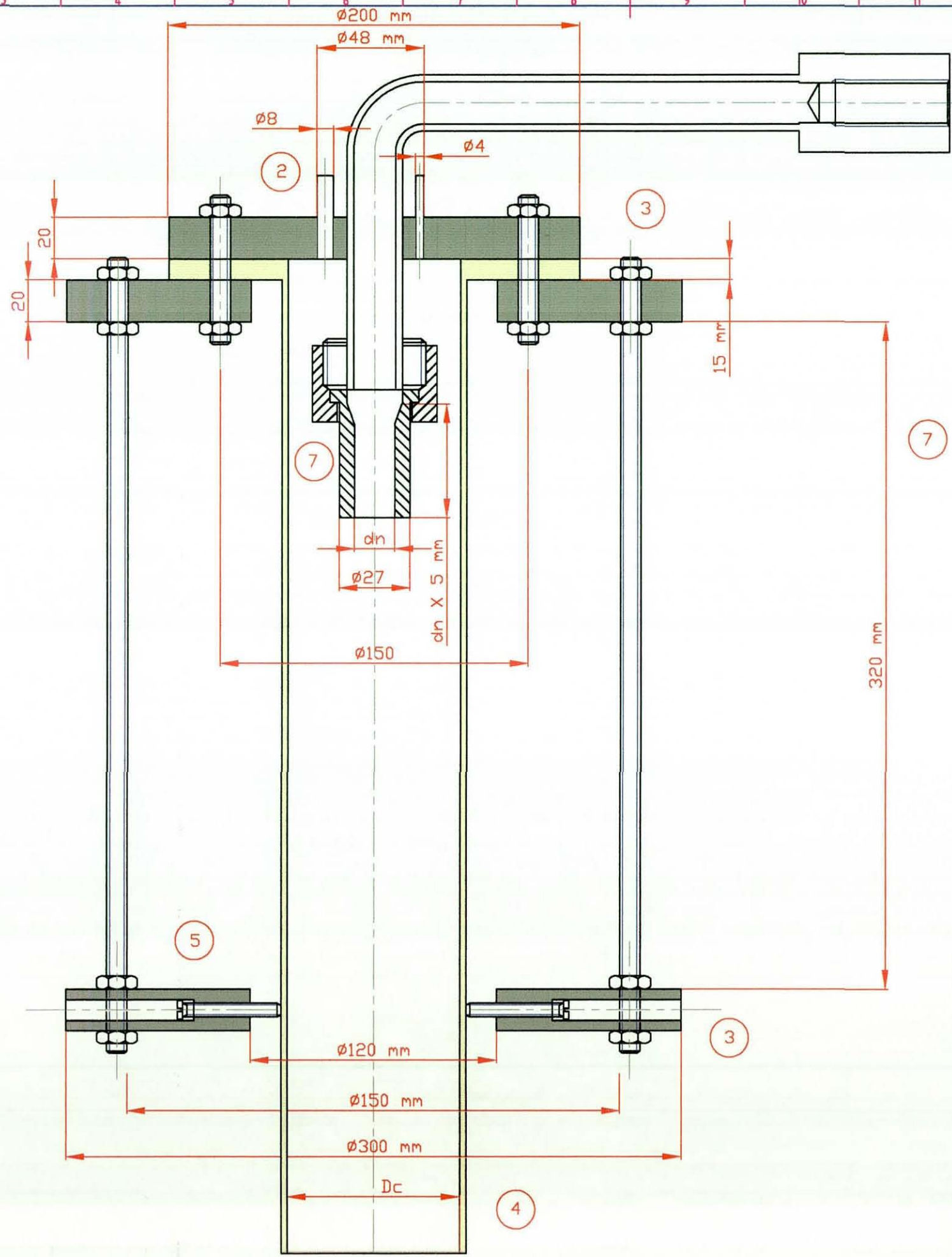
Appendix IV Risk Assessment

Risk Assessment Record

Assessment Number

Department <i>Chemical Eng</i>		Location <i>Pilot Plant Lab</i> <i>5035</i>		Assessor <i>BADER AI-AZI</i>		Date <i>13/12/2004</i>	
Room No./Area		Risk Identified <i>(see Hazard prompt list over page)</i>		Persons at Risk <i>(Groups or numbers)</i>		Controls in Place	
		Assessors Risk Rating <i>(H.M.L. see over page)</i>		Assessors Actions to Further Reduce Risk			
		<i>Electric Shock</i>		<i>1 project team staff</i>			
		<i>Mechanical Hazards</i>		<i>1</i>			
		<i>Hand Tools</i>		<i>1</i>			
		<i>Slips, trips and falls on a level</i>		<i>1</i>			
		<i>Falls from a height</i>		<i>1</i>			
		<i>Space and Confined work area</i>		<i>1</i>			
		<i>Noise / vibration</i>		<i>1</i>			
		<i>Compressed gases</i>		<i>1</i>			
Assessors Comment				Supervisors Comment			
				<i>G. Graham 14.12.04</i>			
Assessors Signature <i>[Signature]</i>		Date <i>13/12/04</i>		Supervisors Signature <i>[Signature]</i>			
Reassessment Date		Date <i>13/12/04</i>					

Appendix V Technical Designs



1

2

3

5

3

4

7

dn = 6, 8, 12 and 15 mm

Dc = 23, 38, 50, 71 and 89 mm

- 1 Feed - Liquid
- 2 Feed - Air
- 3 PVC Flanges
- 4 Perspex Downcomer Flanges
- 5 Nylon Bolts
- 6 Stainless Steel Screwed Rods
- 7 PVC Caps

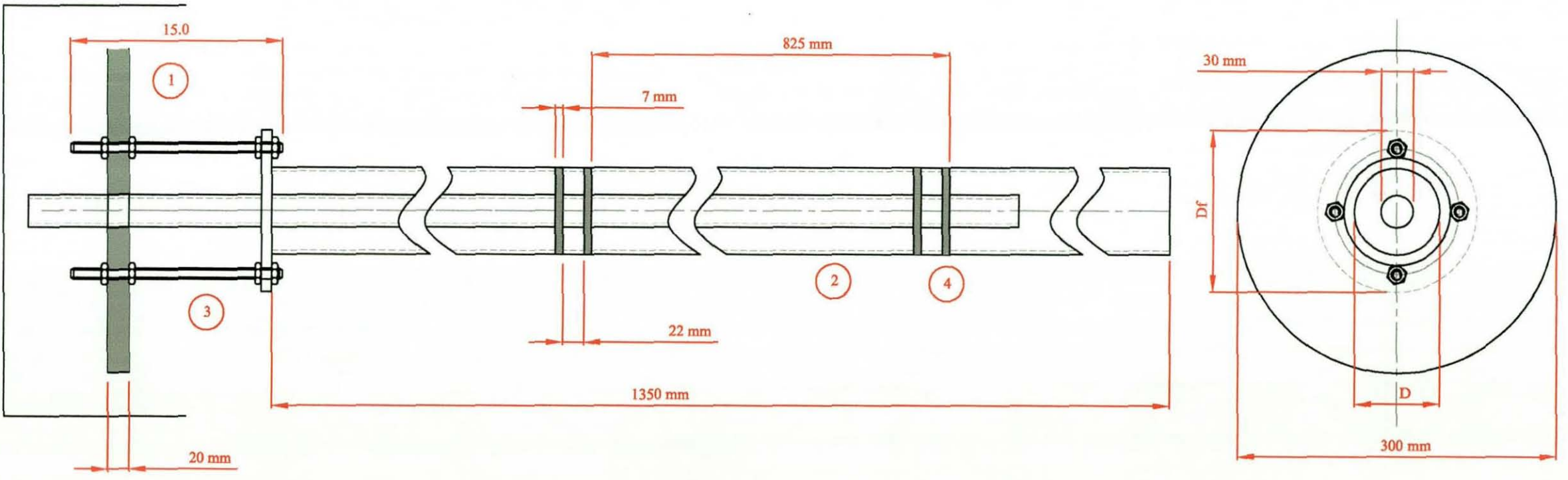
Designed by: Bader Al-Anzi Date DATE: 15 / 11 / 04 Scale: 1 : 0.9

New Air Entrainment Equipments

Df = 240 and 300 mm

D = 74, 94 and 144 mm

- ① PVC Supporting Flange
- ② Perpex Annulus and Downcomer
- ③ Stainless Steel Screwed Rods
- ④ Stainless Steel Shim



Designed by: **Bader Al-Anzi** Date DATE: 15/01/06 Scale: 1 : 0.3

New Air-Lift column Equipment

Appendix VI Publications

10th Int. Conf. on Multiphase Flow in Industrial Plant, Tropea (VV), Italy
© 2006 Centro Editoriale e Libreria UNICAL, Rende (CS), Italy
ISBN: 88-7458-049-5

AIR ENTRAINMENT RATES IN A CONFINED PLUNGING LIQUID JET REACTOR

B. Al-Anzi, I.W. Cumming, and C.D. Rielly

*Department of Chemical Engineering, Loughborough University,
Loughborough, Leics, LE11 3TU, UK.
Email: B.Al-Anzi@lboro.ac.uk
Email: I.W. Cumming@lboro.ac.uk
Email: C.D.Rielly@lboro.ac.uk*

ABSTRACT

The effects of the jet velocity, nozzle diameter, jet length and confining downcomer diameter on the gas entrainment ratio, Q_g/Q_l , have been investigated in a confined plunging liquid jet reactor. Various downcomer diameters (23 – 89 mm), jet lengths (200 – 400 mm) and nozzle diameters (6 – 15 mm) were used. Further experiments studied the effects of various downcomer lengths on Q_g/Q_l , which led to a better understanding of conditions where gas could disentrain within the confining column. The highest gas entrainment ratios were achieved when the downcomer to nozzle diameter was greater than about 5, so long as the liquid superficial velocity was sufficient to carry bubbles downward. A non-dimensional correlation relating Q_g/Q_l to Re_j , L_j/d_n and D_c/d_n has been obtained, which satisfactorily characterised the experimental results. Mechanisms are proposed in the present study that explain gas disentrainment and other phenomena inside the confining downcomer as the jet velocity is varied.

1. INTRODUCTION

Gas-liquid reactors are employed in a variety of processes, such as aerobic wastewater treatment, air pollution abatement, froth flotation and fermentation, where typically the objective is to contact the two phases to promote mass transfer. The plunging jet reactor concept has been in use for several decades, as a means of achieving high mass transfer rates by entraining gas bubbles into a liquid, at low capital and operating costs. In comparison to conventional sparged systems, such as bubbling a gas into a liquid pool, plunging jet devices are able to improve gas absorption rates by creating a fine dispersion of bubbles and by increasing the contact time between the gas bubbles and the water, at relatively low power inputs.

Plunging jets can be operated either as unconfined or confined devices. In an *unconfined* system the liquid jet plunges into an open liquid pool, creating a conical downflow dispersion of fine bubbles and a surrounding upflow of larger coalesced bubbles, as shown in fig. 1 (a). In this case, the penetration depth of the bubbles is small, due to the spreading of the submerged jet and hence the bubble contact time with the liquid is short. In a *confined* system a downcomer column is used to surround the liquid jet, as is shown in fig. 1(b) and hence the entrained bubbles may be carried to large depths by the liquid downflow. In the work described here, the liquid superficial velocity is usually sufficiently large to produce a two-

Submitted to Chinese Journal of Chemical Engineering
(CJCE).

AIR ENTRAINMENT RATES IN A CONFINED PLUNGING LIQUID JET REACTOR

B. Al-Anzi, A. Abusam and A. Shahalam*

*Kuwait Institute for Scientific Research,
Water Resources Division / Water technologies department
P.O. Box 24885, Safat 13109, Kuwait*

ABSTRACT

Plunging jets system can be applied industrially for entrainment of gas into a liquid, e.g. to oxygenate water during secondary treatment of wastewater in biological processes, and processes for air pollution control, flotation and fermentation. Plunging jets systems can be classified into unconfined and confined systems. However, the commonly used system is the unconfined plunging jet system, which is simply a tank filled with liquid to which a jet nozzle is located at the top. In such a system, bubbles have only a short residence time and therefore high rates of mass transfer cannot be obtained. Surrounding the jet by a confining column, however, allows much greater air penetration depth to be achieved.

In this study, effects of the jet velocity, nozzle diameter, jet length and confining downcomer diameter on the gas entrainment ratio (Q_g / Q_j) of a confined plunging jet reactor were investigated. Various downcomer diameters (23 – 89 mm), jet lengths (200 – 400 mm) and nozzle diameters (6 – 15 mm) were used in the study. Further, effects of various downcomer lengths were also studied. It is found that maximum gas entrainment can be achieved when the downcomer is greater than about 5 times the nozzle diameter. A non-dimensional correlation, which relates gas entrainment ratio, Reynolds number, jet length, and downcomer diameter to nozzle diameter ratio, is developed. This correlation satisfactorily characterised the experimental results, and therefore, it can be used for choosing the best combination of process variables that provide highest net air entrainment rate.

Nomenclature

ρ	density
ε	voidage fraction
D_r	air ring diameter surrounding the jet
A	cross-sectional area
d	diameter
D_c	downcomer diameter

Accepted in April by Saudi Innovation Conference 2007, Upon Tyne, Newcastle, UK.

MECHANISMS OF A CONFINED PLUNGING LIQUID JET REACTOR

B. Al-Anzi

*Department of Chemical Engineering, Loughborough University,
Loughborough, Leics, LE11 3TU, UK
E-mail: B.Al-Anzi@lboro.ac.uk*

ABSTRACT

Plunging jets can be applied industrially for entrainment of a gas into a liquid, *e.g.* to oxygenate water during secondary treatment processes. In comparison to conventional sparged systems, such as bubbling a gas into a liquid pool, plunging jet devices are able to improve gas absorption rates by creating a fine dispersion of bubbles and by increasing the contact time between the gas bubbles and the water, at relatively low power inputs. Two systems are commonly employed for this purpose unconfined and confined plunging systems. However, the vast majority of the work on plunging jet mechanisms has been conducted with unconfined plunging liquid jets, whereas relatively little has been reported with regard to a confined jet reactor.

In the study reported here a confined plunging liquid jet reactor has been utilized to investigate the effects of the mean variables; jet velocity (V_j), nozzle diameter (d_n), jet length (L_j) length and confining downcomer diameter (D_c) on the gas entrainment mechanisms and ratio, Q_g / Q_j . Various ranges of downcomer diameters (23 – 89 mm), jet lengths (200 – 400 mm) and (6 – 15 mm) nozzle diameters were used. The highest gas entrainment ratios were achieved when the downcomer to nozzle diameter was greater than about 5. New mechanisms are proposed in the present study that explains air disentrainment, bubble formation and other interesting observations inside the confining downcomer as the jet velocity is varied.

Keywords: air entrainment ratio, confined system, main variables, mechanisms.

Introduction

Gas entrainment can naturally occur due to the impact of a moving liquid, at high velocity, into a stagnant pool of the same fluid. This phenomenon can be helpful or

Submitted to Chemical Engineering Science Journal in March, 2007.

AIR LIFT COLUMN PERFORMANCE IN A CONFINED PLUNGING LIQUID JET REACTOR

B. Al-Anzi *

Department of Chemical Engineering, Loughborough University, Loughborough, UK

Abstract

The effects of the nozzle diameter and annulus diameter on water flow rate in the riser have been investigated experimentally and in a novel approach to modelling the reactor system. Various nozzle diameters (8 – 15 mm) and annulus diameters (74 – 144 mm) were used. The hydraulic model is developed to predict the water flow rate (Q_{la}) in the annulus that carries the gas-liquid mixture by the plunging jet. The model is based on an energy balance carried out over the annular riser. This model is tested against experimental data over a range of liquid flow rates, nozzle and annulus diameters; it was found that the theoretical model predicted the experimental data accurately. The agreement improves as the jet velocity increases with decreasing nozzle diameter for a given condition. This accuracy is affected slightly as the annulus diameter increases. Better predictions are achieved with narrower annular risers. Results also show that Q_{la} increases as annulus diameter increases, however superficial liquid velocity in the annulus (j_{la}) decreases. The annulus effect on gas entrainment rate (Q_g) was found to be negligible.

Keywords: Air-lift column; hydraulic model; plunging jet; induced water flow; nozzle diameter; annulus diameter

Introduction

Gas-liquid reactors are employed in a variety of processes, such as aerobic wastewater treatment, air pollution abatement, froth flotation and fermentation, where typically the objective is to contact the two phases to promote mass transfer. The plunging jet reactor concept has been in use for several decades, as a means of achieving high mass transfer rates by entraining gas bubbles into a liquid, at low capital and operating costs. In

* Correspondence to: B. Al-Anzi, Department of Chemical Engineering, Loughborough University, Loughborough LE11 3TU, UK.
E-mail: B.Al-Anzi@lboro.ac.uk

